majority TiN phase. As detailed below, this Ti_3O_5 phase is also present in the sintered pellets which are exposed to air.

DRIFT experiments were performed to correlate the above results with surface species adsorbed on the S-EXP and L-EXP powders. Shown in Figure 5-4 is DRIFT data collected at room temperature for the S-EXP (a) and L-EXP (b) powders. For clarity, the spectra have been offset along the y axis after normalization. One can easily see that except for the two broad peaks below 1000 cm^{-1}, these materials have qualitatively similar amounts of the same species adsorbed on their surfaces. Ti – O stretching bands account for the peaks at 556-564 cm^{-1} and 703-786 cm^{-1} [8]. The greater intensity of these phonon vibrations in the materials exposed for longer times suggests a greater degree of oxidation in the L-EXP powders. At higher wavenumbers, one can see a number of overlapping bands corresponding to stretching frequencies of OH groups. Peaks at 3715 cm^{-1}, 3665 cm^{-1}, 3685 cm^{-1}, and 3655 cm^{-1} have been identified as OH groups on anatase and rutile [7]. Additionally, the peak at 1625 cm^{-1} likely corresponds to a single H-O-H deformation band which has been identified on the surfaces of anatase [9]. N-H_x stretching vibrations are typically found in the 3030 – 3300 cm^{-1} region [10]. These modes are often coupled with a strong NH_4^+ deformation bending band near 1429 cm^{-1} [10]. These coupled modes have been observed on the surfaces of oxidized nano-TiN with assignments of 3100 and 1400 cm^{-1} respectively [5]. Sakka suggested the presence of these modes was due to the creation of NH_3 from TiN and adsorbed H_2O as shown [5]:

$$TiN + 2H_2O \rightarrow TiO_2 + NH_3 + \frac{1}{2}H_2$$

Finally, the peak at 1260 cm^{-1} is likely due to the detection of a C-O stretching band that has been observed at 1200 – 1275 cm^{-1} [10].

Shown in Figure 5-5 is the DRIFT spectra for S-EXP at room temperature (a) and after heating to 500 °C (b). Based on the differences in these two spectra, one can coordinate the observed evolution of gas species from the surface to the TGA/MS data presented earlier in Figures 5-2 and 5-3. First, the disappearance of the broad band in the 3600 – 3800 cm^{-1} range, as well as the single peak at 1625 cm^{-1}, confirms that physisorbed water has been removed from the surface of these powders. Secondly, the

Synthesis, Processing and Properties of Nanocrystalline Nitrides

by

Darren Thomas Castro

Submitted to the Department of Materials Science & Engineering
on August 8, 1997 in Partial Fulfillment of the Requirements
for the Degree of Doctor of Science in Ceramics

ABSTRACT

With their high strength and resistance to heat, wear and corrosion, the nitride family of ceramics demonstrates great promise in a number of engineering applications. However, there are many difficulties in sintering pure nitrides due to their covalent bonding and high melting points as well as the low quality of the commercially available powders. This thesis addresses current challenges to ceramic nitride technology through unique nanocrystalline synthesis and processing. Nanocrystalline processing has been successfully employed to attain low-temperature sinterability and unusual properties in oxide ceramics. However, due primary to the synthesis and handling difficulties of the nitrides, there has been much less investigation of nanocrystalline nitrides. The focus of this thesis lies in synthesizing and processing nanocrystalline nitride ceramics with low-temperature sinterability by exploiting the high diffusivities, extreme reactivities and ultrafine microstructure characteristic of nanocrystalline materials.

The high-quality, non-agglomerated nanocrystalline powders were synthesized through a novel tubular reactor, designed and built as part of this thesis project. This reactor makes use of a forced gas flux and filtration system to increase nanocrystal production rate and collection efficiency, as well as improve the properties (particle size, degree of agglomeration, surface area) of the nanocrystals synthesized beyond those produced by alternate synthesis routes. A key in tailoring the characteristics of the powder produced in the reactor is the use of a microwave-generated plasma. This high temperature N_2-plasma, in addition to facilitating the nitridation of the nanoparticles, serves to extend the time for particle growth by coalescence, leading to a less agglomerated and more monodisperse-sized product.

The effects of synthesis parameters on the generation of nanoparticles, in terms of the size, morphology, and composition of the particles produced in the Si-N and Ti-N systems are presented. The nano-Si synthesized (particle size: 6 nm, surface area: 485 m^2/g) undergoes external nitridation and conversion to Si_3N_4 by the relatively low temperature of 1050 °C. The Si_3N_4 (particle size: 11 nm, surface area: 270 m^2/g) and TiN (particle size: 9 nm, surface area: 225 m^2/g) nanoparticles produced in this reactor are among the very highest, if not the highest, quality (smallest size, highest surface area, least

agglomeration) powders currently cited in the literature for these nitrides. An analysis of the nitridation kinetics in the Si-N and Ti-N systems differentiates between the formation processes of these materials in this reactor.

Sintering results in the TiN system demonstrate the enhanced sinterability of nano-TiN and the tremendous potential for pressureless sintering of monodisperse, high surface area nanocrystalline nitride powders. The sintering results also highlight the need for processing which addresses the proclivity for oxidation of these materials. The processing scheme outlined generated dense, nano-structured TiN, with final grain sizes of ~140 nm, through a pressureless sintering process emphasizing improved powder handling procedures. These fine-grained materials have values of H_v (23.2 GPa) which are among the highest recorded in the literature for bulk TiN. These sintering and property results are particularly noteworthy in comparison to those noted in the literature due to the complicated processing conditions required by other researchers in previous efforts utilizing lower quality starting powders.

Thesis Supervisor: Jackie Y. Ying
Title: Raymond A. and Helen E. St. Laurent Associate Professor of Chemical Engineering

Acknowledgments

I thank my advisor, Professor Jackie Y. Ying, for her guidance and enthusiasm throughout this work, her encouragement of my professional development and for many helpful discussions. I also thank my thesis committee members, Professors Yet-Ming Chiang and John Vander Sande, whose valuable suggestions significantly improved this thesis work and document.

I thank the members of the Nanostructured Materials Research Laboratory for their friendship, help and support over the past five years. In particular, I thank Dr. Andreas Tschöpe for all he taught me about scientific research and vacuum reactor technology and for many helpful discussions during the first years of this work. I thank Kenneth Bryden and Doron Levin, the other two "founding" grad students of the lab, for numerous discussions filled with useful advice and for generally making the lab a much more pleasant place to work. I thank Martin Panchula for his advice on topics ranging from microscopy to processing as well as his friendship. Thanks also to Michael Wong for his help with the IR studies, Andrey Zarur for his assistance with the mass spectrometer, and Duane Myers for his help with the reactor. I also acknowledge the support of all the other members of the research group: Edward Ahn, Ruma Chakraverty, Mark Fokema, John Lettow, Christian Mehnert, Neeraj Sangar, Chen-Chi Wang, Lei Zhang, and Zhibo Zhang. I also thank the UROPs who were of assistance in this project: Andrew Carrillo, Susan Shi and Jessica West. Thanks also to Linda Mousseau and Ellen Weene for their help and patience in dealing with my accounting and paperwork.

I thank Mike Frongillo from the Center for Materials Science and Engineering for his assistance in the high resolution TEM studies as well as all he taught me about SEM, TEM and research at MIT. I also thank Professor Michael Cima, as well as John Centorino and Leonard Rigione from his lab, for the use of his ceramics processing equipment, in particular the glovebox with the attached furnace.

Most of all, I thank my family. The encouragement, patience and love of my fiancée, Debbi Sloat, during the final stages of this work was a crucial factor in my success. I thank her for all her support and greatly look forward to our future together. I also owe much to my parents, Larry and Trisha Castro, who have always supported me in everything that I have attempted and instilled in me the values that have made me who I am.

This research was sponsored by the Office of Naval Research (N00014-94-1-0546), with partial equipment support provided by the AT&T Foundation and the National Science Foundation (MIT CMSE: DMR90-22933). I am also grateful for the support of a National Defense Science & Engineering Graduate Fellowship from the U.S. Army Research Office.

TABLE OF CONTENTS

LIST OF FIGURES

LIST OF TABLES

LIST OF SYMBOLS

a	product particle radius
a	coefficient of thermal reflection (Chapter 2)
a	characteristic dimension of the hardness impression (Chapter 5)
a_o	lattice parameter
A	cross-sectional area of the reactor
b	stoichiometric coefficient for the nitride reaction
c	characteristic dimension of the radial/median crack
c_o	radial crack dimension
C	inherent flaw or crack length
C_{N2}	surface concentration of nitrogen on a particle
d	particle diameter
d_{hkl}	interplanar spacing
d_{obs}	observed d spacing
d_{theo}	theoretical d spacing
δ	density of a material
δ_M	density of a metal
δ_x	distance particles are from collection substrate
D	diffusivity
D_B	grain boundary diffusion coefficient
D^{eff}	effective diffusivity due to microcracking
D^N	diffusivity of nitrogen
D_V	volume diffusion coefficient
D.F.	driving force for sintering
E	Young's modulus
E_o	Young's modulus at 100% density
ε	dimensionless activation energy

η	viscosity of a gas
EXP	air-exposed powders
g_{O2}	weight gain (grams) due to O_2 pickup
G	grain diameter
γ, γ_S	surface free energy
ΔH_f	heat of formation
HCS	H.C. Starck commercial powders
HIP	hot isostatically pressed samples
H_v	Vicker's hardness
I	current
k_s	constant term for localized crack initiation
κ	cooling rate
K_c	fracture toughness
K_{sl}	coefficient of service life
L	camera length
L	length of dislocation pile-up
λ	mean free path of the gas molecules
λ_{trans}	translational part of the heat conductivity of a gas
m	molecular mass of gas
M_{O2}	mols of O_2 molecules required for surface coverage
M_w	molar mass of the metal
n	constant in sintering rate equations
N	number of molecules per volume
N_{Av}	Avogadro's number
N_{O2}	number of O_2 molecules required for surface coverage
Ω	atomic volume
p	constant in sintering rate equations

P	power
P	pressure (Chapter 2, 3, 4)
P	peak load during indentation test (Chapter 5)
P_{app}	applied load during pressure-assisted sintering
P_O	atmospheric or initial gas pressure
Q	incoming gas flow rate
R	resistance (Chapter 2)
R	Debye diffraction ring radius (Chapter 4)
R	particle radius (Chapter 5)
r	particle radius
r_o	original radius of particle
ρ	pore radius
ρ_M	molar mass of metal
S	pumping speed
S_a	B.E.T surface area
σ	diameter of gas molecules (Chapter 2)
σ	fracture strength (Chapter 5)
σ_g	geometric standard deviation
t	time
t_{coal}	time during which particle growth may occur by coalescence
T	temperature
T_{ad}	adiabatic temperature
T_o	initial temperature
τ	time for complete conversion (Chapter 4)
τ	shear stress (Chapter 5)
τ_o	dislocation flow stress
τ_{aggl}	characteristic agglomeration time

τ_{coal} characteristic coalescence time

Th throughput (leak rate in a vacuum apparatus)

UN800 unexposed to air below 800 °C

V potential difference

V volume of chamber

v gas velocity

v_{ther} thermophoretic velocity

WOM powders produced without the microwave plasma

WM powders produced with the microwave plasma

x particle neck size (radius)

X fractional conversion

y composition (at% N)

Z Pilling-Bedworth ratio

ζ grain boundary thickness

Chapter 1

Introduction and Research Objectives

1.1 Properties, Applications, Synthesis and Processing of TiN and Si_3N_4

1.1.1 Properties of TiN and Si_3N_4

The nitride family of ceramics demonstrates great promise in a number of engineering applications. TiN and Si_3N_4, in particular, are two of the most potentially useful ceramic materials of the future because of their hardness and high temperature properties. In Table 1-1 [1, 2] the properties of TiN and Si_3N_4 are compared to two other competing engineering materials, yttria stabilized zirconia (ZrO_2) and stainless steel 304.

TABLE 1-1: Properties of TiN and Si_3N_4 Compared to Other Materials [1,2]

Property	TiN	Si_3N_4	ZrO_2	S.S. 304
Bulk density (g/cm^3)	5.35	3.2	6.05	7.9
Elastic Modulus (GPa)	490	310	210	193
Hardness (GPa)	20	17.7	12.8	1.5-3.9
Fracture Toughness ($MPa\ m^{1/2}$)	3.7 – 4.3	4.9	8.5	>100
Thermal Expansion ($10^{-6}/°C$)	9.4	3.5	11.0	20
Thermal Conductivity (W/m °C)	25	32	1.7	16

1.1.2 Applications of TiN and Si_3N_4

TiN, due to its good intrinsic properties, such as high hardness, electronic conductivity and low coefficient of friction, is potentially very useful in demanding engineering applications. However, due primarily to low sintering activities in microcrystalline powders, TiN has been mostly used as a coating, rather than a monolithic material, and is not a mainstream structural ceramic [3].

TiN coatings provide high wear resistance, a low coefficient of friction and chemical stability to coated tools during machining processes [4] and have been found to increase coated tool life and speed. A quantitative assessment of these benefits may be measured by K_{sl} (the coefficient of service life, defined as the ratio of the service life of a coated cutting tool to the service life of an uncoated cutting tool) as measured in cutting titanium and steel alloys. TiN coated thread taps had a K_{sl} value of 1.5, while TiN coated drills had a K_{sl} value of 1.8 [5].

In addition to its use as a cutting tool coating, there have been efforts to develop a sinterable TiN for use in bulk cutting tool components. 10% of the world's consumed cobalt is used as a binder material for tungsten carbide components which, due to their excellent wear and corrosion-resistant properties, are used extensively in cutting tool applications. However, due to a lack of domestic ore reserves, cobalt must be imported to the U.S. from foreign and occasionally politically unstable sources. Thus there have been many efforts to try to develop alternative hard refractory materials and binder combinations. Because titanium compounds (such as TiN, TiC, and TiCN) typically use Ni as a binder, and given that sources of Ni are more stable and cheaper than Co, the development of a sinterable TiN for bulk cutting tool applications, for use with or without Ni, has been a focus of efforts [6]. As a basis for comparison to the properties of TiN listed in Table 1-1, for a sub-micron WC-Co (5 wt%), H_v is 18 GPa and K_c is 11 MPa $m^{1/2}$ [7].

The metallic-like conductivity of TiN (200 Ω^{-1} m^{-1} [8]) makes it useful as an electrically conductive ceramic for applications such as self-heating crucibles or for use as a ceramic which can be shaped by electro-discharge machining. However, the high melting point of TiN (2950 °C) makes fabrication of pure monolithic articles for these purposes, even by hot pressing, difficult [9].

Due to its high strength and resistance to oxidation and thermal shock, Si_3N_4 has potential structural applications in advanced heat engine components such as rotor blades, combustion chambers, piston caps and cylinder liners. By extending operating temperatures of these engines beyond the limits of metallic superalloys, one increases the thermal efficiency while lowering the specific fuel consumption. Additional benefits include decreased weight, leading to lower stresses in rotating components, reduced dependency on strategic materials, such as cobalt and chromium, used in metallic

superalloys, as well as decreased complexity of the engine system through the use of non-cooled components [10].

A second major area of Si_3N_4 application is in ball bearings. Bearings for high speed, high stress applications require high strength and hardness over the temperature range of operation, a low coefficient of friction and high surface finish [11]. While many ceramics meet these requirements, Si_3N_4, with its relatively high fracture toughness, has performed significantly better than other ceramics such as Al_2O_3 or SiC. When failures occur, they typically are via spall formation, originating at flaws due to residual porosity or impurity inclusions, or via non-uniform wear [11].

1.1.3 Synthesis of TiN and Si_3N_4

The typical low-quality commercial TiN powders (particle size > 1 μm) are most often produced by gas nitriding of Ti powders or by chemical synthesis with titanium-based salts [12]. Finely divided Ti is typically nitrided at 1000 to 1400 °C for 1 to 4 hours, after which the product is ground and the process is repeated to obtain stoichiometric TiN [6]. Other synthesis routes for TiN powders include the preceramic polymer route involving the pyrolysis of ceramic precursors [13] as well as the carbothermal reduction of TiO_2, a process with the drawback of producing a low-purity powder [9]. There have also been efforts to produce TiN by self-sustaining high-temperature synthesis (SHS) [14]. It was shown that these materials are often not fully converted, and that the product of combustion was a mixture of TiN and solid solutions of nitrogen in Ti with a non-uniform density [14]. The production of reaction-bonded titanium nitride (RBTN) utilizing high surface area Ti with gaseous nitrogen yields a very porous product [3].

Due to the low-quality of the powders produced by the above routes and the difficulties in sintering those powders, the most common route to TiN production is through chemical vapor deposition (CVD) processes where mixtures of $TiCl_4 - N_2 - H_2$ are reacted and TiN is deposited at 900-1000 °C (or at somewhat lower temperatures for plasma assisted CVD) [15]. The synthesis of TiN by this route is limited to thin coatings of material. Additional drawbacks to this technique include the production of HCl vapors that must be removed by a caustic scrubber or cold trap [15].

Based on the above considerations, the gas-phase reaction route has been recommended for producing high-quality TiN powders [6]. Gas-phase reactions tend to produce more homogeneous refractory materials than conventional solid-to-solid or gas-to-solid reactions due to the occurrence of nucleation in free space [6]. An additional benefit to the gas phase reaction route is the potential for producing an oxygen-free material. Carbothermal reduction of TiO_2 starts with an oxygen-containing material and will never be a route to the production of oxygen-free products. Metal Ti which is ground into a fine powder before reacting with nitrogen will also always contain oxygen due to the high reactivity of Ti powder which readily adsorbs gaseous species onto its surface and oxidizes. Given the difficulties in processing oxygen-contaminated powders [16], the gas phase reaction route for the production of TiN is potentially very useful. Recent efforts in this area using similar gases to those used in the CVD process have produced TiN powders with particle sizes ranging from 100 – 200 nm with surface areas of 20 – 30 m^2/g [17].

Si_3N_4 can be synthesized by many of the same routes as TiN. These include a direct synthesis from the raw components, such as milling of Si in an NH_3 atmosphere or SHS reactions, and the carbothermal reduction of SiO_2. Gas-phase synthesis routes involving the use of $SiCl_4$ or SiH_4 with NH_3 as well dissociation/pyrolysis reactions using $Si(NH)_2$ have also been used with success. The formation of high-quality Si_3N_4 powders is much less of an issue than it is with TiN and will not be addressed further here. See [18] for a recent review of Si_3N_4 synthesis techniques.

1.1.4 Processing of TiN and Si_3N_4

The benefits and properties of TiN and Si_3N_4 described above are only attained when the material is fully or near fully dense. Residual porosity greatly deteriorates the properties of any ceramic, especially one for high-temperature use. However, in order to densify these nitrides, sintering aids are typically needed due to the low diffusivities and covalent bonding in these materials [3, 19]. These sintering aids have a great influence (usually negative) on the properties of the resultant sample.

For the production of bulk TiN, the most common fabrication techniques are conventional sintering or hot pressing in the presence of metal additives such as Al, Co or Ni [20,21]. When a low melting point material is added to a poorly sinterable material, it

can improve sinterability by the liquid phase promotion of particle rearrangement with the solution-reprecipitation of solids. Thus, these additives play an important role in promoting densification but cause the precipitation of a second phase at the grain boundaries of the TiN [20].

In the case of Si_3N_4, oxides such as MgO, Al_2O_3, and Y_2O_3 are the typical sintering additives introduced in varying amounts [22-26] to the starting Si_3N_4 powder. The oxide additive reacts with the SiO_2 surface layers and the nitride phase of Si_3N_4 to form a liquid phase at the sintering temperature (typically 1600-1850 °C). Upon solidification, this liquid phase is retained either as a glassy or crystalline phase at the grain boundaries. This intergranular phase can soften at moderately elevated temperatures leading to a degradation of mechanical properties [27]. Residual impurities (metallic or otherwise) can also be retained in this phase leading to further deterioration of high-temperature properties [19]. Thus, it would be desirable to develop nitride powders capable of being sintered at lower temperatures without the use of sintering additives.

1.2 Research Motivation

The challenges to the utilization of TiN and Si_3N_4 can be met by a better control of the starting powder's characteristics and the processing history of the finished component. This thesis presents an approach for improving the sinterability of nitride materials by exploiting the high surface areas and ultrafine microstructure of nano-nitrides produced by a modified nanocrystalline synthesis.

In order to facilitate densification and improve the quality of a ceramic, a number of recommendations [28,29] and experimental verifications [29-31] have been made regarding the ideal starting powder:

1) For the preparation of dense green structures, equiaxed and spherical particles are advantageous due to packing considerations.

2) A slight variation in powder particle size leads to ordered packing and an absence of density variation in the green body. Substantial density variations in green bodies will become amplified in sintering resulting in internal flaws and abnormal grain growth.

3) Enhanced sintering kinetics can be realized through the use of fine powders of < 1 μm in diameter (Herring scaling law [32]).

4) Hard aggregates/agglomerates with their open arrangement of crystallites lead to the development of large pores. A close-packed aggregate may undergo preferential intra-aggregate sintering and pull away from the remaining green body. Thus, no agglomeration, or very loose agglomeration which can be broken during processing, is preferred.

5) A high degree of chemical and crystal purity can lead to enhanced reaction kinetics. Impurity inclusions due to milling media or atmospheric dust are sources of mechanical flaws.

Nanocrystalline synthesis and processing offers a means to generate a starting powder with these desirable characteristics. Nanocrystalline materials were pioneered by Gleiter and co-workers [33-35] in the early 1980s. The nanostructured compacts consist of polycrystals of 5-20 nm, such that as much as 20-50% volume fraction of the solid corresponds to incoherent interfaces (grain boundaries) between crystals of different orientations. Due to short diffusion distances, high driving forces and enhanced mobilities associated with the nanostructure, many conventional restrictions of kinetics and phase equilibria can be overcome [36]. Furthermore, the large fraction of atoms residing in the grain boundaries and interfaces of these novel materials potentially allow for new atomic arrangements, resulting in unique behavior [36]. It has been shown by numerous researchers [36,37] that nanocrystalline materials exhibit properties markedly different from their conventional, chemically identical counterparts.

For ceramics, benefits from a nanocrystalline synthesis and processing route may be experienced in both the sinterability of these materials and in the properties and characteristics of the resultant microstructure.

Due to sintering kinetics considerations, the optimum powders for densification should be mono-sized, such that all the pores are of the same size and may be eliminated simultaneously during sintering. Additionally, as the driving force for sintering is the reduction of surface energy, a high surface area starting powder is extremely desirable. Finally, the very fine grains and large volume fraction of grain boundaries typical of nanocrystalline materials enhance diffusivities and sintering in the compacted specimens.

Specifically, compared to a typical ceramic powder with grain sizes in the 1 μm range, a nanocrystalline ceramic powder with a grain size of ~0.01 μm (10 nm) can lead to a greatly increased sintering rate as shown by Eqn. (1-1),

$$\frac{d\rho}{dt} = \frac{A\gamma_s\Omega}{kT}\left\{\frac{D_V}{G^3} + \frac{\zeta D_B}{G^4}\right\} \qquad (1\text{-}1)$$

where $d\rho/dt$ is the sintering rate, γ_S is the surface free energy, Ω is the atomic volume, D_B and D_V are the grain boundary and volume diffusion coefficients respectively, A is a constant, ζ is the grain boundary thickness, and G is the grain diameter [38]. A 100-fold decrease in G (i.e. 1 μm to 0.01 μm) can theoretically lead to a 10^6 to 10^8 increase in sintering rate. A more economical sintering process is then possible at lower temperatures. Such a result has been reported for nano-TiO_2 which was sintered at temperatures 400-600 °C lower than conventional sintering temperatures and without the need for sintering additives [39]. A similar result on nanostructured WC-Co powder having lower sintering temperatures and shorter sintering times, compared to conventional material, has been reported [7]. Thus, as has been readily demonstrated with the densification of nanocrystalline oxide ceramics, lower temperature sintering with a reduced amount of sintering additive or without any additive would appear to be very promising for nano-nitrides.

Benefits from a nanocrystalline synthesis and processing approach can also be seen in the resultant microstructure of the sintered ceramic. The inert gas condensation method [40,41], by which a number of nanocrystalline materials are produced, typically yields a narrow log-normal size distribution of particles [36]. This type of distribution has led to good green body packing and normal grain growth [39]. Such starting powder could also prevent the formation of large internal flaws [42]. Besides reducing the formation of large internal flaws, the narrow distribution in powder size should also lead to a reduction in the variation of the flaw size in the finished components. When particle size varies, fracture stress varies in the material due to the statistical distribution of flaws within the ceramic [43], making engineering utilization of these materials more difficult. Finally, given that the final grain size in a densified ceramic material is directly related to the particle size of the starting powder [42] (Figure 1-1), nanocrystalline materials are

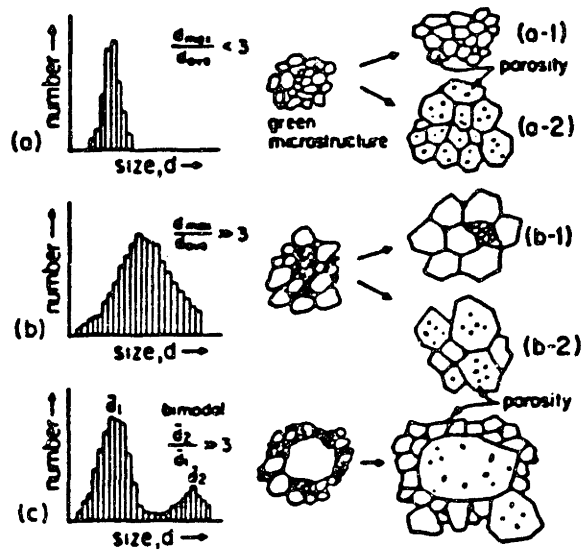

Figure 1-1: Schematic representation of the effects of particle size distribution on the sintered microstructure. For example, in (a-1), with a narrow size distribution and control of the grain boundary-pore interaction, a dense sintered ceramic with a grain size slightly larger than the starting particle size can be produced [42].

uniquely positioned to be utilized in the production of ceramic materials with an ultrafine microstructure and a corresponding improvement in material properties.

However, as outlined in Chapter 2, various limitations prevent the production of nanocrystalline nitrides by the traditional inert gas condensation technique by which a variety of nanocrystalline metals and oxides have been produced. Other nanocrystalline synthesis routes such as ball-milling or chemical precipitation have also been established for the synthesis of various nanocrystalline metals or oxides, but are not very feasible for nitride synthesis. For instance, ball milling of the very hard nitride materials typically leads to very high levels of metallic impurities from the balls and vials [44]. Chemical precipitation approaches are limited by the very reactive, air-sensitive reagents required, which must be kept isolated from air or oxides and/or oxynitrides will result. Further limitations to the chemical synthesis approach involve the use of corrosive compounds such as liquid ammonia [45]. Thus, a new synthesis approach is required for the production of highly sinterable, nanocrystalline nitride powders. This thesis describes a new synthesis technique by which such nanocrystalline nitride powders can be produced and presents processing and property results of the nanocrystalline nitride systems.

1.3 References

[1] M.L. Torti, "The Silicon Nitride and Sialon Families of Structural Ceramics," in Treatise on Materials Science and Technology, (Academic Press, 1989).

[2] H. Holleck, "Material Selection for Hard Coatings," *J. Vac. Sci. Technol. A*, **4** [6] 2661-2669 (1986).

[3] A. Pivkina, P.J. van der Put, Y. Frolov and J. Schoonman, "Reaction-Bonded Titanium Nitride Ceramics," *J. Europ. Ceram. Soc.*, **16** 35-42 (1996).

[4] H.E. Rebenne and D.G. Bhat, "Review of CVD TiN Coatings for Wear-resistant Applications: Deposition Processes, Properties and Performance," *Surface and Coatings Technology*, **63** 1-13 (1994).

[5] R.K. Saidakhmedov, M.G. Karpman, and G.P. Fetisov, "Multicomponent Ion-Plasma Nitride Coatings Based on Titanium, Vandium and Chromium," *Metal Sci. & Heat Treatmt.*, **35** [9-10] 495-498 (1993).

[6] D.D. Harbuck, C.F. Davidson, and M.B. Shirts, "Gas-Phase Production of Titanium Nitride and Carbide Powders," *J. Metals*, **38** [9] 47-49 (1986).

[7] L.E. McCandlish, B.H. Kear and B.K. Kim, "Processing and Properties of Nanostructured WC-Co," *NanoStr. Mater.*, **1** 119-124 (1992).

[8] Y. Yasutomi, A. Chiba, and M. Sobue, "Development of Reaction-Bonded Electroconductive Silicon Nitride-Titanium Nitride and Resistive Silicon Nitride-Aluminum Oxide Composites," *J. Am. Ceram. Soc.*, **74** [5] 950-957 (1991).

[9] G.V. White, K.J.D. Mackenzie, and J.H. Johnston, "Carbothermal Synthesis of Titanium Nitride," *J. Mater. Sci.*, **27** 4287-4293 (1992).

[10] D.C. Larsen, J.W. Adams, L.R. Robinson, A.P.S. Teotia, and L.G. Hill, Ceramic Materials for Advanced Heat Engines: Technical and Economic Evaluation, (Noyes Publications, New Jersey, 1985).

[11] D.W. Richerson and P.M. Stephan, "Evolution of Applications of Si_3N_4-Based Materials," pp. 282-307 in Preparation and Properties of Silicon Nitride Based Materials, eds. D.A. Bonnell and T.Y. Tien, (Trans Tech Publications, Brookfield, VT, 1989).

[12] R.P. Singh and R.D. Doherty, "Synthesis of Titanium Nitride Powders Under Glow Discharge Plasma," *J. Mater. Sci. Lett.*, **9** [2,3] 87-89 (1990).

[13] D. Seyferth and G. Mignani, "Preparation of Titanium Nitride and Titanium Carbonitride by the Preceramic Polymer Route," *J. Mater. Sci. Lett.*, **7** 487-488 (1988).

[14] M.E. Grami and Z.A. Munir, "Effect of Porosity on the Combustion Synthesis of Titanium Nitride," *J. Am. Ceram. Soc.*, **73** [5] 1235-1239 (1990).

[15] Engineered Materials Handbook, "Processing of Ceramics," pp. 810-811, ed. M.M. Gauthier, (ASM International, Materials Park, OH, 1995).

[16] G.W. Elger, D.E. Traut, G.J. Slavens, and S.J. Gerdemann, "Preparation of Submicron Titanium Nitride Powder by Vapor-Phase Reactions," *Metall. Trans. B*, **20B** 493-497 (1989).

[17] J.P. Dekker, P.J. van der Put, H.J. Veringa, and J. Schoonman, "Vapour-Phase Synthesis of Titanium Nitride Powder," *J. Mater. Chem.*, **4** [5] 689-694 (1994).

[18] R.A. Andrievski, "Silicon Nitride: Synthesis and Properties," *Russ. Chem. Rev.*, **64** [4] 291-308 (1995).

[19] J. Weiss, "Silicon Nitride Ceramics: Composition, Fabrication Parameters, and Properties," *Ann. Rev. Mater. Sci.*, **11** 381-99 (1981).

[20] K. Okuda, K. Shibata, M. Yoshinaka, K. Hirota, and O. Yamaguchi, "Fabrication and Mechanical Properties of TiN/ZrO_2 Composites by Hot Isostatic Pressing," *J. Mater. Sci. Lett.*, **15** 1615-1617 (1996).

[21] A. Kamiya and K. Nakano, "Effect of Aluminum Addition on TiN Hot-Press Sintering," *J. Mater. Sci. Lett.*, **14** 1789-1791 (1995).

[22] K. Ichikawa, "The Influence of Si_3N_4 Powder Characteristics on Sintering Behavior," in Silicon Nitride - 1, eds. S. Somiya, M. Mitomo, and M. Yoshimura, (Elsevier Applied Science, London, 1990).

[23] D.E. Wittmer, J.J. Conover, and V.A. Knapp, "Economic Comparison of Continuous and Batch Sintering of Silicon Nitride," *Am. Ceram. Soc. Bull.*, **72** 129-137 (1993).

[24] A.L. Stuijts, "Basic and Practical Aspects in Sintering Nitrogen Ceramics," in Nitrogen Ceramics, ed. F.L. Riley, (Leyden, Noorrdhoff Publishing, 1977).

[25] O. Abe and S. Kanzaki, "Kinetic Parameters for Densification of Silicon Nitride," pp. 731-738 in Ceramic Powder Processing Science, (Proceedings of the 2nd International Conference of the DKG, The American Ceramic Society, Westerville, OH, 1988).

[26] S. Kanzaki, O. Abe, T. Nagaoka, and Y. Nakajima, "Influence of Powder Characteristics on Sinterability and Microstructural Development of Silicon Nitride," pp. 739-746 in Ceramic Powder Processing Science, (Proceedings of the 2nd International Conference of the DKG, The American Ceramic Society, Westerville, OH, 1988).

[27] O. Unal, J.J. Petrovic, and T.E. Mitchell, "Mechanical Properties of Hot Isostatically Pressed Si_3N_4 and Si_3N_4/SiC Composites," *J. Mater. Res.*, **8** [3] 626-634 (1993).

[28] R.J. Brook, "Powder Design for Sintering," pp. 667-672 in Ceramic Powder Processing Science, (Proceedings of the 2nd International Conference of the DKG, The American Ceramic Society, Westerville, OH, 1988).

[29] W.H. Rhodes, "Agglomerate and Particle Size Effects on Sintering Yttria-Stabilized Zirconia," *J. Am. Ceram. Soc.*, **64** [1] 19-22 (1981).

[30] E.A. Barringer and H.K. Bowen, "Formation, Packing, and Sintering of Monodisperse TiO_2 Powders," *Comm. of the Am. Ceram. Soc.*, C-199 - C-201 (1982).

[31] S.C. Danforth, W. Symons, K.J. Nielsen, and R.E. Riman, "Processing of Silicon Nitride Powders," in Advanced Ceramic Processing and Technology, Vol. 1, ed. J.G.P. Binner (Noyes Publications, New Jersey, 1990).

[32] C. Herring, "Effect of Change of Scale on Sintering Phenomena," *J. Appl. Phys.*, **21** [4] 301-3 (1950).

[33] H. Gleiter, "Nanocrystalline Solids - A New Class of Materials," in High Purity Materials in Science and Technology - Proceedings III (Properties), (Proceedings of the 6th International Symposium, Dresden, GDR, May 1985).

[34] H. Gleiter, "Nanocrystalline Materials and Nanometer-Sized Glasses," *Europhysics News*, **20** 130-133 (1989).

[35] H. Gleiter, "Nanocrystalline Solids," *J. Appl. Cryst.*, **24** 79-90 (1991).

[36] R.W. Siegel, "Cluster-Assembled Nanophase Materials," *Annu. Rev. Mater. Sci.*, **21** 559-78 (1991).

[37] R. Birringer and H. Gleiter, "Nanocrystalline Materials," pp. 339-349 in Encyclopedia of Materials Science and Engineering, Suppl. Vol. 1, ed. R. W. Cahn (Pergamon Press, 1988).

[38] R.J. Brook, "Fabrication Principles for the Production of Ceramics with Superior Mechanical Properties," *Proc. Brit. Ceram. Soc.*, **32** 7-24 (1982).

[39] R.W. Siegel, S. Ramasamy, H. Hahn, L. Zongquan, L. Ting and R. Gronsky, "Synthesis, Characterization, and Properties of Nanophase TiO_2," *J. Mater. Res.*, **3** [6] 1367-72 (1988).

[40] R. Birringer, H. Gleiter, H.-P. Klein, and P. Marguardt, "Nanocrystalline Materials: An Approach to a Novel Solid Structure with Gas-Like Disorder?" *Phys. Lett. A*, **102** 365-369 (1984).

[41] J.Y. Ying, "Structure and Morphology of Nanostructured Oxides Synthesized by Thermal Vaporization/Magnetron Sputtering and Gas Condensation," *J. Aerosol Sci.*, **24** [3] 315-338 (1993).

[42] E. Barringer, N. Jubb, B. Fegley, R.L. Pober, and H.K. Bowen, "Processing Monosized Powders," in Ultrastructure Processing of Ceramics, Glasses, and Composites, eds. L.L. Hench and D.R. Ulrich, (John Wiley & Sons, New York, 1984).

[43] T.H. Courtney, Mechanical Behavior of Materials, (McGraw-Hill Publishing, New York, 1990).

[44] Y. Ogino, M. Miki, T. Yamasaki, and T. Inuma, "Preparation of Ultrafine-Grained TiN and (Ti,Al)N Powders by Mechanical Alloying," *Mater. Sci. Forum*, **88-90** 795-800 (1992).

[45] T. Wade, C.B. Ross and R.M. Crooks, "Electrochemical Synthesis of Ceramic Materials – An Electrochemical Method Suitable for the Preparation of Nine Metal Nitrides," *Chem. Mater.*, **9** 248-254 (1997).

Chapter 2

Forced Flow Reactor for Nanocrystal Synthesis

2.1 Introduction

2.1.1 Motivation for a Forced Flow Reactor Design

The synthesis of nanocrystalline materials involves an ultrahigh-vacuum (UHV) system with resistively-heated evaporation sources, a cluster collection device and scraper assembly, and a compaction device for *in situ* consolidation of the nanocrystalline powder produced in the chamber [1,2,3]. See Figure 2-1 for a schematic of a typical batch reactor design [4]. The precursor material is evaporated in an inert atmosphere and condenses into clusters from the supersaturated vapor formed above the evaporation source. The nanometer-sized clusters are then transported via natural convection and thermophoresis in a controlled gas atmosphere to the collection substrate, typically a liquid nitrogen cooled cold finger. The nanocrystals are then removed from the collection device with a scraper and consolidated into pellets for further testing and characterization.

Due to inherent limitations in this traditional gas condensation nanocrystalline synthesis approach, a forced flow reactor has been recommended to facilitate scale-up such that one can synthesize larger amounts of material than the few hundred mg/day that are normally produced by the conventional batch-type reactors [5]. The motivation for examining an alternative reactor design comes from the two drawbacks of the existing inert gas condensation process. First, rather than forming larger quantities of nanocrystals, increasing the rate of evaporation in these reactors leads to increased particle size due to the presence of more coalescence partners. Therefore, the rate of nanocrystalline powder production with the natural convection method (gas velocities ~1 m/s) is limited. Second, a scale-up is further complicated since collection efficiency is low due to the loss of sample to the cold surrounding chamber wall in natural convective flow [6].

Two research groups have recently pursued the formation of nanocrystalline metals by evaporation in a flowing gas environment. The application of forced flux in a study by Haas *et al.* was used to produce nanocrystalline metals (Cu and Pd) [6] by removing the nanocrystals quickly from the hot growth zone over the evaporation source. It resulted in a higher production efficiency and particle size reduction (by ~ 45%). The

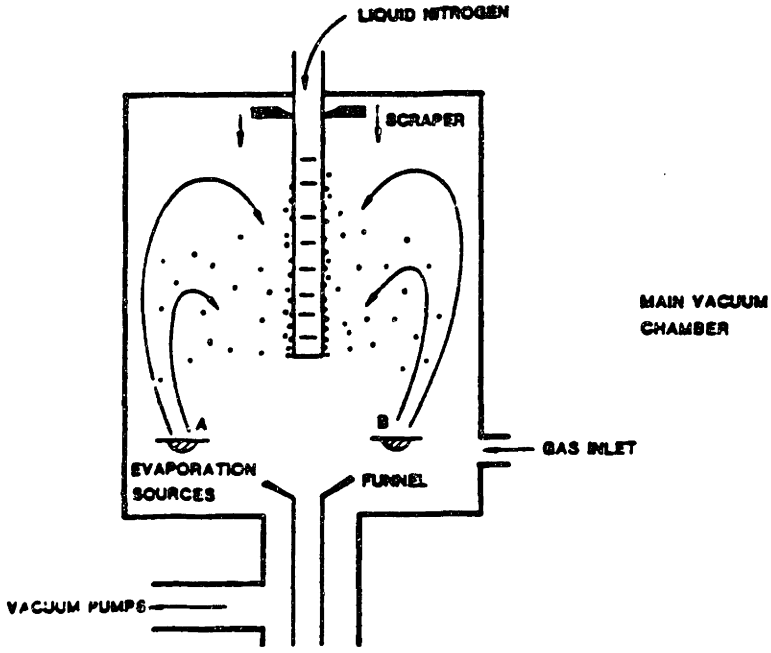

Figure 2-1: Schematic of the conventional batch-type reactor for nanocrystalline synthesis [4].

particle sizes produced still correspond to a log-normal distribution (typical of particles produced by inert gas evaporation [7], such as those formed in the batch-type reactors). The gas flux serves to reduce the residence time and the particle number density. Therefore, the number of potential coalescence partners decreases and a smaller particle size results [6]. Iwama *et al.* has also demonstrated the potential for this synthesis approach by evaporating various materials in a high-velocity gas stream (He or Ar) to produce nano-Ag (< 10 nm), nano-Sb (~ 20 nm) and nano-Mn (< 30 nm) [8, 9].

2.1.2 Motivation for Nitridation Capability in Reactor Design

The batch-type reactors described above may readily synthesize various metals through evaporation or sputtering. Much of the work on nanocrystalline ceramics has been done on oxides where the materials are deposited in their metallic form and then post-oxidized when oxygen or air is introduced into the reactor. However, kinetic limitations prevent room temperature post-nitridation. Furthermore, various metals cannot be evaporated or sputtered in a stagnant nitrogen atmosphere due to nitridation of the metal sources. Additionally, with their very low vapor pressures and very high melting points, almost all nitride ceramics cannot be evaporated directly. A recent review article summarized the synthesis of a large number of nanocrystalline oxides (TiO_2, ZrO_2, Y_2O_3) and intermetallic materials (TiAl) in the gas-condensation chamber. This article also noted the synthesis of MgO, Al_2O_3 and SiC by plasma flame and arc discharge techniques in its discussion of gas-condensation synthesis techniques [10]. However, notable by their absence was the mention of any nanocrystalline nitride materials produced in this manner. An additional drawback to the batch-type reactor design, even in the formation of nanocrystalline oxides, is the agglomeration caused in some cases (such as the formation of nano-TiO_2) during the post-oxidation process. This is due to the necessary rapid introduction of oxygen needed to oxidize nano-Ti which causes temperatures to rise over 600 °C on the collection substrate such that some nearby particles sinter and form dense agglomerates [11].

As a large part of this thesis project, we have constructed a tubular flow reactor, designed with the motivations outlined above, to both scale-up the traditional batch-type reactor process as well as produce high-quality nanocrystalline nitride materials via a gas phase reaction. The innovative separation of the particle generation, nitridation and

collection processes has allowed us to optimize each of these functions in this novel reactor. The reactor, each of these processes, and some of its operating characteristics, are described below in detail.

2.2 Reactor Design and Operation

2.2.1 Introduction

I have included several features in the reactor design to offer better control of synthesis conditions leading to the optimization of the particle size distribution and minimization of agglomeration. The components and features of my reactor are described below; the effect of utilizing this equipment in the synthesis process, as well as the scientific principles explaining the results, are described in detail in Chapters 3 and 4. In order to accomplish the goals of this project, many custom components (37) were designed and built or obtained through modification of off-the-shelf parts. These included pieces as varied as the microwave plasma applicator which was altered so that it could be placed into the synthesis process "in-line" rather than upstream as the manufacturer originally designed and the buna-n seals which I handcrafted such that the gate valves on the filter collection device could be used with NH_3. During the construction and optimization process, the reactor underwent many modifications, some of which are detailed in the following sections.

2.2.2 Operation Overview

A schematic of the final design of the tubular flow reactor is shown in Figure 2-2, and a photograph of the reactor is shown in Figure 2-3. Each experiment began after a satisfactory leak check of the assembled apparatus. The various incoming gas flow rates were set with mass flow controllers (MKS and Sierra Instruments). Helium (He) entered at one end of the reactor and flowed over a resistively heated crucible where metal was evaporating. An IR pyrometer (E^2T Comet) was used for temperature monitoring and control of the evaporation crucible. The metal was vaporized from the thermal evaporation source into the cooler He gas where the decreasing temperature decreased the equilibrium vapor pressure leading to a high supersaturation. At this high supersaturation, the metal vapors rapidly nucleated homogeneously. A vacuum pumping system, consisting of a Leybold Roots Blower WSU2001 backed by a Vane Pump

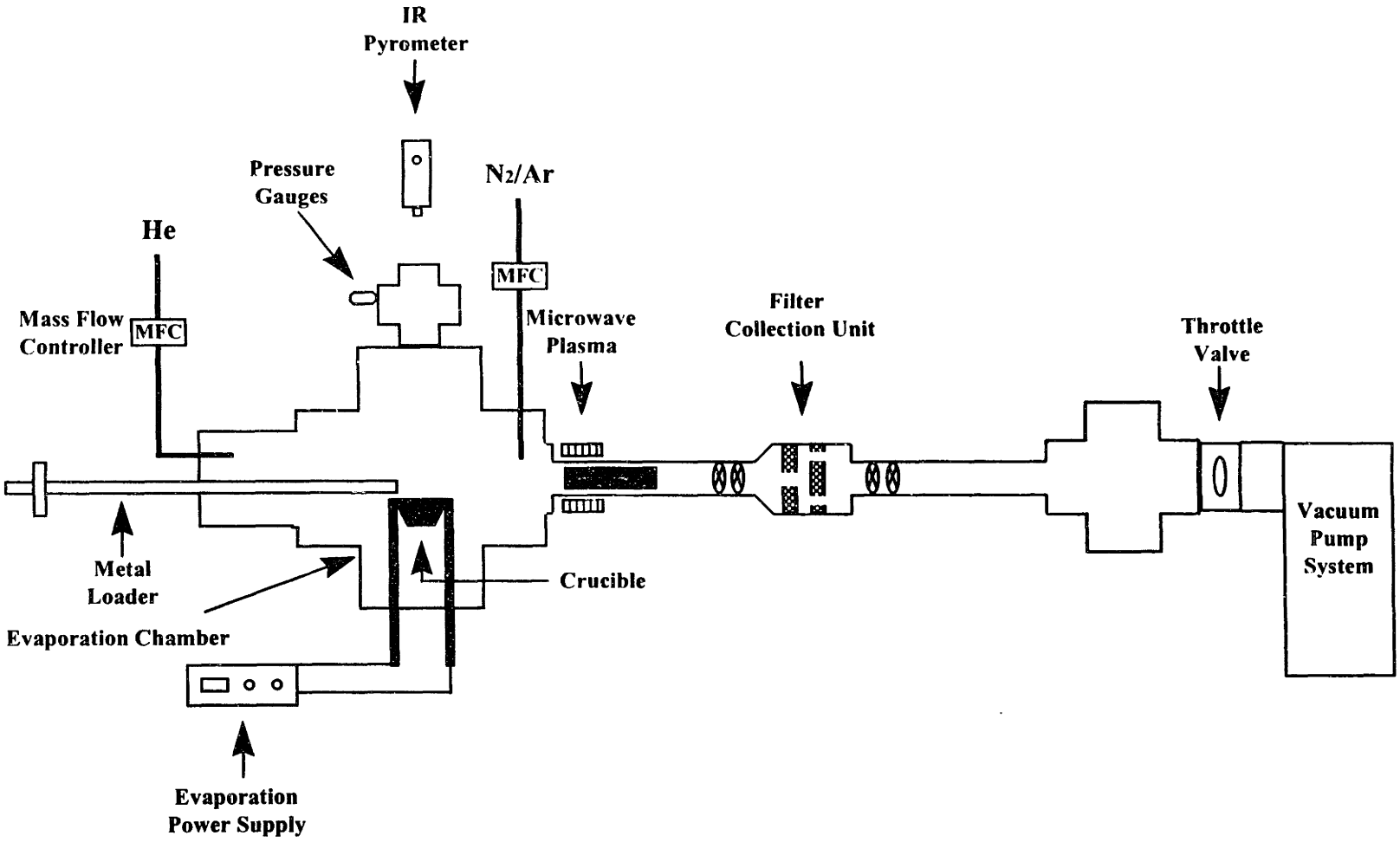

Figure 2-2: Schematic of the forced flow reactor for nanocrystal synthesis.

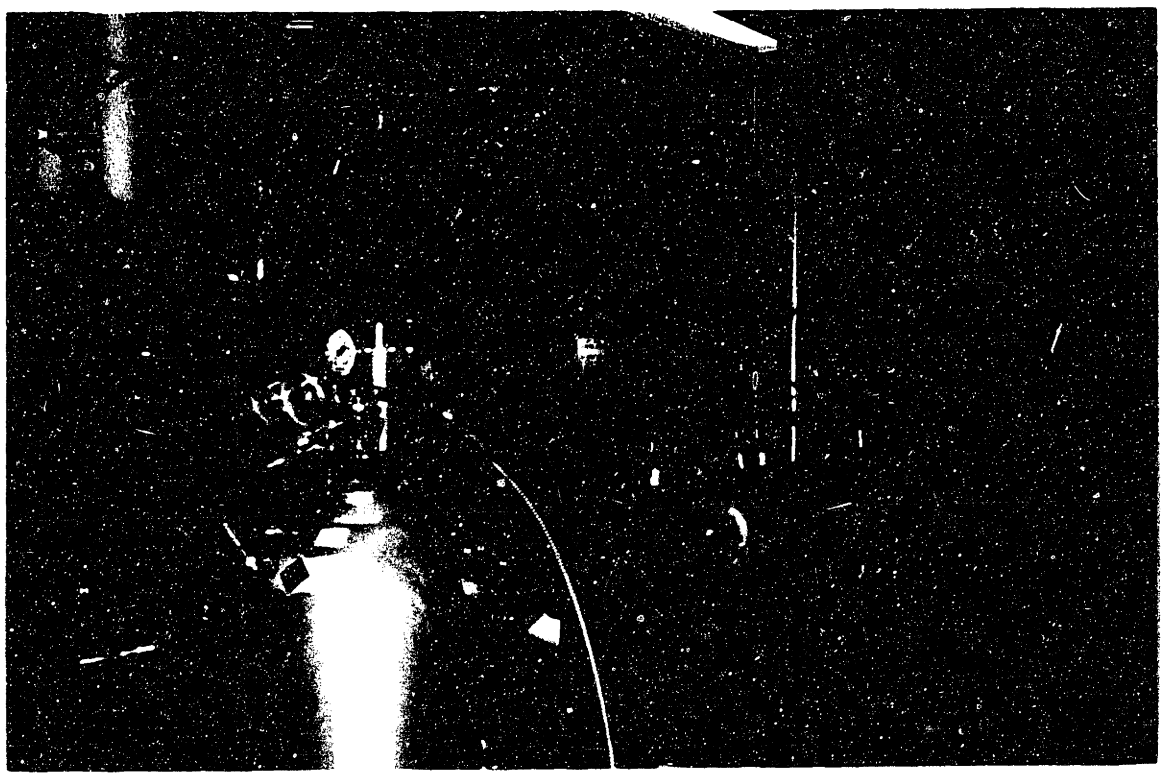

Figure 2-3: Photograph of the forced flow reactor for nanocrystal synthesis.

SV280, continuously removed the metal particles in the gas stream from the growth zone over the evaporation source. Thus, high evaporation rates, leading to high production rates, could be utilized without forming large particles due to coalescence of the particles over the hot thermal evaporation source. Just downstream of the thermal evaporation source, a mixture of nitrogen and argon was injected from a second entrance into the gas stream, and the entire gas mixture, with the entrained particles, passed through a microwave generated plasma zone. This microwave plasma provided a source of nitrogen radicals for *in-situ* nitridation of the evaporated metal nanocrystallites. The particles continued to travel the length of the reactor and were collected by a variety of devices downstream.

2.2.3 Thermal Evaporation Operatio·

The transformers used to power the evaporation source allow the use of both refractory metal (high amperage/low voltage) and carbon (low amperage/high voltage) based evaporation boats. As molten Si is a very aggressive material with unstable evaporation properties, one of the biggest challenges to successful operation involved the selection of a suitable evaporation crucible. Commercially available refractory metal crucibles (W, Ta, etc.) were unsuitable due to alloying with the molten Si metal causing crucible failure, while the available graphite boats were much too small for use at the production rates desired. The challenge then was designing an evaporation boat of suitable volume with a geometry and intrinsic properties such that it would have the appropriate resistance to pass enough current to heat the molten metals to temperatures in excess of 2200 °C, but would not be too thin such that it would fail prematurely. After 16 trials of crucibles differing in geometry and/or material, a tapered graphite (POCO-DFP grade) evaporation boat with a usable volume of 4.37 cm^3 was selected. A custom-designed magnetically coupled transfer device allows metal to be continuously transported from a reservoir at the front of the reactor into the evaporation boat such that the molten metal pool may be continually replenished. The final boat design permits Si evaporation rates of 10.8 g/hr and Ti evaporation rates of 10.6 g/hr. The micrographs in subsequent chapters (Figure 3-2 and Figure 4-4) illustrate that nanocrystallites are effectively produced by this reactor design despite the high evaporation rates. This is

especially impressive considering that in order to produce high-quality nanocrystallites in a batch-type reactor, a typical thermal evaporation rate is on the order of 0.3 g/hr.

The thermal evaporation controller, with feedback supplied by the pyrometer, allowed one to track and control the potential difference (V) and current (I) across the evaporation source during operation. This was critical to maintaining consistent evaporation conditions. During crucible heat-up, the voltage was increased at a rate of 0.25 V/min until the operating temperature was reached. Shown in Figure 2-4 are plots of the resistance ($R = V/I$ [12]) and power ($P = I^2R$ [13]) of the evaporation source during the heat-up and evaporation of Ti for the synthesis of nano-TiN. Figure 2-5 is the corresponding plot of the temperature of the evaporation source for the experiment represented in Figure 2-4. The spikes in the data reflect times when a new Ti pellet was dropped into the evaporation boat. During evaporation, the molten Ti, and the conducting TiN which subsequently formed on the crucible, decreased the resistance of the crucible, leading to the passage of more current (at constant voltage) and an increase in the power dissipated by the crucible. The voltage was subsequently adjusted during operation to compensate for the decrease in resistance, and to maintain fairly constant power and temperature values for the evaporation source.

2.2.4 Downstream Process Control and Velocity Determination

The gas flow, generated by a vacuum pump and controlled with mass flow controllers and a throttle valve, brings the generated nanoclusters quickly out of the hot growth zone to prevent undesirable particle growth. This forced gas flow is also the key to the "scale-up" effort that this reactor represents. In conventional nanocrystalline batch reactors, material is transported only by convection and thermophoresis (at velocities on the order of 1 m/s). By utilizing a forced gas flow, velocities between 3 and 40 m/s could be achieved to produce nanocrystalline materials at a greater rate.

A schematic of the downstream pressure controller system used to control the pressure, gas composition and particle velocity is shown in Figure 2-6 [after 14]. In this type of closed loop feedback control, optimum residence time with the desired gas composition is achieved by independent control of the mass flow of the incoming gases while simultaneously controlling the total pressure of the gas mixture through the use of a motor-driven throttle valve. The gas stream, whose composition and quantity are fixed

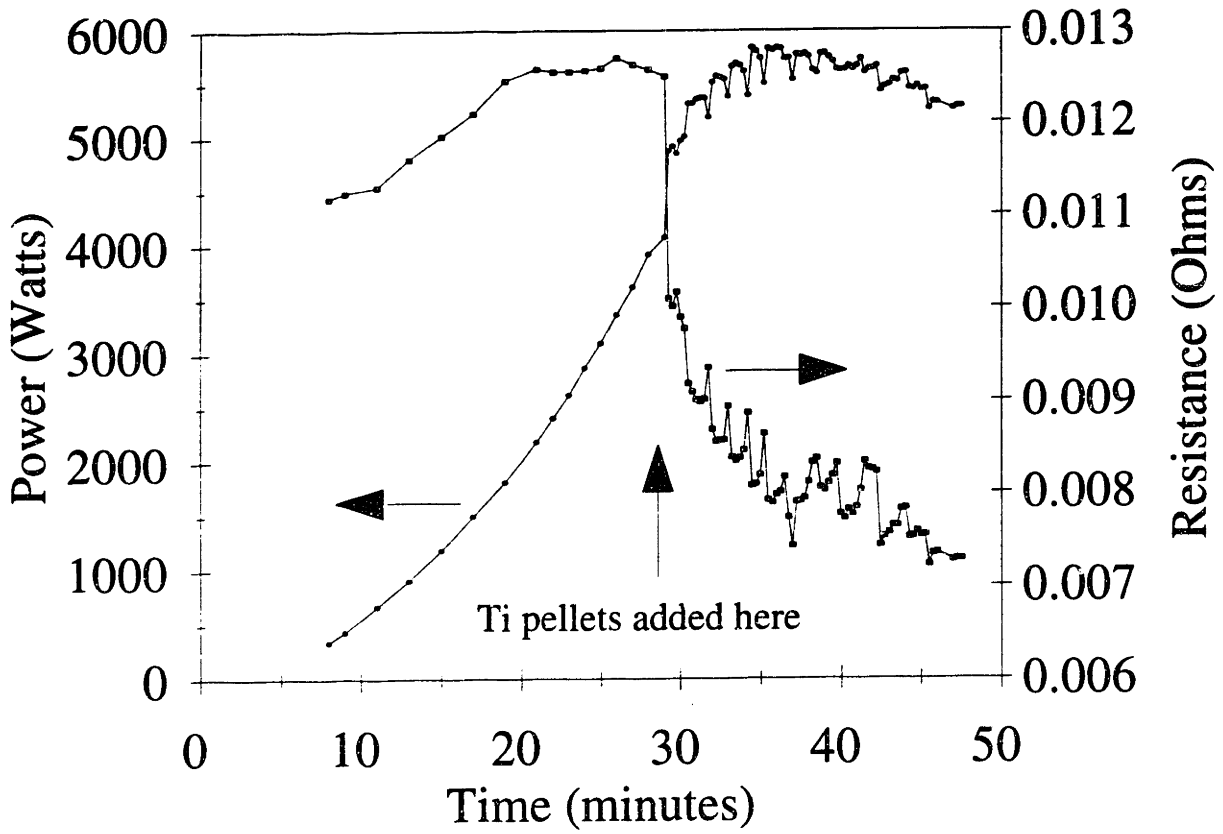

Figure 2-4: Power and resistance of the evaporation source as nano-TiN is being synthesized.

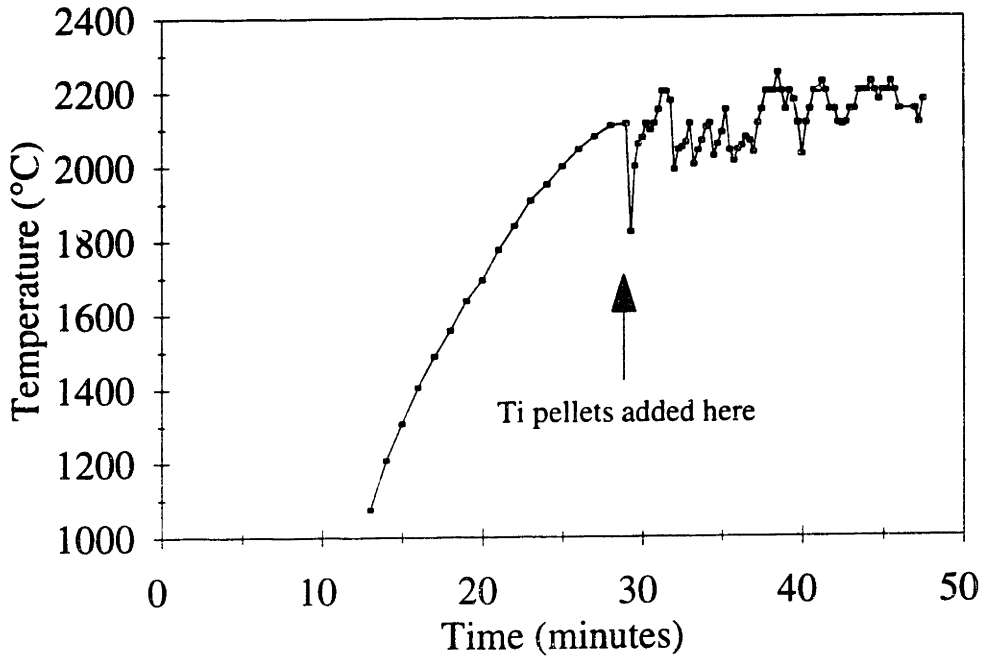

Figure 2-5: Temperature of the evaporation source as nano-TiN is being synthesized.

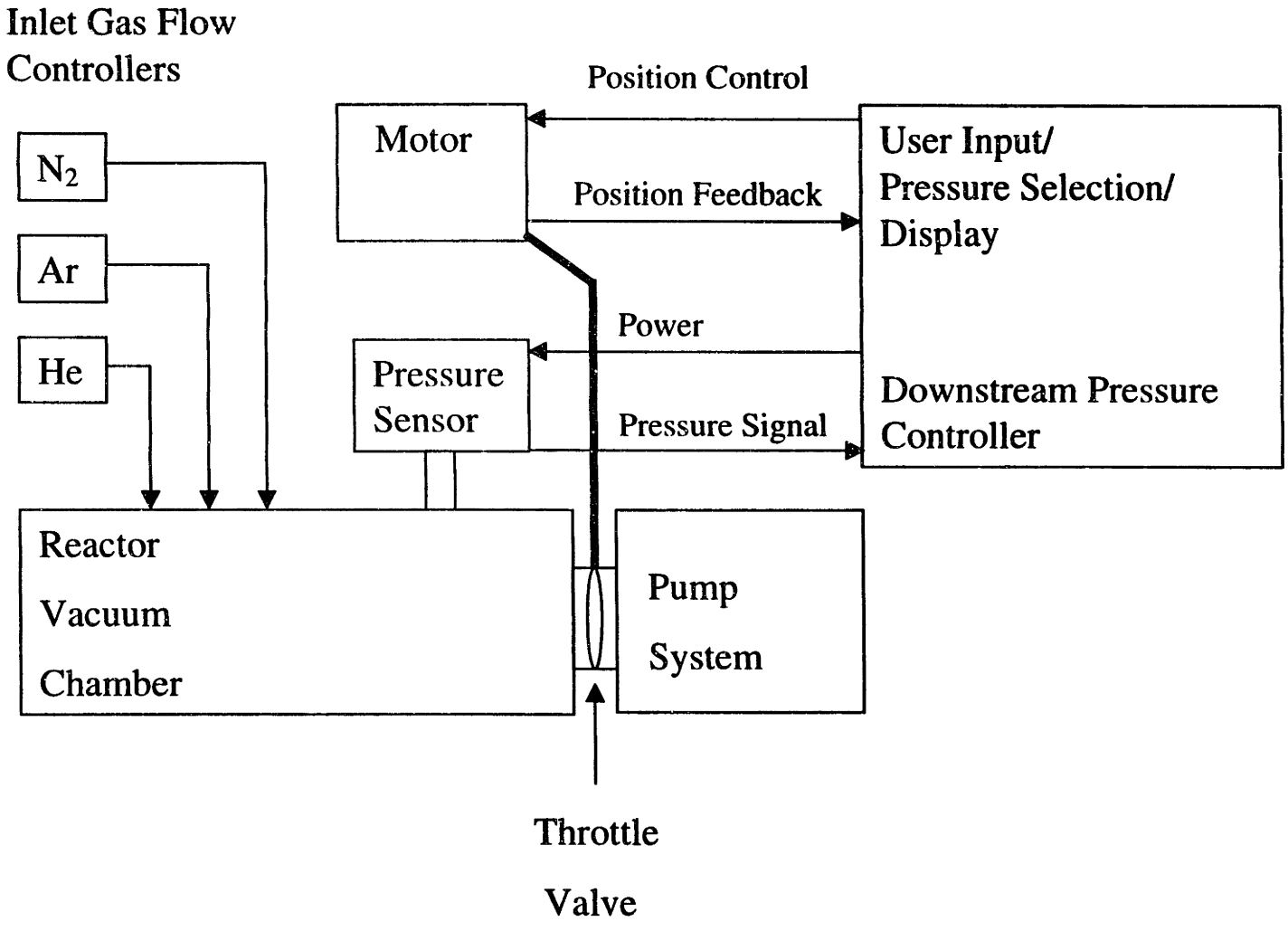

Figure 2-6: Schematic of downstream pressure controller system.

by the mass flow controllers on the inlet gas lines, flows out of the reactor chamber through the restriction of the throttle valve into the vacuum pumping system. To maintain the reactor at the desired pressure set point, the controller reads the pressure value in the chamber from the pressure sensor, compares it to the desired value, and then drives the throttle valve to the appropriate conductance value. In this manner, the desired pressure in the reactor may be maintained despite significant, dynamic changes which occur during the synthesis process. Examples of these changes include those associated with an increase in gas stream temperature due to operation of the microwave plasma and the exothermic product reactions taking place within the reactor, as well as with an increase in the conductance of the collection filter materials as particles are deposited on the filter discs. As will be shown in Chapter 3, the particle size produced is a strong function of the operating pressure. The ability to easily maintain a constant pressure throughout the synthesis process was a key to the uniformity of the particles produced in this reactor.

Knowing the reactor pressure, reactor cross sectional area and incoming gas flow rate (Q), one may determine the gas (and particle) velocity [8]. The gas velocity (v) may be varied and determined as in Eqn. (2-1),

$$v = \frac{P_o \cdot Q}{P \cdot A} \tag{2-1}$$

where P_O and A are the atmospheric gas pressure and the cross-sectional area of the tube, respectively [8].

2.2.5 Microwave Plasma Processing for Nitridation

Direct current (DC) and radio frequency (RF) plasma processing has been used extensively in recent years to produce a variety of ceramic powders (including Si_3N_4 and AlN) by several processing routes [15]. However, very little work has been done with the synthesis of ceramic powders in microwave plasmas. Some oxide powders (ZrO_2 with Al_2O_3 and Y_2O_3) have been produced though microwave plasma synthesis routes utilizing the microwaves as a source of heat for the pyrolysis of nitrate solutions and to excite the reacting gases [16]. There is also one report of the synthesis of $ZrH_{0.6}N$,

resulting from the reaction of $ZrCl_4$ with N_2 or a mixture of N_2/NH_3 (4 vol%) in a microwave plasma [17]. Additionally, silicon nitride films [18] have been formed by reacting silane (SiH_4) with ammonia (NH_3) in a microwave plasma discharge.

In these studies specific to silicon nitride as well as other work on general plasma reactions [19], it was found that the excitation frequency of the plasma can have a major impact on the plasma process. For instance, deposition rates in Si_3N_4 film formation are 10 to 25 times higher when a high frequency (microwave) plasma is used as compared to a low frequency (audio or radio) plasma [18]. A recent study quantitatively examined nitrogen atom behavior in a low pressure microwave generated nitrogen plasma. The N atom flux was measured by a chemical titration method. At a pressure of 0.56 mbar (on the same order as the operating pressure of this reactor), and a microwave power of 250 W (significantly lower than our typical 700 - 850 W), a N atom flux of 5.2×10^{17} cm^{-2} sec^{-1} was measured. The N_2 gas was converted to atomic nitrogen by electron impact dissociation as represented by Eqn. (2-2):

$$N_2 + e^- \rightarrow N + N + e^- \qquad (2\text{-}2)$$

In the region closest to the coupler, most of the ionic species were N_2^+, but a significant fraction (about 15 %) were N^+. Homogeneous ionization reactions were the significant source term and recombination at the walls was the dominant sink term [20,21]. Another study [22] with pressures of 10.67 to 26.67 mbar and microwave powers of 400 to 900 W showed that the atomic nitrogen concentration could be increased by mixing in 10% argon with the nitrogen. The heavier, oscillating argon particles impacting the N_2 particles increased the amount of dissociation beyond that created by electron impact alone (2.1% vs. 0.6%) [22]. Thus, it seemed beneficial to explore the use of a microwave plasma in the synthesis of nitride powders, both from the viewpoint of its potential effectiveness as well as due to the fact that very little work had been done previously in this area.

Based on the above considerations, a microwave (2.45 GHz) applicator (ASTEX 2110/PA38) was added to the reactor directly adjacent to the evaporation chamber along with a second gas entrance just beyond the evaporation source. The upstream gas

entrance is used to introduce He for the evaporation a
nanocrystallites past the evaporation crucible. At the
crucible, a mixture of N_2 and Ar is injected. As this g
applicator, a plasma of activated nitrogen species is ger
nitride the metal nanocrystallites entrained in the forced
the plasma matched that seen by others who descri
microwave plasmas corresponding to electrons, ion
nitrogen [22]. As will be detailed in Chapters 3 and
aided the nitridation process of the various metal nanoc

A complication observed due to the use of the r
increased temperature in the plasma zone, there was a
within the microwave cavity. This caused some an
attempted to pass through the microwave cavity.
particular the nitrogen over the evaporation source, or
detailed in section 4.3.2.

2.2.6 Product Collection Processes

The nanocrystalline materials synthesized flow
in the gas stream and were collected by a variety of tec
device was important because it directly impacted the
and the subsequent handling of the powders collected.

The first generation collection device was a col
rotating, liquid nitrogen-cooled stainless steel disc
thermophoretic force with respect to the gas stream.
reactor was controllably backfilled with air, exposi
moisture, and the particles were scraped off the rotating

Radiometric forces, such as thermophoresis, d
radius (r) to the mean free path of the gas molecules (λ
the result of gas molecules at different temperatures
opposite sides with different mean velocities. If the su
perpendicular to the collection disc) is enough to overc

over the length of the cooled collection substrate, the nanoparticle will be deposited onto the disc [23,24].

The mean free path (λ) in the reactor can be calculated by [25]:

$$\lambda = \frac{1}{\sqrt{2}\,\pi\,\sigma^2 N} \tag{2-3}$$

where σ is the diameter of the gas molecules and N, the number of molecules per volume at a given pressure (P) and temperature (T), can be calculated from [25]:

$$N = \frac{P\,N_{Av}}{R\,T} \tag{2-4}$$

where N_{Av} is Avogadro's number. Using a pressure of 2 mbar (2×10^2 Pa) and a temperature (T) of 423 K for the gas molecules at the end of the reactor where they are collected, $N = 3.425 \times 10^{22}$ molecules/ m^3. Taking an average gas molecule diameter (σ) of 2.5 Å in Eqn. (2-3), $\lambda = 1.052 \times 10^{-4}$ m in the reactor. Thus, r ($3 \times 10^{-9} - 5 \times 10^{-9}$ m) is much less than λ, and the following equation can be used to calculate the thermophoretic velocity (v_{ther}) at which the free nanoparticle moves toward the region of lower temperature [23],

$$v_{ther} = -\frac{1}{5(1+\pi a/8)}\frac{\lambda_{trans}}{P}\Delta T \tag{2-5}$$

under the influence of a temperature gradient (ΔT) at a given pressure (P). a is the coefficient of thermal reflection and may be taken as 1. λ_{trans} is the translational part of the heat conductivity of the gas and may be calculated by:

$$\lambda_{trans} = \frac{15\,R\eta}{4\,m} \tag{2-6}$$

where m is the molecular mass and η is the viscosity of the gas. λ_{trans} is ~ 0.0396 kg m/s^{3}K in the reactor leading to $v_{ther} = 9.83 \times 10^{-3}/\delta_x$ (m/s) where δ_x (m) is the distance the particles are from the disc. With the diameter (length) of the collection disc being 0.1524 m, particles moving at 10 – 25 m/s will have 1.524×10^{-2} – 6.096×10^{-3} sec to be deposited on the disc. Based on the distance from the collection disc, both the thermophoretic velocity and the distance the particle must travel toward the disc to be

collected are known. One can then compare the required time for deposition to the time the particle takes to travel past the disc and determine the probability that a particle, starting at a given distance from the disc, will be collected. These comparisons are shown in Table 2-1. Given the approximations necessary, and the uncertainty in these types of calculations, $v_{ther} = 10 \times 10^{-3}/\delta_x$ (m/s) is taken for the calculations shown in Table 2-1.

TABLE 2-1: Collection Likelihood for Nanoparticles on Liquid N_2 Cooled Disc

Distance from Disc	v_{ther} (m/s)	Dist. Traveled at v_{ther} in 0.015 s	Coll. Likelihood in 0.015 s	Dist. traveled at v_{ther} in 0.006 s	Coll. Likelihood in 0.006 s
0.001 m	10	0.150 m	likely	0.06 m	likely
0.010 m	1	0.015 m	probable	0.006 m	unlikely
0.015 m	0.67	0.010 m	unlikely	0.004 m	unlikely

Given that there is ~ 0.055 m on either side of the collection disc (due to the width of the reactor at that point), one can see from the above calculations that a very small percentage of the gas stream passing the collection disc will be close enough to it to allow for deposition of the nanoparticles entrained. (The above calculation neglected any boundary layer effects around the disc which would be likely to reduce the collection probability even more.) Thus, it is not surprising that this collection technique was found not to be efficient (see Table 2-2). The collection data in that table for the forced flow reactor is for TiN by the various collection methods. The data for the batch-type reactors is from work done on nano-Sn in our laboratory [26]. The differences in collection rates with the liquid-N_2 cooled substrates in each reactor are due primarily to the much higher gas (particle) velocities with the forced gas flow, but the smaller size of the collection disc in the forced flow reactor also has an effect. However, based on the above calculation, it is surprising that thermophoresis was recently advocated as a suitable technique for collection of nanocrystals in a forced flow reactor [6].

An additional difficulty with the liquid N_2 cooled disc occurred when NH_3 was used as a plasma reactant gas for the production of nitrogen radicals in an effort to increase the conversion of Si to Si_3N_4 in the reactor. With only Ar, He and N_2 flowing past this disc, solidification of the gas stream on the collection disc was not a problem

when liquid nitrogen at -195.9 °C was used to cool this disc. However, because NH_3 condenses at -33.2 °C and freezes at -77.8 °C, NH_3 solidified quite readily on the disc. A new cooling mechanism, consisting of a circulating chiller system utilizing an ethanol/methanol/water mixture at -30 °C was added to the reactor to cool the collection disc when NH_3 was used as a process gas.

Table 2-2: Collection Data for Reactors

Reactor Type	Evaporation Rate	Collection Rate: Liquid N_2 Cooled Substrate	Collection Rate: Chilled Walls	Collection Rate: Filter Unit
Batch	~ 0.3 g/hr	~ 0.1 g/hr	-	-
Forced Flow	10.6 g/hr	0.05 g/hr (0.37%)	1.15 g/hr (9.3%)	1.09 g/hr (8.8%)

The second generation collection device stemmed from the observation that small amounts of particles were deposited at room temperature along the length of the glass tube connecting the evaporation chamber to the original collection chamber where the collection disc was mounted. By intentionally cooling this entire tube, which had a diameter of 7.62 cm and a length of 1.04 m, a very large collection substrate was created. A brine solution (-20 °C) of 60 wt% ethylene glycol with 40 wt% water was recirculated through a 4" PVC pipe that was fitted and sealed around the entire tube length. This chilled tube could be disconnected from the rest of the reactor and powders on its interior wall could be scraped off and collected using a plastic plunger. This modification led to greatly improved collection efficiencies (see Table 2-2). However, the product powders are also subjected to air exposure during scraping in this collection approach.

Because we were concerned about the effect of air exposure of nanocrystalline nitride powders on their sintering behavior and interfacial chemistry, we decided to add a collection device with the capability of handling these high surface area nitrides without exposure to the atmosphere. Therefore, a third generation collection unit based on a valved filter collection device was added to the reactor to allow for powder removal from the reactor without exposure to air. A significant effort was devoted to improving the collection efficiency of this unit. A variety of polymer-based membrane materials, porous metals and metal felts with various pore sizes were utilized in several

configurations to optimize the yield of the collection procedure while continuing to satisfy the gas flow and operating pressure requirements of the synthesis process.

A variety of polymer-based filters (Millipore Flouropore Membrane) with different pore sizes (0.2 μm, 1.0 μm, 3.0 μm) were examined for their performance. However, the polymer-based filters presented a significant problem in handling. In order to accommodate the flow rates required, they had to be very thin. This often led to tearing of these materials while mounting them in the collection device. A bigger problem was their typically low throughputs associated with their relatively smaller available pore sizes as compared to other filtration materials. Particularly as they started to get coated, the gas throughput would drop significantly, leading to an untenable rise in the operating pressure of the reactor as the throttle valve opened fully in an attempt to compensate for the increased flow resistance and reduced flow rate.

Therefore, due to the handling and throughput difficulties of the polymer-based filters, as well as concern about temperature constraints, a metal-based filter was utilized for this third generation collection device. Due to their thickness, even with pore sizes ranging from 60 – 100 μm the available porous metals (Mott and Newmet Krebsöge) had flow rates that were too low, or pressure drops that were too high, to be used effectively in this device. However, the right balance between mechanical properties, permeability and collection efficiency was found in a stainless steel fiber felt mat material (SIKA-FIL from Newmet Krebsöge). This material consists of 316 stainless steel fibers 4 – 100 μm thick which are rolled and sintered on a mesh screen backing. The filters used were 36% – 45% porous and had a nominal, average pore diameter of 18 – 25 μm (manufacturer's reference values). The effectiveness of these filters, despite their large pore size relative to the nanocrystalline particles collected, stems from the development of an "ultra-filter" of nanoparticles deposited on the metal filter. Particles which are smaller than the pore size of the filter may be trapped through adsorption by the micro-roughness of the pore walls during diffusion by Brownian motion through the filter. With time, a "dust cake" consisting of nanoparticles develops on the surface of the metal filter. This cake may then greatly increase the efficiency of the filter by trapping additional particles by a blocking mechanism now that the size of the pores in the cake are on the same order as the nanoparticles themselves [27].

In order to compensate for the pressure drop in the filter media as it becomes loaded, a pattern of holes was placed in these filters. In an attempt to minimize the decrease in collection efficiency due to these holes, two filters with different hole patterns were mounted 0.64 cm apart in the filter collection unit. On both the upstream (Figure 2-7a) and downstream filter (Figure 2-7b), four holes (drill size #32, 0.1160" for 4-40 threaded holes) at 90° intervals on a bolt circle with a radius of 1.70" were used to attach the filters. One hole (radius = 0.5") was placed in the center of the upstream (front) disc. On the downstream (rear) filter disk, eight holes (drill size #16, 0.1770") were made at 45° intervals on a bolt circle with a radius of 1.44". These eight holes are offset by approximately 22.5° from the four #32 holes and were placed as close as possible to the mounting ring support such that the particles would have to travel the maximum distance across the downstream filter after they passed through the center hole of the upstream filter. In order to boost the efficiency of this unit further, the collection filter unit was wrapped in Cu tubing and liquid N_2 was run through the tubing during operation.

Following a synthesis run in the reactor, the reactor was backfilled with high purity N_2. The four gate valves on the filter collection device were closed (to isolate both the product and the reactor) and the collection unit was moved to a glovebox (H_2O < 1 ppm, O_2 < 15 ppm) for powder removal and further processing. Evidence of the success of this unit in preventing exposure of the product to air comes from the observation that when removing the collection unit pieces from the glovebox, small residual remnants of pyrophoric TiN powders on or in the unit catch fire upon exposure to air when the glovebox antechamber is opened.

As shown in Table 2-2, this combination of filters, holes and cooling designs proved very effective in collecting the nanocrystalline powders while permitting the high gas flow rates to be maintained at the required pressure. High quality nano-TiN materials can be collected at a rate of 1.09 g/hr. This represents an increase of 2270% over the collection attempts using the liquid nitrogen-cooled disc (0.05 g/hr). Given that the evaporation rate of Ti in our reactor is 10.6 g/hr, our collection rate of 1.09 g/hr of TiN means that 8.8% of this evaporated Ti is collected as TiN. This reactor represents a 10-fold increase over the collection rates (~ 0.1 g/hr) achievable in the traditional batch-type reactors for the synthesis of nanocrystalline materials.

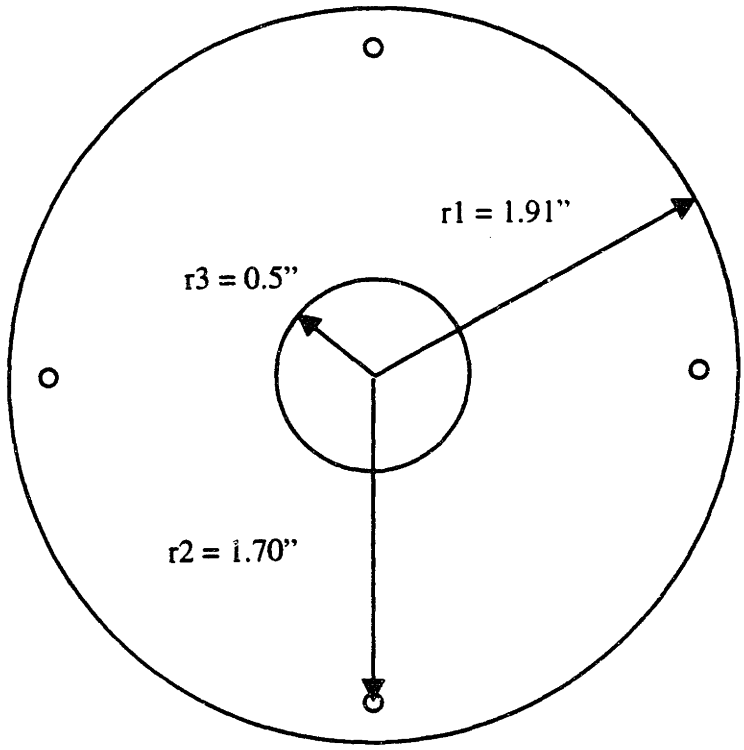

Figure 2-7a: Schematic of upstream filter disc.

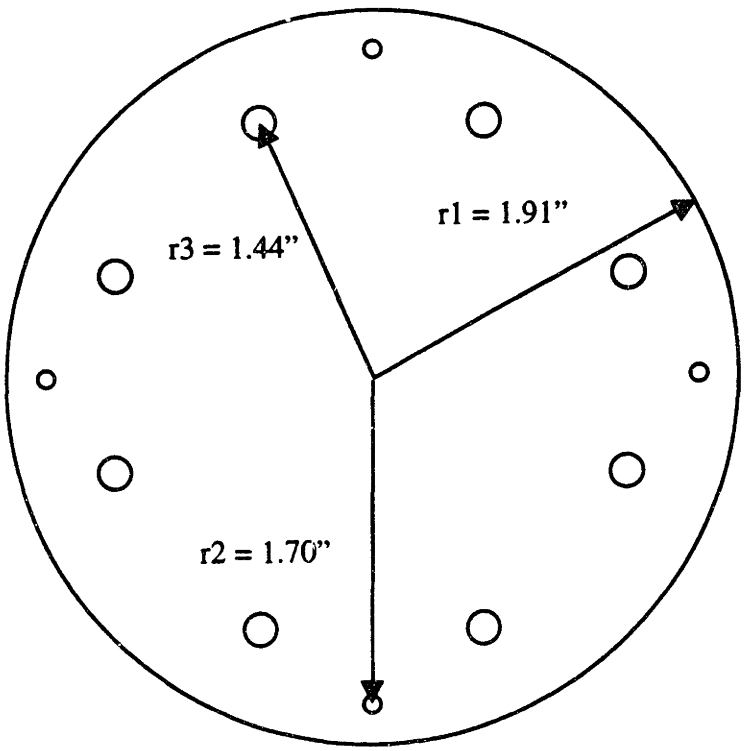

Figure 2-7b: Schematic of downstream filter disc.

2.2.7 Reactor Gaseous Stream Analyzed by Mass Spectrometer

In order to attempt to gauge the effectiveness of the microwave ionization process, as well as determine the background levels of oxygen and other contaminants in the reactor during nanoparticle synthesis, a Mass Spectrometer (Hewlett Packard Mass Selective Detector – HP 6890) was connected at the downstream end of reactor, just in front of the throttle valve. The first experiment measured the levels of various ions in the gas stream exiting the reactor as the microwave plasma was turned on, operated at 700 W, and turned off. The levels of mass numbers 14 and 28 detected are shown in Figure 2-8a. The gases are turned on and the mass spectrometer sampling valve opened after 7 minutes. One can see a significant rise in the level of 28 (N_2) and a smaller rise in the level of 14 (N). Most interesting is the fact that the level of 32 (O_2) dropped below the "background" (gas lines connected) level in the mass spectrometer, which is fitted with a turbo pump operating at 1.2 x 10^{-6} mbar. The 32 level detected indicate that O_2 is present in the reactor gas stream at a level of only ~75 ppm and thus should have little, if any, effect on the synthesis of the nitride materials produced. The microwave plasma was turned on at the 26-minute mark, after a plateau in the 28 and 14 levels was reached indicating a steady state measurement of those levels. There was no difference in the level of 14 detected with or without the microwave plasma in operation. This is not surprising given the speed with which N^+ will recombine with itself or on the walls of the reactor; however, a small drop in the 28 level was observed as the microwave plasma was turned on. Given the fact that when the microwave was turned off at the 47-minute mark the 28 level recovered to its previous value in the absence of the microwave plasma, it appears that this is indirect evidence of the ionization of N_2 in the microwave plasma. The ionized N is likely recombining on the walls, accounting for the drop in the 28 level, and/or recombining with itself, in which case there is no observed drop in the 28 level due to these N. The reactor gases were left running until the 67-minute mark. When they were shut off at that point, the 32 level increases to that of the mass spectrometer background value, while the 14 and 28 levels decrease to their respective background levels.

Shown in Figure 2-8b is data for 14 and 28 levels during the operation of the reactor for the synthesis of nano-TiN. As was observed above, as gases began to flow at the 21-minute mark, the 14 and 28 levels increase. When the microwave plasma was

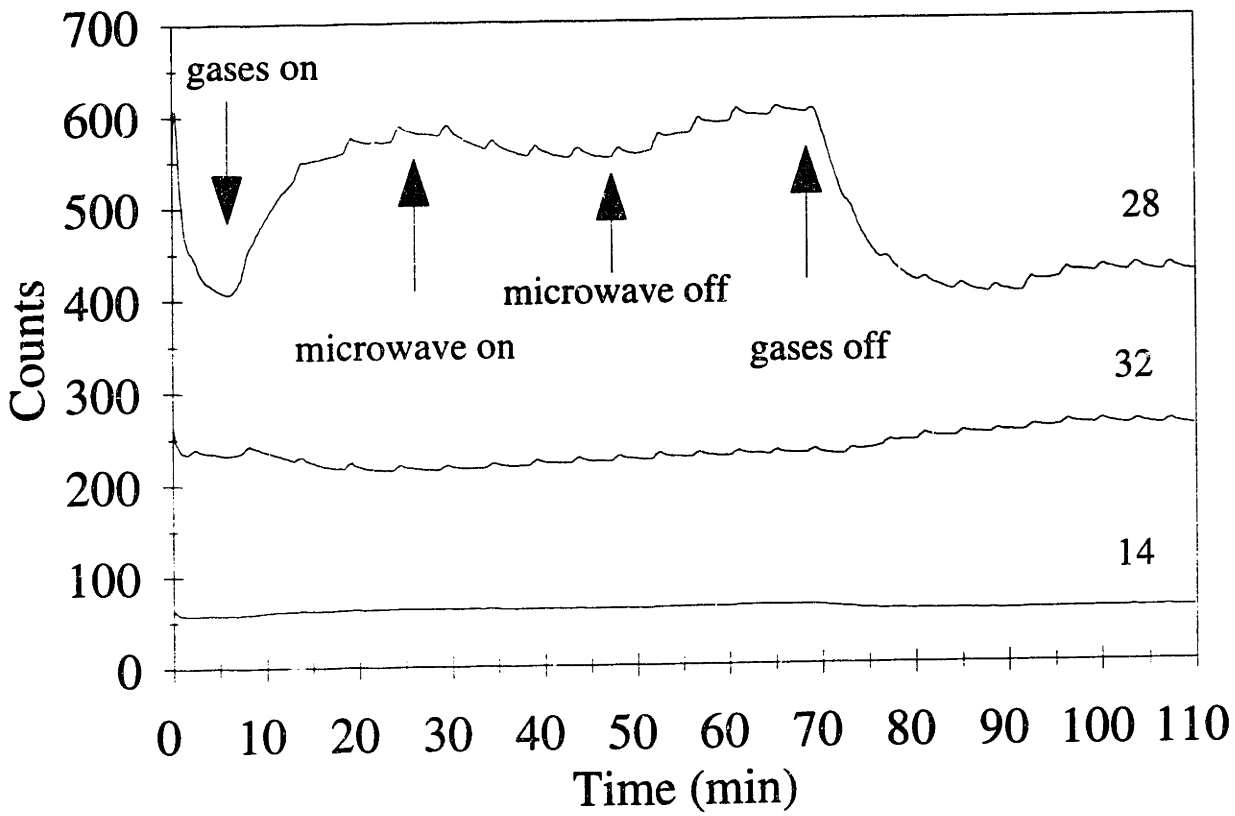

Figure 2-8a: Mass spectrometer data collected as microwave plasma is cycled on and off once.

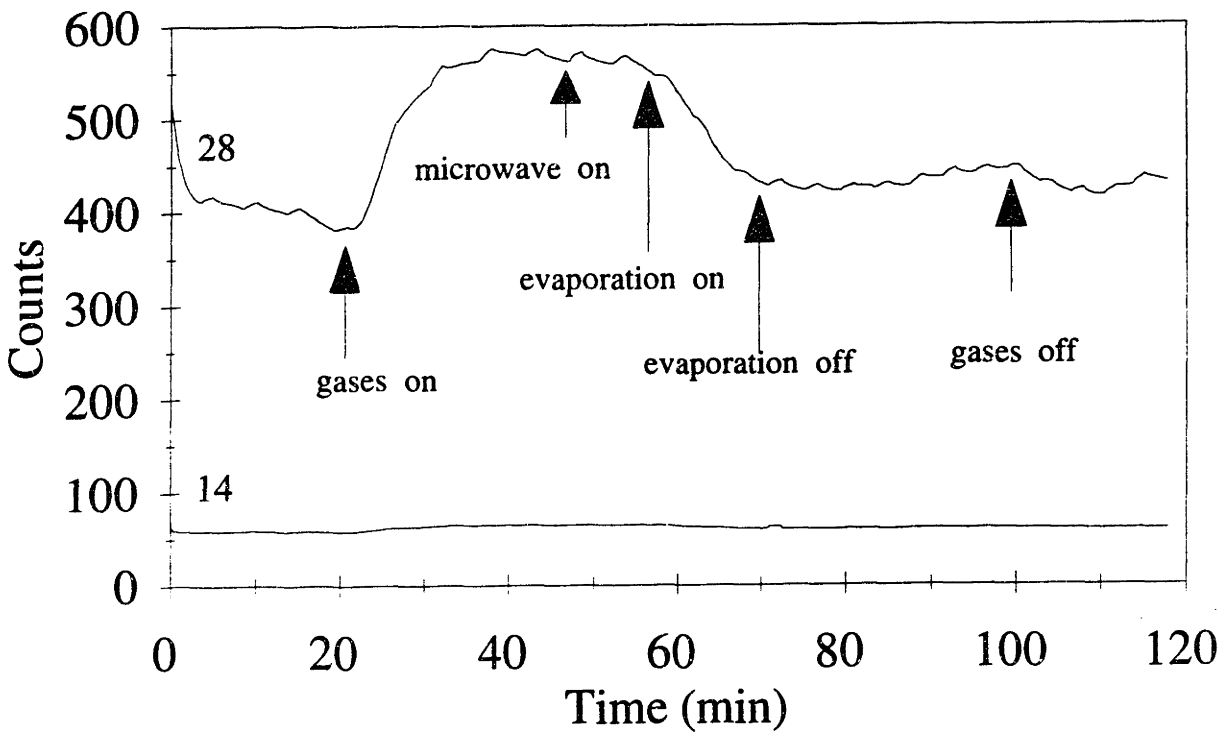

Figure 2-8b: Mass spectrometer data collected as nano-TiN is being synthesized.

turned up to 700 W after 49 minutes, a small drop in the 28 level was observed, with the 14 level unchanged as noted above. Evaporation of Ti, and synthesis of nano-TiN, began at the 58-minute mark. One can see that there was then a much bigger drop in the 28 level, suggesting that the ionized N is now not recombining with itself, and thus leading to only a small drop in 28 level due to wall recombination, but is combining with the evaporated Ti to produce TiN. Further evidence for this assertion is seen in the slight reduction in the 14 levels as Ti evaporation begins. It was hoped that an increase in the levels of 61.88 (TiN) might be observed to give direct, rather than indirect, evidence of TiN formation in the gas phase. However, given the distance of more than 2 m between the mass spectrometer detector and the evaporation source, it is not surprising that no TiN was detected. Additionally, the levels of 79.88 (TiO_2), 64 (TiO), 47.88 (Ti) and 12 (C) were unchanged from the background levels detected in the mass spectrometer. The Ti evaporation was shut off at 69 minutes and one can observe the 28 level starting to recover to its "pre-evaporation" level before the gases were shut off at 99 minutes. The 14 level does return to its "pre-evaporation" value.

As a further indication and measure of the degree to which the reactor was oxygen-free, the reactor's leak rate was determined and rechecked prior to each synthesis run to ensure that a reassembly or modification had not caused a leak in the vacuum system. The leak rate in a vacuum apparatus can be calculated by determining it as a throughput (*Th*) using the following equation [28]:

$$Th = P * S \tag{2-7}$$

where P is the pressure in the reactor and S is the "pumping speed" of the leak. With the knowledge of the volume (V) of one's chamber, by measuring the time (t) it takes for leaks to change (increase) the pressure in a reactor from one value (P_o) to another (P) when the vacuum pumps are sealed off, this "pumping speed" (S) may be determined by [28]:

$$S = \frac{V}{t} \ln\left(\frac{Po}{P}\right) \tag{2-8}$$

By using Eqns. (2-7) and (2-8), the leak rate in this reactor was determined to be 1.66 x 10^{-4} atm-cc/sec. Given that there are more than 140 connections and joints in this reactor

with the potential for leaking, this is a very good leak rate. The ultimate pressure of the reactor with the two small mechanical pumps (Balzers 008B) was 1.1 x 10^{-2} mbar.

2.2.8 Synthesis of Al Nanoparticles

In addition to the experiments with Si and Ti described in subsequent chapters, some work was also done with the production of nano-Al in this reactor. As is the case with the Si-based and Ti-based materials described later, these Al powders had among the very highest surface areas and smallest particle sizes described in the literature. When many metals with low melting temperatures, such as Al, are produced in the batch-type reactors, due to the proximity of the collection substrate to the hot evaporation source, recrystallization leading to grain growth of nanoparticles may occur on the cold finger. By placing the collection point in this reactor farther away from the evaporation/generation source, high quality nano-Al (surface area = 105 m^2/g, particle size = 27 nm) can be produced and preserved. The smallest nano-Al produced by other researchers is 50–200 nm [29] and 50-80 nm [30] in diameter.

2.2.9 Other Benefits of Our Reactor Design

There are several other benefits to the design implemented for this reactor. The first is that it provides a very flexible process. Almost any metal with a melting point below 1900 °C may be evaporated in this reactor. While only the production of pure metals and nitrides has been explored to date, it is anticipated that the synthesis of high quality nanocrystalline oxides, not subject to the post-oxidation agglomeration problem, may be synthesized in this reactor by using oxygen, rather than nitrogen, in the microwave plasma. An investigation of Si_2N_2O synthesis with this reactor is currently being planned by introducing N_2 and O_2 into the microwave plasma gas stream. A second major benefit is that the raw materials used in this reactor are relatively inexpensive simple gases and metal pellets. An additional benefit related to the simplicity of the starting materials is that no hazardous gaseous byproducts are produced. (The NH_3 was not as effective for nitridation as was pure N_2; its use in the reactor has been discontinued). This is in comparison to competing chemical vapor synthesis processes which may produce such byproducts as HCl or HF and require the use of caustic scrubbers or cold traps to treat these corrosive and/or toxic gases [31].

2.3 Summary

A novel tubular reactor design with separate units for the nanoparticle generation, nitridation and collection processes to allow the optimization of each process has been constructed. This reactor represents a 10-fold increase over the production rates achievable in the traditional batch-type reactors for the synthesis of nanocrystalline materials. While the conventional single chamber reactors are limited to the production of nano-metals and nano-oxides, with this new forced flow reactor, high-quality nanocrystalline nitride materials have been successfully synthesized. The availability of such new materials enables the study of their unique surface chemistry, sinterability and microstructure-property relationships.

2.4 References

[1] R.W. Siegel, "Cluster-Assembled Nanophase Materials," *Annu. Rev. Mater. Sci.*, **21** 559-78 (1991).

[2] J.Y. Ying, "Structure and Morphology of Nanostructured Oxides Synthesized by Thermal Vaporization/Magnetron Sputtering and Gas Condensation," *J. Aerosol Sci.*, **24** [3] 315-338 (1993).

[3] H. Gleiter, "Nanocrystalline Materials," *Prog. Mater. Sci.*, **33** 223-315 (1989).

[4] H. Gleiter, "Nanocrytalline Solids," *J. Appl. Cryst.*, **24** 79-90 (1991).

[5] R.W. Siegel and J.A. Eastman, "Synthesis, Characterization, and Properties of Nanophase Ceramics," pp. 3-14 in Multicomponent Ultrafine Microstructures (Mat. Res. Soc. Symp. Proc. Vol. 132, MRS, Pittsburgh, PA, 1989).

[6] V. Haas, H. Gleiter, and R. Birringer, "Synthesis of Nanostructured Materials by the Use of a Thermophoretic Forced Flux System," *Scripta Metall. Mater.*, **28** 721-724 (1993).

[7] C.G. Granqvist and R.A. Buhrman, "Ultrafine Metal Particles," *J. Appl. Phys.*, **47** [5] 2200-2219 (1976).

[8] S. Iwama and K. Hayakawa, "Vaporization and Condensation of Metals in a Flowing Gas with High Velocity," *NanoStr. Mater.*, **1** 113-118 (1992).

[9] S. Iwama and K. Mihama, "Nanometer-Sized Beta-Mn and Amorphous-Sb Particles Formed by the Flowing Gas Evaporation Technique," *Nanostr. Mater.*, **6** 305-308 (1995).

[10] R.A. Andrievskii, "Review: Nanocrystalline High Melting Point Compound-Based Materials," *J. Mater. Sci.*, **29** 614-631 (1994).

[11] H. Hahn, J. Logas, and R.S. Averback, "Sintering Characteristics of Nanocrystalline TiO_2," *J. Mater. Res.*, **5** [3] 609-14 (1990).

[12] D. Halliday and R. Resnick, Fundamentals of Physics, 3rd ed., p. 645, (John Wiley & Sons, New York, 1988).

[13] D. Halliday and R. Resnick, Fundamentals of Physics, 3rd ed., p. 652, (John Wiley & Sons, New York, 1988).

[14] Edwards Vacuum Products, product literature.

[15] A.J. Becker, T.N. Meyer, F. M. Smith, and J.F. Edd, "Plasma Process Routes to Synthesis of Carbide, Boride and Nitride Ceramic Powders," pp. 335-346 in Plasma Processing and Synthesis of Materials (Mat. Res. Soc. Symp. Proc. Vol. 98, MRS, Pittsburgh, PA, 1987).

[16] D. Vollath and K.E. Sickafus, "Synthesis of Ceramic Oxide Powders in a Microwave Plasma Device," *J. Mater. Res.*, **8** [11] 2978-2984 (1993).

[17] D. Vollath and K.E. Sickafus, "Synthesis of Nanosized Ceramic Nitride Powders by Microwave Supported Plasma Reactions," *Nanostr. Mater.*, **2** 451-456 (1993).

[18] Y. Tessier, J.E. Klemberg-Sapieha, S. Poulin-Dandurand, and M.R. Wertheimer, "Silicon Nitride from Microwave Plasma: Fabrication and Characterization," pp. 183-189 in Plasma Processing (Mat. Res. Soc. Symp. Proc. 68, MRS, Pittsburgh, PA, 1986).

[19] M.R. Wertheimer and M. Moisan, "Comparison of Microwave and Lower Frequency Plasma for Thin Film Deposition and Etching," *J. Vac. Sci. Technol. A.*, **3** [6] 2643-2649 (1985).

[20] T.C. Wei, L.R. Collins, and J. Phillips, "Measurement and Modeling of Nitrogen Ion Behavior in the Afterglow of a Microwave Plasma," *J. Appl. Phys.*, (1994).

[21] T.C. Wei, L.R. Collins, and J. Phillips, "Dynamics of Charged Species in the Afterglow Region of a Low-Pressure Microwave Plasma," *J. Phys. D: Appl. Phys.*, **28** [2] 295-304 (1995).

[22] C. Chave, C. Boiss-Laporte, J. Marec, and P. Leprince, "Nitrogen Microwave Discharge as a Source of Excited Neutral Species for Possible Surface Treatment," *Mater. Sci. Eng. A*, **140** 494-498 (1991).

[23] L. Waldmann and K.H. Schmitt, "Thermophoresis and Diffusiophoresis of Aerosols," pp. 137-162 in Aerosol Science, ed. C.N. Davies, (Academic Press, New York, 1966).

[24] N.A. Fuchs, The Mechanics of Aerosols, pp. 56-58, (The MacMillian Company, New York, 1964).

[25] G.W. Castellan, Physical Chemistry, 3rd ed., p. 751, (The Benjamin/Cummings Publishing Company, Inc., Reading, MA, 1983).

[26] K.J. Bryden and J.Y. Ying, unpublished results, MIT.

[27] L. Svarovsky, Solid-Gas Separation, pp. 85-117, (Elsevier Scientific Publishing Company, New York, 1981).

[28] Kurt J. Lesker Company Catalog 6, Technical Tables, pp. 24-28, ed. M.L. Salago, (Clairton, PA, 1996).

[29] A. Inoue, B.G. Kim, K. Nosaki, T. Yamaguchi, and T. Masumoto, "Production of Ultrafine Al and AlN particles by Plasma-Alloy Reaction and Their Microstructure and Morphology," *J. Appl. Phys.*, **71** [8] 4025-4029 (1992).

[30] P.R. Taylor, S.A. Pirzada, D.L. Marshall, and S.M. Donahue, "Generation of Nano-Crystalline Metals in a Transferred Arc Thermal Plasma Reactor," pp. 215-225 in Plasma Synthesis and Processing of Materials, ed. K. Upadhya, (The Minerals, Metals & Materials Society, Warrendale, PA., 1993).

[31] Engineered Materials Handbook, "Processing of Ceramics," pp. 810-811, ed. M.M. Gauthier, (ASM International, Materials Park, OH, 1995).

Chapter 3

Synthesis and Characterization of Si and Si_3N_4 Nanoparticles

3.1 Introduction

Due to its high strength and resistance to oxidation, thermal shock, wear and corrosion, Si_3N_4 has great potential for applications such as advanced heat engine components and ball bearings. However, in order to densify conventional Si_3N_4, sintering additives such as MgO, Al_2O_3, and Y_2O_3 are typically needed. The oxide additive reacts with the SiO_2 surface layers to form a liquid phase at sintering temperatures. Upon solidification, this oxide phase is retained at the grain boundaries. If this intergranular phase is glassy, it can soften at moderately elevated temperatures leading to a degradation of the mechanical properties of the nitride component [1]. As detailed in Chapter 1, the particle size dependence of sintering rates as well as the large volume fraction of grain boundaries and enhanced grain boundary diffusion coefficients in nanocrystalline materials can lead to improved sintering kinetics and the potential for lower temperature sintering with less or no sintering additive. Thus, the first material system investigated in the forced flow reactor was Si_3N_4.

3.2 Experimental Details

3.2.1 Synthesis of Nano-Si in Forced Flow Reactor

In order to characterize the reactor's operation, the effect of reactor pressure and gas velocity on the Si particle size and morphology was examined. The reactor was operated at pressures ranging from 0.5 mbar to 11.3 mbar, and He gas velocities ranged from 12.5 to 40 m/s. Evaporation temperatures ranged from 1575 – 1625 °C, corresponding to Si vapor pressures of ~ 0.4 – 0.8 mbar [2].

3.2.2 External Nitridation of Nano-Si

The as-prepared nanocrystalline Si was nitrided in both a thermal gravimetric analyzer (Perkin-Elmer TGA7) and a differential thermal analyzer (Perkin-Elmer DTA7) to follow nitridation and crystallization kinetics. The flowing nitrogen gas used was purified with an oxygen trap and a liquid nitrogen trap. Heating rates for all experiments were 5 °C/min while the final temperature varied from 1100 to 1600 °C with various soak times. For DTA experiments, the samples were run in an alumina cup and covered with

alumina powder. The samples were placed loosely in an alumina pan liner in the TGA analysis.

3.2.3 Synthesis of Nano-Si_3N_4 with N_2 in Forced Flow Reactor

In order to achieve *in situ* nitridation of the Si particles in the reactor, the microwave plasma source described in Chapter 2 was added to the reactor. A series of experiments utilizing nitrogen (N_2) as the gaseous source for nitrogen radicals in the plasma was completed. These experiments explored the effects of N_2 content in the gas stream and microwave power on the composition, phase(s) and surface area of the resulting powders.

For the first set of these experiments, the N_2 gas flow was fixed at 2.5 standard-liters per minute (slm) while the argon (Ar) flow was fixed at 0.38 slm. The helium (He) gas flow was set at 1.7, 3.4 and 7.0 slm. This set the N_2 volume content of the total gas flow at 55%, 40% and 25% respectively. The lower limit of 1.7 slm was chosen as the minimal amount of He required to move the evaporated Si particles out of the growth zone over the thermal evaporation source at a velocity of 3.0 m/s. A lower amount of He flow, and thus slower particle velocity past the evaporation source, could potentially lead to the production of more larger particles with the high evaporation rates utilized. The upper limit of 7.0 slm of He was the idealized gas flow from the experiments outlined above on the production of nano-Si (no N_2 plasma, gas velocity = 12.5 m/s, P = 2 mbar). With the addition of the N_2 and Ar to the gas stream, injected 0.1 m downstream of the evaporation source to prevent nitridation of the metallic melt, the particle/gas velocity through the reactor rose to 17.5 m/s for the intermediate He gas flow amount of 3.4 slm. However, this was still within the limits of the 10 - 25 m/s established above for the production of high surface area, unagglomerated, nano-Si powders in this reactor, and the actual gas velocity over the evaporation crucible was lower than 17.5 m/s. The amount of N_2 in the gas flow was chosen based on estimates of the efficiency of the microwave ionization process and the amount of atomic nitrogen needed to produce a given quantity of Si_3N_4 per unit time of operation. The Ar (15 vol% of the N_2 flow) was added to the gas stream in order to increase the atomic nitrogen concentration in the microwave plasma. The heavier, oscillating Ar atoms impacting the N_2 molecules increased the

amount of dissociation beyond that created by electron impact alone. A total pressure of 2 mbar was used for all these experiments.

Microwave power was applied at 150 W, 500 W, 700 W, 850 W and 980 W. These values represent the forward applied power. Reflected power levels, representative of power absorbed by the cavity or diverted to other loss mechanisms, ranged from 1 to 150 W. At higher forward powers, the losses were greater.

From the work of other researchers on the production of Si_3N_4, it is known that the nitrogen deficiency of a powder decreases as that powder becomes more white in appearance, the color characteristic of Si_3N_4 [3, 4]. Conversely, the higher the free Si content, the darker is the silicon nitride powder [4]. Therefore, the focus of our experiments was on changing the variables of microwave power and gas flow to produce a powder that was qualitatively the "whitest" in appearance by visual inspection. Microwave power or gas levels that did not appear promising were not pursued further. Nitridation levels were subsequently quantitatively assessed by chemical analysis techniques.

As outlined below, the Si_3N_4 particles that proved to have the greatest degree of conversion were synthesized with 40% N_2 content in the gas stream at 850 W of microwave power, and had a residence or reaction time of ~0.05 - 0.10 seconds in the plasma plume of nitrogen radicals. Due to the high gas velocities and large gas flux, this plume extended ~ 40 cm downstream of the plasma applicator, thereby extending the reaction zone beyond the limits of the actual applicator itself. However, with the higher gas flow rates at a constant pressure, there was also an increase in the particle velocity, thereby keeping the overall reaction time approximately constant. Thus, if one reduced the amount of gas flow with the goal of increasing the residence time in the plasma by slowing the particles down, one also shortened the length of the reaction zone of excited N_2 species, as determined by the extent of the pink afterglow region. At greater gas flow, there was also a decrease in the mean free path of the gas molecules. In order to quantify these effects on the nitridation of Si, another set of experiments was performed such that the N_2 composition in the gas stream was fixed at 40 vol%, but that the total amount of gas flowing was doubled as well as halved from those quantities which had previously yielded the greatest conversion (He = 3.4 slm, N_2 = 2.5 slm, Ar = 0.38 slm).

3.2.4 Synthesis of Nano-Si_3N_4 with NH_3 in Forced Flow Reactor

In an effort to increase the conversion of Si to Si_3N_4 in the reactor, NH_3 was used as a plasma reactant gas for the production of nitrogen radicals. Because NH_3 is a much less stable gas molecule than N_2, which has a triple bond joining the two nitrogen atoms, it was anticipated that a microwave plasma utilizing NH_3 would be more effective at producing fully converted Si_3N_4 nanoparticles. Although the total energy for the complete dissociation of ammonia (1167 kJ/mol) is greater than the required energy for the dissociation of molecular nitrogen (950 kJ/mol), the energy barrier for the formation of NH_x· radicals (x = 0, 1 and 2) is much lower (330, 377 and 460 kJ/mol, respectively) [5]. Thus the formation of reactive nitrogen from the ammonia route is kinetically more favorable.

NH_3 contents in the gas stream were varied from 40 to 50 vol%, with and without the use of Ar in the mixture. Additionally, since literature [6] suggested that doping N_2 with 4 vol% NH_3 increased the dissociation and the efficiency of the reaction in a nitrogen microwave plasma, mixing N_2 with NH_3 in various proportions was also performed. For instance, a mixture of 10 vol% NH_3 with 90 vol% N_2 was employed such that 40 vol% of the total gas stream still contained nitrogen species.

3.2.5 Other Efforts to Increase Nitridation

When the above experiments did not produce a fully converted Si_3N_4, other variables in the synthesis process were also explored. The effect of varying the reactor pressure away from 2 mbar on the microwave plasma was studied. Additionally, the temperature range of 1450 °C-1950 °C was examined in order to evaluate the effects of evaporation temperature on the nitridation of the Si.

3.2.6 Characterization of Nano-Si and Nano-Si_3N_4 Produced in Forced Flow Reactor

The B.E.T. (Brunawr-Emmett-Teller) surface area of the as-prepared nano-Si and Si_3N_4 produced in the reactor was determined by nitrogen adsorption (Micromeritics ASAP 2000) after degassing at 150 °C at 2.7 x 10^{-3} mbar. Particle size and morphology characterizations were performed by transmission electron microscopy (TEM). In some cases, the particles were directly deposited on carbon grids mounted on the collection disc. In other instances, collected or heat-treated particulates were ground and suspended

in isopropanol, and then deposited on TEM grids. An Akashi-002B microscope operating at 200 kV was used for all TEM studies of the Si and Si_3N_4 particles. The as-prepared and nitrided materials, after various heat treatments, were examined by X-ray diffraction (XRD) using a Rigaku 300 diffractometer with Cu K_α radiation for $2\theta = 10°$ to 70° as well as a Siemens D5000 θ-θ diffractometer with Ni-filtered Cu K_α radiation for $2\theta = 10°$ to 90° to determine the phases present and to analyze their crystallite size by peak broadening with the Scherrer formula.

Chemical analysis on these materials were performed by Luvak Inc. (Boylston, MA). For the Si analysis, the sample was decomposed using a combination of an acid digestion followed by an alkali salt fusion. The sample was then analyzed in solution for silicon using direct current plasma emission spectroscopy (ASTM E1097 with a Beckman SpectraSpan VI Spectrometer). Oxygen and nitrogen were analyzed by inert gas fusion (ASTM E1019 with a Leco TC136). Hydrogen analysis was done by a vacuum fusion technique (ASTM E107 with a National Research Model 912 analyzer).

3.3 Results and Discussion

3.3.1 Chemical Analysis of Starting Si Pellets

The impurity levels of the starting Si pellets are shown in Table 3-1. These values reflect the quality of the optical grade Si used (>99.95% pure).

3.3.2 Effect of Reactor Synthesis Parameters on the Production of Nano-Si

The as-synthesized nano-Si consists of approximately spherical, crystalline particles. The powder removed from the reactor has a dark brown appearance from surface exposure to air. Shown in Figure 3-1 is a plot of particle size versus reactor pressure. The gas (particle) velocity was kept constant at 12.5 m/s for these experiments. By varying the pressure, average particle sizes ranging from 5.7 to 9.5 nm were obtained. The error bars represent both the spread in particle sizes and the uncertainty due to resolution on the TEM negatives at various magnifications. As has been reported by others previously, particle size increased with increasing reactor pressure due to confinement of the particles in the growth region above the evaporation source [7]. Figure 3-2 is a TEM micrograph of representative Si particles ~7 nm in diameter obtained at 7 mbar and a gas velocity of 12.5 m/s. Their lattice fringes are clearly visible and were

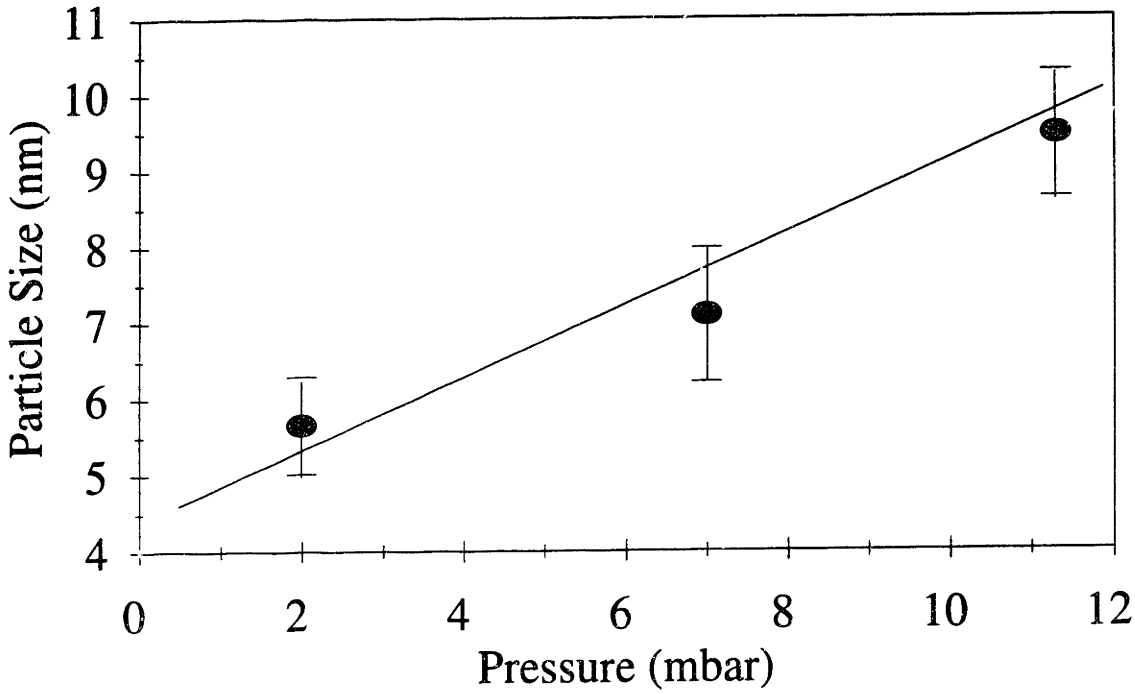

Figure 3-1: Particle size as a function of reactor pressure at a gas velocity of 12.5 m/s.

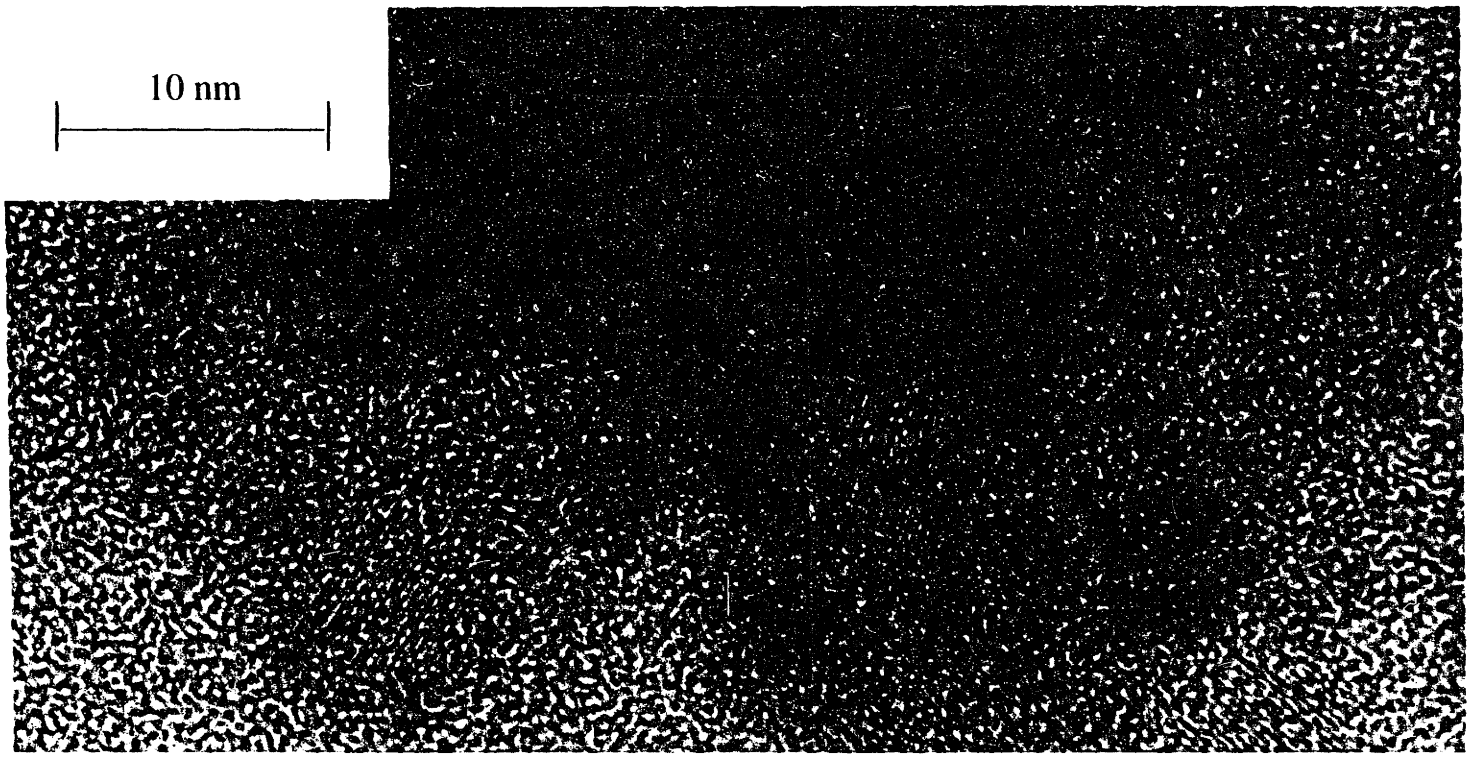

Figure 3-2: Nanocrystalline silicon particles produced at 7 mbar pressure and gas velocity of 12.5 m/s.

measured to obtain a *d*-spacing of 3.06 Å. This corresponds to the (111) plane in silicon with an interplanar spacing of 3.14 Å. While the XRD and chemical analysis data presented below show clearly that these particles contain oxygen, there is no amorphous oxide layer visible on these crystallites. This most likely is due to the smaller amount of amorphous shell material that the electron beam travels through relative to the amorphous background of the carbon grid. This effect has been seen by other researchers on similarly sized Si nanoparticles [8].

TABLE 3-1: Chemical Analysis of Si Pellets

Element	(wt%)
Bismuth	0.0150
Nitrogen	0.0019
Oxygen	0.0028
Cobalt	0.0008
Aluminum	0.0005
Copper	0.0010
Iron	0.0057
Titanium	0.0006
Zinc	0.0012
Niobium	0.0005
Vanadium	0.0005
Boron	0.0035
Antimony	0.0070
Molybdenum	0.0012
Strontium	0.0009

There was no significant difference in the size or morphology of particles produced at gas velocities of 12.5, 15 and 25 m/s, with a reactor pressure of 2 mbar. Discrete crystalline particles of ~ 6 nm were seen in all cases. Weertman *et al.* found a threshold velocity of 9 – 20 m/s in their forced flow reactor, below which there was no effect on particle size [9]. Given the vagaries of determining a gas velocity due to

varying cross-sections throughout reactors, this is in reasonable agreement with our results.

At a gas velocity of 40 m/s, an amorphous film was deposited on the collection substrate. The product consisted of thin flakes of material rather than individual particles. With the higher gas velocities, this is likely due to the more rapid quench rate of the Si (on the order of 4.1 x 10^4 K/sec) and the fact that the Si atoms could not coalesce and order before they reached the liquid nitrogen cooled collector. A similar effect in a flow reactor has been observed by Iwama and Hayakawa in their synthesis of ultrafine metal particles [10]. They found that depending on the distance from the evaporation point to the collection point and the He gas velocity, materials produced fell into either a "film formation" region or a "particle growth" region. Based on the size of our reactor and their data, the transition from particle growth to film formation in our reactor should occur at ~30 m/s (see Figure 3-3). The length "L" in this figure (the distance from the evaporation source to the collection point) for our reactor when these experiments were performed was approximately 1600 mm. This plot would also suggest that at a velocity below ~18 m/s the Si particles are growing by a coalescence mechanism. As described above, we found nano-Si particles formed at and below gas velocities of 25 m/s, in reasonable agreement with this data.

Based on the study of reactor synthesis parameters, a pressure of 2 mbar and a gas velocity of 12.5 m/s was selected for continuous production of nanocrystalline Si. These materials were further characterized as follows.

The as-prepared Si material shows weak crystalline Si XRD peaks. Figure 3-4 shows representative XRD results for the various synthesized Si-based materials. Figure 3-4a is the XRD pattern for the nano-Si. A Si crystallite size of 3.9 nm was determined by the Scherrer formula.

The significant differences in the pore-size distribution of these materials, as compared to a conventional silicon powder, can be seen in the B.E.T. N_2 adsorption data shown in Figure 3-5. The as-prepared nano-Si material has a B.E.T. surface area of 485 $\pm$ 5 m^2/g. The surface area of the conventional Si (Alfa Aesar) is 1.3 m^2/g. In addition to having a lower average pore size, the nano-Si powder also has a narrower pore size distribution than the conventional Si powder.

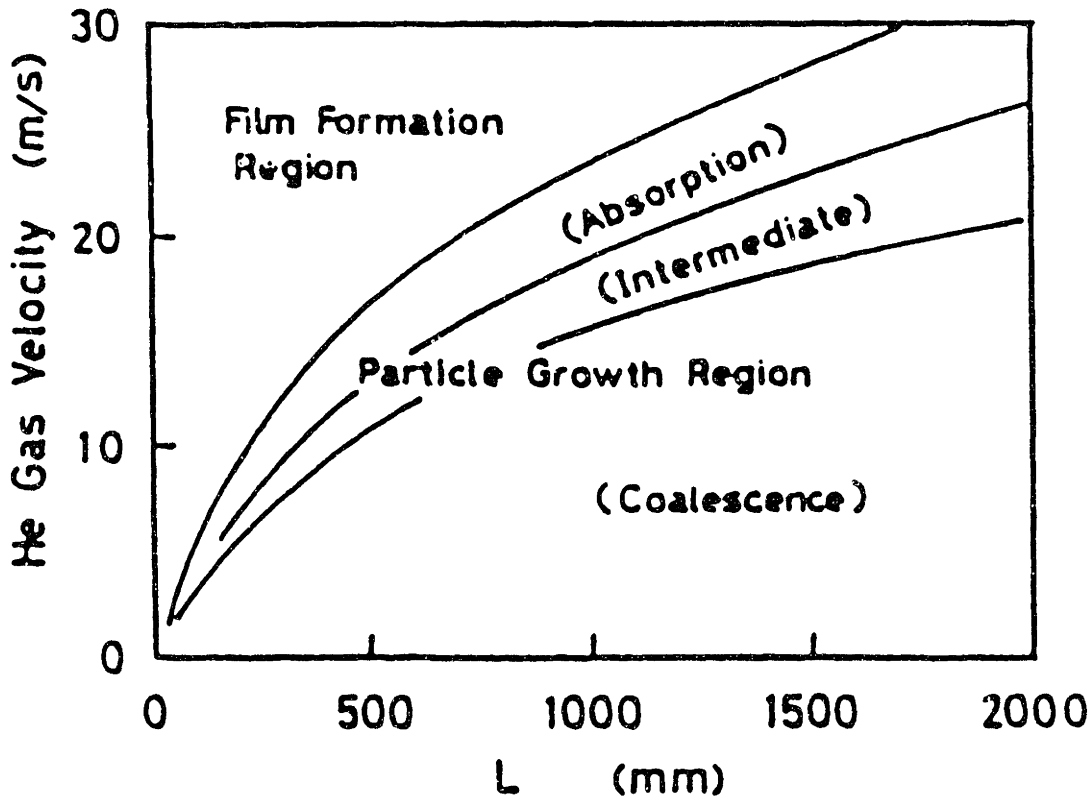

Figure 3-3: Condensation diagram for the flowing gas reactor of Iwama [10].

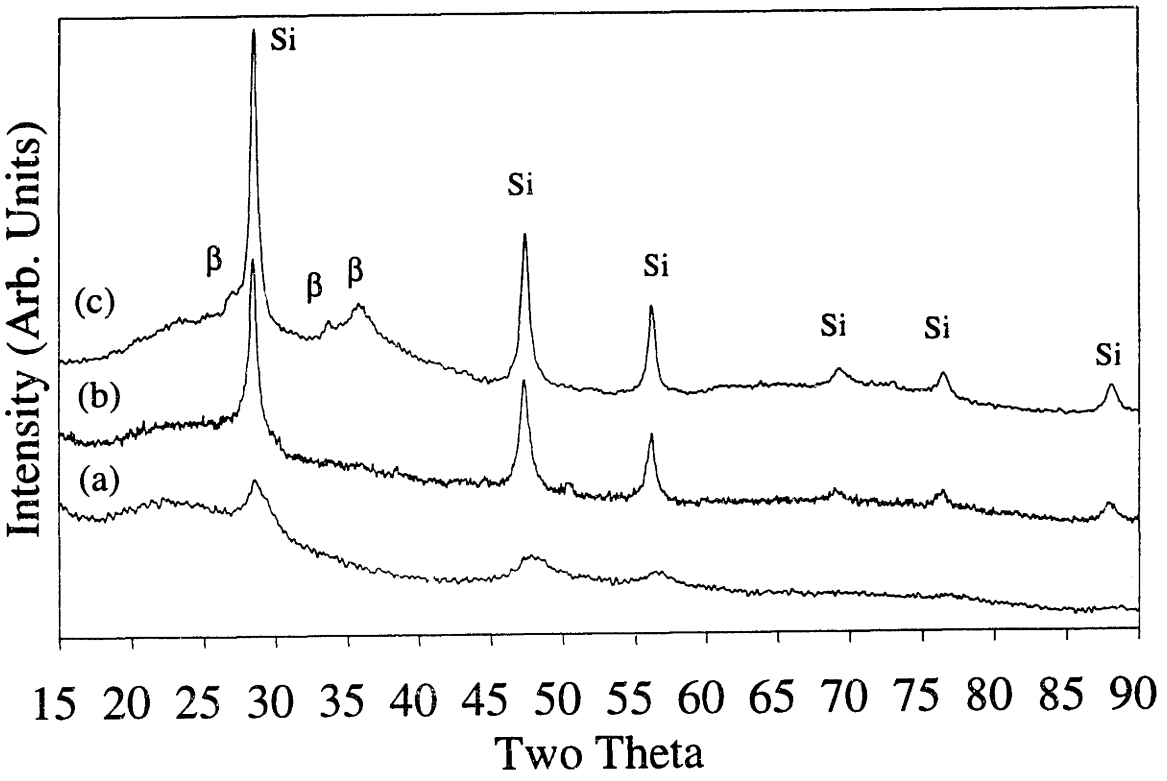

Figure 3-4: XRD pattern of as-prepared (a) Si (no plasma), (b) Si/Si_3N_4 (NH_3 plasma) and (c) Si/Si_3N_4 (N_2 plasma)

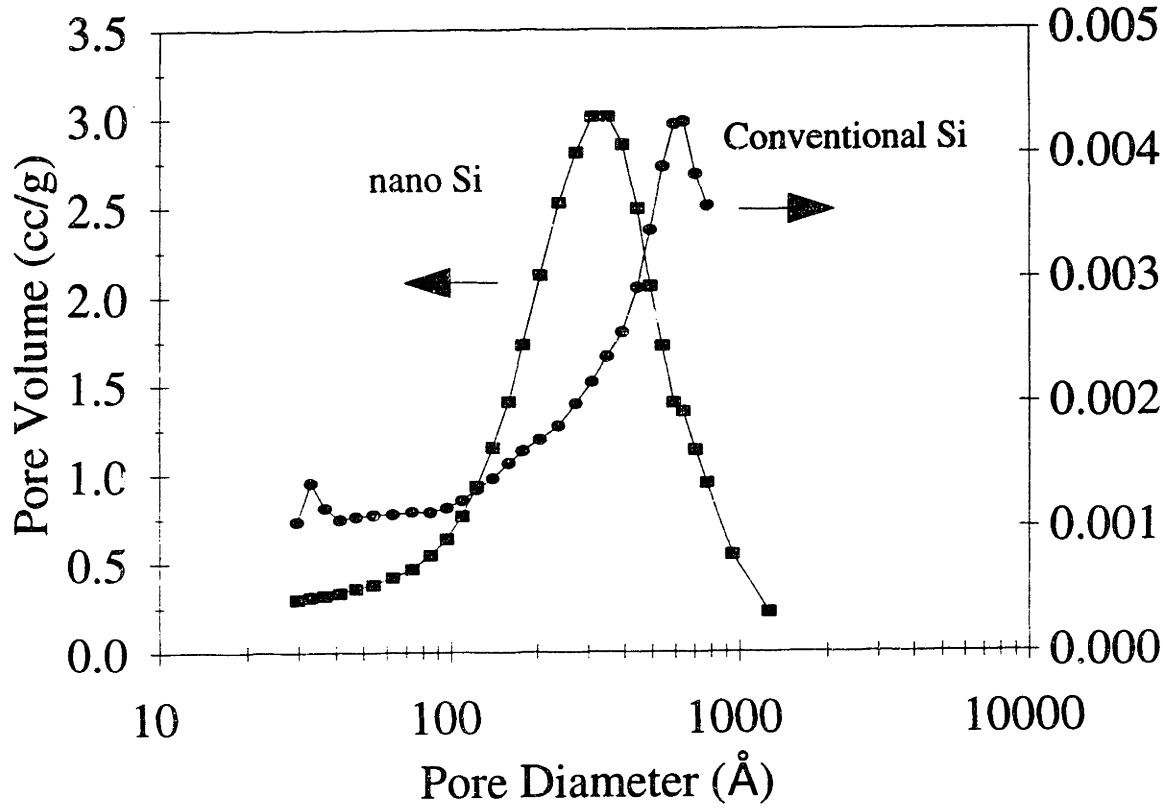

Figure 3-5: BJH pore size distribution of nanocrystalline and conventional Si powders.

From the B.E.T surface area (S_a) and density (δ) of a material, one may calculate a "BET-equivalent" particle diameter (d). By assuming spherical particles, no agglomeration and no porosity, one may write the following for the B.E.T. surface area (S_a) in m^2/g:

$$S_a = \frac{\text{Area of particle}}{\text{Volume of particle} * \delta}$$

$$= \frac{4\pi r^2}{\frac{4}{3}\pi r^3 * \delta}$$

$$= \frac{3}{r * \delta}$$

with $r = d/2$,

$$d = \frac{6}{S_a * \delta} \qquad (3\text{-}1)$$

An indication of the validity of the assumptions of no agglomeration or porosity may be seen by comparing the B.E.T.-equivalent particle diameter to that measured directly via TEM. The presence of agglomeration will lead to a larger apparent B.E.T.-equivalent diameter while porosity will yield a smaller B.E.T.-equivalent particle diameter. Equivalence, or near equivalence, of B.E.T. and TEM particle sizes may be taken as evidence of little to no agglomeration or porosity in a given powder. This is the case with the Si particles produced at a pressure of 2 mbar and a gas velocity of 12.5 m/s. These materials had a B.E.T.-equivalent diameter of 5.3 nm and a TEM diameter of 5.7 nm.

The chemical analysis results on these powders provide evidence of the extreme reactivity of these high surface area materials. The oxygen content of these materials was 28.7 wt%. As O_2 levels in the reactor during synthesis are at the 75 ppm level, as shown by the mass spectrometry data in Chapter 2, this oxygen is most likely incorporated onto the Si upon exposure to air when the material is removed from the reactor. Only an extremely small amount of nitrogen (0.3 wt%) was detected in these powders; the compositional balance was Si (71 wt%).

It is clear that with the extremely high surface areas of nanocrystalline materials, they are vulnerable to oxidation and adsorption of large amounts of gaseous species. It is of interest to perform a simple calculation to estimate the amount of weight that one adsorbed monolayer of oxygen would contribute to a material such as this nano-Si. Taking the Leonard-Jones hard sphere diameter for the O_2 molecule of 3.433 Å [11], the cross-sectional area covered by one O_2 molecule would be 9.256 x 10^{-2} nm^2. The question then is (a) how many such molecules does it take to cover a given surface area and (b) how much do those molecules weigh. Assuming one has a 1 gram sample of the nanocrystalline material and setting N_{O_2} as the number of O_2 molecules required for coverage, one can write:

$$N_{O_2} * (10^{-9}\ m/nm)^2 * (0.09256\ nm^2) = S_a\ (m^2)$$

Rearranging and dividing by N_{Av} one obtains the number of mols of O_2 molecules, M_{O_2}

$$M_{O_2} = N_{O_2} / 6.022 \times 10^{23} = S_a * 1.7939 \times 10^{-5}$$

Multiplying by the molecular weight of O_2, 32 g/mol, gives the number of grams, g_{O_2}, due to O_2 pickup (per a 1 gram basis of nanocrystalline sample):

$$g_{O_2} = 5.7406 \times 10^{-4} * S_a$$

This number can then be easily converted to determine the total % of sample weight which is due to the oxygen adsorption:

$$\%\ \text{wt due to } O_2 \text{ adsorption} = [\ g_{O_2} /(1 + g_{O_2})]\ * 100$$

In terms of the original surface area (S_a), this equation can then be written as:

$$\%\ \text{wt due to } O_2 \text{ adsorption} = \frac{5.7406 \times 10^{-4} * S_a}{(5.7406 \times 10^{-4} * S_a) + 1} * 100 \qquad (3\text{-}2)$$

Thus, for the nano-Si produced with a surface area of 485 m^2/g, an estimate of the percentage of sample weight due to a single monolayer of O_2 is 21.8%. Given that much

more than a monolayer may actually be reacted with the surface Si in the form of SiO_x oxidation, the total O_2 content of 28.7 wt% measured in these particles is not surprising.

The properties of this nanocrystalline Si powder are significantly better than those of other nano-Si cited in the literature, particularly that produced by gas phase formation processes. Laser-induced formation from SiH_4 gave Si powders with a particle size range of 10 – 100 nm, an average size of 47 nm and a B.E.T. surface area of 57 m^2/g [3]. Spherical, ultrafine Si powder of diameter 20 - 50 nm was produced by an arc-plasma method; no surface area data was reported [12]. A recent effort using a rf-plasma enhanced chemical vapor deposition system for the gas phase reaction of silane produced Si particles sized 20 – 30 nm with a surface area of 162 m^2/g [13]. The only Si in the literature with properties comparable to the nano-Si produced in this reactor is nano-Si produced by ultrasonic dispersion of thin sections of porous silicon in organic solvents. This results in the formation of Si nanocrystallites ranging in size from 2 - 10 nm; no surface area data was reported [8].

3.3.3 Nano-Si External Nitridation Results

The high surface areas of the Si described above enabled nitridation and conversion to Si_3N_4 under a N_2 gas flow at relatively low temperatures. Nitriding temperatures for conventional Si range from ~1200 °C to 1450 °C [14]. Ultrafine Si powder of diameter 20 - 50 nm produced by an arc-plasma method could be nitrided at 1100 °C if unexposed to air, or at 1200 °C if exposed to air, as these materials were [15]. As shown in Figure 3-6, nitridation of our nano-Si was initiated at a low temperature of ~ 500 °C and was completed by ~1050 °C. The larger surface area of this nano-Si provides more nucleation sites and more exposed Si where nitridation can occur.

The first evidence of Si_3N_4 X-ray crystallinity is found in a sample held at 1500 °C under N_2 gas flow for 30 minutes. The diffraction pattern indicated the formation of an α-Si_3N_4 phase in the sample. DTA reflects a major exothermic peak at 1490-1560 °C which may be attributable to crystallization of Si_3N_4. This suggests that the nitride formed during nitridation between 500 °C and 1050 °C is amorphous. After a 1-hour hold at 1600 °C, the peaks for crystalline α-Si_3N_4 become well-defined. This material has the typical grayish white color of α-Si_3N_4. The formation of α-Si_3N_4, relative to β-

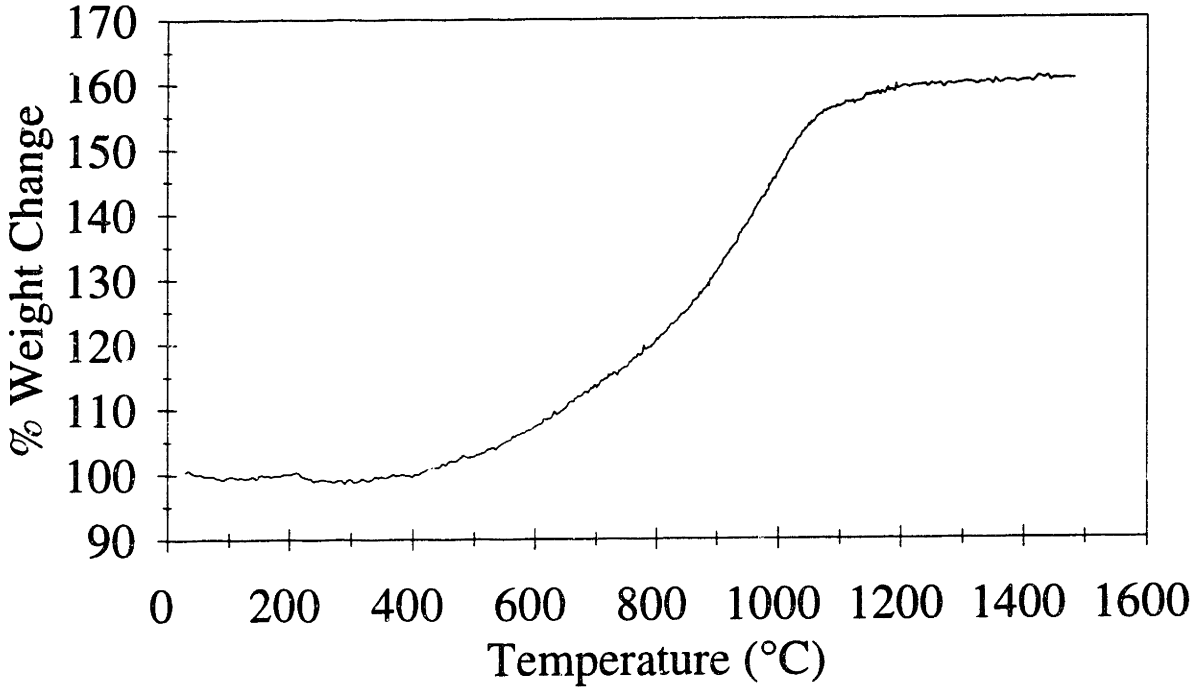

Figure 3-6: TGA data showing Si-to-Si_3N_4 conversion by 1050 °C.

Si_3N_4, may have been favored due to the high surface area of the starting Si powders and the oxygen associated with their surface encouraging the formation of α-Si_3N_4 [16].

After a 3-hour soak at 1600 °C in a flowing nitrogen atmosphere, an additional set of diffraction peaks unrelated to Si_3N_4 was also observed (Figure 3-7a). The additional diffraction peaks were similar to those of a crystalline, non-stoichiometric silicon oxide (SiO_x) produced earlier in the construction of this reactor when air leaks were a problem such that substantial oxygen was present during the Si nanocrystal synthesis (Figure 3-7b).

TEM micrographs of the crystalline Si_3N_4 particles formed during heat treatment to 1600 °C for 1 hour in a flowing nitrogen atmosphere are shown in Figures 3-8 and 3-9. The particles varied in size and shape with an average size of 70 nm. While many crystallites were nearly spherical, others were oblong and needle-like. The interconnected network-like appearance of the particles in Figure 3-8 is most likely due to sintering which has taken place between adjacent particles which were in contact with one another during the elevated temperature soak. In Figure 3-9, one may see a shell around some of these particles likely due to oxidation with the formation and crystallization of a SiO_x layer with a thickness of 1.27 nm. The lattice fringes in the top particle were measured to obtain a *d*-spacing of 6.48 Å. This corresponds to the (100) plane in β-Si_3N_4 with a nominal interplanar spacing of 6.58 Å.

Chemical analysis results on these nitrided powders show an oxygen content of 9.7 wt%, a nitrogen content of 34.7 wt% and a silicon content of 55.6 wt%. This suggests that a very large portion of the initially adsorbed oxygen was volatilized during the conversion process.

3.3.4 Results for the Production of Nano-Si_3N_4 with N_2 in the Forced Flow Reactor

Shown in Figure 3-10 is the effect of varying the nitrogen content in the gas stream on the weight ratio of N:Si incorporated into the final product. Conversions for microwave plasma powers of 850 W (a) and 700 W (b) are shown. (Because stoichiometric Si_3N_4 is ~ 60 wt% Si and ~ 40 wt% N, stoichiometric Si_3N_4 has a N:Si ratio of 0.667. This value is shown as a solid line in Figure 3-10.) When N_2 made up only 25 vol% of the gas flow, it appears there was not enough atomic nitrogen present to allow for the full conversion to Si_3N_4. There was no benefit to additional amounts of N_2

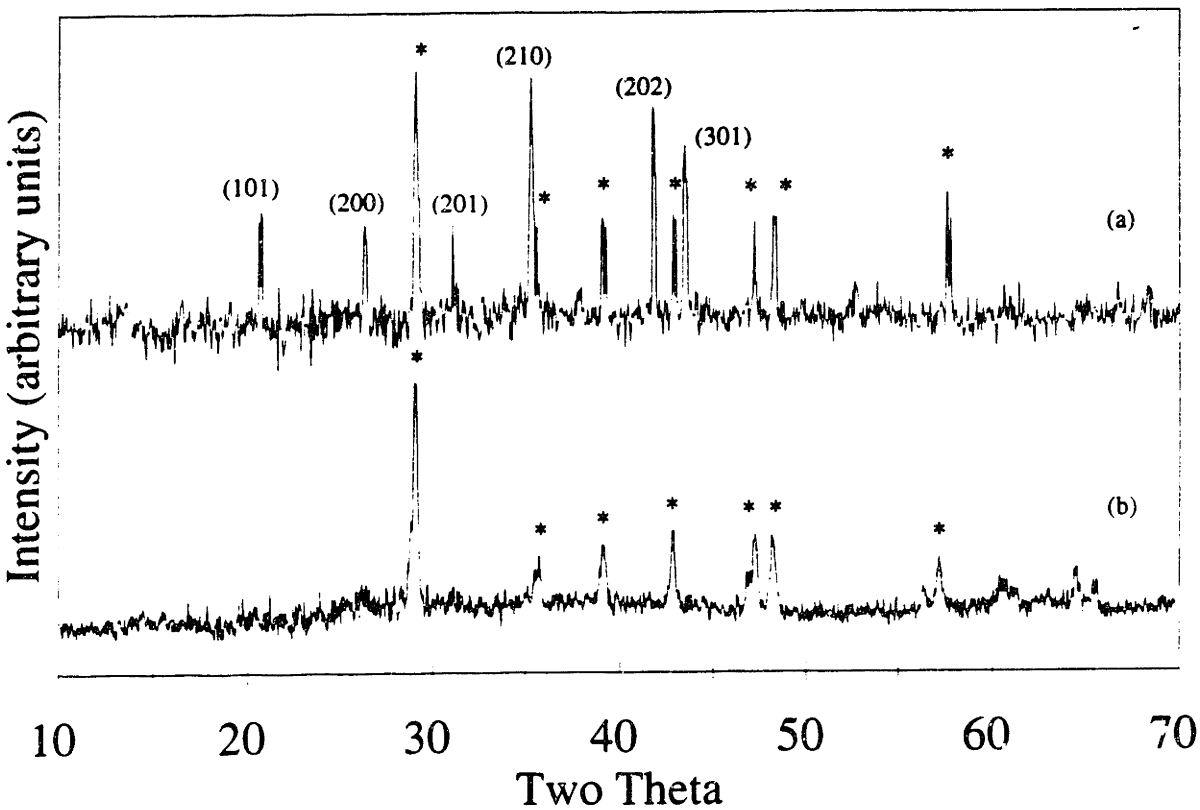

Figure 3-7: (a) XRD data showing material heat treated at 1600 °C for 3 hours in a flowing nitrogen atmosphere developed additional peaks (*) unrelated to the α-Si_3N_4 phase (indexed). These additional peaks were similar to the diffraction peaks of a crystalline, non-stoichiometric SiO_x produced when the reactor had air leakage during the synthesis (b).

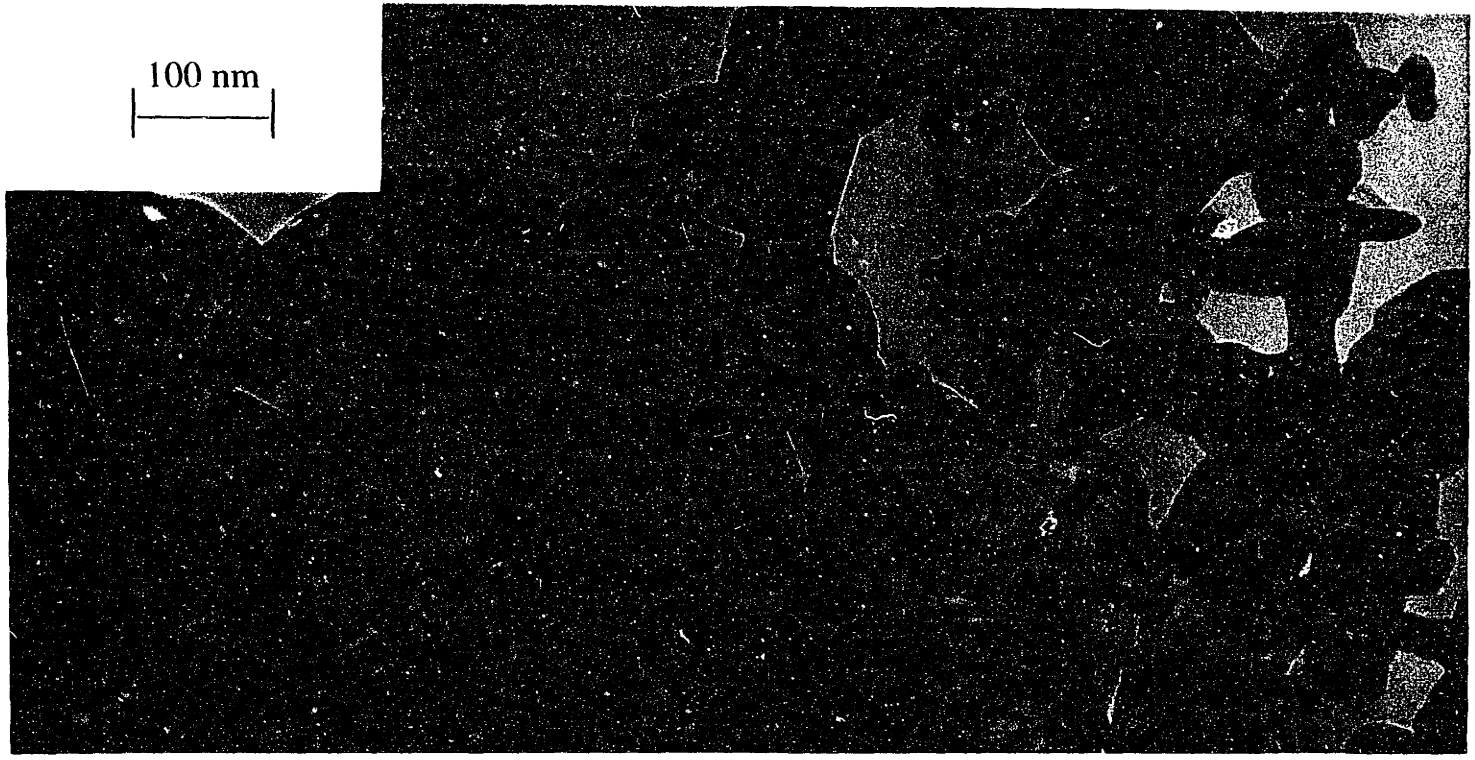

Figure 3-8: TEM micrograph of Si_3N_4 particles formed during heat treatment to 1600 °C for 1 hour in a flowing nitrogen atmosphere.

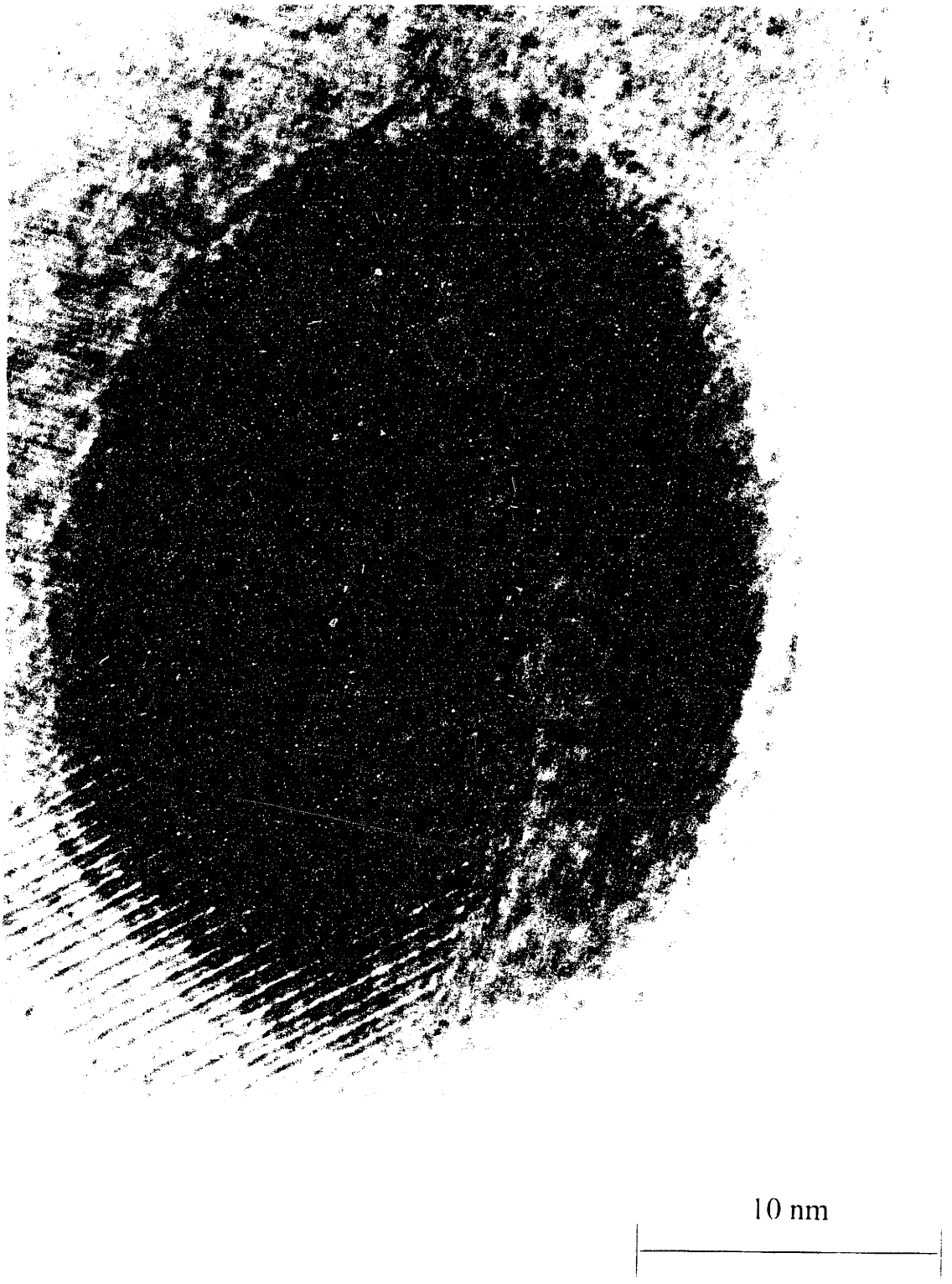

Figure 3-9: TEM micrograph of Si_3N_4 particles formed during heat treatment to 1600 °C for 1 hour in a flowing nitrogen atmosphere.

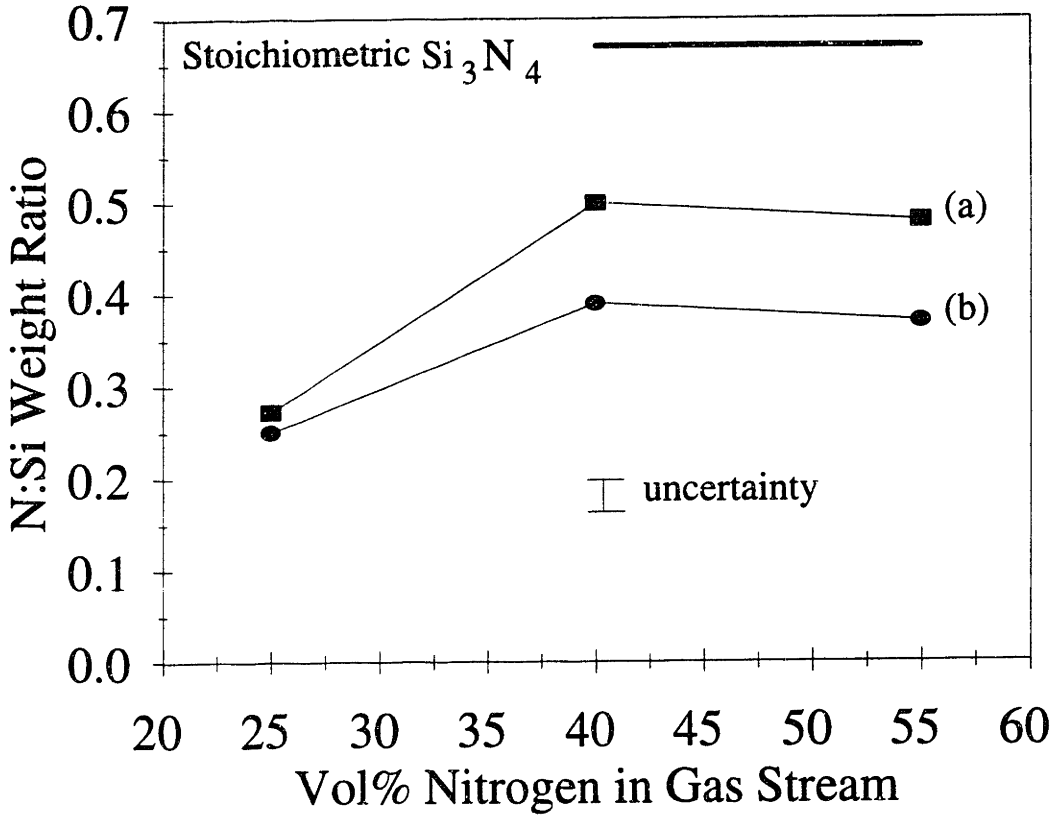

Figure 3-10: Effect of nitrogen content in the gas stream on the N:Si weight ratio of powders produced in a microwave plasma of (a) 850 W and (b) 700 W.

beyond 40 vol% of the total gas flow. This may be the result of a plateau effect whereby the plasma is dissociating its maximum possible number of N_2 molecules, and an increase in the overall amount of pure N_2 available has no effect on the nitridation process. An alternate explanation would be that the rate of nitridation is being limited by something other than the amount of N species in the gas stream. It will be shown that this second scenario is more likely the case. The minor drop in the N:Si ratio between 40 and 55% nitrogen content lies within the experimental uncertainty in measuring the composition of these materials.

The effect of the variation of microwave power, with the N_2 content in the gas stream fixed at 40%, on the N:Si weight ratio in the final product is shown in Figure 3-11. One can see that with increasing microwave plasma powers up to 850 W, increasing amounts of N are incorporated into the product materials, but that no microwave power level allows the full conversion of Si to stoichiometric Si_3N_4. The increase in conversion with increasing power is due to the fact that as the power is increased, one achieves a larger number of dissociated N atoms [17]. Other researchers have seen a similar linear increase in reaction rate with increasing plasma powers due to a greater yield of activated species with increased electron temperatures [18]. The maximum available microwave power (980 W on our 1000 W system) was less effective at converting the nano-Si. The reason for this is likely seen in the higher levels of reflected power observed at 980 W as compared to those seen at 850 W. At 980 W, the power diverted to loss mechanisms was ~ 150 W, while at 850 W the reflected power levels were ~ 50 W. The higher loss levels in the former led to less effective coupling of the microwaves to the plasma and a less efficient process. Operation at 980 W had the additional difficulty of a reduced powder yield. As compared with the other levels of microwave power utilized, about 50% less material was produced at 980 W. A possible explanation for this result is found in a report of higher power densities in an rf plasma significantly decreasing the powder yield in the synthesis of Si_3N_4 from a SiH_4/NH_3 discharge [19]. Anderson *et al.* attributed the decreased yield at higher power densities to electron collision reactions breaking up the Si_3N_4 product [19].

As outlined above, the Si_3N_4 particles that proved to have the most nitrogen incorporated were synthesized with 40 vol% N_2 content in the gas stream at microwave power levels of 850 W. These powders had a residence time of ~0.05 - 0.10 seconds in

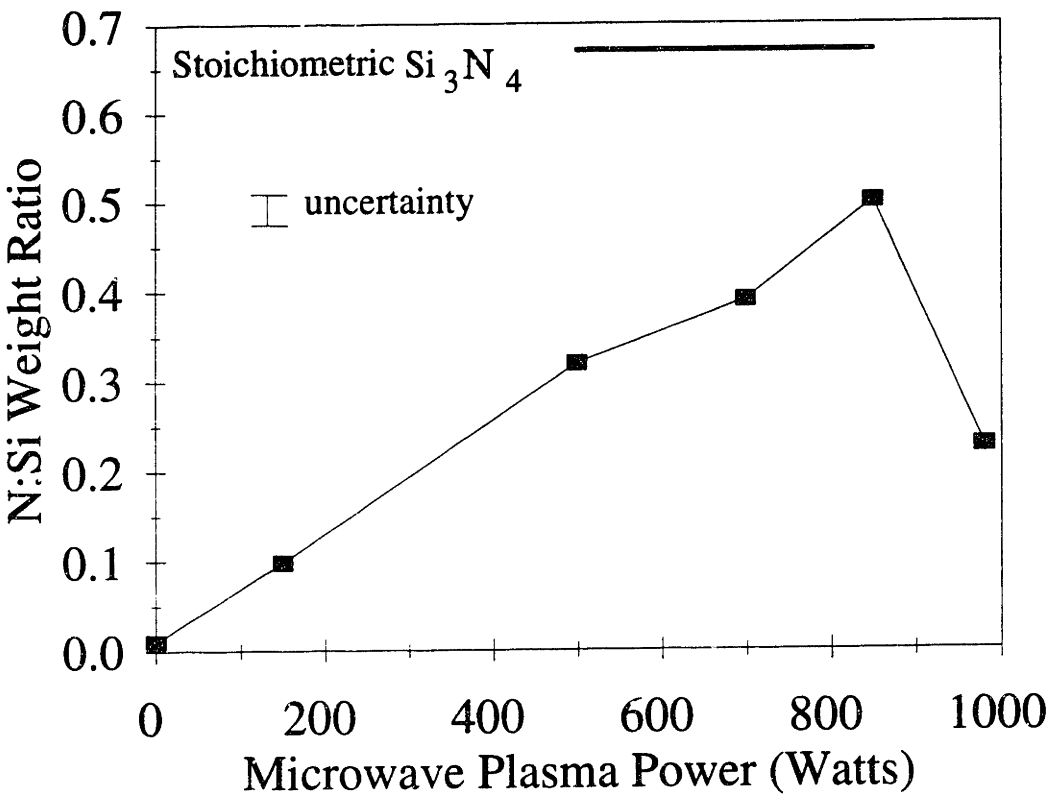

Figure 3-11: Effect of microwave plasma power on the N:Si weight ratio of powders produced in a gas stream with a N_2 content of 40 vol%.

the plasma plume of nitrogen radicals. In order to quantify the effect of varying the total amount of gas flow on the conversion of the Si, another set of experiments was performed such that the N_2 composition in the gas stream was fixed at 40 vol%, but that the total amount of gas flowing was doubled as well as halved from those quantities which had previously yielded the greatest conversion (He = 3.4 slm, N_2 = 2.5 slm, Ar = 0.38 slm). Higher overall flow rates served to increase the reaction length scale with a simultaneous increase in the particle velocity. Figure 3-12 is a plot of the N:Si weight ratio as a function of the total amount of gas, with the N_2 content fixed at 40 vol% and the microwave power at 850 W. (The data point at 6.28 slm is the best conversion data point from the above experiments). When flowing at the lowest overall gas flow rates, the mean free path for collisions is longer, leading to less effective nitridation. Increasing the flow rate gives rise to a larger reaction region and a shorter mean free path for reactant collision, but also reduces the residence time in the plasma due to the higher gas velocities. Thus, a variation in the total gas flow rates had no significant beneficial effect on the nitridation process.

3.3.5 Characterization of Nano-Si_3N_4 Produced with N_2 in the Reactor

As described above, the greatest degree of conversion was achieved for Si_3N_4 powders produced with 850 W of microwave power and 40 vol% N_2 gas flow content. These materials were further characterized by chemical analysis, B.E.T. surface area measurements, XRD and TEM. These samples consisted of 28.3 wt% nitrogen, 15.1 wt% oxygen, and 56.6 wt% silicon, leading to a N:Si weight ratio of 0.50 (somewhat less than the value of 0.667 for stoichiometric Si_3N_4). No other elements were detected by semi-quantitative analysis. These oxygen contents are again reflective of the very high surface areas (270 m^2/g) of these materials as well as the thermodynamic instability of nitrides relative to oxide compounds.

The XRD pattern of the as-prepared Si_3N_4 materials produced with the N_2 plasma is shown in Figure 3-4c. The primary crystalline phase is Si (12.2 nm crystallite size) with a smaller amount of β-Si_3N_4 (4.5 nm crystallite size). Given that chemical analysis showed the presence of significant amounts of nitrogen in this material, the absence of major crystalline Si_3N_4 diffraction effects under X-ray stimulation suggests that the majority of Si_3N_4 in this material is amorphous. This is not too surprising given the

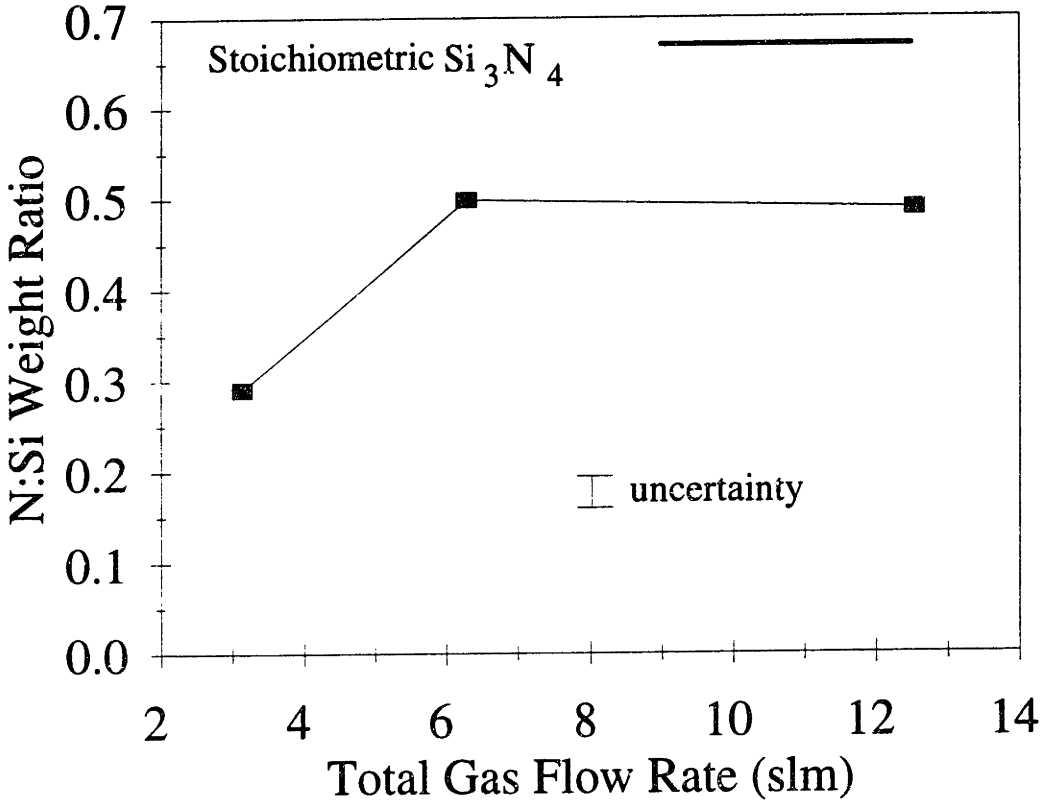

Figure 3-12: Effect of variations in the overall gas flow rate on the N:Si weight ratio of powders produced at 850 W in a gas stream with a fixed N_2 content of 40 vol%.

preponderance of other similar formation processes for Si_3N_4, such as reactions with gaseous precursors, which produce amorphous Si_3N_4 [3,20-22]. The increased Si crystallite size (as compared to 3.9 nm in the Si produced without the plasma) is likely due to Si particle coalescence and growth occurring in the high-temperature microwave plasma.

Although the β-Si_3N_4 phase is the "high-temperature" phase of Si_3N_4, its formation and presence in these materials is also not too surprising for two reasons. The first of these is that it has been previously suggested by Jennings [16] and recently reiterated by Pigeon *et al.* [23] that the reaction between solid silicon and atomic nitrogen, as produced in the plasma in a certain quantity, results in the preferential formation of the β-phase of Si_3N_4. The second factor related to the formation of β-Si_3N_4 is the observation by Iwama of high-temperature phases synthesized in his forced flow-type reactor. He attributed the formation of particles of β-Mn, a high-temperature phase of Mn, in his flow reactor to the enhanced quenching rate of the forced flow of inert gas quenching in a structure created from the high-temperature Mn vapor [24]. Iwama also made use of a microwave cavity attached to his thermal evaporation chamber to prepare γ (fcc) iron, the high-temperature phase of iron. He found that γ-phase (fcc) was produced in greater quantities relative to α-phase (bcc), the low-temperature phase of iron, as the microwave power was increased. He attributed the formation of γ-Fe to a phase transformation from the α-phase occurring in the high-temperature plasma, followed by the rapid quenching in of this phase by the flowing carrier gas as the particles left the plasma [25].

In order to confirm that the majority of the Si_3N_4 produced in our reactor with the N_2 plasma was amorphous, these materials were heated in argon to crystallize the various phases present. Heating in argon prevented additional nitridation of the silicon beyond that which occurred in the reactor during initial synthesis. Shown in Figure 3-13 are XRD patterns of the as-prepared material (a) and after heating to 1450 °C in argon (b). One can see the presence of significant amounts of α- and β-Si_3N_4 in these materials after heating to the elevated temperature. The first evidence of α-phase formation is at 1300 °C; the onset of significant crystallization of the amorphous Si_3N_4 occurs at 1400 °C. This crystallization temperature was in excellent agreement with Cannon *et al.* who observed crystallization of their amorphous Si_3N_4 particles (17 nm) between 1300 and

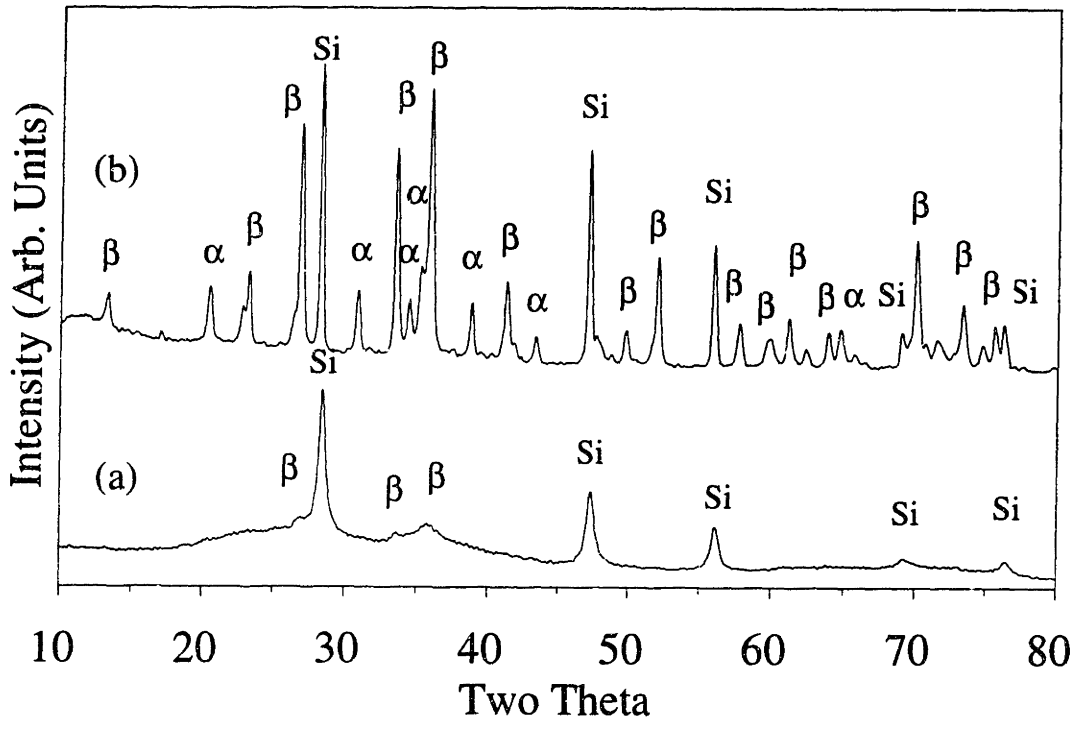

Figure 3-13: XRD patterns of as-prepared Si/Si_3N_4 (N_2 plasma) (a) and after heating to 1450 °C in argon (b).

1400 °C [3], as well as Wang *et al.* [26] who also observed crystallization of their nanostructured amorphous Si_3N_4 at 1400 °C. Shown in Figure 3-14 is a plot of crystallite size versus temperature for the (a) Si, (b) β-Si_3N_4 and (c) α-Si_3N_4 phases. One can see that below the onset of significant crystallization at 1400 °C, there is little to no grain growth with crystallite sizes less than 20 nm for all phases. However, above this temperature, there is significant growth. Wang *et al.* observed similar behavior in their nanostructured Si_3N_4. They attributed this phenomena to the fact that during the transformation from the amorphous state to the crystalline one, atoms are very mobile due to bond breakage [26]. Thus, the easier migration of atoms can lead to crystallization with simultaneous grain growth in the amorphous nano-Si_3N_4 produced by both our efforts and those of Wang.

TEM examinations of Si/Si_3N_4 synthesized with the N_2-plasma showed that the particles of this material were fairly unagglomerated and had an average size of 10.5 nm. The particles ranged in size from 8 to 30 nm. In confirmation of the XRD results, one can see in Figure 3-15 that the majority of the Si_3N_4 particles are amorphous. TEM was also able to locate the excess (unnitrided) crystalline Si observed in XRD. A number of the Si_3N_4 particles had a "shell-core" structure as shown in Figure 3-16a. This morphology consisted of an amorphous shell of material surrounding a crystalline core. The lattice fringes in the center crystalline portion of these particles were measured to obtain a *d*-spacing of 3.16 Å. This corresponds to the (111) plane in Si with an interplanar spacing of 3.14 Å. The doubling of periodicity observed in the Si core of Figure 3-16a is due to the presence of the hexagonal phase of Si where ABAB stacking has replaced the ABCABC stacking of cubic Si [27,28]. The implication of the "shell-core" structure is that these Si/Si_3N_4 particles were formed by the nitridation of the crystalline Si particles, such as those shown in Figure 3-2, evaporated upstream of the microwave plasma. The difficulties in full conversion then stem from inadequate time for the reaction front to propagate through the product layer, the amorphous shell of what is presumably Si_3N_4, to fully convert the entire Si particle to Si_3N_4.

A small number of crystalline β-Si_3N_4 particles (Figure 3-16b) were also observed. The lattice fringes of this particle were measured to obtain a *d*-spacing of 6.50 Å. This corresponds to the (100) plane in β-Si_3N_4 with a nominal interplanar spacing of 6.58 Å. This TEM image with a clearly different morphology than the particle shown in

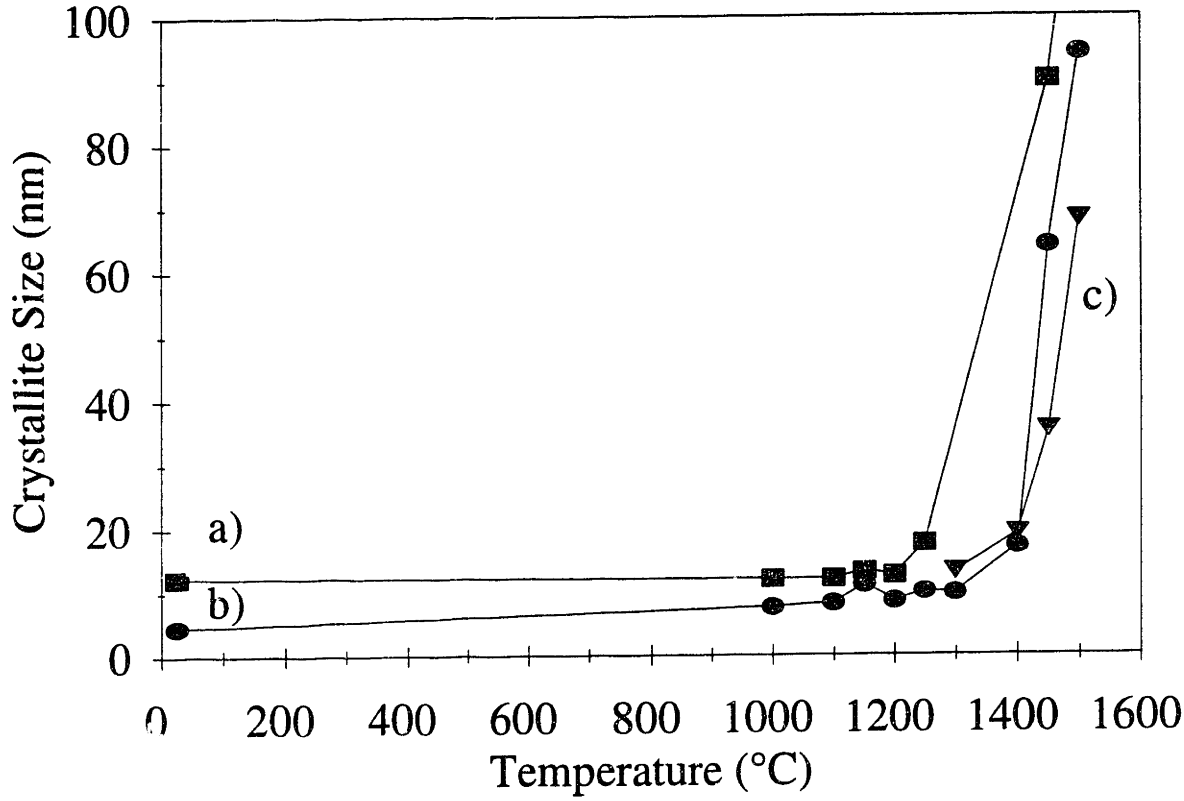

Figure 3-14: Crystallite size of (a) Si, (b) β-Si_3N_4 and (c) α-Si_3N_4 phases for Si/Si_3N_4 powders (N_2 plasma) heated under argon.

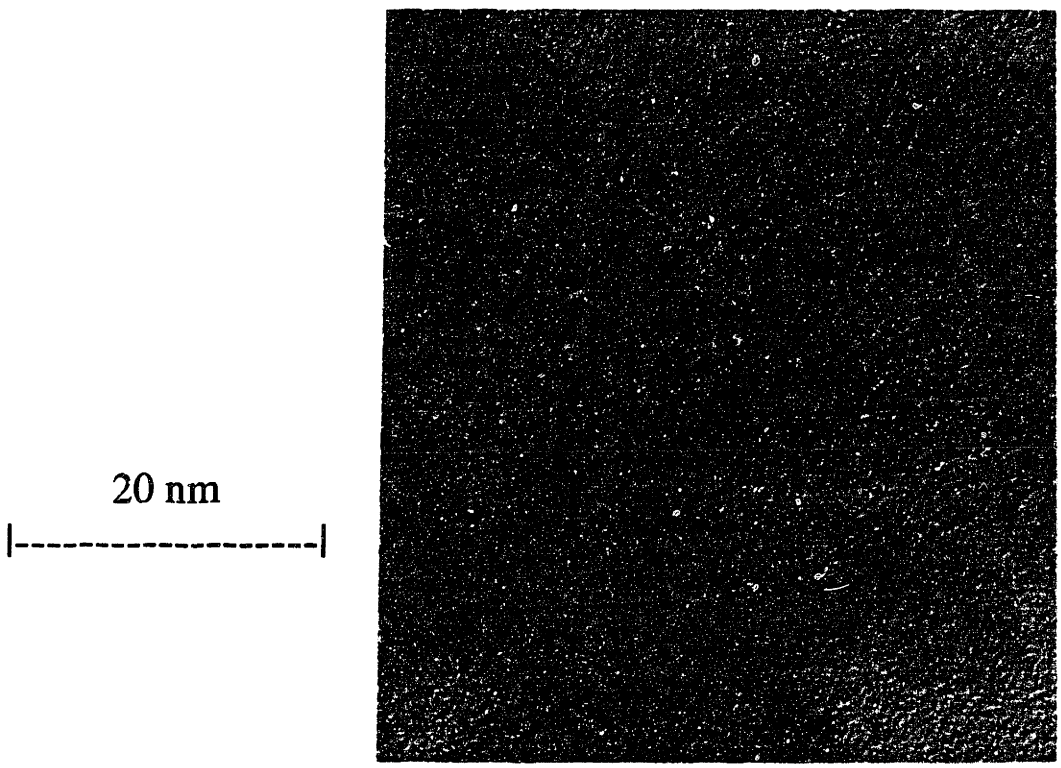

Figure 3-15: TEM micrograph of the primarily amorphous Si_3N_4 particles. A crystalline Si particle and a crystalline Si_3N_4 particle are also visible.

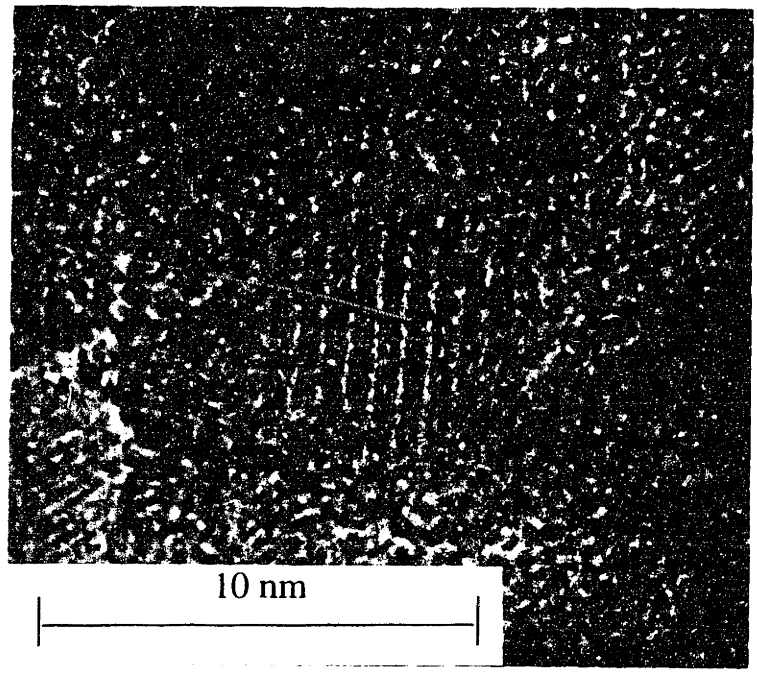

Figure 3-16a: TEM micrograph of Si/Si_3N_4 particle with amorphous shell due to incomplete nitridation. The crystalline core is unreacted hexagonal Si.

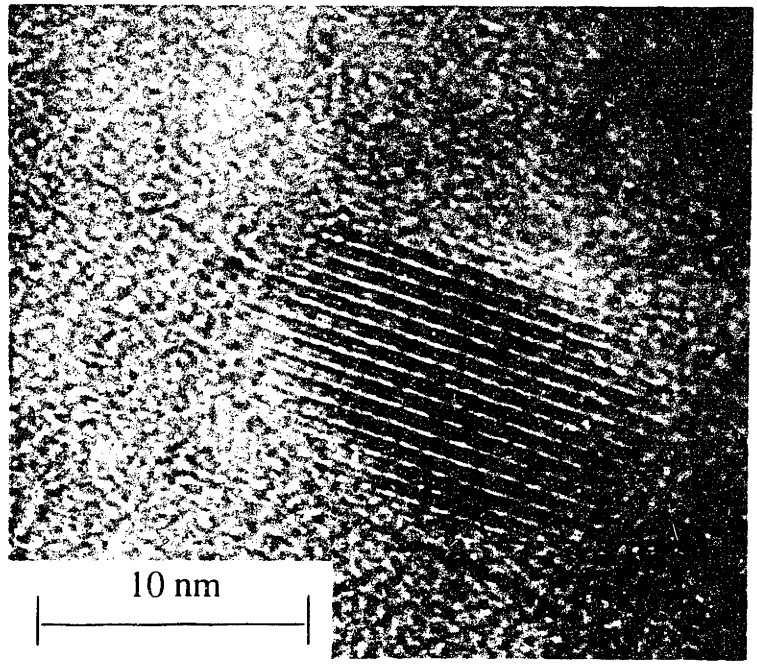

Figure 3-16b: TEM micrograph of β-Si_3N_4 particle.

Figure 3-16a suggests a second growth mechanism may be occurring for these particles. As will be shown in Chapter 4, there is an appreciable backflow of N_2 from the microwave plasma applicator, especially at elevated plasma power levels. It appears that the small amount of β-Si_3N_4 formed may result from the formation of β-Si_3N_4 molecules in the gas phase over the evaporation source as the Si vapor species react with the N vapor species. Thus there are no reaction time or diffusion limitation issues concerning nitrogen to address in such a case (Figure 3-16b), as will be shown to be limiting the formation of Si_3N_4 by the nitridation process suggested by the particle in Figure 3-16a. (This analysis will be presented in section 4.4). This type of alternate formation would fit with Iwama's observation of β-Mn being quenched in following formation from the gas phase. Alternately, these β-Si_3N_4 particles could be formed early enough in the reactor, from the nitridation of the evaporated and condensed Si particles, such that they have sufficient time to crystallize and transform in the microwave plasma from the amorphous state in which they were formed to the β-Si_3N_4 phase observed. This explanation would correlate well with Iwama's second observation regarding the phase transformation of γ-Fe from α-Fe in his microwave plasma [25].

3.3.6 Results for the Production of Nano-Si_3N_4 with NH_3 in the Forced Flow Reactor

The NH_3 plasma was less effective than the N_2 plasma in converting the Si nanoparticles to Si_3N_4 in the reactor. NH_3 at any amount, down to 2% of N_2 flow, served to "quench" the microwave plasma, as observed visually as well as on the microwave leakage detector, and did not produce any additional nitridation. The optimal conversion with NH_3 was achieved at 700 W with the "standard" gas mixture outlined above (He = 3.4 slm, NH_3 = 2.5 slm, Ar = 0.38 slm).

The XRD pattern of these materials shown in Figure 3-4b showed only Si peaks (crystallite size 10.0 nm) with no Si_3N_4 peaks. The smaller Si crystallite size, relative to the 12.2 nm found for the N_2 plasma, is indicative of the less intense, lower temperature process and smaller plasma that was generated through the use of the NH_3. The B.E.T. surface area of these materials was 230 m^2/g. The TEM particle size was 12.1 nm. These samples consisted of only 19.3 wt% nitrogen, with 18.2 wt% oxygen, 62.2 wt% silicon and 0.29 wt% H, leading to a N:Si weight ratio of 0.31, significantly less than the value of 0.50 achieved with the N_2 plasma or the value of 0.667 for stoichiometric Si_3N_4.

Indicative of its lower degree of nitridation, these particles were a brassy tan color in appearance, in contrast to the whitish brown of the more converted Si_3N_4 produced with the N_2 plasma.

There are several potential reasons cited in the literature for why the NH_3 plasma was less effective at nitriding than was the N_2 plasma. There is a report of an arc plasma process that utilized NH_3 in the production of Si_3N_4 [21]. Ishizaki *et al.* found that adding greater amounts of NH_3 resulted in a greater silicon residue in their Si_3N_4 product. They attributed this to the fact that as NH_3 is ionized, it is divided into one part atomic nitrogen and three parts atomic hydrogen. This produces a higher hydrogen partial pressure in the surroundings of the plasma gas, consequently lowering the nitrogen partial pressure for a fixed overall pressure, leading to a lower nitridation efficiency [21]. Another possible problem with the use of NH_3 in these types of reactions is suggested by Lee who reported an extremely short lifetime of NH_x radicals [20]. These radicals changed immediately to N_2 and H_2 which resulted in retarding the nitridation and formation of Si_3N_4 [20]. Related to this issue is the problem outlined in another report which suggests that the concentration of N_2^+ is substantially decreased by the formation of nitrogen-hydrogen molecules by the following reaction as a result of the use of hydrogen containing species in a plasma [29]:

$$N_2^+ + H_2 \rightarrow (N_2H)^+ + H$$

In addition to consuming the nitrogen, this reaction decreases the overall energy of the species in the plasma [30]. Thus, while the initial creation of ionized N species may be easier in a NH_3 plasma, difficulties stemming from the hydrogen in the process prevented the NH_3 plasma from nitriding the Si nanoparticles as effectively as the N_2 plasma did. An additional benefit of the N_2 plasma is that N_2 is much easier to handle than NH_3, and there are no concerns about its toxicity or corrosiveness.

3.3.7 Results of Other Efforts to Increase Nitridation

The effectiveness of plasma processes is a function of a number of variables, including the overall pressure being utilized. In order to evaluate the effect of reactor pressure on the microwave plasma, the reactor pressure was varied from 1.15-10.0 mbar,

with the gases flowing at their usual levels (He = 3.4 slm, N_2 = 2.5 slm, Ar = 0.38 slm). The changes in pressure had a dramatic effect on the intensity of the plasma. Given that this visual "intensity" is loosely correlated to the effectiveness of the plasma in terms of temperature and ionization ability, a microwave leakage detector was used to quantify this effect of varying pressure on the plasma with greater measured power densities implying more effective operation of the plasma. To take these measurements, the microwave shielding around the plasma applicator was removed and the leakage detector probe was mounted next to the applicator. (I stayed a safe distance from the reactor such that the $1/r^2$ dependence of the escaping microwaves prevented any safety hazard). Figure 3-17 is a plot of the microwave leakage detected as a function of pressure for an applied power of 850 W. As shown there, 2 mbar is close to the optimum pressure condition in terms of this parameter, so operation at other pressures was unlikely to achieve higher levels of nitridation and was not attempted.

For the above syntheses, Si was evaporated at temperatures ranging from 1575 – 1625 °C. In order to evaluate the effects of evaporation temperature on nitridation of the Si, evaporation temperatures of 1450 °C and 1950 °C were used with the conditions found above to have the most effective conversion (microwave power = 850 W, N_2 content = 40 vol% and overall gas flow fixed at 6.28 slm). At 1450 °C, just above the melting point of Si (1410 °C), insufficient Si was evaporated during the course of a 68-minute production run to collect enough sample for chemical analysis. (The thinking was that with lower evaporation rates, there would be fewer Si nanoparticles produced, thereby increasing the efficiency of the nitridation process by providing fewer Si particles with which the activated N_2 species could react.) Evaporating at the higher temperature of 1950 °C had the expected effect of evaporating greater quantities of Si leading to less overall nitridation and conversion due both to greater quantities of individual Si particles to convert as well as an increase in the size of the individual evaporated Si particle due to more coalescence partners, thereby requiring a larger Si volume to be nitrided. The N:Si weight ratio in these materials was only 0.12 with less than 10 wt% nitrogen incorporated.

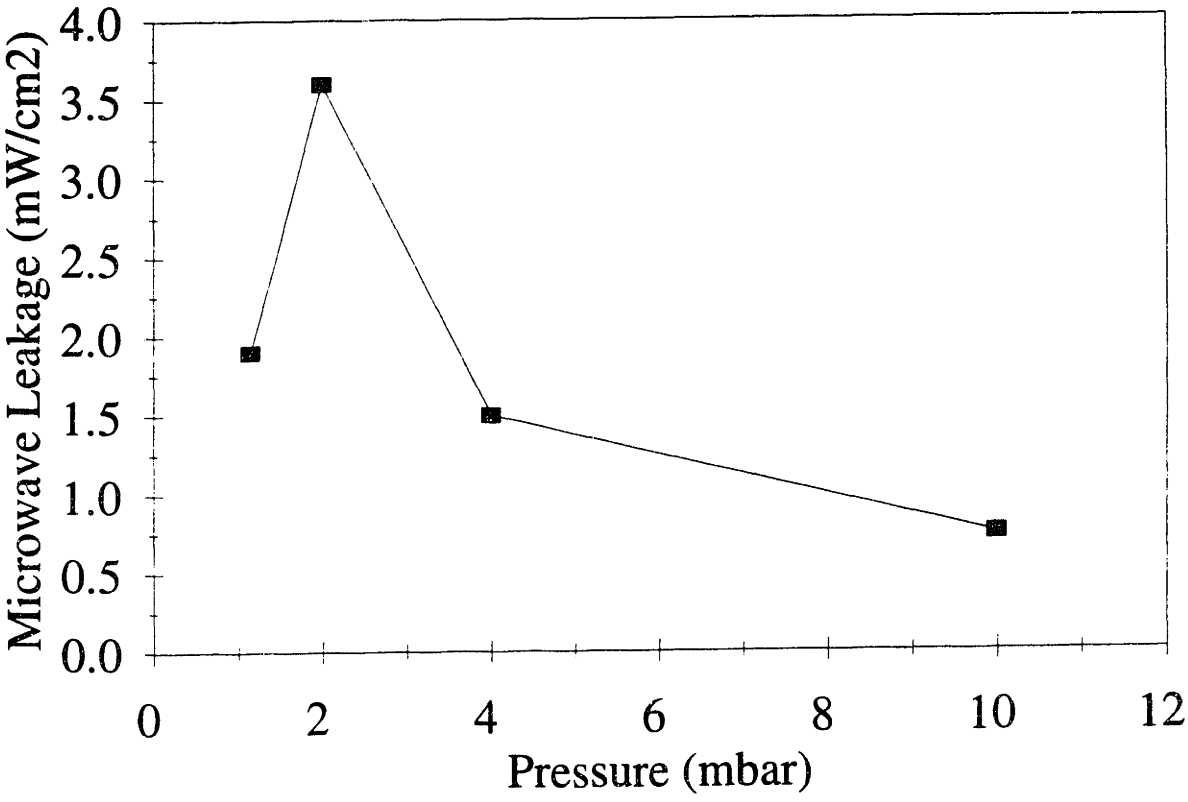

Figure 3-17: Effect of pressure on detected microwave plasma leakage (intensity).

3.4 Summary

The effects of reactor parameters such as pressure and gas velocity on the synthesis of nano-Si and nano-Si_3N_4 particles were studied. Si nanocrystallites were produced with an extremely high surface area (485 m^2/g) and were easily nitrided in flowing N_2 at low temperatures (1050 °C) with no special handling precautions. Although a variety of synthesis conditions were explored, it was not possible to produce fully converted nano-Si_3N_4 in the reactor as it is currently configured. The Si/Si_3N_4 produced has a very high surface area (270 m^2/g) and a small particle size (10.5 nm). The nitrided portions of most particles are amorphous, in the form of a shell surrounding the unnitrided crystalline Si core. The kinetic analysis in Chapter 4 elucidates this growth mechanism and shows that the formation of Si_3N_4 in a process such as that occurring in the reactor is limited by the very slow diffusion of N through this product layer shell.

3.5 References

[1] O. Unal, J.J. Petrovic, and T.E. Mitchell, "Mechanical Properties of Hot Isostatically Pressed Si_3N_4 and Si_3N_4/SiC Composites," *J. Mater. Res.*, **8** [3] 626-634 (1993).

[2] ASM Committee on Vacuum Heat Treating, "Heat Treating in Vacuum Furnaces and Auxiliary Equipment," pp. 492-495 in ASM Handbook: Vol. 4 – Heat Treating (ASM International, 1991).

[3] W.R. Cannon, S.C. Danforth, J.S. Haggerty, and R.A. Marra, "Sinterable Ceramic Powders from Laser-Driven Reactions: II, Powder Characteristics and Process Variables," *J. Am. Ceram. Soc.*, **65** [7] 330-335 (1982).

[4] T. Rouxel and B. Piriou, "Free Silicon and Crystallization in Silicon Nitride Based Ceramics and in Oxynitride Glasses," *J. Appl. Phys.*, **79** [12] 9074-9079 (1996).

[5] A. Chang, S.W. Rhee, and S. Baik, "Kinetics and Mechanisms for Nitridation of Floating Aluminum Powder," *J. Am. Ceram. Soc.*, **78** [1] 33-40 (1995).

[6] D. Vollath and K.E. Sickafus, "Synthesis of Nanosized Ceramic Nitride Powders by Microwave Supported Plasma Reactions," *Nanostr. Mater.*, **2** 451-456 (1993).

[7] C.G. Granqvist and R.A. Buhrman, "Ultrafine Metal Particles," *J. Appl. Phys.*, **47** [5] 2200-2219 (1976).

[8] R.A. Bley, S.M. Kauzlarich, J.E. Davis, and H.W.H. Lee, "Characterization of Silicon Nanoparticles Prepared from Porous Silicon," *Chem. Mater.*, **8** 1881-1888 (1996).

[9] M.H. Teng, J.J. Host, J.-H. Hwang, B.R. Elliott, J.R. Weertman, T.O. Mason, V.P. Dravid, and D.L. Johnson, "Nanophase Ni Particles Produced by a Blown Arc Method," *J. Mater. Res.*, **10** [2] 233-236 (1995).

[10] S. Iwama and K. Hayakawa, "Vaporization and Condensation of Metals in a Flowing Gas with High Velocity," *Nanostr. Mater.*, **1** 113-118 (1992).

[11] R.B. Bird, W.E. Stewart, and E.N. Lightfoot, Transport Phenomena, p. 744, (John Wiley & Sons, New York, 1960).

[12] K. Tanaka, K. Ishizaki, S. Yumoto and T. Egashira, "Production of Ultra-fine Silicon Powder by the Arc Plasma Method," *J. Mater. Sci.*, **22** 2192-2198 (1987).

[13] J. Dutta, I.M. Reaney, C. Bossel, R. Houriet, and H. Hofmann, "Crystallization of Amorphous Nano-Sized Silicon Powders," *Nanostr. Mater.*, **6** 493-496 (1995).

[14] F.L. Riley, "Silicon Nitridation," pp. 121-133 in Progress in Nitrogen Ceramics, ed. F.L. Riley, (Martinus Nijhoff Publishers, Hague, Netherlands, 1983).

[15] K. Ishizaki, S. Yumoto, K. Tanaka, "Production of Silicon Nitride by Gas Nitridation of Ultra-fine Silicon Powder," *J. Mater. Sci.*, **23** 1813-16 (1988).

[16] H.M. Jennings, "Review: On Reactions Between Silicon and Nitrogen," *J. Mater. Sci.*, **18** 951-967 (1993).

[17] T.C. Wei, L. Collins, and J. Phillips, "Measurement and Modeling of Nitrogen Ion Behavior in the Afterglow of a Microwave Plasma," *J. Appl. Phys.*, (1994).

[18] C. Gomez-Aleixandre, O. Sanchez and J.M. Albella, "Effect of RF Plasma on Silicon Nitride Deposition From SiF_4/NH_3 Gas mixtures in a Hot Wall Reactor," pp. 107-112 in Plasma Processing and Synthesis of Materials III (Mat. Res. Soc. Symp. Proc. Vol. 190, MRS, Pittsburgh, PA, 1990).

[19] H. Anderson, T.T. Kodas and D.M. Smith, "Vapor-Phase Processing of Powders: Plasma Synthesis and Aerosol Decomposition," *Ceram. Bull.*, **68** [5] 996-1000 (1989).

[20] H.J. Lee, K. Eguchi, and T. Yoshida, "Preparation of Ultrafine Silicon Nitride, and Silicon Nitride and Silicon Carbide Mixed Powders in a Hybrid Plasma," *J. Am. Ceram. Soc.*, **73** [11] 3356-3362 (1990).

[21] K. Ishizaki, T. Egashira, K. Tanaka, and P.B. Celis, "Direct Production of Ultra-fine Nitrides (Si_3N_4 and AlN) and Carbides (SiC, WC and TiC) Powders by the Arc Plasma Method," *J. Mater. Sci.*, **24** 3553-3559 (1989).

[22] E.A. Leone, S. Curran, M.E. Kotun, G. Carrasquillo, R. van Weeren, and S.C. Danforth, "Solid-State ^{29}Si NMR Analysis of Amorphous Silicon Nitride Powder," *J. Am. Ceram. Soc.*, **79** [2] 513-517 (1996).

[23] R.G. Pigeon, A. Varma, A.E. Miller, "Some Factors Influencing the Formation of Reaction-Bonded Silicon Nitride," *J. Mater. Sci.*, **28** 1919-1936 (1993).

[24] S. Iwama and K. Mihama, "Nanometer-Sized Beta-Mn and Amorphous-Sb Particles Formed by the Flowing Gas Evaporation Technique," *Nanostr. Mater.*, **6** 305-308 (1995).

[25] K. Hayakawa and S. Iwama, "Preparation of Ultrafine γ-Fe Particles by Microwave Plasma Processing," *J. Cryst. Growth*, **99** 188-191 (1990).

[26] T. Wang, L. Zhang, and C. Mo, "A Study on Growth and Crystallization Behavior of Nanostructured Amorphous Silicon Nitride," *Nanostr. Mater.*, **4** [2] 207-213 (1994).

[27] P. Pirouz, J. Yang, F. Ernst, and H.J. Möller, "Hexagonal Silicon: A New HREM Study," pp. 199-204 in High Resolution Microscopy of Materials, (Mat. Res. Soc. Symp. Proc. Vol. 139, MRS, Pittsburgh, PA, 1989).

[28] C.J.D. Hetherington, "HREM of Defects in Silicon at Twin Intersections," pp. 123-134 in High Resolution Electron Microscopy of Defects in Materials, (Mat. Res. Soc. Symp. Proc. Vol. 183, MRS, Pittsburgh, PA, 1990).

[29] E.J. Hellund, The Plasma State, pp. 90-91 (Reinhold Publishing Corporation, New York, 1961).

[30] O. Matsumoto, M. Konuma and Y. Kanzaki, "Nitriding of Titanium in an R.F. Discharge: Effect of the Addition of Hydrogen to Nitrogen on Nitriding," *J. Less Comm. Metals*, **84** 157-163 (1982).

Chapter 4

Synthesis and Characterization of Nano TiN particles

4.1 Introduction

As outlined in Chapter 1, TiN possesses good intrinsic properties, such as extreme hardness, good wear resistance, a low coefficient of friction, and electronic conductivity, and is potentially useful in various applications such as cutting tools and self-heating crucibles. However, it is not currently utilized as a mainstream structural ceramic due to problems in sintering and processing pure, monolithic TiN. The challenges in sinterability preventing the more wide-spread use of TiN stem from both the low quality of the commercially available powders as well as the inherently low diffusivities in these materials. Both of these factors lead to the required use of high reaction temperatures or exotic processing to attempt to densify these materials. TiN is currently most commonly used as a coating material, deposited in CVD-type processes, to improve the service life of cutting tools. When it is used in a "bulk" form, it is typically pressure densified with additives such as Ni, Co or Al. While these additives facilitate densification, they are often retained as a secondary phase in the sintered part and adversely affect the final properties of that component. However, with the enhanced sintering kinetics achievable with the use of nanocrystalline materials, it may be possible to produce a dense, monolithic TiN through a pressureless sintering process. Thus, the reactor described in detail in Chapter 2 was used to produce nano-TiN.

4.2 Experimental Details

4.2.1 Synthesis of Nano-TiN in Forced Flow Reactor

A He gas stream (3.0 slm) flowed over the crucible where Ti was evaporated at T = 2000-2200 °C, corresponding to Ti vapor pressures of ~ 0.3 – 1.6 mbar [1]. (See Figure 2-5 for a plot of evaporation temperature versus time during TiN synthesis). A vacuum pumping system, operating at a pressure of 2 mbar, removed the evaporated particles in the He flow from the growth zone over the evaporation source. Evidence of the high evaporation rates due to operation so near the vapor pressure of Ti can be seen in the observation of a smoke plume, appearing as a grayish haze, over the evaporation source. A mixture of N_2 (2.28 slm), comprising 40 vol% of the total gas flow, and Ar (0.330 slm) was injected into the He gas stream 0.1 m downstream of the evaporation

source. The gas mixture and entrained particles entered the microwave plasma applicator operating at 700 W where the N_2 in the gas mixture was dissociated to provide a source of nitrogen radicals for reaction with the Ti clusters. The particles were collected downstream on the collection filter described in 2.2.6. Following a synthesis run, the reactor was controllably backfilled with air for the air-exposed TiN and the particles were removed in the open atmosphere. For the unexposed TiN, the reactor was controllably backfilled with N_2, and the particles were removed in an Ar-filled glovebox (H_2O < 1 ppm, O_2 < 15 ppm). TiN was made with and without the microwave plasma applicator in operation. The particles synthesized with the microwave plasma in operation (700 W) are designated "WM." The particles synthesized without the microwave plasma in operation are designated "WOM."

4.2.2 Characterization of Nano-TiN

Characterization of the nanocrystalline TiN powders was performed by nitrogen adsorption (Micromeritics ASAP 2000) and transmission electron microscopy (TEM) (JEOL CX, 200 kV). Chemical analysis for bulk oxygen and nitrogen content was performed by inert gas fusion (LECO TC136) as described in Chapter 3. X-ray diffraction (XRD) (Siemens D5000) with Ni-filtered Cu K_α radiation was used to determine the phases present and the crystallite size. ESCA (Electron Spectroscopy for Chemical Analysis) data was acquired using Mg K_α X-rays. The ESCA characterization was performed by Werner Hoheisel of the Bayer Corporation, the parent company of H.C. Starck, in Leverkusen, Germany.

4.3 Results and Discussion of the Synthesis of Nano-TiN

4.3.1 Chemical Analysis of Ti Pellets

The surface of the starting Ti pellets used for thermal evaporation was analyzed for O and N content by cutting a pellet in half lengthwise and removing the center core material to leave only the outer "shell" of the pellet for analysis. Bulk values for O, N, and other metallic impurities were determined by analyzing the central core material. The values for these impurities are shown in Table 4-1. As shown there, the surface of the Ti pellets is slightly preferentially oxidized. Other than the oxygen, there were no

impurities present in an amount likely to have a significant effect on the synthesis or sintering of the nano-TiN made from this raw Ti.

TABLE 4-1: Chemical Analysis for Impurities in Ti Pellets

Element	"surface" (wt%)	"bulk" (wt%)
Nitrogen	0.011	0.008
Oxygen	0.186	0.167
Nickel	-	0.015
Aluminum	-	0.010
Chromium	-	0.014
Iron	-	0.037
Silicon	-	0.006
Tin	-	0.007
Zirconium	-	0.001
Vanadium	-	0.002
Copper	-	0.014

4.3.2 Characterization of Nano-TiN WM Particles

The black WM TiN particles had B.E.T. surface areas ranging from 210 - 250 m^2/g, with an average value of 225 m^2/g. This surface area for TiN is the highest reported value that we are aware of in the existing literature.

The only phase detected via XRD was TiN (Figure 4-1). No Ti peaks or peaks related to nitrogen deficient or non-stoichiometric titanium-nitrogen compounds such as Ti_2N, Ti_4N_{3-x}, Ti_3N_{2-x}, $TiN_{0.30}$, or $TiN_{0.26}$ were seen. Shown in Figure 4-2 is the phase diagram of the Ti-N system showing the large number of these nonstoichiometric compounds possible in the Ti-N system as well as the range of stoichiometry possible for TiN [2].

In a crystalline lattice with semi-infinite size, exact diffraction conditions give rise to sharp, well-defined diffraction phenomena. However, with crystal sizes of only one or two orders of magnitude larger than the X-ray wavelength, diffraction conditions become weaker leading to peak broadening which can be utilized in the Scherrer formula [3] or

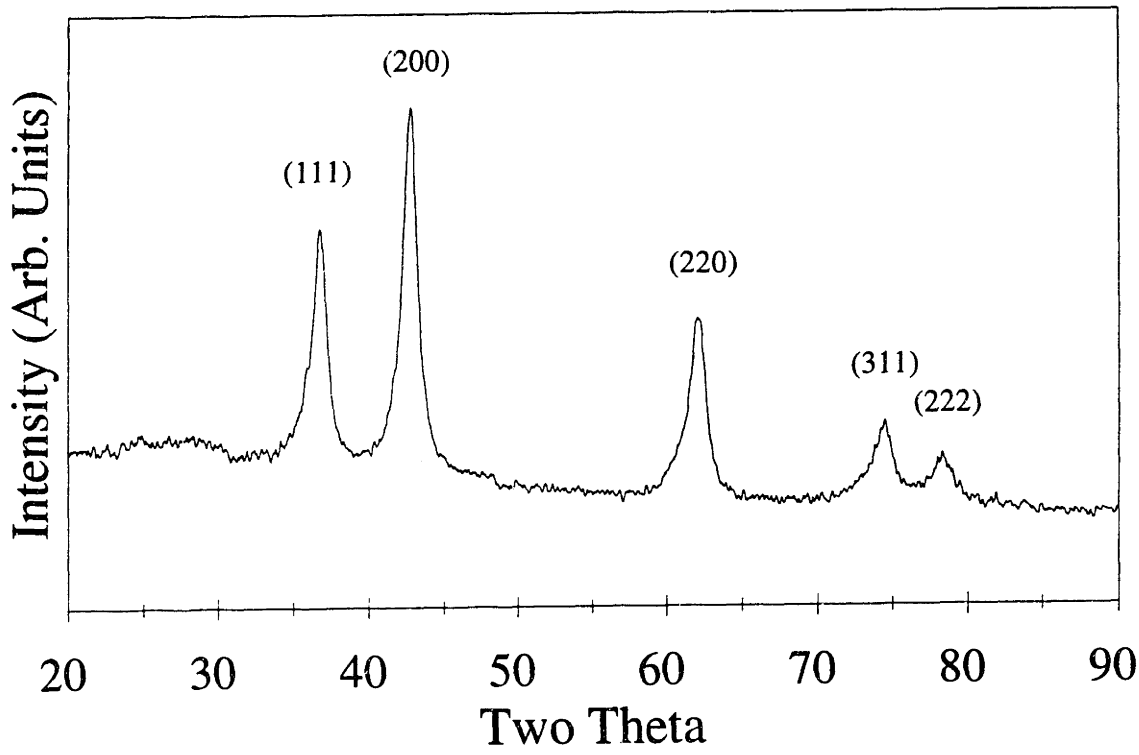

Figure 4-1: XRD pattern of as-prepared WM nano-TiN.

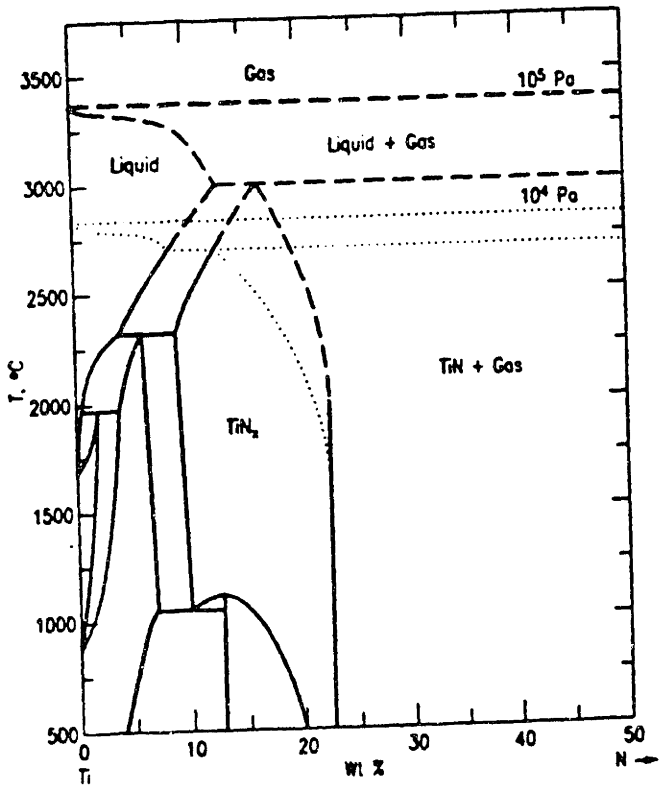

Figure 4-2: Phase diagram of the Ti-N system [2].

the Korchendörfer method [4] to determine a volume-averaged crystallite/grain size in nanocrystalline materials. With two peaks of the same reflection, such as (111) and (222) in TiN, it is possible to use the Kochendörfer method to separate crystal size and strain in a sample [4]. After correction for instrumental broadening effects, the Kochendörfer analysis gave a crystallite size of 6.3 nm, slightly smaller than the value of 8.6 nm determined by the Scherrer technique. The strain in these materials, which may also contribute to peak broadening, was determined by the Kochendörfer analysis to be 0.0054%. This extremely small value is not surprising given the synthesis route of these materials utilizing homogeneous nucleation and growth from the vapor phase. Nanocrystalline materials synthesized by other techniques such as ball-milling may possess long-range strain fields of dislocations leading to measured strains of 1–2% and an increased difficulty in measuring the crystallite size. In Figure 4-1, one can see that the resolution of the higher order (222) peak is a bit complicated by the small grain size of these samples. Given that the Scherrer equation was derived for cubic crystals, assumes that the strain is zero, as verified for the nano-TiN by the Kochendörfer analysis, and is useful for crystal sizes up to ~ 100 nm (vs. crystal sizes of only ~ 50 nm in the Kochendörfer technique), the Scherrer formula utilizing the (111) peak was used for all subsequent XRD grain size analyses with these materials.

Assuming that the composition of a TiN material varies only with respect to the stoichiometry, then the lattice parameter can be correlated to the amount of nitrogen present in the TiN lattice [5,6]. Given the issues of non-stoichiometry present in the synthesis of the nano-Si_3N_4, very careful efforts were made to determine a_o, the lattice parameter, in these materials. The lattice parameter was determined from peak positions by Cohen's method [3] using the average of measurements on 5 different samples. LaB_6 was used as an internal standard to more precisely fix peak locations. a_o was determined to be 4.238 ± 0.001 Å (within 0.1% of the theoretical JCPDS #38-1420 value of 4.2417 Å for TiN). As shown in the Kochendörfer analysis above, there is no significant strain contribution or effect on the lattice parameter in these materials.

Lattice parameter and composition data in TiN from several sources was used by Wriedt and Murray [6] in establishing the least-squares relation:

$$a_o \pm 0.002 = 4.159 + 0.00164y \qquad (4\text{-}1)$$

between the lattice parameter a_o (in Å) and composition y (at% N) in TiN. This relationship yields a value of a_o = 4.241 Å for the lattice parameter at 50 at% N, in good agreement with the JCPDS value of 4.2417 Å. With the above value of a_o (4.238 Å) and no consideration of the "± 0.0002" term, y = 48.2 at% N. Taking into account the experimental uncertainty in the determination of a_o (± 0.001 Å) as well as that of the least squares fit, the composition value y may range from 46.3 to 50.0 at% N. Given that stoichiometric TiN is 50 at% N, the a_o value of 4.238 Å implies that, within the experimental uncertainty, the WM crystallites are fully stoichiometric TiN. Additional evidence for this assertion will be seen in the chemical analysis and ESCA data presented later in this section.

The TEM diffraction pattern of these materials is shown in Figure 4-3. By measuring the diameter (= 2R) of the Debye diffraction rings shown in Figure 4-3, the TEM diffraction pattern was indexed to be that of TiN, within a constant error typical of these types of measurements and calculations [7], by using

$$d_{hkl} = \lambda L/R \qquad (4\text{-}2)$$

where d_{hkl} is the interplanar spacing (Å), λ_{200KV} = 0.02507 Å, L = camera length = 53.96 cm (determined for the JEOL CX used with a calibration specimen of TlCl), and R is the ring radius measured (cm). The R measurements, made on the original negative, and observed d spacing values are shown in Table 4-2 along with the theoretical d spacing values for TiN (from JCPDS # 38-1420).

Chemical analysis showed that the oxygen content of the WM powders was 18.4 wt%, the N content was 19.8 wt %, and the Ti content was 61.8 wt%. This gives a molar ratio for N/Ti = 1.10, compared to a value of 1.0 for stoichiometric TiN. Recalling Eqn. (3-2), with a surface area of 225 m^2/g, one could expect 11.4 wt% oxygen due merely to 1 monolayer of adsorbed O_2. As the lattice parameter was determined to within 0.1% of the JCPDS value for TiN, the oxygen likely lies on the surface and not in the lattice of these materials, although the very small amounts of O in the starting Ti pellets are likely incorporated into the powders as they are formed. The experimental uncertainty in the chemical analysis leads to an uncertainty level of ± 0.10 in the molar N/Ti ratio

Figure 4-3: Nano-TiN (WM) electron diffraction pattern.

calculation. Thus, the value of 1.10 for the WM particles corresponds to stoichiometric N/Ti within uncertainty, although, if they are nonstoichiometric, it indicates that these particles have a slight excess of nitrogen.

TABLE 4-2: Calculation of Interplanar Spacings in Nano-TiN

Debye Ring #	(hkl)	Radius (cm)	d_{obs} (Å)	d_{theo} (Å)	Δ (%)
1	(111)	0.580	2.332	2.4492	- 4.7
2	(200)	0.670	2.019	2.1207	- 4.8
3	(220)	0.955	1.417	1.4997	- 5.5
4	(311)	1.155	1.171	1.2789	- 8.4
5	(222)	1.170	1.156	1.2245	- 6.2
6	(420)	1.520	0.890	0.9485	-5.6

Shown in Figures 4-4(a) and (b) are TEM micrographs of WM particles taken at locations just a few μm away from each other on the TEM grid. These micrographs indicate the formation of two primary particle shapes – a spheric morphology (a) and a cubic morphology (b). Both the cubic and spherical particles showed highly crystalline structure in TEM, in both visible lattice structure and electron diffraction. In the WM particles, on average, ~ 70% of the particles observed were "cube"-shaped and ~ 30% of the particles observed were "sphere"-shaped. This suggests that at least two different particle growth mechanisms were in effect here.

The spherical particles are most likely formed in the gas stream by "external" nitridation from the exterior toward the interior of a condensed Ti particle. These spheres are likely formed in the same manner suggested by Figure 3-16(a) for nitridation of the Si particles. That is, they react with the N_2 downstream from the Ti evaporation point, and nitridation occurs by the diffusion of N through the TiN product layer into the center of the composite particle where the N reacts with the unreacted Ti core. These starting Ti particles (cores) were likely generated from the evaporation and growth of Ti clusters from the Ti melt in the thermal evaporation source.

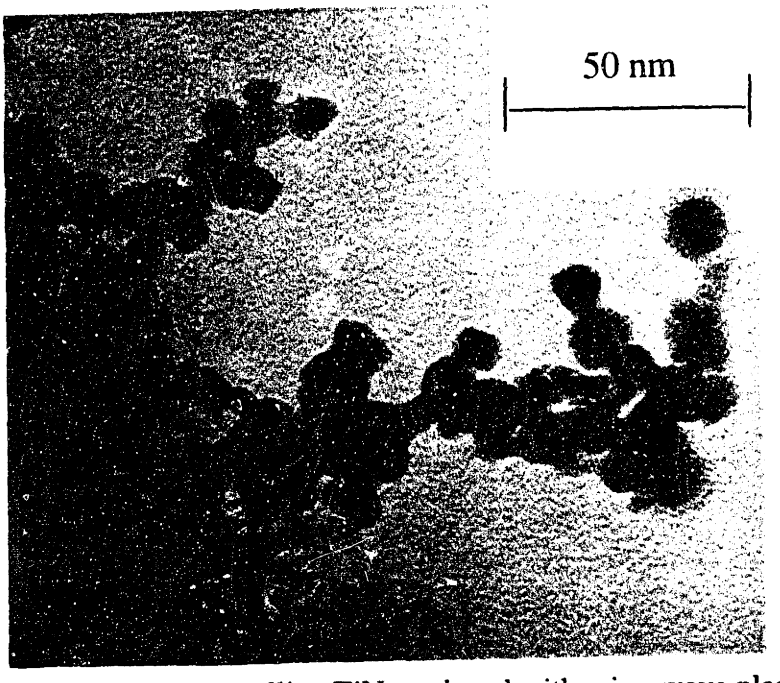

Figure 4-4a: Nanocrystalline TiN produced with microwave plasma.

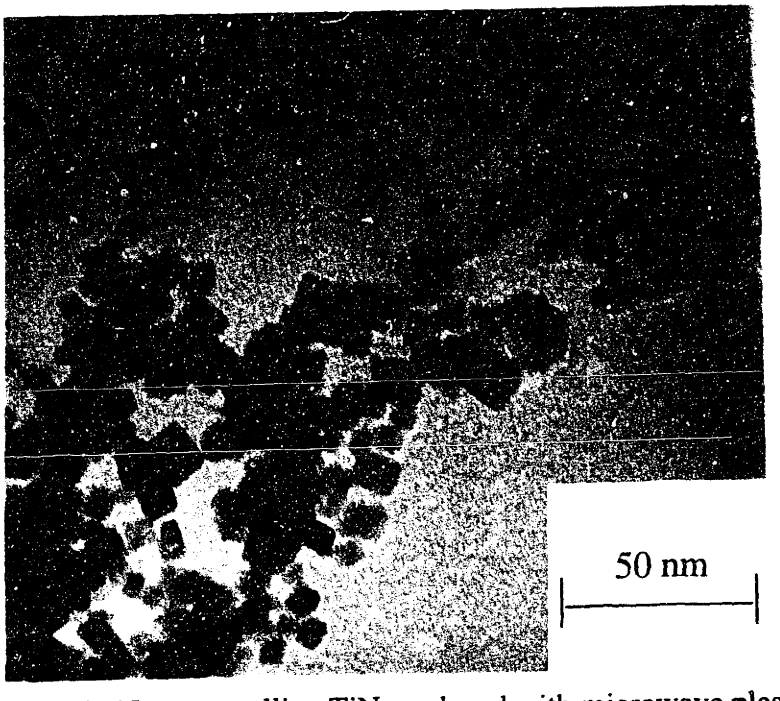

Figure 4-4b: Nanocrystalline TiN produced with microwave plasma.

However, the cubic particles were more likely formed by a mechanism involving growth from TiN molecules condensed from the gas phase. Both experiment and electronic structure theory show that stoichiometric and substoichiometric TiN crystallizes in a sodium chloride (cubic) structure [8]. The formation of these TiN molecules may take place by one of at least two possible mechanisms; the results observed are likely due to a combination of both of these growth routes. During the evaporation process, a thin layer of TiN forms on the slightly cooler ends of the crucible while molten Ti remains in the hottest center regions at all times. Evidence for the formation of this TiN coating comes both from its metallic, gold appearance as well as XRD data on pieces of the crucible. Additionally, XRD of material deposited on the metal loader, positioned above and just slightly to the rear of the thermal evaporation source, reveals the presence of several TiN phases (Ti_2N, TiN, $TiN_{0.30}$). Other researchers have also observed the formation of nitrogen-deficient Ti_2N close to their Ti emitter during the synthesis of TiN on stainless steel substrates in a plasma vacuum deposition process [9]. This evidence of TiN formation in the evaporation chamber implies the presence of nitrogen upstream from its injection point. This nitrogen may be present from two sources, leading to two routes for the direct formation of TiN molecules in the gas phase. First, N_2 may be upstream due to the change in pressure at the microwave applicator as described in section 2.2.5. Thus, the evaporated Ti, also in the gas phase, may react directly with this N to form TiN gas molecules and "self-assemble" directly into the "cubic" NaCl structure of TiN. A second, less effective, pathway for the formation of TiN gas molecules is the evaporation of the TiN formed on the crucible source. While complete data for the vapor pressure behavior of TiN does not exist, Pollard and Woodward report that TiN undergoes decomposition to Ti and N molecules in a vacuum of 1.33×10^{-4} mbar at 1450 °C [10]. There is an additional report of the volatilization and decomposition of TiN at 2230 °C at 1 mbar [11], close to the synthesis parameters at which the reactor was operated. Thus, one may generate gaseous Ti and N by this evaporation route as well. It may be possible for the Ti present from the evaporation and dissociation of TiN to cluster with other Ti clusters in the gas phase, form Ti spheres and be "externally" nitrided. However, given their close proximity to other N atoms, present due to the dissociation event, while they are in the gas phase, it seems more probable that this Ti would reform as TiN gas molecules which could then

grow to directly form the TiN "cubes" observed. Evidence for this self-assembly mechanism comes from time of flight mass spectrometry which was used to investigate $(TiN)_n^+$ clusters produced by a laser-induced plasma reactor source [8]. Chen and Castleman found that even at small cluster sizes, such as $Ti_4N_4^+$ and $Ti_9N_9^+$, the atoms in the cluster rearranged themselves to achieve this cuboid structure, the stable geometric structure for TiN with a minimum energy [8]. It should be noted that one group of researchers have suggested that the formation of TiN particles in these types of processes may proceed by surface nitridation of the starting Ti, vaporization of the nitride from the surface and condensation of the nitride vapor directly into the nitride particles in the free space of the gas [12]. However, Stearns and Kohl detected TiN molecules in the vapor over solid TiN at 2006 to 2183 °C in an amount consisting of less than 0.002% of the total gas mixture [13]. Given the additional evidence cited above that the TiN phase dissociates as it vaporizes to Ti and N molecules [10], this alternate growth mechanism seems unlikely.

Given that such a large percentage of the WM TiN particles have this cubic structure, the "B.E.T.-equivalent diameter" derivation done in 3.3.2 based on spherical particles is not valid. Following the derivation done in 3.3.2, for cubic particles, the B.E.T.-equivalent diameter is:

$$d = \frac{12}{S_a * \delta} \tag{4-3}$$

Based on the 70% cube and 30% sphere mix of particles, the B.E.T.-equivalent diameter for the WM TiN of 225 m^2/g particles is 8.5 nm. As was the case with the Si particles, this value is in excellent agreement with that determined by TEM (8.8 nm) and is indicative of the unagglomerated nature of these particles.

ESCA measurements on WM particles which had been exposed to air provided information about the chemical composition of the surface of these powders. These measurements showed that the O content was 23.7 wt%, the Ti content was 47.5 wt%, the N content was 14.6 wt% and the C content was 14.2 wt%. A key result is the molar ratio of N/Ti = 1.05, indicating that these materials are stoichiometric or slightly nitrogen-rich, in agreement with the LECO chemical analysis data presented earlier. Of interest also is

the apparently very high O and C levels detected. However, many other researchers have reported a similar surface enrichment of O and C on TiN [14-17]. For instance, Danek *et al.* reports air exposed stoichiometric TiN films with 8.8 wt% C on the surface [15]. This enrichment in O and C species is typically attributed to the formation of carbonate and carboxy-compounds associated with the adsorption of CO and CO_2 from the ambient atmosphere.

The position of the core level peaks in ESCA can also provide information about the local chemical environment of various elements. For example, the Ti $2p_{3/2}$ level has a binding energy of 454 eV in pure Ti, while it is 454.6 eV in TiC, 455.2 eV in TiN and 458.7 eV in TiO_2 [18,19]. Shown in Figure 4-5 is the ESCA data for the Ti 2p levels. The appearance of the paired doublets, which can be ascribed to TiN and TiO_2, is very common in TiN materials which have been exposed to air due to surface oxidation of the TiN [16,19,20,21,22]. Shown in Table 4-3 is a comparison of reported positions for the Ti 2p core levels in TiN and TiO_2 to those seen in the data in Figure 4-5. The comparison to Naβ's work [21] is particularly useful because that measurement was done on air-exposed nanometer-sized (30 – 40 nm) TiN particles. The excellent agreement shown in Table 4-3 indicates that the air-exposed WM powders have an appreciable amount of titanium oxide on their surfaces.

TABLE 4-3: Comparison of Ti 2p Core Levels

Core Level	Ramqvist [22]	Hofmann [19]	Naβ [21]	This Work
Ti $2p_{3/2}$ in TiN	455 eV	455.2 eV	455 eV	455.0 eV
Ti $2p_{3/2}$ in TiO_2	458 eV	458.0 eV	458 eV	458.3 eV
Ti $2p_{1/2}$ in TiN	461 eV	461.1 eV	461 eV	460.9 eV
Ti $2p_{1/2}$ in TiO_2	464 eV	463.5 eV	464 eV	463.9 eV

Even "unexposed" nano-TiN materials, synthesized by the Bayer Corporation, which see only 10-20 ppm oxygen in a glovebox environment as our particles do, show the Ti 2p doublets corresponding to both Ti-O and Ti-N bonding [23]. This suggests that exposure to only a few ppm of oxygen can result in the formation of a passivating titanium oxide layer on high surface area nano-nitrides such as TiN. Holm also found

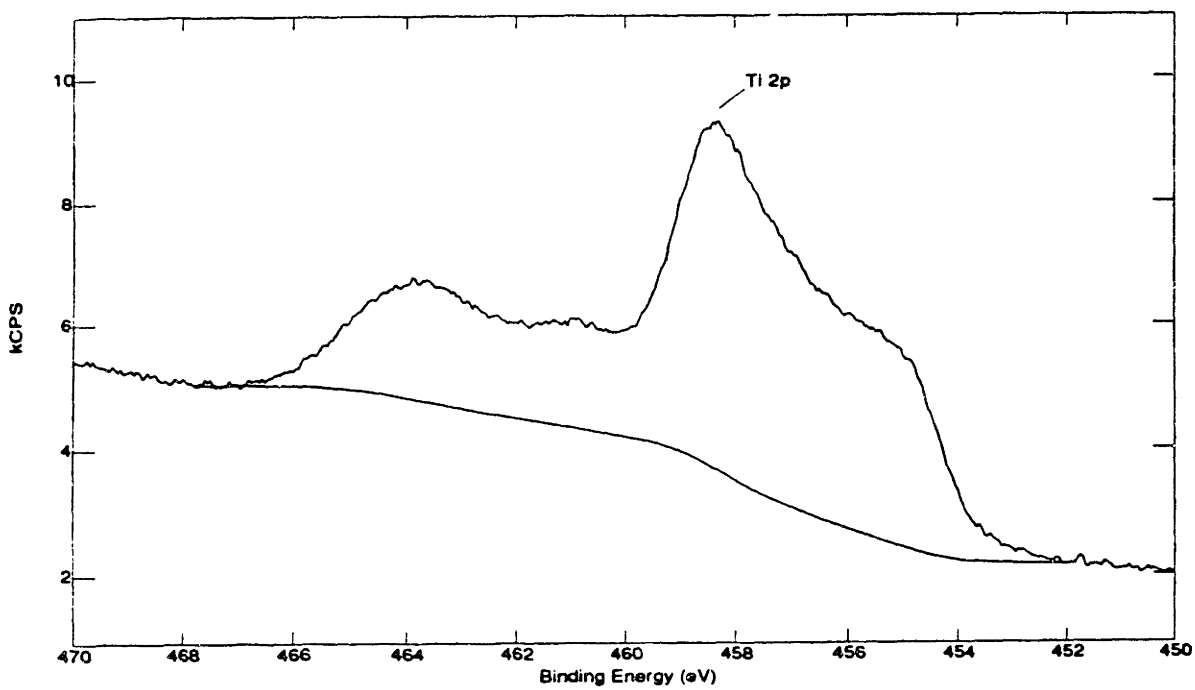

Figure 4-5: ESCA data for Ti 2p on EXP-WM.

that with a longer exposure time to air, the intensity of the TiN ESCA peaks decreased while the magnitude of the TiO_2 peaks increased, indicating greater surface oxidation with time [23]. As will be detailed in Chapter 5, this preponderance for oxidation, even in a glovebox environment, has important implications for the sinterability of these materials and the levels of incorporated oxygen one would obtain in the final sintered part.

The XRD lattice parameter measurement, the LECO chemical analysis data, and the ESCA chemical analysis results all suggest that the WM particles are fully nitrided TiN. Possible kinetic reasons for the successful nitridation of Ti and the incomplete conversion of Si in this reactor are detailed at the end of this chapter in section 4.4.

A summary and comparison of some key powder characteristics of the best TiN currently being synthesized is presented in Table 4-4. Recall Eqn. (3-2) and note the increasing oxygen content with increasing surface area in the powders once they are exposed to air, as well as the large average particle size and broadness of the particle size range found in other TiN powders.

TABLE 4-4: Comparison of TiN Powder Properties

Researcher/Source	B.E.T. Surface Area	TEM Particle Size Range	Oxygen Content
Commercial (H.C. Starck)	5 m^2/g	800 - 19,000 nm	0.8 wt%
T. Rabe and R. Wäsche (H.C. Starck) [24]	43 m^2/g	8 - 25 nm	3.2 wt%
G.P. Dransfield and A.G. Jones (Tioxide) [25]	59 m^2/g	10 - 30 nm	6.6 wt%
D.T. Castro and J.Y. Ying (WM)	**225 m^2/g**	**4 -14 nm**	**18.4 wt%**

The Tioxide process [25] utilizes the vapor phase reduction of $TiCl_4$ with NH_3 for the manufacture of TiN (T59). Byproducts of this process include HCl and excess $TiCl_4$. H.C. Starck is developing better TiN powders than the best one currently commercially available and characterized at the top of Table 4-4. The characteristics reported in the literature for one such experimental powder synthesized by chemical vapor reaction at ~1200 °C are also shown in Table 4-4 [24].

The bulk of the previous work on the processing of nano-TiN has been done by Andrievski [17, 26, 27]. The nano-TiN powders he uses for the bulk of his work, and to which our sintering results will be compared in section 5.3.5, are synthesized by nitriding titanium hydride in a DC-plasma [26]. These powders have a surface area of 14 m^2/g, an oxygen content of 2.5 wt%, an average particle size of 80 nm and a lattice parameter of 4.230 Å, indicating that they are slightly nitrogen-deficient (43.3 at% N) [26].

4.3.3 Characterization of Nano-TiN WOM Particles

There were no significant differences in the B.E.T. surface area (~230 m^2/g), XRD phase (TiN only), and XRD crystallite size (9.1 nm) of the WOM TiN particles compared to the WM particles. However, values of the lattice parameter and the chemical analysis results suggest that the materials produced without the microwave plasma are nitrogen-deficient. a_o was determined to be 4.232 Å, which gives a y value of 44.5 at% N from Eqn. (4-1). As shown above, experimental uncertainty introduces ~ ± 2 at% N uncertainty to this value. The 44.5 at% N corresponds to a Ti-N compound of $TiN_{0.80}$. This composition is well within the nonstoichiometric TiN_x phase field shown in Figure 4-2. Thus, only TiN, and no excess Ti peaks, is detected in the XRD data.

Chemical analysis showed that the oxygen content of the WOM powders was 20.1 wt%, the N content was 15.2 wt %, and the Ti content was 64.7 wt%. This gives a value for the molar ratio N/Ti = 0.80, again indicating the nitrogen deficiency of the WOM powders. This decreased nitridation is likely due to a lack of ionization of the reactants and a decrease in thermal energy without the microwave plasma in operation.

The WOM powders were a mix of ~ 50% cubic particles and ~ 50% spherical particles. The fact that there was a lesser number of cube-shaped particles in the WOM powders correlates with the above assertion that this particle morphology results, in part, from the backflow of N_2 from the microwave plasma applicator. With it not in operation for the synthesis of the WOM powders, there is no pressure differential due to temperature so the amount of N_2 backflow is less and thus fewer particles are formed from TiN gas molecules. However, there is likely still some backflow of N_2 due to the constriction of the microwave plasma applicator. Additionally, the minor effect of evaporation of TiN from the crucible would still be a mechanism for formation of these cubic particles. Thus, the cube-like morphology is still observed in large quantities of

particles. The TEM particle size of the WOM materials was 6.6 nm, while the B.E.T.-equivalent particle size, using a 50/50 mix of cubes and spheres, is 7.5 nm. This larger B.E.T.-equivalent particle size as compared to the TEM particle size may hint at the more agglomerated nature of the WOM particles, relative to the WM ones, discussed below in more detail.

4.3.3 Comparison of n-TiN WM and WOM Particles

As shown in Figure 4-6, the more significant differences between the particles produced with (WM) and without (WOM) the microwave plasma was in the degree of agglomeration. The WM powders consisted primarily of clusters of $\leq$ 100 particles, while the WOM materials consisted of very large particle aggregates linked by chains of other particles. The WM and WOM specimens were prepared for TEM by sonication for 5 minutes in ethanol to disperse the powders. In order to verify that the observed difference in agglomeration was not a result of unequal sonication during TEM specimen preparation, the WOM particles were sonicated for 100 minutes as well. The same levels of chaining, linkage and agglomeration were observed in the WOM particles in these specimens as well. This extended sonication also demonstrated that the agglomeration was of a hard nature that could not be readily broken.

Another significant difference between the WM and the WOM powders is in the particle size distributions shown in Figure 4-7. While the average TEM particle size of the WOM particles (6.6 nm) is smaller than that of the particles made with the plasma (8.8 nm), the distribution is broader. Thus, as compared to the WOM powders, the WM nano-TiN should be more conducive to sintering for two main reasons. First, the lower level of agglomeration of the WM powders will reduce the formation of large pores. The agglomeration-related large pores typically require higher sintering temperatures and longer sintering times to eliminate than those pores formed due to packing between individual particles. An additional, related sintering benefit to the lower degree of agglomeration in the WM powders is that the grain size of a fully dense ceramic which is consolidated by pressureless sintering will generally never be less than the starting agglomerate size [28]. Secondly, the narrower particle size distribution of the WM powders will lead to a greater uniformity in the pore size distribution as well. Ideally, one would prefer a completely monodisperse pore size distribution such that all the inter-

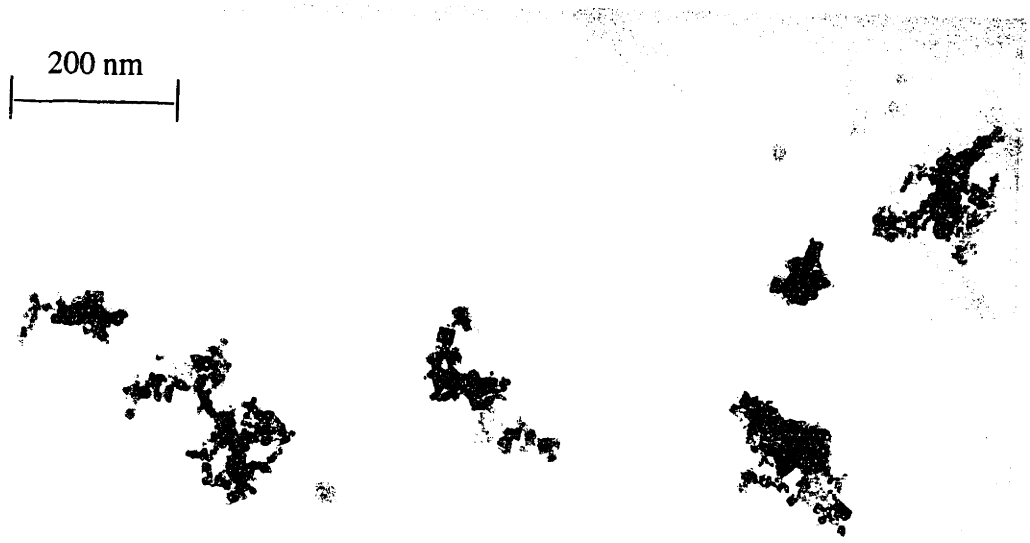

Figure 4-6a: Nanocrystalline TiN particles produced with the microwave plasma (WM).

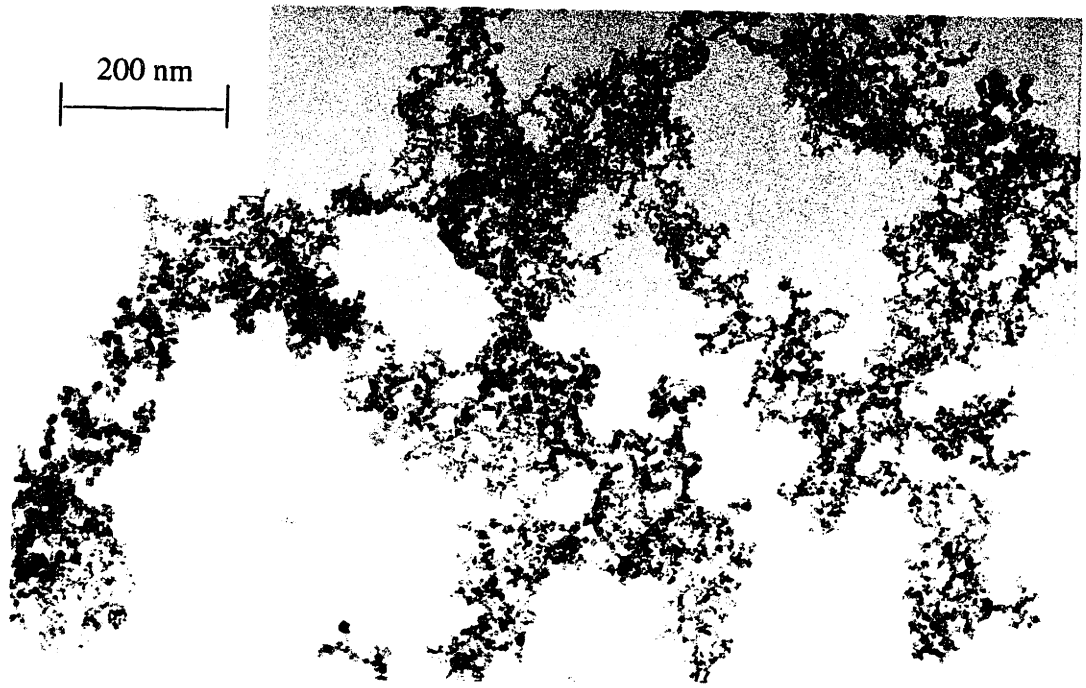

Figure 4-6b: Nanocrystalline TiN particles produced without the microwave plasma (WOM).

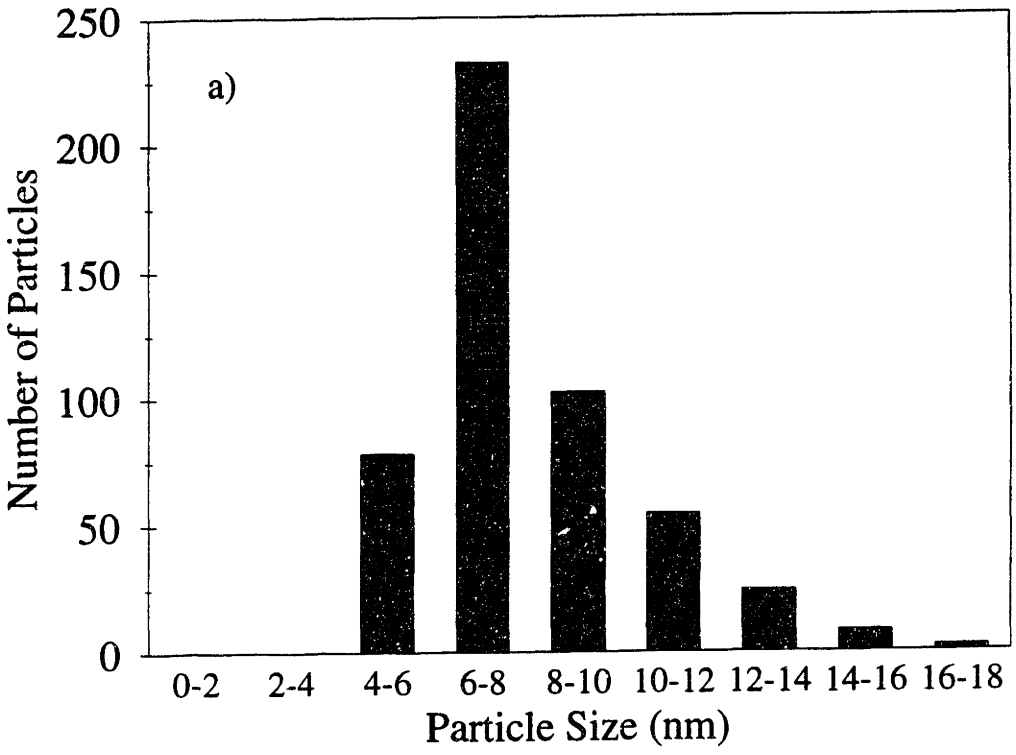

Figure 4-7a: Particle size distribution for nano-TiN produced with the microwave plasma (WM).

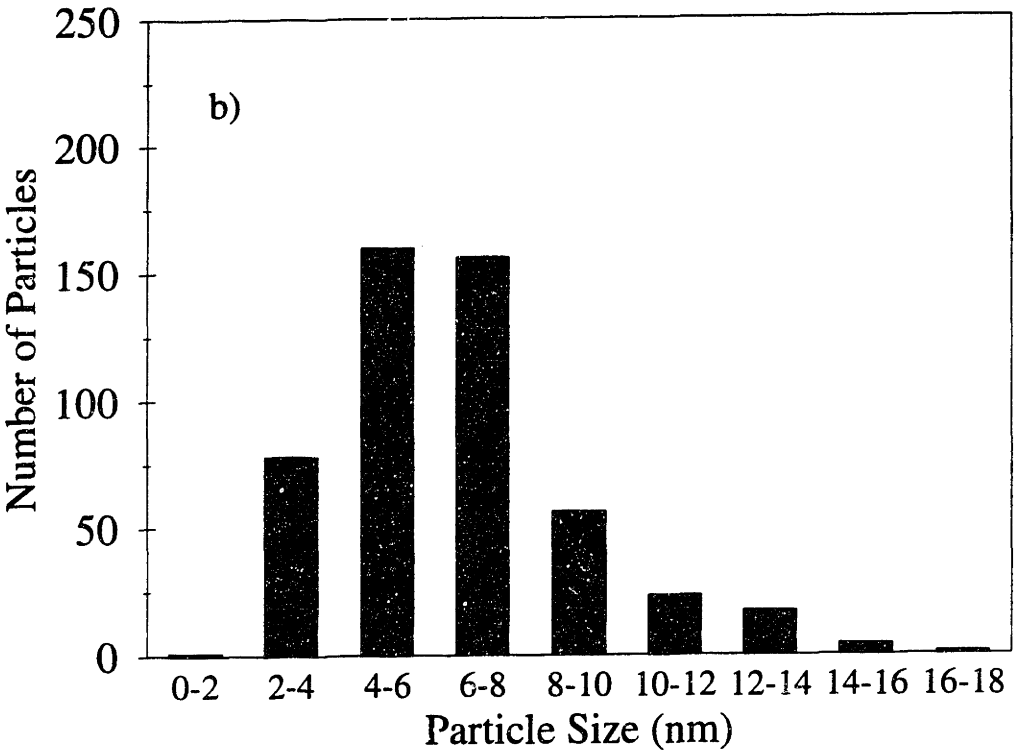

Figure 4-7b: Particle size distribution for nano-TiN produced without the microwave plasma (WOM).

particle pores are the same size and may disappear simultaneously upon sintering without undesirable grain growth. The effects of the differing levels of agglomeration and particle size distributions on the sinterability of these powders is described in Chapter 5.

The fact that the WM particle size distribution reflects a narrower log-normal distribution can be quantified by the geometric standard deviation σ_g, a measure of the spread of a log-normal size distribution and defined as the size at 84.13% divided by the size at 50% in a log-probability plot [29,30]. The log-normal distribution, with its asymmetric bell shape and tail toward larger diameters, is typical of particle growth processes from a supersaturated vapor [31]; a smaller value of σ_g indicates a sharper, narrower distribution [32]. σ_g for the WM and WOM powders is 1.25 and 1.41, respectively.

It is interesting to compare this value for σ_g of 1.25 to that reported by other researchers in the synthesis of nanocrystalline materials. Granqvist, in his early work describing the inert gas condensation synthesis of crystalline particles, cited a range for σ_g of 1.36 to 1.60. [31]. More recently, a σ_g range of 1.36 to 1.53 for nanophase Ni synthesized from a blown arc has been reported [30]. Haas *et al.* reports values of σ_g for their forced flow reactor of 1.7 for the synthesis of nano-Cu and 1.6 for the synthesis of nano-Pd [33]. Haas also notes that these values are lower than those they determined for materials synthesized from a sputtering route in a conventional batch-type reactor (1.9 for nano-Cu and 1.81 for nano-Pd) [33]. Thus, one can see the particle size distribution achieved in our synthesis with the microwave plasma is significantly narrower than those reported in the literature. It is also worth noting the extensive agglomeration, significantly more than that found in our reactor, visible in TEM images of the powders produced in the forced flow reactors of reference [30] and [33].

4.3.5 Discussion of Particle Formation Processes

Based on the above results, it is clear that the microwave plasma has introduced a greater degree of uniformity to the synthesis process. The effectiveness of the microwave plasma in reducing particle agglomeration and narrowing the particle size distribution during synthesis is most likely due to two features of the microwave plasma not directly related to its functionality in ionizing N_2 for the nitridation reaction.

The first of these secondary features is that, as shown in Eqn. (2-2), the microwave plasma dissociates the N_2 molecules by an electron bombardment process. Thus, the impinging electrons are likely charging the particles as they pass through the microwave field, leading to the creation of an electrostatic repulsion between the particles that aids in preventing them from coming in contact with one another. At elevated temperatures, but below those temperatures required for particle growth by coalescence, aggregate growth and agglomeration occur when particles come into contact with one another and stick. With a reduction in the probability of particles contacting one another, the potential for sticking and agglomeration is also reduced. Bossel's research into the synthesis of nano-Si powders in a RF plasma process found that repulsion between charged clusters has an affect on the agglomeration and growth processes [34].

The second feature of the microwave plasma that benefited the synthesis of particles in this reactor is the elevated temperatures present in the microwave plasma. While measuring the temperature in a plasma is problematic [35,36], there has been an attempt to determine the temperature in a similar low-pressure nitrogen microwave plasma [35]. Phillips used both a shielded and an unshielded chromel-alumel thermocouple to measure the temperature of a 200 W, 2.45 GHz plasma operating at 0.56 mbar. Temperatures were measured at various locations in the plasma, and equations were developed using the values measured to extrapolate temperatures closer to the center of the plasma. According to his results, the unshielded thermocouple probably gave readings somewhat higher than the actual temperature of the plasma due to interference from the plasma, while the shielded thermocouple likely gave lower values due to heat transfer effects. Thus, the temperatures he determined likely formed an upper and lower boundary around the actual temperature in the plasma. Using the equations developed by Phillips, the temperature bound on the plasma in our reactor at a distance of 0.5 cm from the center of the plasma likely ranged from 830 °C to 2160 °C, with temperatures at the center bounded by 970 °C and 2530 °C. Taking the midpoints of these outer limits gives temperatures of roughly 1500 °C for 0.5 cm in either direction from the center of the plasma and 1750 °C at the center of the plasma. These temperatures should be taken as first estimates only, given that the gas flow rate as well as the plasma power likely has a significant effect on this parameter. The higher flow rates in our reactor of ~ 5610 sccm, as compared to 7 sccm for Phillips's work, would likely lead to lower plasma

temperatures. However, the higher plasma power of 700 W in our microwave plasma, as compared to 200 W for Phillips, would lead to higher temperatures in our reactor than those determined from Phillip's equations. Nonetheless, based on these calculations, as well as anecdotal reports of melting the quartz tubes in these applicators with insufficient cooling, it would seem reasonable to assume a temperature in the range of 1500 – 1750 °C for the interior of the microwave plasma.

Before detailing the impact of a region of high temperature at a distance from the initial evaporation source, it would be beneficial to briefly describe the inert gas condensation particle synthesis and growth process. The following summary is based on a description by Flagan [37].

In inert gas condensation, a metal is vaporized from a hot source into a cooler gas where the decreasing temperature decreases the equilibrium vapor pressure leading to a high supersaturation. At high supersaturation, the vapors rapidly nucleate homogeneously, forming large numbers of extremely small particles. After a short initial burst of growth by condensation, the particles then grow by Brownian coagulation as they move away from the source. Here coagulation is taken to describe particle combination with complete coalescence to form individual particles. At later times, with cooling to lower temperatures, due to the decreasing mobility of the atoms in the small particles and decreasing excess surface free energy driving forces, coalescence slows and the particles begin to turn into and grow as agglomerated clusters. Within these clusters, the primary particles may still be identified, but necks between particles grow only to a limited extent before the next collision event. Once the particles start to agglomerate, "growth" of the cluster accelerates due to the fact that the larger aggregates present a large target for impingement of the more mobile smaller particles. Thus, once agglomerates begin to form, they grow more rapidly than dense, single particles, often at the expense of dense particle growth [37].

Based on the above growth process, one can now begin to consider how the high temperature microwave plasma may affect the particle formation process in this reactor. The fundamental difference between this reactor and most others described in the literature, is that with the high temperature plasma zone just downstream of the area in which the nanoparticles are initially formed, there is an extension of the coalescence growth zone. This is due to a reduction in the cooling rate of the particles. Koch and

Friedlander have shown that t_{coal}, the time during which particle growth may occur by the "favorable" process of coalescence, is expressed as:

$$t_{coal} = \frac{T_o}{\varepsilon \kappa} \tag{4-4}$$

where κ is the cooling rate, T_o is the initial temperature and ε is a dimensionless activation energy [38]. Thus lower cooling rates lead to longer times for growth by coalescence.

An alternate way of thinking about the same concept was outlined by Flagan [37]. There he asks, given that this transition from growth by coalescence to growth by agglomeration occurs, what are the characteristic times for each growth process and when does the transition take place. One wants to extend the time before which the characteristic coalescence time (τ_{coal}), modeled as a sintering process, surpasses the characteristic agglomeration time (τ_{aggl}), modeled as a particle collision process. That is, as long as:

$$\frac{\tau_{coal}}{\tau_{aggl}} < 1 \tag{4-5}$$

particle growth will occur by coalescence rather than agglomeration. As shown in Figure 4-8 [37], with lower cooling rates, the transition from growth by coalescence to growth by agglomeration occurs after a longer time. (Figure 4-8 shows the variation of the characteristic times for agglomeration and coalescence of Si nanoparticles and the product particle radius with growth time. Cooling rates of 0 K/s, 10^2 K/s and 10^4 K/s are shown.) Thus, Flagan asserts, the key to superior powder synthesis is to extend the time for growth by coalescence as long as possible, with one technique for doing so being a reduction in the cooling rate. If one is to then quench the particles rapidly while still in the coalescence growth region before reaching the onset of agglomeration, one may significantly reduce the amount of agglomeration present in the synthesized particles.

Thus, the extension of the particle growth zone in our reactor has in and of itself led to less agglomeration by extending the time before which growth by agglomeration commences. Additionally, Matsoukas and Friedlander have also shown that small primary particles grow into larger agglomerates in a given time than the same volumetric concentration of large primary particles [39]. Thus, the overall larger primary particle

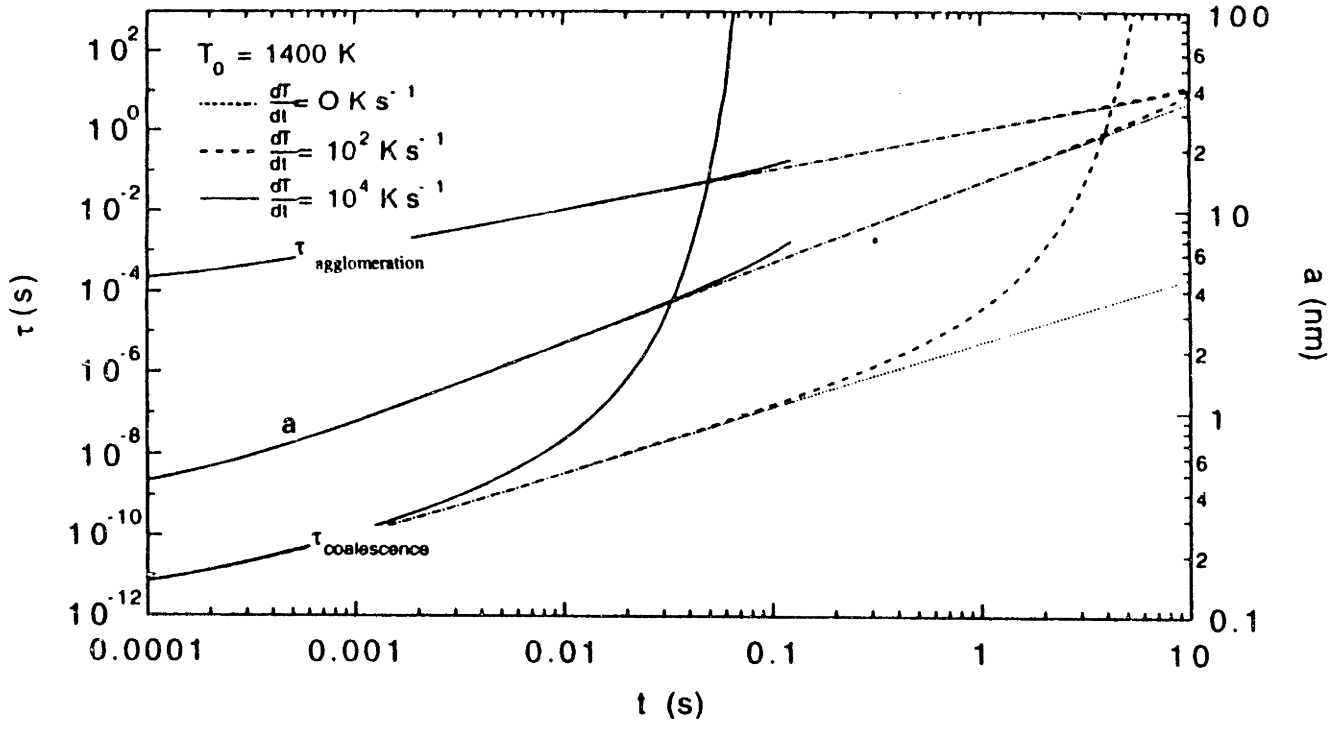

Figure 4-8: Variation of the characteristic times for agglomeration and coalescence of Si nanoparticles and the product particle radius ("a") with growth time. Cooling rates of 0 K/s, 10^2 K/s and 10^4 K/s are shown [37].

size, achieved with longer growth times, also serves to reduce the degree of agglomeration. Yet another benefit to a longer growth time by coalescence is described by Pratsinis, who suggests that the width of the size distribution narrows as particle growth dominates because it allows any initial differences in synthesized particle size to become negligible [29].

Thus, the higher average particle size (8.8 nm) for the WM particles produced with the microwave plasma versus that of the WOM particles produced without the plasma (6.6 nm) is likely due to the high temperature of the plasma extending the particle growth zone allowing additional growth by coalescence as the particles pass through the plasma. As the microwave plasma causes lower cooling rates and allows longer coalescent growth times, the particle size distribution is permitted to sharpen to produce the extremely monodisperse distribution observed. Finally, while the charged particles may be repelling one another and reducing agglomeration by electrostatic repulsion, the extension of this time for growth by coalescence also serves to reduce the agglomeration in the WM powders. Therefore, the microwave plasma functions in a dual capacity as both a source of thermal energy for the extension of the coalescence zone and as an aid to overcoming kinetic inhibitions to the nitridation process through the ionization of the N_2.

4.4 Comparison of Nitridation Kinetics in Si-N and Ti-N Systems

4.4.1 Gas-Solid Reaction Model

In an effort to better understand the differences in the kinetic processes occurring during the nitridation of the Ti and Si nanoclusters in my reactor, the expanding sharp interface model (SIM) for gas-solid reactions was utilized. It should be noted that this analysis is only applicable to those nitride particles which were formed by nitridation of the spherical metal nanoparticles. These would be the Si/Si_3N_4 "amorphous shell-Si core" particles and the spherical TiN particles. It also should be noted that these calculations were performed to get a qualitative sense of the difference between the two processes, one of which led to the full nitridation of Ti and one of which had incomplete nitridation of the Si nanoparticles. It is not suggested that the nitridation process taking place in the reactor is exactly analogous to that presented here or that the absolute values of these calculations are rigidly applicable to the reactor synthesis results.

The gas-solid reaction model is legitimate to use in this instance due to the small particle sizes synthesized in the reactor. The intermolecular mean free path in the vapor phase, $\lambda = 1.052 \times 10^{-4}$ m as calculated in section 2.2.6, is far greater than the likely interparticle separation in the gas stream. Thus, gas-solid collisions are far more frequent than gas-gas collisions, and the metal nitride (MN) particles formed are most likely by gas-solid reactions between nitrogen and metal (M) as shown:

$$N_2 + b\,M \rightarrow MN \qquad (4\text{-}6)$$

In the SIM model, there are three potential rate-limiting steps: (1) the diffusion of nitrogen through the gas film surrounding the particle, (2) the diffusion of nitrogen through the developing product layer, and (3) the chemical reaction at the metal-metal nitride interface [40]. As detailed below, other researchers have shown previously that for the formation of both Si_3N_4 and TiN, diffusion of nitrogen through the nitride product layer is the rate-determining step.

The early suggestion by Atkinson that the rate-determining step in the nitridation of silicon may be solid-state diffusion of the reactants through the product layer [41] has been further analyzed. Jennings states that all diffusion modeling efforts neglect the diffusion of Si through Si_3N_4 because the Si is too large, relative to the N atom, and does not diffuse through Si_3N_4 [42]. The recent work of both Pigeon and Varma [43] and Wuu and Schoenung [44] support the above assertion that nitrogen diffusion is rate-determining in the formation of Si_3N_4. Pigeon and Varma, upon whose work much of this analysis is based, found that the Si_3N_4 product layer that develops upon nitridation restricts free nitrogen diffusion to the unreacted silicon core. They also found that the reaction at the Si-Si_3N_4 interface and the nitrogen diffusion through the external boundary gas film layer are faster than the diffusion of nitrogen through the product layer, and hence are not rate-determining [43]. Wuu and Schoenung also present a model and calculations to show clearly that the diffusion of nitrogen through the nitride layer is much slower than the reaction kinetics, and is therefore rate-limiting [44].

For the Ti-N system, Elger *et al.* used gas phase vapor reactions utilizing $TiCl_4$ + Mg + NH_3 and found that they produced a nitrogen-deficient powder with a median particle size of 280 nm). They reported that the TiN forms a coating on the surface of the Ti

particle and that diffusion of nitrogen through this product layer, to react with the unconverted Ti in the particle, was the rate-limiting step [45]. Another study of the nitriding of Ti particles sized from 46 to 74 μm in an RF plasma found that the kinetics of nitridation obeyed a parabolic law, indicating that the diffusion of nitrogen through the nitride layer was the rate-determining step [46]. Grami and Munir also report that the diffusion of nitrogen through TiN is rate-controlling during combustion synthesis [47]. Finally, Pivkina *et al.*, in their work on reaction-bonded TiN, report that a surface coating of TiN shields the interior Ti particles thereby preventing full conversion. They ascribe their difficulties in full conversion by this synthesis route to a diffusion self-limitation [48].

Therefore, one is justified in modeling the gas-solid reactions taking place in the reactor as ones limited by the diffusion of nitrogen through the nitride product layer to the unreacted core. In these instances, the time (τ) for complete conversion as limited by this mechanism can be modeled as:

$$\tau = \frac{\rho_M \, r_o^{\,2}}{6 \, b \, D \, C_{N2}} \qquad (4\text{-}7)$$

where ρ_M is the molar mass of the metal, r_o is the original radius of the metal particle, b is the stoichiometric coefficient for the reaction of the metal plus nitrogen going to the nitride, D is the diffusivity of N through the product layer and C_{N2} is the surface concentration of nitrogen on the particle [40]. For the reaction of either Si or Ti plus N_2 going to the metal nitride in this reactor for the synthesis conditions outlined above and in Chapter 3, the values for the parameters in Eqn. (4-7) are essentially equivalent for both the Si-N system and the Ti-N system except for the diffusivity term, D. For instance, the value of r_o for Si was taken as 2.85 nm, as determined in Chapter 3. The value of r_o for Ti was estimated by scaling the size of the nitrided TiN particle, measured to be r = 4.4 nm, with the same proportion of growth as was found in the Si_3N_4 system. That is, for Si, an initial particle with a radius of 2.85 nm grew to 5.25 nm in the nitrided form, an increase by a factor of 1.84. Thus, r_o for Ti was taken as 2.4 nm. Therefore, for the conversion of Si to Si_3N_4,

$$\tau_{Si_3N_4} = \frac{3.53 \times 10^{-7} \text{ cm}^2}{D} \qquad (4\text{-}8)$$

and for the conversion of Ti to TiN,

$$\tau_{TiN} = \frac{1.92 \times 10^{-7}\ cm^2}{D} \tag{4-9}$$

4.4.2 Calculation of the Relevant Diffusivities

The differences in the reaction times for the conversion of TiN and Si_3N_4 stem primarily from differences in the diffusivity of N in these materials; the differences in the N diffusivities arise from the nature of the bonding in these two substances. The extensive covalent bonding in Si_3N_4 leads to great bonding strengths, but also low N self-diffusion coefficients, which then require the use of sintering additives and very high sintering temperatures in Si_3N_4 [49]. As the electrons involved in the bond are shared by the atoms, diffusion of N in Si_3N_4 is further slowed for steric arrangement and electroneutrality considerations [49]. TiN has unusual bonding characteristics that give rise to properties usually associated with covalently bonded materials, such as good thermodynamic stability, extreme hardness, and a high melting point, but at the same time has electrical and thermal properties similar to those found in metallically bonded materials [50]. The mixed bonding in TiN causes these characteristics, with strong covalent bonding of the hybridized *p* and *d* electrons and delocalized *d-d* metallic bonding on the Ti metal sublattice [51, 52].

The differences in the bonding in these materials manifests itself in the magnitude of various properties which are indicative of the nature of the bonding in a substance. For instance, a general indication of bond character is the heat of formation, ΔH_f. Smaller values of ΔH_f are indicative of metallic bonding while larger (negative) values correspond to a more covalently bonded material. $\Delta H_f°$ for TiN is –338.1 kJ/mol, while $\Delta H_f°$ for Si_3N_4 is –743.5 kJ/mol [53]. These bonding variances are also seen in the electronegativity differences of these materials. Using Pauling's electronegativity scale [54], the electronegativity difference for TiN is 1.50, while it is 1.14 for Si_3N_4, indicative of the greater degree of covalent bonding in Si_3N_4.

Thus, due to the covalent nature of the bonding in Si_3N_4, diffusion of nitrogen is extremely slow. In comparison, because TiN is a more metallically bonded material, it has much faster nitrogen diffusion. Using a temperature of 1200 °C, a more conservative estimate of the temperature in the plasma than that determined in section 4.3.5 due to heat

transfer issues, the diffusion coefficients of nitrogen in Si_3N_4 and in TiN can be obtained from expressions in the literature.

For the diffusion of N in β-Si_3N_4, Kijima and Shirasaki determined the expression [55]:

$$D^{N}_{\beta-Si_3N_4} = 6.8 \times 10^{6} \exp\left[\frac{-777.3\,kJ}{RT}\right] \frac{cm^2}{sec} \qquad (4\text{-}10)$$

leading to a value for D^N in β-Si_3N_4 at 1200 °C of 1.84 x 10^{-21} cm^2/sec. Using this value in Eqn. (4-8) leads to conversion times on the order of 1.92 x 10^{14} seconds for Si_3N_4 particles. (According to the work of Kijima and Shirasaki [55], D^N in α-Si_3N_4 at 1200 °C is 6.55 x 10^{-21} cm^2/sec, very comparable to the value in β-Si_3N_4. D^N in β-Si_3N_4 was selected due to the observation of the β-Si_3N_4 phase in the particles formed in the reactor as described in section 3.3.5.)

For the diffusion of N in TiN, Levinskii *et. al.* determined the expression [56]:

$$D^{N}_{TiN} = 5.4 \times 10^{-3} \exp\left[\frac{-304.7\,kJ}{RT}\right] \frac{cm^2}{sec} \qquad (4\text{-}11)$$

leading to a value for D^N in TiN at 1200 °C of 6.88 x 10^{-11} cm^2/sec, ~ 10 orders of magnitude faster than that in Si_3N_4. Using this value in Eqn. (4-9) leads to conversion times on the order of 2.79 x 10^3 seconds for the TiN particles.

However, the above numbers are gross overestimates of the conversion times because both Si_3N_4 and TiN undergo a volumetric expansion upon conversion from the metal, leading to a slightly microporous product layer with microcracks. This expansion may be quantified by the Pilling-Bedworth ratio (PBR). The PBR for Si_3N_4 is 1.22, which, according to [57], suggests that a coherent nitride film would not be expected to form on the silicon surface. The PBR for TiN is 1.09; there are experimental observations of Ti particles swelling during the nitridation process [48].

These values for the PBR indicate the probable existence of microscopic channels in the nitride linking the unreacted metal surface to the nitrogen in the gas stream. Nitridation starts from the outer surface and proceeds inward continuously, inducing crack formation at the particle surface due to volume expansion at the core of the particle. This cracking leads to a significant enhancement in the diffusivity of nitrogen, and thus, an effective diffusivity, D^{eff}, should be used in the above calculation. In fact the

parameter D in Eqn. (4-7) is an effective diffusivity term to account for these cracks and fissures in the product layer. However, the above calculations were shown using D^N to emphasize the differences in the chemical bonding, and hence the diffusivities, in TiN and Si_3N_4 which will still have an effect on the nitridation process despite the existence of microcracking in the product layer.

D^{eff} has recently been determined for nitrogen in the single particle conversion of Si to Si_3N_4 [43]. Pigeon and Varma used the SIM model reduced to:

$$\frac{1}{(Z-1)}\left\{Z-\left[(1-Z)(1-X)+Z\right]^{2/3}\right\}-(1-X)^{2/3}=\left(\frac{2b\,C_{N_2}\,M_w\,D^{eff}}{\delta_M\,r_o^{\,2}}\right)t \qquad (4\text{-}12)$$

where δ_M is the density of the metal, r_o is the original radius of the metal particle, b is the stoichiometric coefficient for the reaction of the metal plus nitrogen going to the nitride, D^{eff} is the effective diffusivity for nitrogen diffusion through the microporous product layer, C_{N_2} is the surface concentration of nitrogen on the particle, M_w is the molar mass of the metal, X is the fractional conversion, Z is the PBR and t is time [43]. Eqn. (4-12) yields a linear relationship for the left-hand side versus time, with the slope given as the quantity in parenthesis.

Pigeon and Varma then used nitridation conversion data for 5 - 10 μm Si particles to determine D^{eff} at various temperatures from the slopes on plots of the left-hand side of Eqn. (4-12) versus time at each temperature. Assuming a temperature dependency of the Arrhenius form, they plotted ln (D^{eff}) versus 1/T to determine the activation energy of D^{eff}. This process yielded an expression for D^{eff} in Si_3N_4 of:

$$D^{eff}=14.725\,\exp\left(-\frac{310\,\text{kJ mol}^{-1}}{RT}\right)\frac{\text{cm}^2}{\text{sec}} \qquad (4\text{-}13)$$

At 1200 °C, D^{eff} in the Si_3N_4 system is 1.49 x 10^{-10} cm^2/sec, leading to conversion times of 2.36 x 10^3 seconds, still an extremely long time.

Given that no such analysis had been performed for the Ti-N system, we took some recent conversion data for the synthesis of TiN [58] and performed the same analysis to determine D^{eff} for the conversion of Ti to TiN. Rode and Hlavacek studied the conversion of Ti to TiN in conditions (atmospheres, heating rates, particle sizes (5

μm), etc.) very similar to those of Pigeon and Varma. Additionally, they referenced the work of Pigeon and Varma and stated that their study was also an effort to "separate the intrinsic single-particle (conversion) kinetics from global effects." In fact, listed as a secondary objective was "to provide the practitioner with a matrix of high-quality conversion vs. time curves to be used for design purposes." Hence, the application of Pigeon and Varma's analysis to this data was reasonable.

As outlined above, Eqn. (4-12) was used to calculate D^{eff} at various temperatures. These values were then used to generate a ln (D^{eff}) vs. 1/T plot to determine the activation energy for D^{eff} in TiN. Our R^2 value for this portion of the analysis was 0.987, as compared to 0.968 for the work by Pigeon and Varma, and yielded an expression for D^{eff} in TiN of:

$$D^{eff} = 1.788 \times 10^{-7} \exp\left(-\frac{31 \text{ kJ mol}^{-1}}{RT}\right) \frac{\text{cm}^2}{\text{sec}} \qquad (4\text{-}14)$$

At the same 1200 °C temperature, D^{eff} for N in the TiN system is 1.41×10^{-8} cm^2/sec, two orders of magnitude faster than in Si_3N_4, leading to a much faster calculated conversion time of 13.6 seconds.

A key to this result is the order of magnitude difference in activation energies in Eqns. (4-13) and (4-14). While the value of 31 kJ/mol may seem somewhat low for this type of process, a study utilizing a CVD process for the formation of TiN from H_2, N_2 and $TiCl_4$ at atmospheric pressure found that the deposition reaction rate for the formation of TiN was controlled by mass-transport of the reactants and had an apparent activation energy of 47.3 kJ/mol [59]. Furthermore, according to Elliott *et al.* [60], an activation energy of 10 – 85 kJ/mol may correspond to a diffusion-controlled reaction, such as this one, where mass transport of one of the species is the rate-determining step.

Because of their high thermodynamic stability, the formation of nitrides is typically extremely exothermic. Thus, the local temperature at the particle surface is likely much in excess of the 1200 °C used in the above calculations. Experimental evidence of this assertion is seen in the fact that upon evaporation of Ti, and subsequent reaction to TiN, the pressure in the reactor increases causing the throttle valve to the vacuum pumps to open ~5° further to maintain a constant pressure and compensate for the increase in temperature due to the exothermic reaction. An estimate of the local

temperature on a particle undergoing nitridation may be determined from the adiabatic temperature, T_{ad}.

The adiabatic temperature is the calculated reaction temperature under an adiabatic condition. Under a more open system such as that found in my reactor, however, heat releases from the particles to the surrounding gas leading to significant heat losses and lower local temperatures. However, T_{ad} can be used as a general indication of the temperature at a combustion front [61]. This maximum temperature to which the product can be raised as a result of an exothermic reaction can be calculated from the thermodynamic functions of heat capacities and enthalpies of formation and transformation [61, 62].

Thermodynamic differences in TiN and Si_3N_4 lead to differences in the values for their respective adiabatic temperatures. T_{ad} for TiN is 4900 K; for Si_3N_4, T_{ad} is 4300 K [61,63,64]. Both of these temperatures are greatly in excess of the 1200 °C used in the above calculations. Of further note, there is experimental evidence that the temperature measured on smaller particles in these types of reactions is higher than that on larger particles due to the lower thermal mass of smaller particles [62].

Thus, to continue the above analysis, using the adiabatic temperatures to estimate D^{eff} in each system, one can determine a conversion time on the order of 2.3 seconds for the TiN particles and a surprisingly fast 1.4×10^{-4} seconds for the Si_3N_4 particles. This very rapid conversion time for Si_3N_4 is a result of the much greater temperature dependence of D^{eff} in Si_3N_4 with the order of magnitude larger activation energy. Extrapolating D^{eff} so far out of the temperature range in which it was determined likely contributes to this erroneous result.

Another difference between Si_3N_4 and TiN to consider in this discussion is the degree of non-stoichiometry found in these materials and how variations in the stoichiometry are accommodated by the structure of these materials. As shown in section 4.3.2, the nano-TiN is stoichiometric TiN within the experimental uncertainty. However, as shown in Figure 4-2, TiN_x does exist over a very wide range of stoichiometry (30 – 55 at% N) [6]. Such extensive composition ranges in TiN are primarily associated with vacancies on the N sublattice [52]. Thus, a one atomic percent variation, from 50 at% N to 49 at% N, could translate into one vacancy for every 50 nitrogen sites. This high vacancy concentration would likely serve to increase the diffusivity of N in these

materials. Si_3N_4, however, is a line compound, unlikely to have much of a defective structure [65], and thus no enhanced N diffusivity for reasons of non-stoichiometry.

An additional factor to consider is that these reactions are taking place in a plasma of activated N species. This plasma enhances the kinetics of the formation process through ionization and dissociation of the reactive molecules. For example, there are reports that ion nitriding processes in glow discharge plasmas may enhance the diffusivity of nitrogen in Ti [66]. Another report suggests an enhancement of the surface migration rate of reacting molecules with activated N^+ radicals generated by a RF plasma in a TiN CVD process [14].

Thus, the actual conversion times we observe in our reactor are much faster than those calculated above for T = 1200 °C; however, the above modeling demonstrates how differences in the chemical bonding of the two systems studied can impact their respective conversion times. The relative conversion times of ~ 10 seconds for the TiN particles and ~ 2000 seconds for the Si_3N_4 particles, as determined with D^{eff} and a temperature of 1200 °C, give insight into the formation process of these materials in this reactor and help to explain the difficulties in synthesizing fully converted, stoichiometric Si_3N_4 in this reactor.

4.5 Summary

Through the use of our unique reactor, we have demonstrated the viability of a new synthesis process for the production of extremely high surface area nano-TiN. These materials have the highest surface areas and smallest particle size range reported in the literature. The microwave-generated plasma improves powder properties by extending the time for growth by coalescence leading to a less aggregated and more monodisperse sized product. Additionally, the microwave plasma serves as an aid to overcoming kinetic inhibitions and permits full nitridation and production of stoichiometric nano-TiN. The differences in the nitridation performance in the silicon nitride system and the titanium nitride system can be accounted for by differences in the bonding and diffusivity of N in these materials.

4.6 References

[1] ASM Committee on Vacuum Heat Treating, "Heat Treating in Vacuum Furnaces and Auxiliary Equipment," pp. 492-495 in ASM Handbook: Vol. 4 – Heat Treating (ASM International, 1991).

[2] Phase Diagrams for Ceramists: Volume X – Borides, Carbides and Nitrides, ed. A.E. McHale, p. 426, (The American Ceramic Society, Westerville, OH, 1994).

[3] B.D. Cullity, Elements of X-Ray Diffraction, 2nd ed., (Addison-Wesley, London, 1978).

[4] A. Kochendörfer, " *Z. Kristallogr.*, "Die Bestimmung von Teilchengröβe und Gitterverzerrungen in kristallinen Stoffen aus der Breite der Röntgenlinien," **105**, 393-480 (1944)

[5] J.P. Dekker, P.J. van der Put, H.J. Veringa, and J. Schoonman, "Vapour-phase Synthesis of Titanium Nitride Powder," *J. Mater. Chem.*, **4** [5] 689-694 (1994).

[6] H.A. Wriedt and J.L. Murray, "The N-Ti System," *Bull. Alloy Phase Diag.*, **8** [4] 378-388 (1987).

[7] D.L. Misell and E.B. Brown, Electron Diffraction: An Introduction for Biologists, (Elsevier Science Publishers, New York, 1987).

[8] Z.Y. Chen and A.W. Castleman, "Growth of Titanium Nitride: From Clusters to Microcrystals," *J. Chem. Phys.*, **98** [1] 231-235 (1993).

[9] A. Richard, P. Jacquot, H. Michel, and M. Gantois, "Excited Atomic and Molecular States in Reactive Plasmas Used for Titanium Nitride Deposition on Steel Surfaces," *J. Phys. D: Appl. Phys.*, **18** 1701-1708 (1985).

[10] F.H. Pollard and P. Woodward, "The Stability and Chemical Reactivity of Titanium Nitride and Titanium Carbide," *Trans. Faraday Soc.*, **46** [3] 190-199 (1950).

[11] Handbook of Binary Metallic Systems: Structure and Properties, "Nitrogen-Titanium", pp. 607-619, ed. N.V. Ageev, (Israel Program for Scientific Translations, Jerusalem, 1966).

[12] S. Iwama, K. Hayakawa, and T. Arizumi, "Ultrafine Powders of TiN and AlN Produced by a Reactive Gas Evaporation Technique with Electron Beam Heating," *J. Crystal Growth*, **56** 265-269 (1982).

[13] F.J. Kohl and C.A. Stearns, "Mass Spectrometric Studies of the Vaporization of Refractory Carbides and Nitrides," NASA Report SP-227, Aerospace Structural Materials, 173-185 (1970).

[14] Y. H. Chang, J.S. Chun, J.E. Oh, S.J. Won, S.H. Paek, H.D. Lee, S.I. Lee, J.S. Choi, and J.G. Lee, "Enhancement of Titanium Nitride Barrier Metal Properties by Nitrogen Radical Assisted Metalorganic Chemical Vapor Deposition," *Appl. Phys. Lett.*, **68** [18] 2580-2582 (1996).

[15] M. Danek, M. Liao, J. Tseng, K. Littau, D. Saigal, H. Zhang, R. Mosely, and M. Eizenberg, "Resistivity Reduction and Chemical Stabilization of Organometallic Chemical Vapor Deposited Titanium Nitride by Nitrogen RF Plasma," *Appl. Phys. Lett.*, **68** [7] 1015-1016 (1996).

[16] N.C. Saha and H.G. Tompkins, "Titanium Nitride Oxidation Chemistry: An X-Ray Photoelectron Spectroscopy Study," *J. Appl. Phys.*, **72** [7] 3072-3079 (1992).

[17] R.A. Andrievskii, "Synthesis and Properties of Nanocrystalline Refractory Compounds," *Russian Chem. Rev.*, **63** [5] 411-427 (1994).

[18] J.E. Sundgren, A. Rockett, and J.E. Greene, "Microstructural and Microchemical Characterization of Hard Coatings," *J. Vac. Sci. Technol. A*, **4** [6] 2770-2783 (1986).

[19] S. Hofmann, "Characterization of Nitride Coatings by Auger Electron Spectroscopy and X-Ray Photoelectron Spectroscopy," *J. Vac. Sci. Technol. A*, **4** [6] 2789-2796 (1986).

[20] M.J. Vasile, A.B. Emerson, and F.A. Baiocchi, "The Characterization of Titanium Nitride by X-Ray Photoelectron Spectroscopy and Rutherford Backscattering," *J. Vac. Sci. Technol. A*, **8** [1] 99-105 (1990).

[21] R. Naβ, S. Albayrak, M. Aslan, and H. Schmidt, "Processing and Sintering of Nanosized TiN," pp. 47-54 in Advanced Materials in Optics, Electro-Optics and Communication Technologies, P. Vincenzini, ed., (Techna Srl, 1995).

[22] L. Ramqvist, K. Hamrin, G. Johansson, A. Fahlman, and C. Nordling, "Charge Transfer in Transition Metal Carbides and Related Compounds Studied By ESCA," *J. Phys. Chem. Solids*, **30** 1835-1847 (1969).

[23] R. Holm, Bayer, unpublished data.

[24] T. Rabe and R. Wäsche, "Sintering Behavior of Titanium Nitride Powders," *Nanostr. Mater.*, **6** 357-360 (1995).

[25] G.P. Dransfield and A.G. Jones, "The Pressureless Sintering of an Ultrafine, Plasma Synthesized Titanium Nitride Powder," pp. 529-534 in Euro-Ceramics II: Basic Science and Processing of Ceramics, (DKG, Cologne, 1993).

[26] R.A. Andrievskii, V.I. Torbov, and E.N. Kurkin, "Nanocrystalline Titanium Nitride," pp. 649-655 in Plansee Proceedings: Coating Technology, Volume 3, (Metallwerk Plansee, Reutte, 1993).

[27] R.A. Andrievskii, "Review: Nanocrystalline High Melting Point Compound-Based Materials," *J. Mat. Sci.*, **29** 614-631 (1994).

[28] M.J. Mayo, "Thermomechanical Stability of Nanocrystalline Microstructures and Their Role in Enhancing Superplastic Deformation," pp. 541-550 in Superplasticity in Advanced Materials, ed. S. Hori, M. Tokizane, and N. Furushiro, (The Japan Society for Research on Superplasticity, 1991).

[29] S.E. Pratsinis, T.T. Kodas, M.P. Dudukovic, and S.K. Friedlander, "Aerosol Reactor Design: Effect of Reactor Type and Process Parameters on Product Aerosol Characteristics," *Ind. Eng. Chem. Process Des. Dev.*, **25** [3] 634-642 (1986).

[30] M.H. Teng, J.J. Host, J.-H. Hwang, B.R. Elliott, J.R. Weertman, T.O. Mason, V.P. Dravid, and D.L. Johnson, "Nanophase Ni Particles Produced by a Blown Arc Method," *J. Mater. Res.*, **10** [2] 233-236 (1995).

[31] C.G. Granqvist and R.A. Buhrman, "Ultrafine Metal Particles," *J. Appl. Phys.*, **47** [5] 2200-2219 (1976).

[32] R.V. Hogg and E. A. Tanis, Probability and Statistical Inference, (MacMillan Publishing Company, New York, 1993).

[33] V. Haas, H. Gleiter, and R. Birringer, "Synthesis of Nanostructured Materials by the Use of a Thermophoretic Forced Flux System," *Scripta Metall. Mater.*, **28** 721-724 (1993).

[34] C. Bossel, J. Dutta, R. Houriet, J. Hilborn, and H. Hofmann, "Processing of Nano-Scaled Silicon Powders to Prepare Slip Cast Structural Ceramics," *Mater. Sci. Eng. A.*, **A204** 107-112 (1995).

[35] T.C. Wei, L.R. Collins, and J. Phillips, "Dynamics of Charged Species in the Afterglow Region of a Low-Pressure Microwave Plasma," *J. Phys. D: Appl. Phys.*, **28** 295-304 (1995).

[36] M. Konuma and O. Matsumoto, "Nitriding of Titanium in a Radio Frequency Discharge," *J. Less-Comm. Metals*, **52** 145-152 (1977).

[37] R.C. Flagan and M. M. Lunden, "Particle Structure Control in Nanoparticle Synthesis from the Vapor Phase," *Mater. Sci. Eng. A.*, **A204** 113-124 (1995).

[38] W. Koch and S.K. Friedlander, "Particle Growth by Coalescence and Agglomeration," *J. Aerosol Sci.*, **21** S73-S76 (1990).

[39] T. Matsoukas and S.K. Friedlander, "Dynamics of Aerosol Agglomerate Formation," *J. Colloid and Interface Sci.*," **146** [2] 495-506 (1991).

[40] O. Levenspiel, Chemical Reaction Engineering, 2nd ed., pp. 357-377, (John Wiley & Sons, New York, 1972).

[41] A.Atkinson, P.J. Leatt, A.J. Moulson, and E.W. Roberts, "A Mechanism for the Nitridation of Silicon Powder Compacts," *J. Mater. Sci.*, **9** 981-984 (1974).

[42] H.M. Jennings, "Review: On Reactions Between Silicon and Nitrogen," *J. Mater. Sci.*, **18** 951-967 (1993).

[43] R.G. Pigeon and A. Varma, "Quantitative Kinetic Analysis of Silicon Nitridation," *J. Mater. Sci.*, **28** 2999-3013 (1993).

[44] J.C. Wuu and J.M. Schoenung, "Synthesis of Silicon Nitride Powder Through Nitrogen Gas Atomization," *J. Mater. Sci.*, **29** 6259-6267 (1994).

[45] G.W. Elger, D.E. Traut, G.J. Slavens, and S.J. Gerdemann, "Preparation of Submicron Titanium Nitride Powder by Vapor-Phase Reactions," *Metall. Trans. B*, **20B** 493-497 (1989).

[46] T. Okubo, H. Kawamura, K. Kusakabe, and S. Morooka, "Plasma Nitriding of Titanium Particles in a Fluidized Bed Reactor at a Reduced Pressure," *J. Am. Ceram. Soc.*, **73** [5] 1150-1152 (1990).

[47] M.E. Grami and Z.A. Munir, "Effect of Nitrogen Pressure and Diluent Content on the Combustion Synthesis of Titanium Nitride," *J. Am. Ceram. Soc.*, **73** [8] 2222-2227 (1990).

[48] A. Pivkina, P.J. van der Put, Y. Frolov, and J. Schoonman, "Reaction-Bonded Titanium Nitride Ceramics," *J. Europ. Ceram. Soc.*, **16** 35-42 (1996).

[49] G. Ziegler, J. Heinrich and G. Wotting, "Review: Relationships Between Processing, Microstructure and Properties of Dense and Reaction-Bonded Silicon Nitride," *J. Mater. Sci.*, **22** 3041-3086 (1987).

[50] G. Ernsberger, J. Nickerson, T. Smith, A.E. Miller, and D. Banks, "Low Temperature Oxidation Behavior of Reactively Sputtered TiN by X-Ray Photoelectron Spectroscopy and Contact Resistance Measurements," *J. Vac. Sci. Technol. A.*, **4** [6] 2784-2788 (1986).

[51] H.G. Tompkins, "The Initial Stages of Oxidation of Titanium Nitride," *J. Appl. Phys.*, **71** [2] 980-983 (1992).

[52] L.H. Bennett, A.J. McAlister and R.E. Watson, "Interstitial Compounds," *Phys. Today*, **30** 34-41 (1977).

[53] The NBS Tables of Chemical Thermodynamic Properties, *J. Physical and Chemical Reference Data*, **11** [2] pp. 2-112 and 2-210, (National Bureau of Standards, 1982).

[54] Table of Periodic Properties of the Elements, Sargent-Welch Scientific Company, (Skokie, Illinois, 1980).

[55] K. Kijima and S. Shirasaki, "Nitrogen Self-Diffusion in Silicon Nitride," *J. Chem. Phys.*, **65** [7] 2668-2671 (1976).

[56] Y.V. Levinskii, Y.D. Strogonov, S.E. Salibekov, M.K. Levinskaya and S.A. Prokofev, "Investigation of the Diffusion of Nitrogen in Titanium," *Inorganic Mater.*, **4** [12] 1799-1803 (1968).

[57] F.L. Riley, "Silicon Nitridation," pp. 121-133 in Progress in Nitrogen Ceramics, ed. F.L. Riley, (Martinus Nijhoff Publishers, Hague, Netherlands, 1983).

[58] H. Rode and V. Hlavacek, "Detailed Kinetics of Titanium Nitride Synthesis," *AIChE Journal*, **41** 377-388 (1995).

[59] N. Nakanishi, S. Mori, and E. Kato, "Kinetics of Chemical Vapor Deposition of Titanium Nitride," *J. Electrochem. Soc.*, **137** [1] 322-328 (1990).

[60] J.F. Elliott, M. Gleiser, and V. Ramakrishna, Thermochemistry for Steelmaking, Vol II: Thermodynamic and Transport Properties, p. 715 (Addison-Wesley Publishing Company, Reading, MA, 1963).

[61] Z.A. Munir, "Synthesis of High Temperature Materials by Self-Propagating Combustion Methods," *Ceram. Bull.*, **67** [2] 342-349 (1988).

[62] J. Subrahmanyam and M. Vijayakumar, "Review: Self-Propagating High Temperature Synthesis," *J. Mater. Sci.*, **27** 6249-6273 (1992).

[63] Z. A. Munir, S. Deevi, and M. E. Grami, "The Synthesis of Titanium Nitride By a Self-Sustaining Combustion Method," *High Temp. – High Press.*, **20** 19-24 (1988).

[64] N.P. Novikov, I.P. Borovinskaya, and A.G. Merzhanov, "Thermodynamic Analysis of Self-Propagating High-Temperature Synthesis Reactions," pp. 174 in

Combustion Processes in Chemical Technology and Metallurgy, A.G. Merzhanov, ed., (Chernogolovka, 1975).

[65] R.A. Andrievskii, "Silicon Nitride: Synthesis and Properties," *Russ. Chem. Rev.*, **64** [4] 291-308 (1995).

[66] R.P. Singh and R.D. Doherty, "Synthesis of Titanium Nitride Powders Under Glow Discharge Plasma," *J. Mater. Sci. Lett.*, **9** [2,3] 87-89 (1990).

Chapter 5

Processing and Properties of Nano-TiN

5.1 Introduction

As outlined in Chapter 1, the most common fabrication techniques for producing dense, monolithic TiN are conventional sintering or hot pressing in the presence of additives such as Al, Co or Ni metal. While these additives play an important role in promoting densification, they typically adversely affect the final properties of the sintered material. However, as also outlined in Chapter 1, nanocrystalline starting materials have the potential for greatly enhanced sinterability over their conventional counterparts. Due to its high driving force for sintering, stemming from the reduction of surface energy in the high surface area powder, as well as its monodispersity and non-agglomerated nature, the nano-TiN described in Chapter 4 should be highly sinterable. In order to evaluate the additive-free sinterability of these powders, as well as the resultant properties, a series of sintering experiments along with microstuctural and mechanical properties characterization were performed. Additionally, in order to examine the effects of exposure to air on the sinterability of these high surface area nitrides, sintering approaches which minimized the exposure of the powders to the atmosphere were compared to sintering processes of air-exposed powders with no special handling procedures.

5.2 Experimental Details

5.2.1 Sintering-Related Powder Characterization

In order to measure the types of gases likely to be evolved during sintering of these high surface area materials, a mass spectrometer (Hewlett Packard Mass Selective Detector – HP 6890) was used to directly monitor the gases evolved during heating of the commercial and nano-TiN powder. These materials were ramped at 5 °C/min to 1400 °C under a flow of Grade 5.0 He, purified further by the use of two oxygen traps while weight changes were simultaneously measured in a thermogravimetric analyzer (Perkin Elmer Series 7 TGA). The exhaust stream from the TGA was analyzed by the mass spectrometer (MS). Nano-TiN samples which had been exposed to air for 1 day, denoted "S-EXP" for short exposure time, and 8 months, denoted "L-EXP" for long exposure time, were compared with a sample of the commercial TiN, denoted "HCS" for the

manufacturer, H.C. Starck. Samples were dried under the flowing He at 25 °C for at least 1 hour after loading into the TGA until their weight was stable.

These same materials, with short and long exposure times, were also characterized by Infrared (IR) Spectroscopy techniques scanning from 400 cm^{-1} to 4400 cm^{-1} (Bio-Rad FTS-60A). Diffuse reflectance infrared spectroscopy (DRIFT) was performed on samples of these powders diluted with KBr in a 50/50 mixture by weight. Spectra were collected on samples under flowing He (Grade 5.0) at room temperature. Spectra were also collected on samples heated at 5 °C/min under flowing He (Grade 5.0) and held at 100 °C, 200 °C, 300 °C, 400 °C, and 500 °C to correlate surface species at various temperatures with the MS and TGA data. In diffuse reflectance spectra, absorbence does not vary directly with the first power of concentration, and it is necessary to transform absorbence data into Kubelka-Munk units to generate an approximate linear relation between key variables [1,2]. All data presented are expressed in Kubelka-Munk units. As a basis for comparison, PA-FTIR spectra were also collected on materials which had been exposed for short and long times. Unexposed materials, loaded and sealed in the IR test cell in the glovebox, were also evaluated by both of the above IR techniques.

5.2.2 Powder Processing

Three processing routes for the nano-TiN described in Chapter 4 were pursued. A schematic of these processing routes, which are detailed below, is shown in Figure 5-1. The first of these three routes involved pressureless sintering of air-exposed powders which received no special handling. These will be referred to as "EXP" (exposed) powders. The second processing route prevented exposure to air below 800 °C. These samples will be referred to as "UN800" (unexposed below 800 °C). For consistency and comparison purposes, in certain experiments, some data points were collected at 600 °C for the UN800 materials. In these instances, the materials were unexposed only below 600 °C, but the UN800 label is used for the entire series. The final processing route utilized hot-isostatic pressing to prevent exposure to the atmosphere below the final sintering temperature. These samples will be referred to as "HIP" (hot isostatically pressed). As a basis for comparison, one of the best commercial TiN materials from H.C. Starck (Grade B) was processed in a manner identical to that described below for the

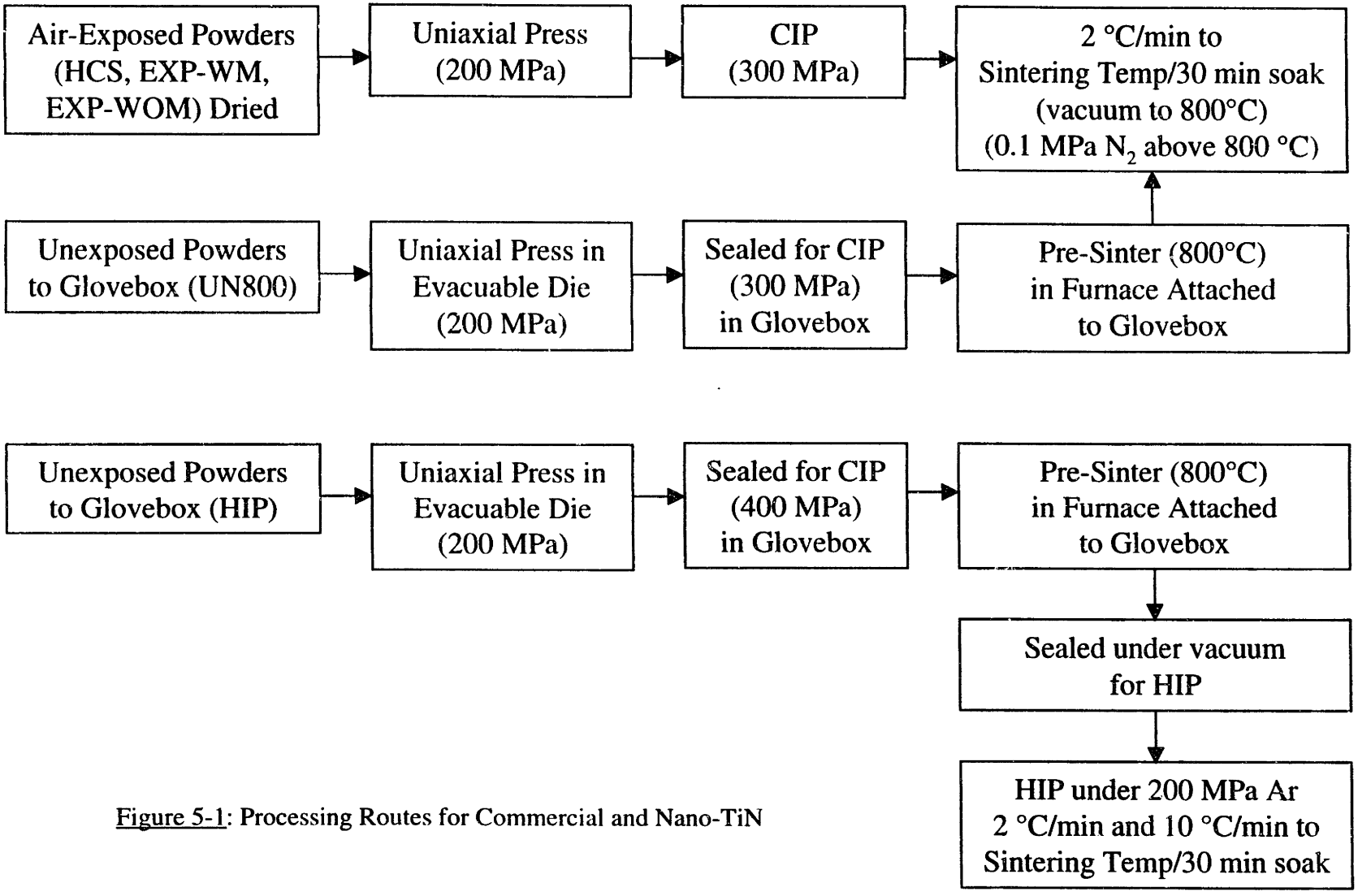

Figure 5-1: Processing Routes for Commercial and Nano-TiN

EXP powders. These materials had an average particle size of 1.3 - 1.9 μm and a B.E.T. surface area of 2 m^2/g. These samples will be delineated as "HCS" (for H.C. Starck).

Following a synthesis run in the reactor, the EXP powders were created by controllably back-filling the reactor with air, so as to prevent pyrophoric combustion. Those powders were then removed from the reactor in the open atmosphere. The EXP powders were dried (150 °C, 1.33 x 10^{-3} mbar) and pressed (200 MPa) in an evacuable pellet die. After cold isostatic pressing (300 MPa), the pellets were ramped under vacuum (2 x 10^{-2} mbar) at 2 °C/min to 800 °C. The furnace atmosphere was then switched to a 0.1 MPa overpressure of flowing N_2, and the pellets were ramped at 2 °C/min to the sintering temperature (600 –1600 °C) for a 30 minute soak. The pellets were then quenched to room temperature at 50 °C/min. As outlined in Chapter 4, there were significant differences between nano-TiN powders produced with (WM) and without (WOM) the microwave plasma. The "EXP" designation, when used in the below analysis and discussion, corresponds to those materials synthesized with the microwave plasma. These powders had less agglomeration with the more narrow particle size distribution. For clarity in some sintering comparisons, those exposed materials produced without the microwave plasma will be designated "EXP-WOM," while those exposed powders produced with the microwave plasma will be explicitly labeled, "EXP-WM."

The valved filter collection device described in Chapter 2 allowed particles to be removed from the reactor without exposure to the atmosphere. Following a synthesis run, the reactor was backfilled with high purity N_2 and gate valves were closed to allow the filter collection unit to be removed from the reactor and placed into a glovebox (H_2O < 1 ppm, O_2 < 15 ppm) for powder removal for the UN800 materials. The particles were removed from the filter collection unit under a high purity Ar atmosphere in the glovebox and were uniaxially pressed (200 MPa) in an evacuable pellet die. The formed pellets were then ejected from the die in the glovebox and sealed in rubber bags for cold isostatic pressing (CIP) (300 MPa). Following the CIP procedure, the pellets were returned to the glovebox, removed from the CIP bags and transferred directly to a furnace connected to the glovebox. The pellets were ramped in this furnace under flowing N_2 at 10 °C/min to 800 °C to allow some sintering to take place with a resultant reduction in surface area before the materials were ever exposed to air. At this point, the pellets were briefly exposed to air for ~15 seconds as they were transferred to a higher temperature furnace

for final sintering as described previously with a ramp rate of 2 °C/min to the sintering temperature for a 30 minute soak. Again, below 800 °C the pellets were heated under vacuum; above 800 °C, the sintering atmosphere was a 0.1 MPa overpressure of N_2.

The HIP powders were removed from the reactor and uniaxially pressed and sealed for CIPing in the same manner as were the UN800 powders. The CIP level for these samples was increased to 400 MPa. These materials also underwent the "pre-sintering" step at 800 °C. In this instance, the purpose of heating to 800 °C was to ensure complete removal of the organic lubricant used during uniaxial pressing of these powders. All powders (EXP, UN800 and HIP) were uniaxially pressed with this palmatic acid-based lubricant. While the pre-sintering step at 800 °C also removed this binder in the case of the UN800 pellets, in that case the main function of the pre-sintering procedure was to reduce the pellet's surface area for the brief handling in air during transfer between the furnaces. For the HIP samples, the primary function of the pre-sintering step was to remove the organic material to prevent it from being entrapped in the pellets during the HIP process. Following heating at 800 °C, the pellets for HIPing were returned to the glovebox and sealed under vacuum in Pyrex ampoules. Two sets of HIP experiments were performed in Ar. The first set of HIP samples were ramped at 10 °C/min to 825 °C, the softening point of Pyrex glass, under a pressure of 2 MPa. While holding at 825 °C, the Ar pressure was increased to 200 MPa. The pellets were then ramped at 10 °C/min to temperatures ranging from 1150 °C to 1400 °C where they were held for 30 min. The second set of samples was also ramped at 10 °C/min to 825 °C where the same 200 MPa of Ar pressure was applied. They were then ramped at a lower rate of 2 °C/min to final sintering temperatures ranging from 1300 – 1400 °C for 30 min hold times.

5.2.3 Physical Characterization of Sintered Materials

The B.E.T. technique with nitrogen adsorption was used to determine the pore size distribution and surface area of the sintered samples. The actual density of the sintered pellets was assessed by the Archimedes technique. The microstructure was examined via scanning electron microscopy (SEM) (JEOL 6320 FE, 3-15 kV) on both fractured and polished surfaces. Following rough grinding, the polished surfaces were prepared with 6 μm and 1 μm diamond paste followed by a 0.3 μm Al_2O_3 suspension. The average grain size of sintered samples was determined from SEM micrographs using

the linear intercept method [3]. X-ray diffraction (XRD) (Siemens D5000) with Ni-filtered Cu-K_α radiation was used to determine the phases present and the crystallite size, as calculated by the Scherrer formula, in the sintered materials. Chemical analysis was performed as described in Chapter 4.

5.2.4 Mechanical Characterization of Sintered Materials

Data on hardness and fracture toughness was collected via Vickers hardness testing (LECO DM400). Testing was conducted on polished samples at 20 °C with loads of 0.5 – 3 N and deformation times of 15 seconds. The polished surfaces were prepared as described above for SEM. The fracture toughness was assessed via microhardness indentation testing. From the idea that the size of indentation cracks can be used to quantify toughness, Eqn. (5-1) was developed [4]:

$$K_c = 0.016 \pm 0.004 \left(\frac{E}{H}\right)^{\frac{1}{2}} \left(\frac{P}{c_o^{3/2}}\right) \qquad (5\text{-}1)$$

where K_C is the fracture toughness, E is Young's modulus, H is the hardness as determined during the Vickers hardness test, P is the peak load during the test and c_O is the radial crack dimension.

5.3 Results and Discussion

5.3.1 Sintering-Related Powder Characterization

Due to the high surface areas of these materials, the surface properties of unexposed nano-TiN and nano-TiN which had been exposed to air for various amounts of time were studied. The first parameter examined was potential differences in the surface area of materials which had and had not been exposed to air. Although one would not expect oxidation to cause a change in surface area *per se*, Sakka *et al.* report such an observation for nano-TiN [5]. Samples were loaded directly into B.E.T. sample tubes in the glovebox, their surface area was measured, and then the seal on the sample tube was removed to expose the nano-TiN to air for various times. The exact same sample was

then resealed and its surface area remeasured. There was no significant difference ($\leq$ 3%) between the surface areas of unexposed and exposed samples (~ 225 m^2/g).

During the sintering process, a variety of adsorbed gases may be evolved from the high surface area nano-TiN. If this evolution occurs at or near the onset of closed porosity, the potential for entrapment of these gases leading to decreased density is significant. Additionally, a large amount of adsorbed gases may significantly affect the reactivity of the surfaces and interfaces in the compacted nano-TiN or interfere with Ti-N bonding and diffusion. The TGA/MS/IR work was done with the goal of trying to determine what adsorbed gas species may be present on the surface of the powders at various times during the sintering process.

Shown in Figure 5-2 is TGA data for the S-EXP (a), L-EXP (b) and HCS (c) samples. The fact that a weight loss was observed for the air-exposed nano samples, but not for the commercial material, correlates well with data presented by Sakka *et al.* [5]. However, given the significantly higher surface areas of our materials, the greater weight losses detected here, as compared to ~ 5% in Sakka's samples with a surface area of 102 m^2/g, suggest that these materials adsorb even more gas species from the atmosphere than did his powders. At lower temperatures within experimental uncertainty, the S-EXP and L-EXP samples lose the same amount of weight. At the highest temperatures however, the L-EXP samples continue to lose weight. This tail above ~ 1100 °C may be due to the volatilization of small amounts of Ti_xO_y related surface compounds on the more oxidized L-EXP materials. The only weight loss observed for the HCS materials likely stems from the minor dissociation of TiN above 800 °C [6].

The weight losses measured on TGA as shown in Figure 5-2 corresponded to the gases evolved and detected by mass spectroscopy (MS) over various temperature ranges. Shown in Figure 5-3 is the mass spectrometer data for the S-EXP sample. The initial weight loss detected by TGA corresponds to the evaporation of water (18) and removal of physically adsorbed OH which ionizes to mass units 16 (O) and 1 (H). (Mass unit 1 is not detectable in the mass spectrometer due to the use of He (2) as the carrier gas). Between room temperature and 600 °C, mass unit 28 (CO) evolves steadily. At 800 °C there is a sharper drop in weight corresponding to significant mass unit 28 evolution from desorbed carbonates. The mass unit 28 is more likely associated with CO than N_2 due to the very low amounts of mass unit 14 (N) detected as well as the fact that there is no

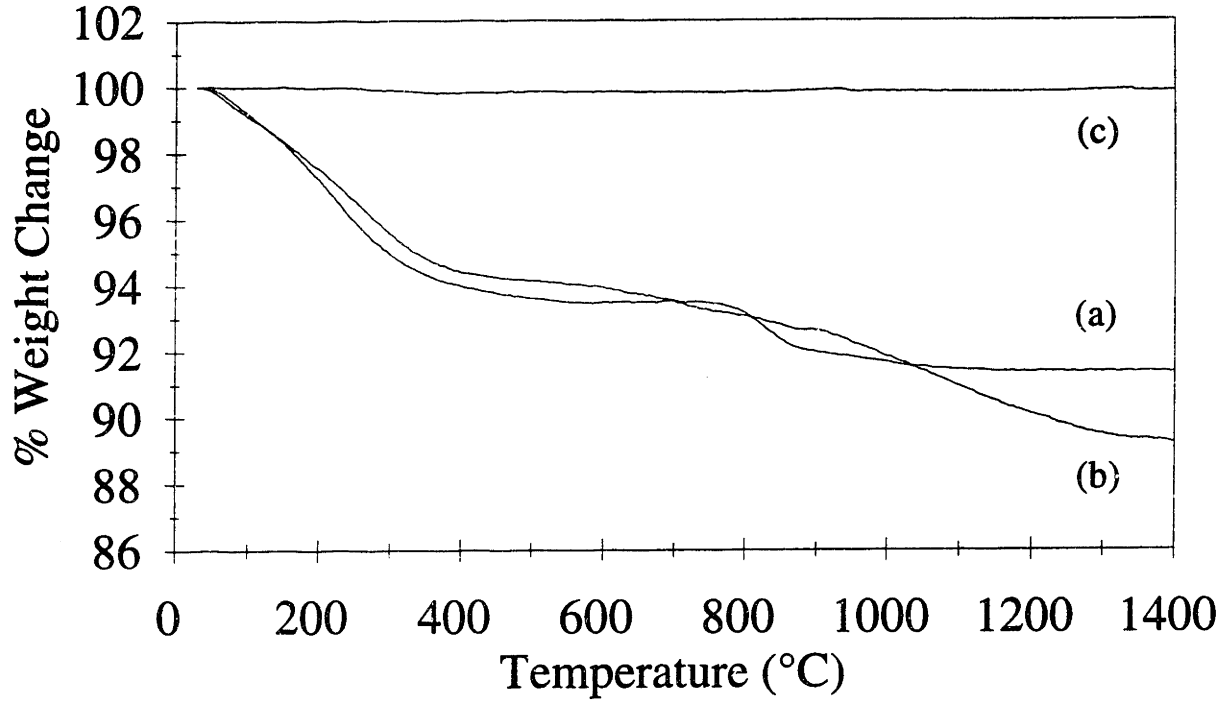

Figure 5-2: TGA data for (a) S-EXP, (b) L-EXP and (c) HCS.

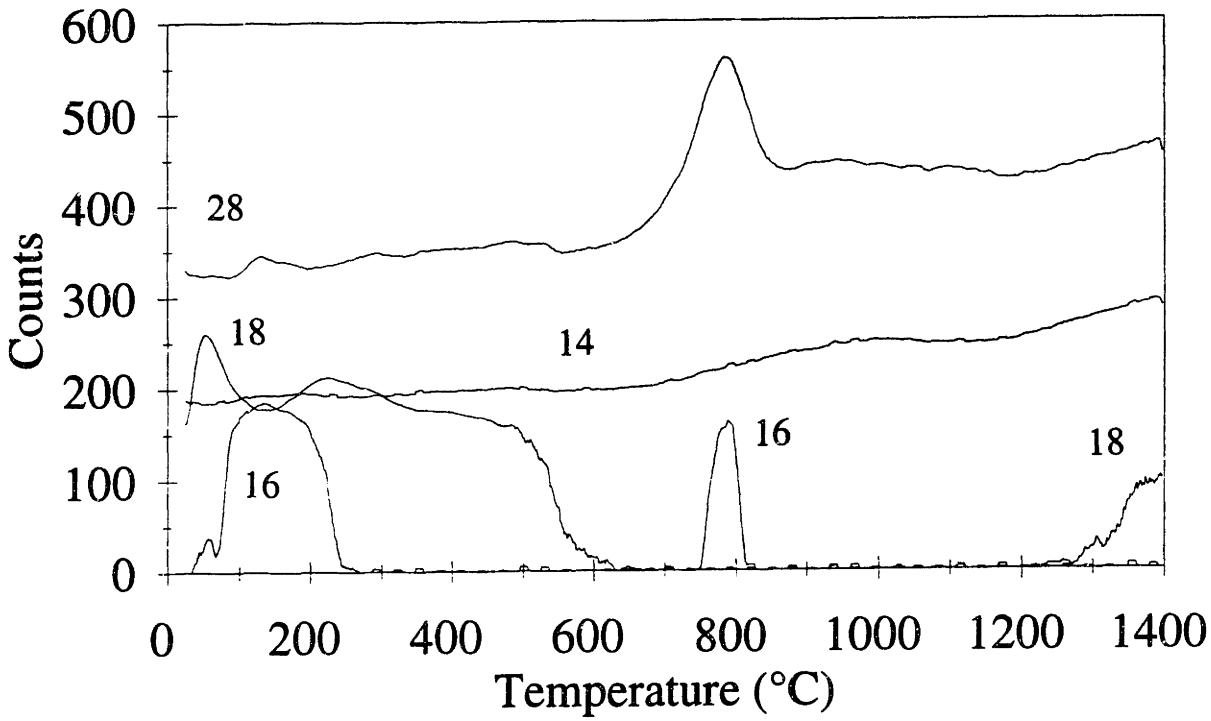

Figure 5-3: Mass spectrometry data for S-EXP.

corresponding increase in the levels of mass unit 14 at 800 °C as the level of mass unit 28 is sharply increasing. The potential for CO evolution during heating of these materials is further supported by the fact that the ESCA measurements described in Chapter 4 detected 14.2 wt% C on the surface of the air-exposed nano-TiN. Also contributing to the sharper weight loss at 800 °C is the evolution of 16 (NH_2) species. The IR studies described below show these N – H compounds to be present on the surfaces of these materials. Above 800 °C, a contribution from N to both the levels of mass units 14 and 28 is likely due to the decomposition of TiN [6]. Above 1300 °C, additional water (18), likely of a chemisorbed nature, was liberated and detected. This high temperature water evolution, potentially occurring near and beyond the onset of closed porosity during sintering, may influence the final sintered densities of the EXP materials due to entrapped porosity stemming from this evolved gas.

An additional potential consequence of the water evolution at both low and high temperatures is an increase in the amount of titanium oxide condensation in the sintered materials. A lower temperature dehydroxylation mechanism taking place during the removal of hydrogen-bonded OH groups from the surface may increase the amount of Ti-O-Ti bonding by the following scheme [7]:

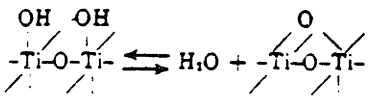

At higher temperatures, a migration of protons or hydroxyl groups could allow the removal of isolated OH groups and the formation of incompletely coordinated Ti atoms [7]:

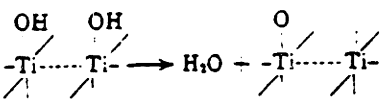

This may partially account for the observation by XRD of the substoichiometric compound Ti_3O_5 in the loose powders resulting from these TGA/MS experiments as well as in the final sintered materials. XRD of the L-EXP product showed that it consisted of ~ 60 vol% Ti-O products, the majority of which was Ti_3O_5, and only ~ 40 vol% TiN, demonstrating the extent of oxidation that takes place at long exposure times. The S-EXP products consisted of a mix of small amounts of Ti_3O_5 and Ti_2O_3 along with the

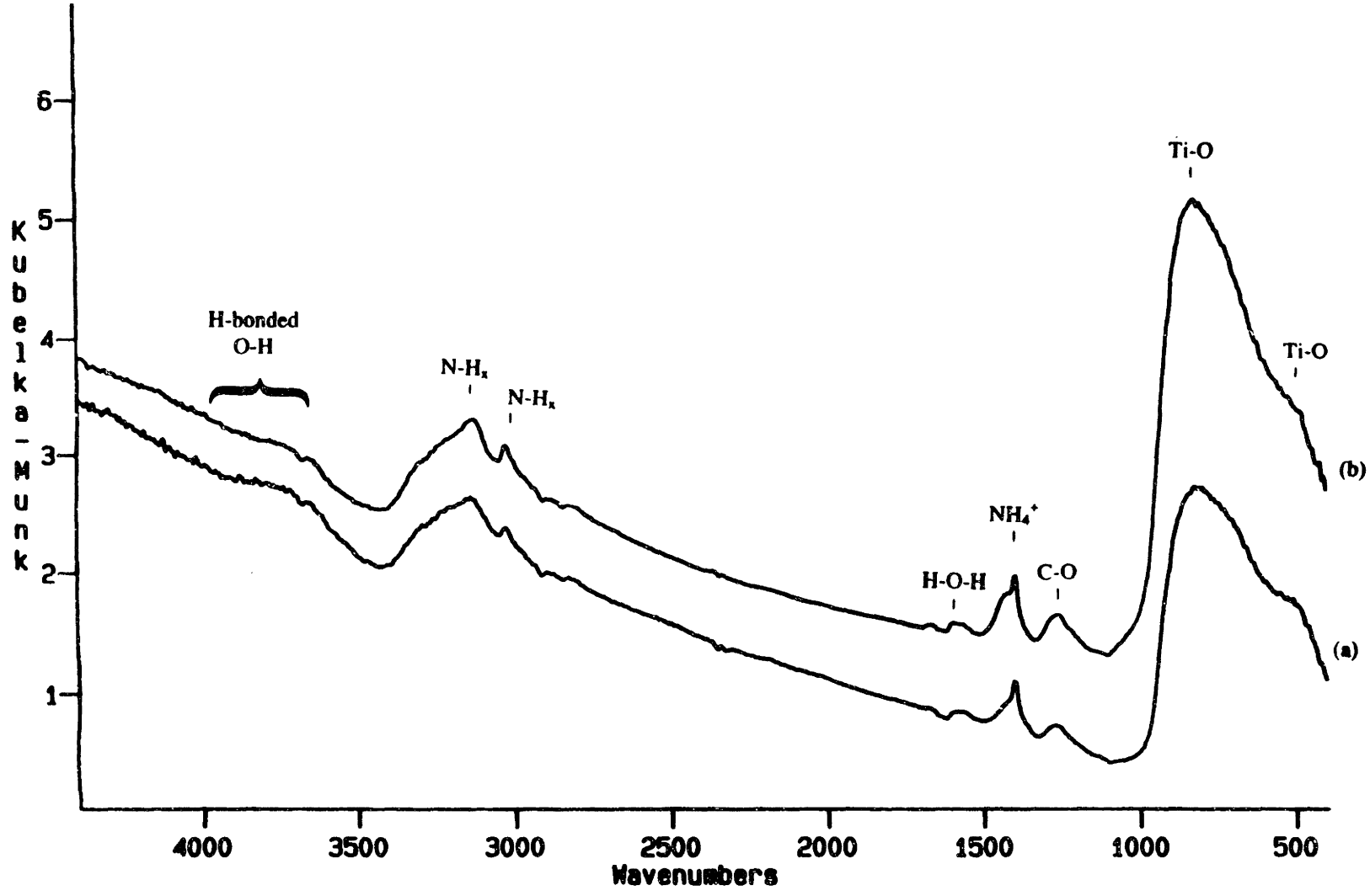

Figure 5-4: DRIFT data at room temperature for (a) S-EXP and (b) L-EXP.

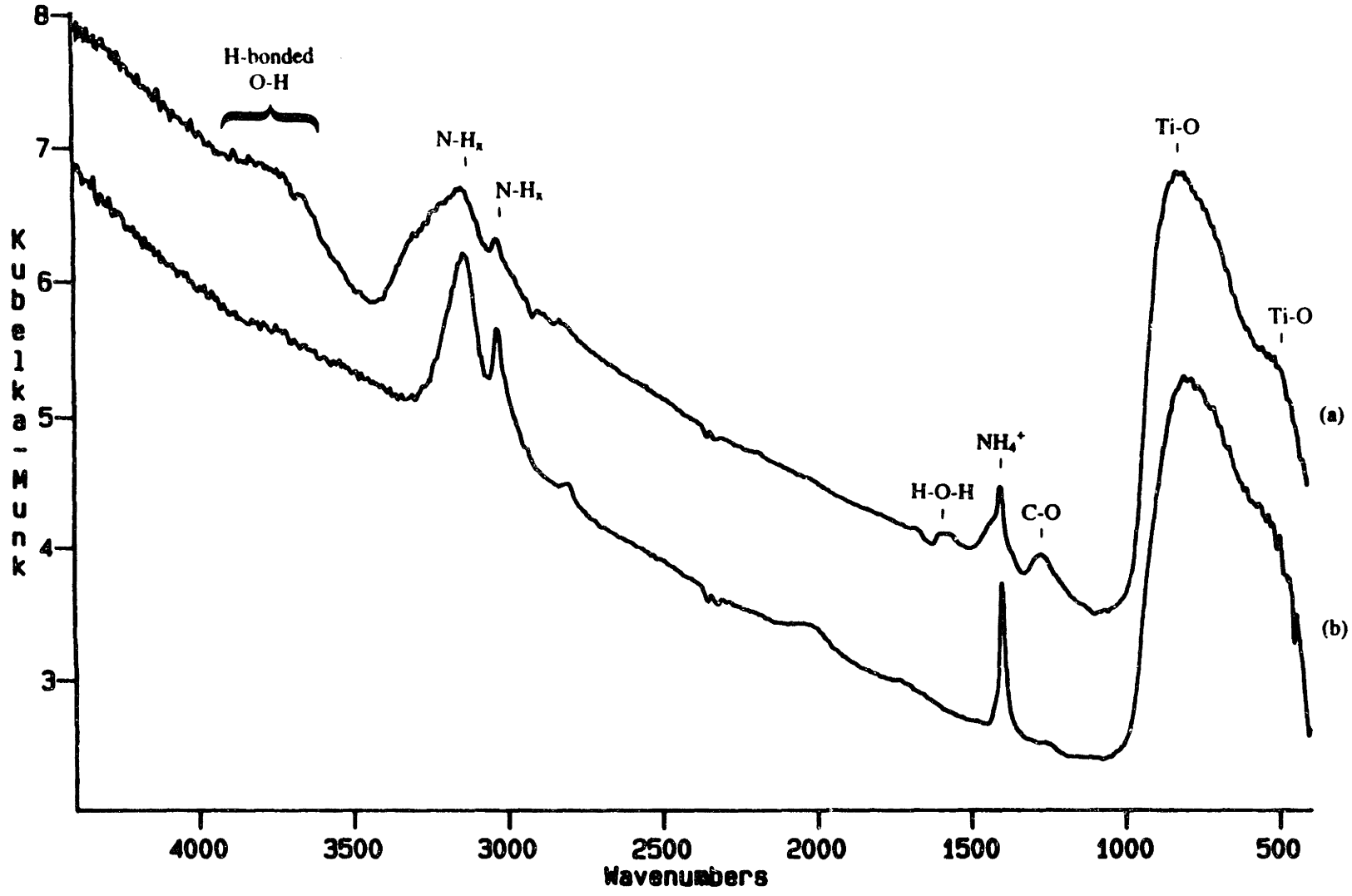

Figure 5-5: DRIFT data at room temperature (a) and 500 °C (b) for S-EXP.

NH_2 species are still present on the S-EXP material at 500 °C, the upper temperature limit of our *in-situ* DRIFT cell. TGA/MS results show that these species are not removed until heat treatment in the temperature range of 750 to 820 °C. Finally, the small C-O peak at 1260 cm^{-1} is decreased in intensity upon heating to 500 °C, matching the observed slight evolution of CO in the MS data. This signal is not eliminated at 500 °C, and, as shown by TGA/MS data, is fully evolved only upon heating to 775 °C.

PA-FTIR also shows the increasing baseline with higher wavenumbers observed in the DRIFT spectra. Based on other infrared studies in the literature, this increased signal at higher wavenumbers appears to be a feature of many nitride materials [11]. PA-FTIR also confirmed the DRIFT observation that there were strong signals for Ti – O stretching vibrations at 755 and 520 cm^{-1} even for the nano-TiN powders which were loaded and sealed in the IR cell in the glovebox without exposure to air. This suggests that even the low levels of oxygen (< 15 ppm) present in the glovebox are sufficient to oxidize the surface of these nitride powders giving rise to Ti – O features. This oxidation of even "unexposed" powders will manifest itself in the sintering results subsequently reported. Additionally, the fact that the TGA weight loss for the S-EXP and L-EXP materials is essentially comparable within experimental uncertainty for T < 1100 °C, as well as the similar nature and quantity of the adsorbed species on their surfaces, suggests that these ultrahigh surface area materials pick up at short times almost all of the gaseous adsorbents which they are going to scavenge, and that further oxidation is the only significant change with time.

5.3.2 Pressureless Sintering Results

5.3.2.1 Densification Performance

The UN800 and HCS pellets sintered at 800 °C, just at the onset of appreciable sintering, were examined via SEM and nitrogen adsorption to determine the pore size distribution and structure of the green bodies. Following removal from the furnace after sintering at 800 °C, the pore size distribution of these pellets was determined from nitrogen desorption isotherms using the BJH theory. This characterization of the "green" bodies, shown in Figure 5-6, demonstrated the much narrower pore size distribution in the compacted nano-TiN as compared to compacts of the commercial TiN (HCS). The average pore diameter in the UN800 compacts was 4.3 nm while the average pore size for

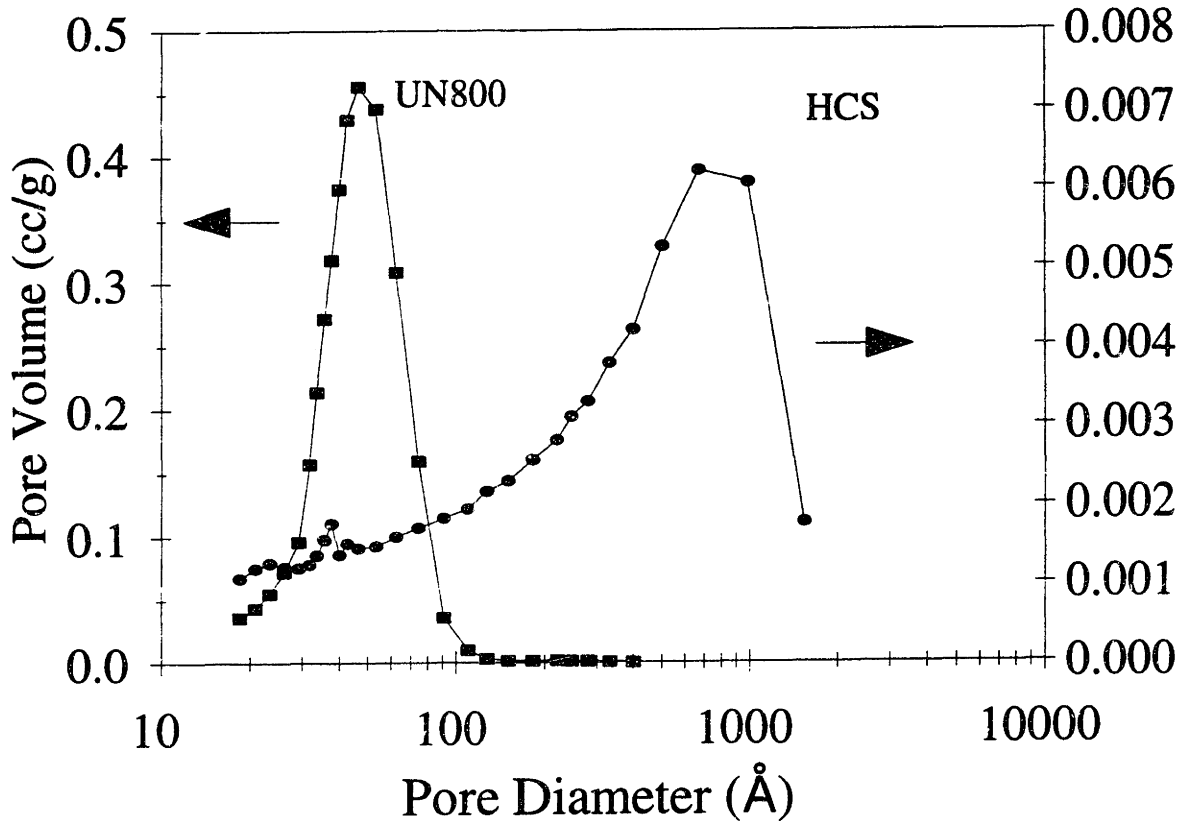

Figure 5-6: BJH pore size distribution of UN800 and HCS compacts sintered at 800 °C.

the compacts made from the commercial materials was 480 nm. The narrow pore size distribution of the nano-TiN compacts resulted from the very narrow particle size distribution of the starting powders and should lead to significantly enhanced sinterability of the nano-TiN. Figure 5-7(a) is an SEM micrograph of the UN800 material sintered at 800 °C. The HCS material sintered at 800 °C is shown at the same magnification in Figure 5-7(b). Note the greater uniformity and the homogeneous particle packing in the UN800 sample.

Values in the literature for the theoretical density of TiN vary considerably. This is due in part to the extreme difficulties in densifying it fully without the use of intentional additives, as well as the potential for unintentional contamination leading to secondary phase formation which may also affect the final density. Values quoted in the literature range from 5.21 g/cm^3 [12] to 5.40 g/cm^3 [13, 14] and also include 5.22 g/cm^3 [15, 16], 5.35 g/cm^3 [17] and 5.388 g/cm^3 [18]. Additionally, as outlined below, these nano-TiN materials incorporate a measurable amount of oxygen in the final sintered materials. For these reasons, the results of the pressureless sintering of the TiN powders shown in Figure 5-8 are plotted using absolute density, not percent of theoretical density.

The green density of the EXP-WOM pellets was exactly identical to that of the EXP-WM pellets. The fact that this quantity was 2.12 g/cm^3 for both materials indicates that there were no significant packing differences due to agglomeration at this low density. The green density of the UN800 pellets was slightly higher, by ~ 3%, than that measured in the EXP pellets. This would suggest the possibility that the absence of adsorbed gases may allow better initial compaction which would potentially be reflected in the final sintering results.

The low green density of the nano-TiN pellets was a function of several factors, including the inherent abrasivesness, brittleness and low ductility of TiN. However, the much bigger effect, and the difference between the HCS and nano pellets, was due to the nanocrystalline nature of the nano-TiN. It has been shown that the compressibility of powders decreases markedly with decreasing particle size [19, 20]. These problems with green density are present in the formation of many nanocrystalline materials because it is difficult to compact them due to a high coefficient of interparticle friction [19]. Even more ductile metal materials, such as Ni, experience this compaction difficulty. A study on nano-Ni and nano-Si_3N_4, both with an average particle size of 15 nm, showed that

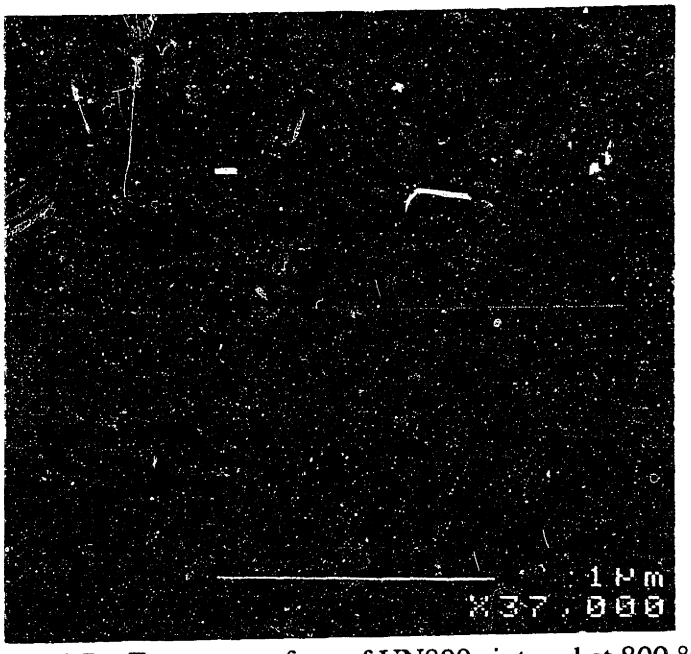

Figure 5-7a: Fracture surface of UN800 sintered at 800 °C.

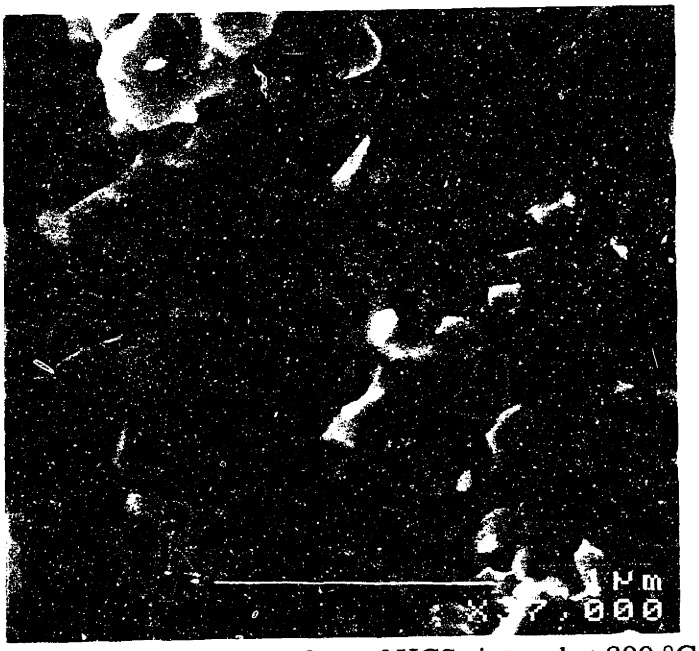

Figure 5-7b: Fracture surface of HCS sintered at 800 °C.

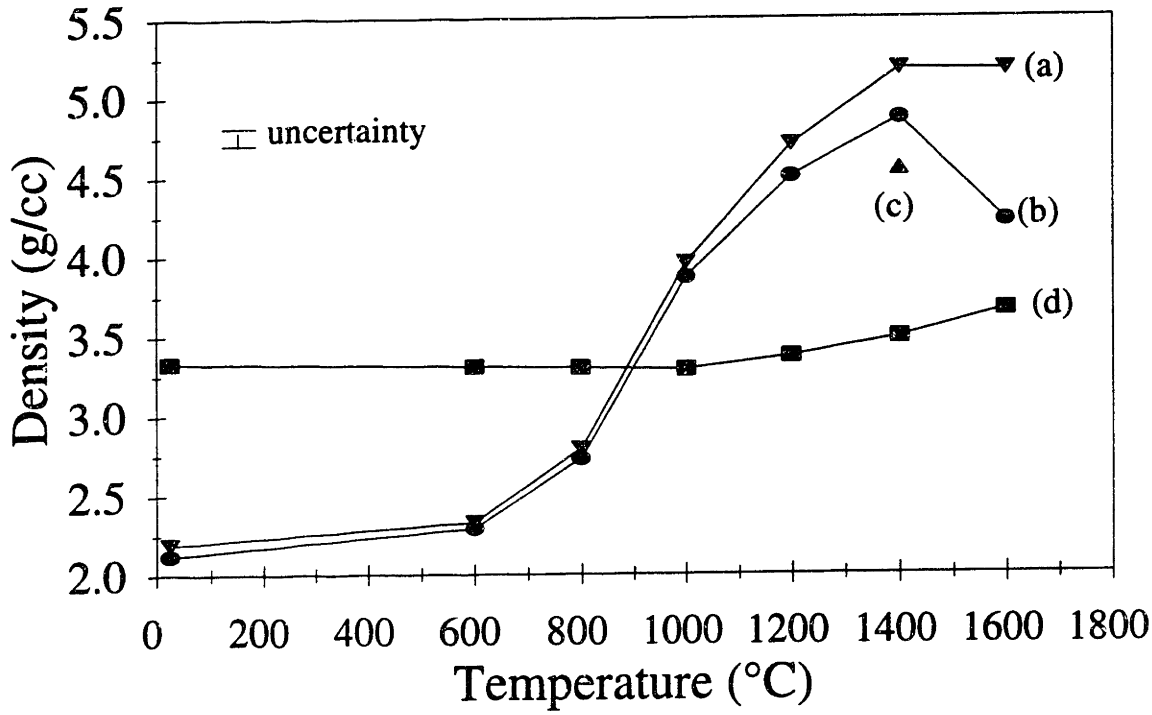

Figure 5-8: Densification during sintering of (a) UN800, (b) EXP-WM, (c) EXP-WOM, and (d) HCS.

these materials could be compacted at room temperature to densities of only 49% and 47%, respectively, with an applied uniaxial load of 1 GPa [19]. Andrievski has also showed the existence of these problems in the compaction of nano-TiN. 1 GPa loads produced somewhat higher green densities of 55 – 60% in his nano-TiN materials. With a load of 7 GPa at room temperature, his green density improved to just under 80% [21]. It should be noted that these compaction levels are very much in excess of that typically used or achievable in most uniaxial compaction processes. However, the data is included here to illustrate that even at the highest obtainable pressures, the compaction of nanocrystalline materials, and nano-TiN in particular, is problematic.

However, despite the differences in their green densities, the nano-TiN sintered to much higher densities than the conventional TiN (HCS). With the careful powder handling procedures outlined for the UN800 materials, dense (99%) TiN was produced through this pressureless sintering process at 1400 °C (Figure 5-8a). The fact that the highest densities achieved with the EXP-WM powder (Figure 5-8b) are lower than those of the UN800 pellets and the drop in density in the EXP-WM pellets seen at 1600 °C are both related to the very large weight loss that occurred upon sintering the EXP-WM materials. The EXP-WM materials sintered at 1400 °C have a 9.2% weight loss upon sintering. This weight loss correlates well with the results reported above for the TGA experiments on exposed powders. By 1600 °C the total weight loss is 14.4%, and, after sintering at 1800 °C, the EXP-WM materials have a cumulative 16.7% weight loss. However, the UN800 materials had an undetectable (< 0.1%) weight loss during sintering. This difference in weight loss, presumably due to the moisture, oxygen and other gas species adsorbed during exposure of the EXP powders, accounts for the bulk of the difference in the final density of these materials. Despite the weight loss, the EXP-WM samples sintered at 1400 °C appear by SEM, on cut and polished surfaces, to be ~95% dense. As would be expected due to its characteristics outlined in Chapter 4, the EXP-WOM powder (Figure 5-8c) demonstrates a poorer sinterability at 1400 °C. Finally, the commercial HCS TiN materials (Figure 5-8d) processed identically to the EXP-WM powders sintered to a much lower density (65%) with very large grain sizes ($\geq$10 μm). There was no weight loss detected in sintering the HCS pellets, due to the low surface area (2 m^2/g) of this commercial powder.

5.3.2.2 Microstructural Development

In order to study the microstructure which develops upon sintering, the sintered pellets were examined via SEM. This characterization verified that the UN800 had sintered to full density by 1400 °C and also confirmed the presence of porosity in samples sintered below this temperature. At 1400 °C, the grain size was determined to be 140 nm ± 15.3 nm (Figure 5-9a), and there were no pores or second phases visible in these materials (Figure 5-9b).

However, SEM reveals the development of a segregated second phase in the EXP-WM materials sintered at 1200 °C. At 1400 °C, as shown in Figure 5-10, a significant amount of this second phase is noted. In addition to being dispersed randomly in very small pockets of 20 – 100 nm in length, this phase also segregated into somewhat larger regions, 500 – 1000 nm in size, in a small number of locations, on the order of 40 regions/cm^2 of surface. By examining these larger regions by EDAX, this phase was shown to be enriched in oxygen (45 at% O) relative to the primary TiN phase (20 at% O). Additionally, substantial cracking at the phase interfaces, likely due to thermal and lattice mismatch between the two phases, was observed. Figure 5-11a is a secondary electron image of one of these areas and Figure 5-11b is a back scattered image of the same area showing that it is clearly a compositionally different, dark, second phase. This segregation and cracking are more developed by 1600 °C, such that this effect is likely contributing, in addition to the measured weight loss, to the observed drop in density at this temperature.

Other work on nano-TiN has also demonstrated the development of small amounts of an oxygen-rich second phase upon sintering [22]. Rabe and Wäsche report sintering results on a nano-TiN under development at H.C. Starck [22]. The powder, described in Chapter 4 with a B.E.T. surface area of 43 m^2/g and an oxygen content of 3.2 wt%, is utilized in a gas pressure (5 MPa N_2) sintering apparatus. They report sintering results on air-exposed powders that indicate the incorporation of 3 wt% oxygen in their final sintered materials. They observed the oxygen concentrating in a secondary, titanium oxide related phase (27 wt% O). The microstructure which develops in their materials looks very similar to that which we observed in the EXP samples. Rabe and Wäsche also report on sintering a Tioxide TiN (T36), different from that reported in Chapter 4, in the same gas pressure apparatus at 1550 °C with a 20 min hold time [23]. This Tioxide TiN

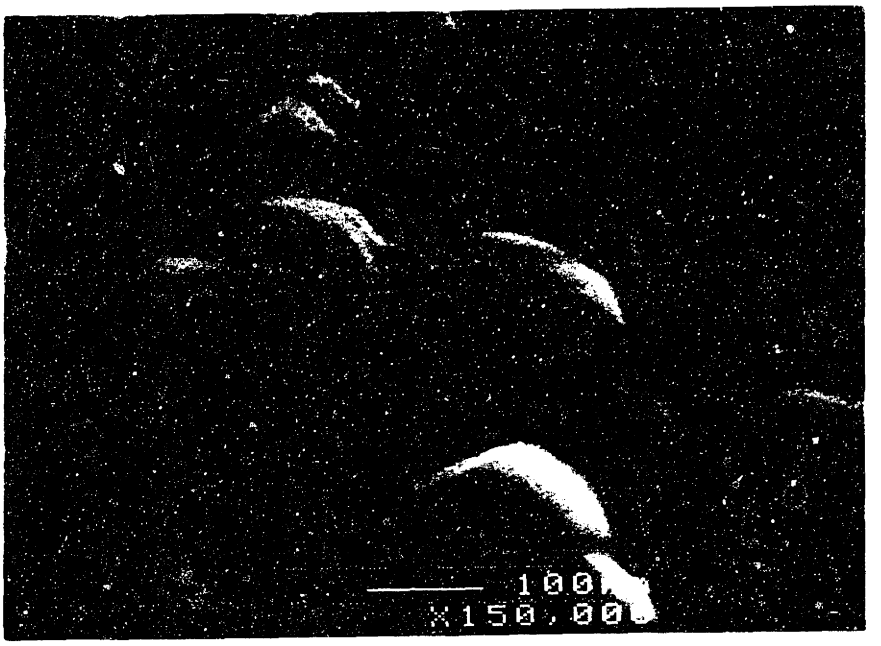

Figure 5-9a: SEM image of thermally etched surface of UN800 sintered at 1400 °C.

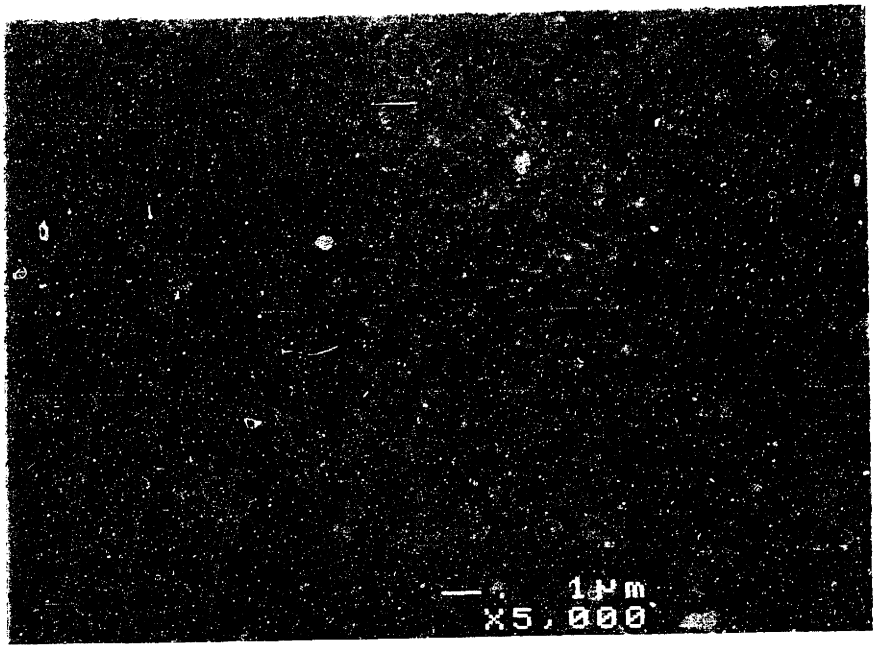

Figure 5-9b: SEM image of polished surface of UN800 sintered at 1400 °C.

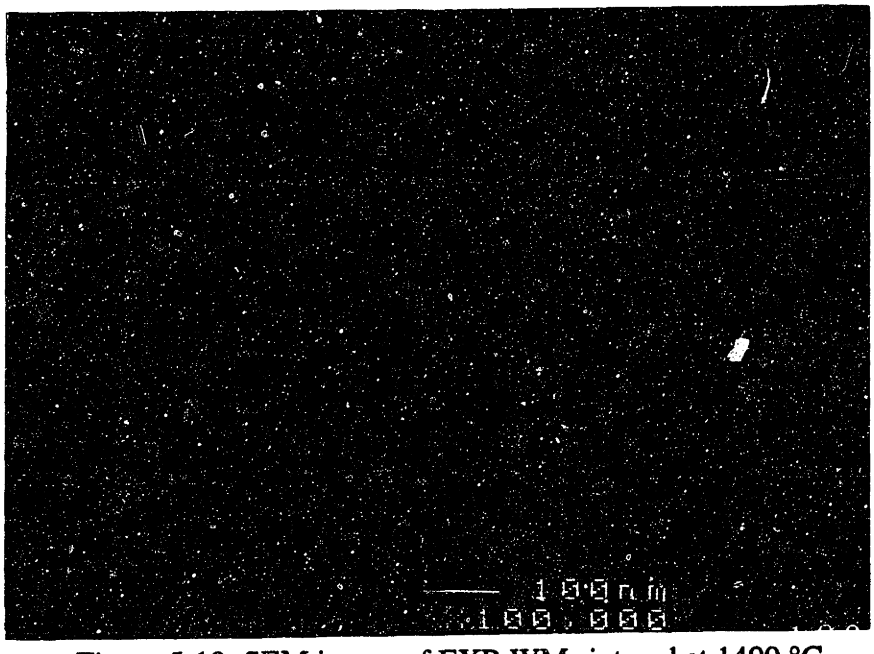

Figure 5-10: SEM image of EXP-WM sintered at 1400 °C.

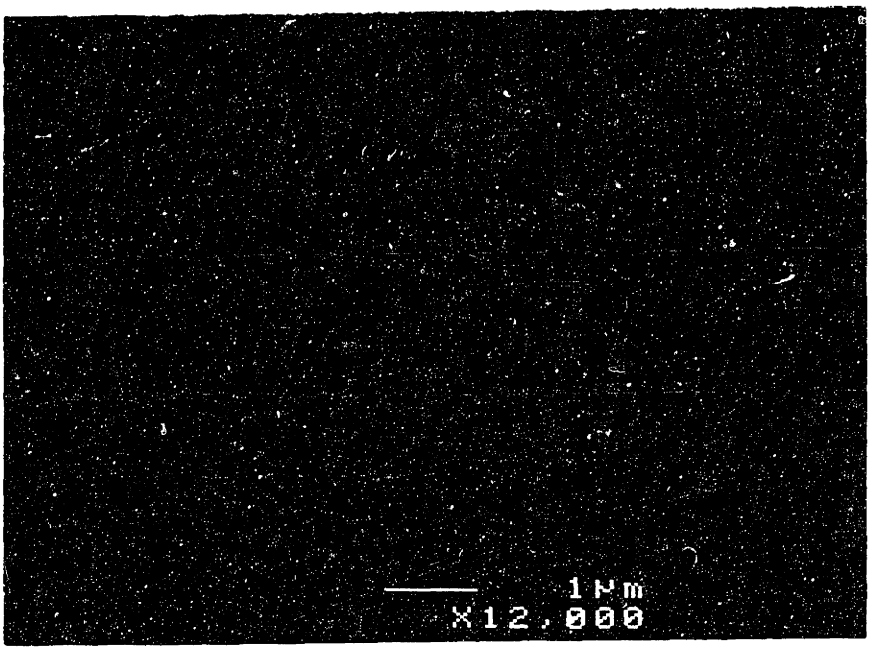

Figure 5-11a: Secondary electron image of very large region of second phase in EXP-WM sintered at 1400 °C.

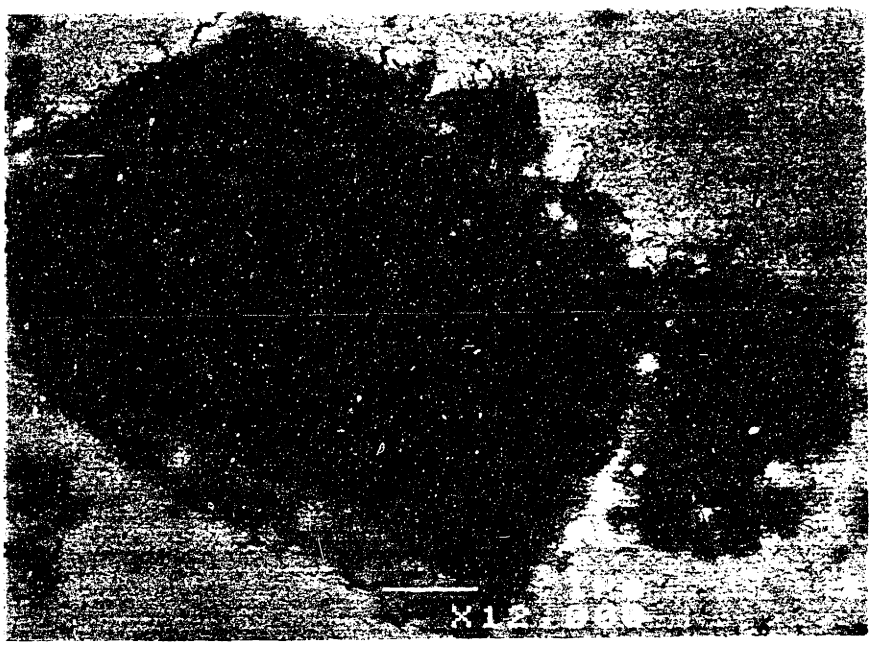

Figure 5-11b: Back scattered image of very large region of second phase in EXP-WM sintered at 1400 °C.

(T36) was also generated by a plasma synthesis technique and had a surface area of 36 m^2/g with a particle size range of 15-30 nm. They reported that the high oxygen content (7.1 wt%) of these powders led to the formation of a considerable amount of an oxygen-rich second phase. Most significantly, they found that the second phase was not homogeneously distributed [24] as we also observed. The fact that this powder (T36) did not sinter as effectively as their powder with the lower initial oxygen content of 3.2 wt% was attributed to a lowering of the surface energy with increasing surface oxide content [23].

The microstructure of the EXP-WOM samples is shown in Figure 5-12. With the lower quality starting powders, these samples sinter less effectively with an increased amount of porosity. Upon sintering, they also develop the dark, second phase observed in the EXP-WM materials.

Shown in Figure 5-13 is an SEM micrograph of the sintered HCS materials. Note the large pores and large grains which develop from this relatively poor starting powder. No second phase develops upon sintering. It is clear from the above results that the microstructure that develops in the sintered samples is a very strong function of the quality of the starting powders and that the careful processing of the UN800 samples has allowed the production of a very promising material.

5.3.2.3 XRD and Chemical Analysis Results

As shown in Figure 5-14, when sintering both the EXP (a) and the UN800 materials (b), appreciable amounts of a Ti_3O_5 phase are crystallized upon sintering. This phase is first detected by XRD at 1200 °C and has developed appreciably by 1600 °C. This fact suggests that it may be related in some manner to the dark second phase observed in SEM. However, the composition of 5 O to 3 Ti doesn't match that determined in EDAX. Additionally, although this phase is present in XRD of the UN800 materials, no dark, second phase is observed via SEM in those materials. It therefore seems more likely that this Ti_3O_5 is present at the grain boundaries in both of these materials. As this phase has a lower density (~4.13 g/cm^3) [25] than TiN, the endpoint density of these materials is lowered as shown in Figure 5-8. The HCS samples showed no evidence of this Ti_3O_5, or other Ti-O phase, at any sintering temperature. The manufacturer's reported oxygen content of the starting powders for these materials was 0.8 wt%. Given

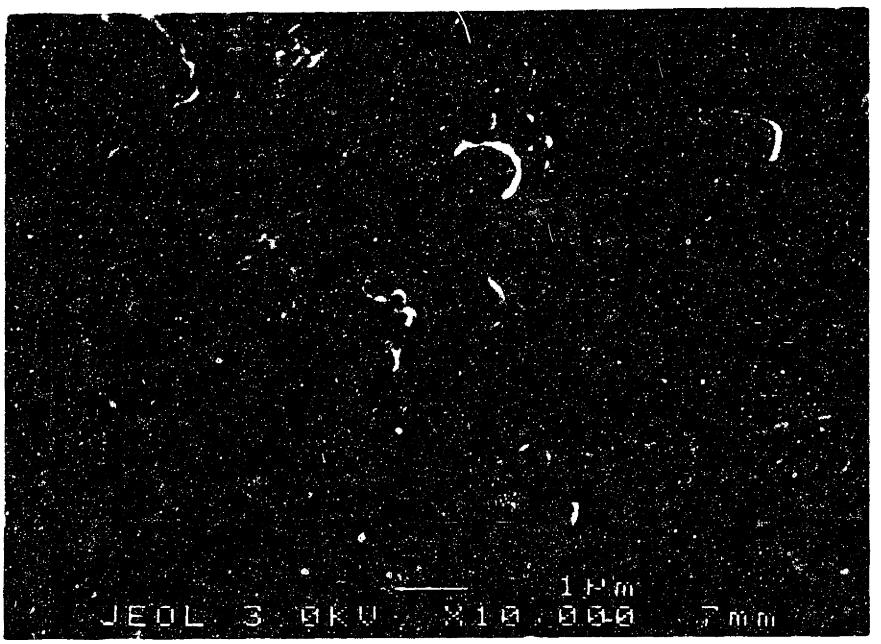

Figure 5-12: SEM image of EXP-WOM sintered at 1400 °C.

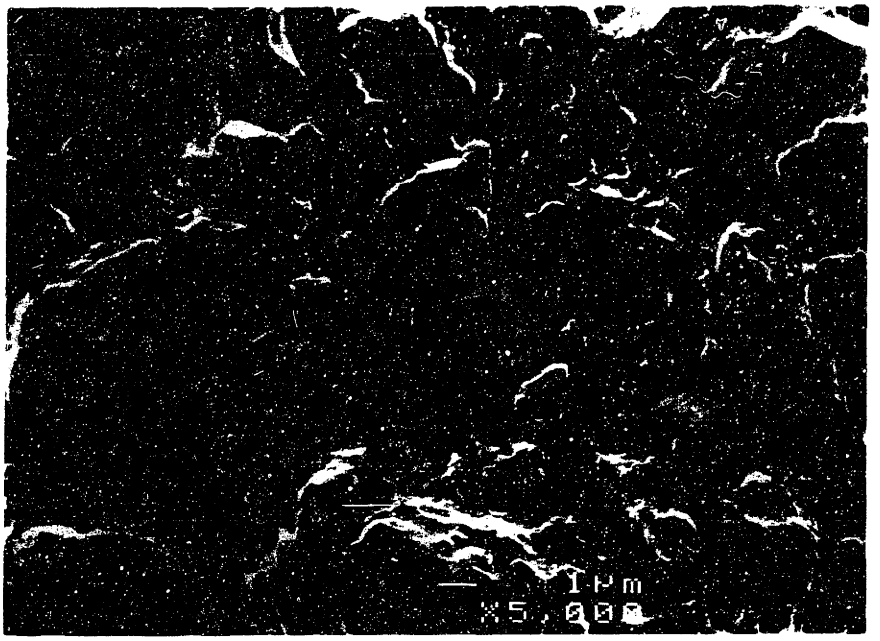

Figure 5-13: SEM image of microcrystalline (HCS) TiN sintered at 1400 °C.

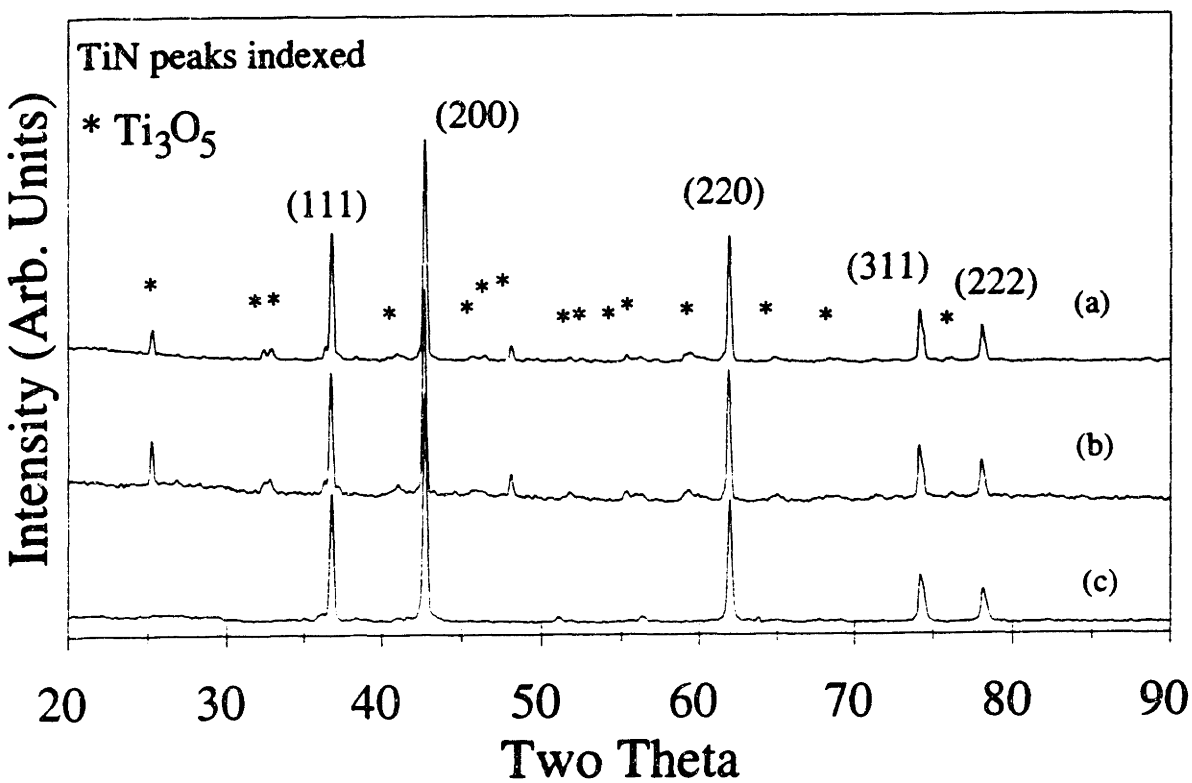

Figure 5-14: XRD data for sintered (a) EXP, (b) UN800 and (c) HIP.

that no Ti-O-N phase is observed in XRD to correlate with the darker, second phase regions observed in SEM of the EXP materials, it seems most probable that this phase is either present in too small an amount to detect via XRD or is X-ray amorphous.

Chemical analysis of sintered samples confirms the presence of experimentally identical levels of oxygen in the EXP and UN800 materials and also demonstrates the reduction of oxygen levels in the sintered materials due to the vacuum treatment incorporated into the sintering process. Chemical analysis on EXP pellets sintered at 1400 °C shows oxygen levels of 12.9 wt%, down from 18.4 wt% in exposed powders, nitrogen levels of 17.6 wt% and titanium present at 69.5 wt%. The UN800 pellets sintered at 1400 °C have virtually identical results, which should be considered the same within experimental uncertainty, for chemical analysis: 13.7 wt% O, 16.7 wt% N and 69.6 wt% Ti. For these two materials, the N/Ti molar ratio = 0.87 and 0.82 respectively, down significantly from the 1.10 of the starting powder, and below the 1.0 ratio of "pure" TiN. This suggests, as seen in XRD, that in the sintered materials some of the excess Ti is bound with O and shows up as Ti_3O_5, whereas before in the raw powder, all the Ti and N were bound together and the O was only incorporated on the surface of those TiN materials. Thus, TiN was the only phase detected via XRD of the as-synthesized powders.

In the EXP materials, the O content is obviously a result of their exposure to air during processing. However, even after sintering at 800 °C in the furnace attached to the glovebox without exposure to air, the UN800 compacts still have a surface area of ~ 95 m^2/g. (See Figure 5-15 for a plot of BET surface area versus sintering temperature for the UN800 materials). Thus, when these samples are removed from the glovebox furnace and transferred quickly to the high temperature furnace, they adsorb a fair amount of oxygen which appears to be incorporated into the sintered materials. Ti_3O_5 has been synthesized previously by the vacuum sintering and reduction of TiO_2 [25]. Thus, it seems probable that heating both the EXP and the UN800 samples under vacuum to 800 °C, after they have been exposed to the atmosphere, likely accounts for the formation of the Ti_3O_5. The fact that significant oxide phases develop and crystallize upon sintering of these high surface area materials is not surprising. There are previous reports of significant room-temperature oxidation of ultrafine TiN powders [5] leading to the formation of TiO_2 and $Ti\text{-}O_x\text{-}N_y\text{-}H_z$ phases. However, the results presented here

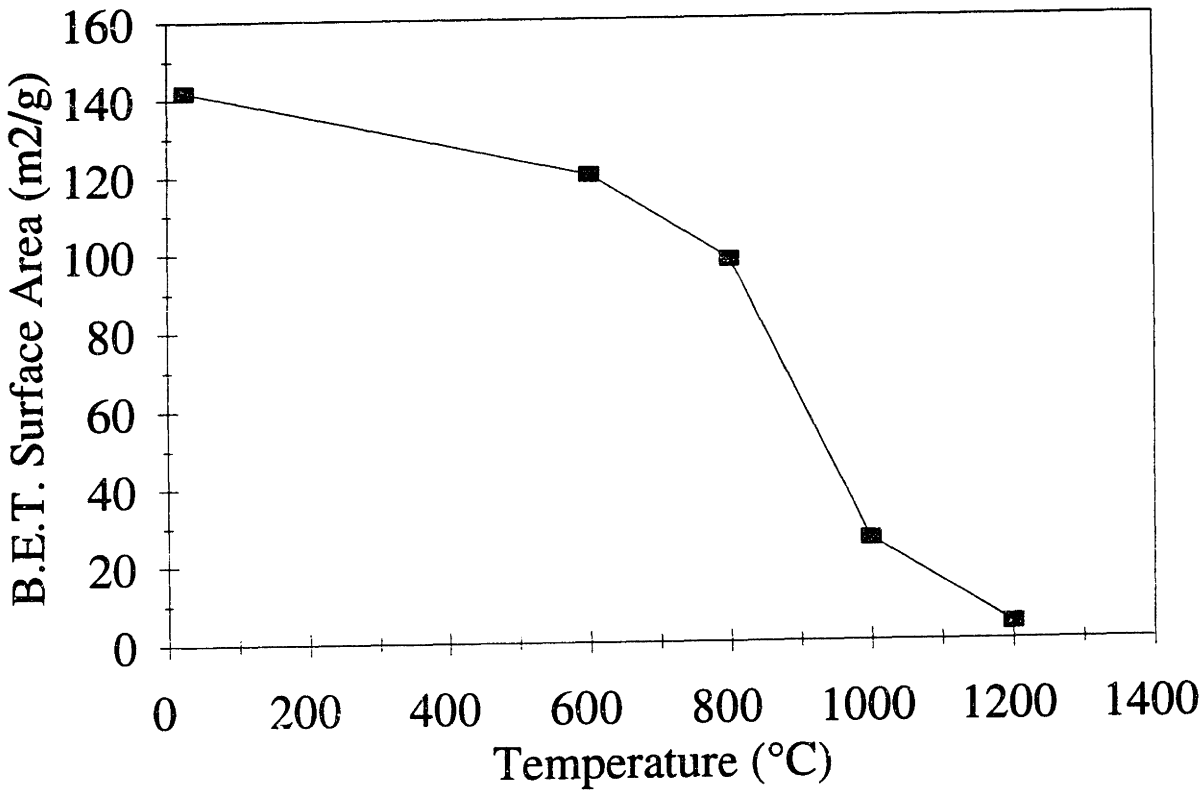

Figure 5-15: BET surface area as a function of sintering temperature for UN800.

demonstrate very clearly the oxidation challenge that must be overcome for the successful utilization of high-quality, nanocrystalline nitride powders.

5.3.2.4 Grain Growth During Sintering of UN800

It is usually difficult to maintain nanometer grain sizes while utilizing pressureless sintering to reach full density. For example, as shown in Figure 5-16, when a typical nanocrystalline ceramic reaches ~90% density, grain growth accelerates rapidly [26]. This phenomenon is also observed in conventional ceramics and is likely associated with the disappearance of the open porosity which has helped to pin grain boundaries during sintering [20, 26-30]. By utilizing a non-agglomerated starting powder, or by adding some small amount of dopant to pin grain boundaries, grain growth during the final stages of sintering may be suppressed [20,31]. Alternatively, grain growth may be limited by a mobile inclusion, such as a pore. Specifically, Kingery and Francois have shown that pores must migrate along with the boundaries during normal grain growth [28]. While pores can move by a variety of mechanisms, such as evaporation-condensation, surface diffusion or volume diffusion, the rate of pore migration is inversely proportional to the pore diameter because the distance of material transport changes in proportion to the pore size [28]. Hence, smaller initial pore sizes are more mobile and can stay with, and restrain, the grain boundary leading to the highest possible densities with minimized grain growth. Brook quantified this balance between pore and grain boundary mobility to generate pore-boundary interaction maps that suggest that the optimal processing for minimization of grain growth involves the avoidance of a region of "separation" where the pores separate from the grain boundaries [29]. He models the pore mobility as a process that is inversely proportional to the pore radius ρ, with a ρ^{-3} or ρ^{-4} dependence [29]. Thus, a reduction in ρ can significantly increase the pore mobility and allow densification to be accelerated relative to grain growth.

An additional benefit to small pore sizes was demonstrated by Bruch [32]. He suggested that there is a critical size to the pore clusters in the original compact. Above this critical size, the pores may consolidate into larger pores which will coalesce and grow, rather than shrink and disappear. Also, as noted by Coble [33], given that the driving force for densification is related to surface curvature, large pores, with a relatively smaller surface curvature, will lead to longer densification times. Thus, the rate

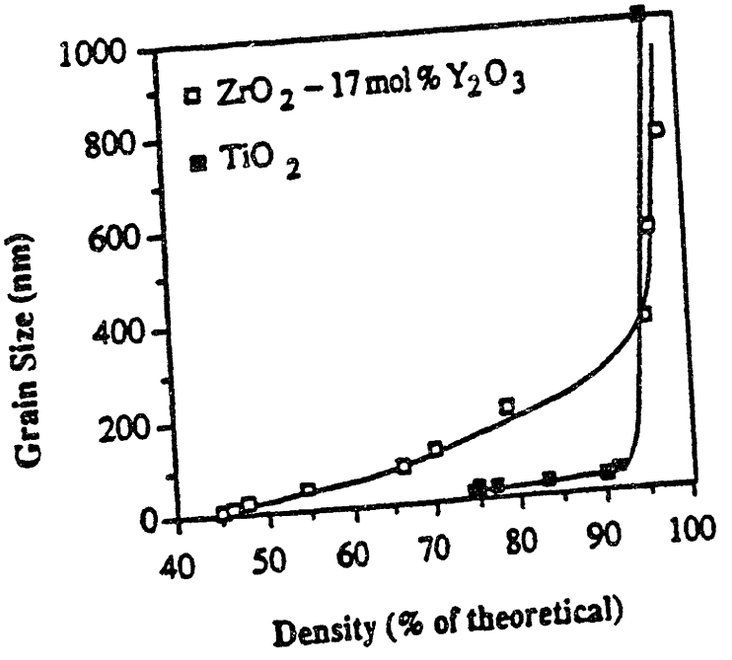

Figure 5-16: Grain size as a function of density during sintering experiments on nanocrystalline TiO_2 and nanocrystalline ZrO_2-17 mol% Y_2O_3 [26].

of sintering is very strongly controlled by the size of the pores present in the initial compact.

These initial pore size distributions are tied directly to the particles size distributions used in creating the initial compact. However, both the absolute particle size and the distribution of the sizes can impact this grain growth-densification balance as well. For instance, it has been shown by Coble and Burke [34], as well as Choi [35], that wide initial particle size distributions predispose toward deleterious, discontinuous, abnormal grain growth. Additionally, given that the transport of matter is required for shrinkage, regardless of the mechanism or pathway, the transport distance will be smaller, and thus the sintering rate higher, with a smaller particle size [34]. A final consideration is the degree of agglomeration in the starting particles. Besides impacting the size of the initial pores as described above, the final grain size in the sintered ceramic is directly linked to the agglomerate size in the starting powder. As a general rule, the grain size in a fully dense ceramic consolidated by pressureless sintering will never be less than the starting agglomerate size [27].

The importance of the above considerations was demonstrated by Vasilos and Rhodes in the late 1960s [20]. Because they recognized the importance of achieving a uniform pore size distribution with a lack of agglomeration, they undertook a procedure whereby they separated the agglomerates from a slip of Y_2O_3-stabilized ZrO_2 and centrifugally cast the remaining, agglomerate-free, basic crystallites. This process allowed them to sinter a material at 1100 °C which was 99.5% dense with a grain size of 200 nm. Conversely, initial non-uniform pore size distributions in agglomerated, non-separated, Y_2O_3-stabilized ZrO_2 materials were reflected in the resultant porous, sintered bodies that had a pore spacing corresponding to that of the initial agglomerates [20].

Mayo has also recently suggested that the key in getting successful densification while minimizing grain growth in nanocrystalline materials lies in starting with as small a pore size as possible in the green body [36]. Rather than pursuing pressure-assisted densification to minimize grain growth, she explored variables in the pressureless sintering technique due to its ease and industrial acceptance. Mayo showed that various manipulations of time and temperature during sintering of nanocrystalline ceramics have no significant effect on the pore size evolution and thus no effect on the final density/grain size combinations that can be achieved. She found that those materials with

the smallest pore sizes, achieved by high compaction pressures (1.2 GPa) or wet processing consolidation techniques, had the fastest densification rates. By starting with a green body with an average pore diameter of 5.6 nm with densification rates sufficiently accelerated with respect to grain growth kinetics, she found that it was possible to produce a 99.9% dense ZrO_2-3mol% Y_2O_3 at 1050 °C with a grain diameter of 85 nm [36]. She also found no influence on the densification rate from the green density *per se*; thus materials with very low green densities, such as the 43% in Mayo's ZrO_2 samples or the 41% in the nano-TiN described here, but very small pore size distributions can achieve full density with minimized grain growth.

Our UN800 nano-TiN materials experience some grain growth with densification in pressureless sintering, but demonstrate the tremendous benefits derived from starting with an extremely fine, unagglomerated powder that packs to yield a compact with a very narrow pore size distribution. As shown in Figure 5-17, at 1200 °C, the grain size in these materials is below 35 nm. For temperatures of 800 °C and below, the grain size was determined by XRD techniques; above this temperature, the grain size as measured from SEM micrographs is plotted. However, it is interesting to note that at 1000 °C, the grain size as determined by XRD was 26.4 nm while that measured by SEM was 24.8 nm. While the materials have reached full density at 1400 °C, the data point at 1600 °C is included to show the continued grain growth which takes place at even more elevated temperatures in the absence of any grain boundary pinning effects. In light of the principles and experiments of others described above, it seems highly likely that the enhanced sinterabilities, without extreme grain growth, observed in our nano-TiN materials are a direct result of the very narrow pore size distribution and the very small average pore size (4.3 nm) in the compacted samples. This pore structure, in turn, is due to the high quality of the initial starting powders produced in our unique reactor.

5.3.3 HIP Sintering Results

While grain growth will accelerate as full density is approached, the sintering results described above suggested that processing at slightly lower temperatures may allow us to produce an even finer grained TiN than the pressureless sintering process yielded (140 nm). A hot isostatic pressing (HIP) process may have the additional advantage of further reducing the amount of oxygen in these materials due to the potential for an even more

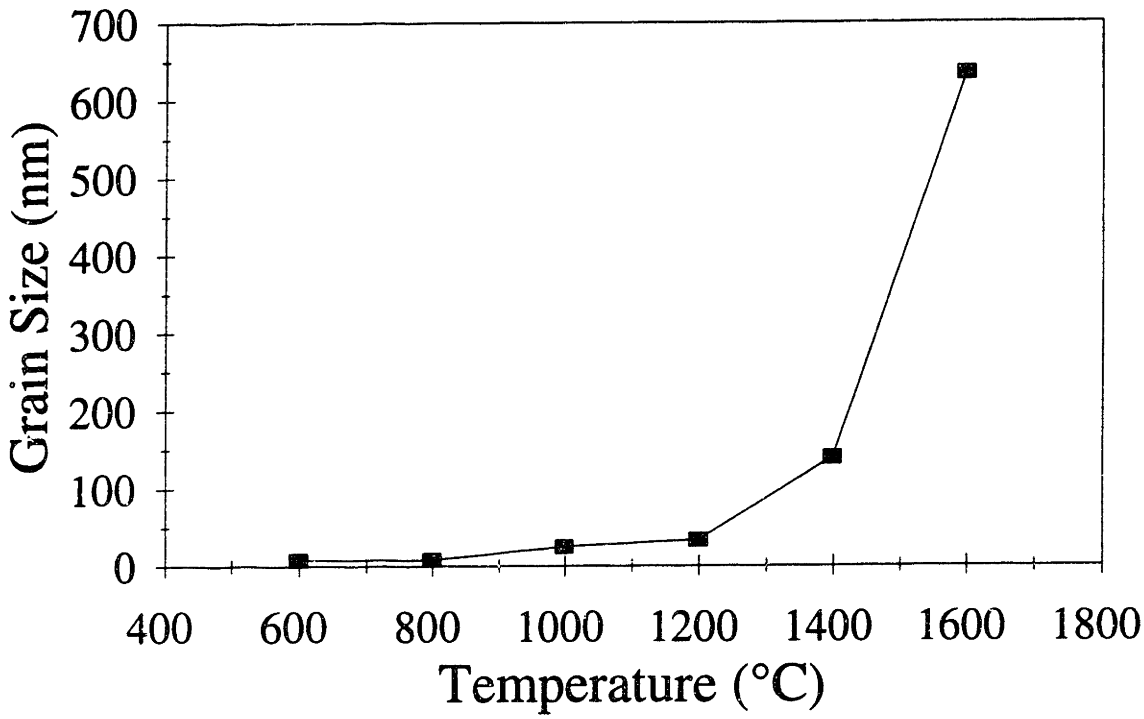

Figure 5-17: Grain size as a function of sintering temperature for UN800.

limited exposure to air than was possible during the processing of the UN800 samples. In pressureless sintering, the driving force for densification is the decrease in surface free energy due to the elimination of high surface area/energy boundaries and solid-vapor interfaces [37]. While there are various models to explain the mechanisms behind densification at various times under various conditions, a common feature to most such models is the presence of a "driving-force" term. In pressureless sintering, the surface energy (γ) is this term and is incorporated into models in different ways depending on the time during sintering for which the model is applicable. For initial stage sintering, the driving force is simply expressed as γ in the following types of sintering-rate equations,

$$\left(\frac{x}{R}\right)^n = \frac{\text{constants}}{R^p} D_i \gamma t \tag{5-2}$$

where x is the neck size (radius) for spherical particles of radius R in contact with each other, D is a diffusion term, t is time, and n and p are also constants that depend on the sintering mechanism chosen [38]. In order to account for changes in pore structure with sintering and to quantify the capillary force that tends to draw two free-standing particles together during sintering, this driving force term due to surface area changes slightly at later sinter stages. For intermediate stages where the pores may be approximated as cylinders of radius ρ, the driving force (*D.F.*) is then:

$$D.F. = \frac{\gamma}{\rho} \tag{5-3}$$

while at the final stages of sintering with closed pores of radius ρ, *D.F.* is given by [38]:

$$D.F. = \frac{2\gamma}{\rho} \tag{5-4}$$

Pressure-assisted sintering processes contribute an additional term to the driving force for densification. When an external pressure is applied, compressive stresses on the particle contacts and/or grain boundaries change the equilibrium defect concentrations there. The vacancy concentration difference created, and its contribution to *D.F.*, may be accounted for during the initial stages of sintering by adding a term $P_{app} R/\pi$ to γ such that the overall driving force for densification is then:

$$D.F. = \gamma + \frac{P_{app} R}{\pi} \tag{5-5}$$

where P_{app} is the applied pressure on a particle of radius R [38]. For later stages of sintering, the applied pressure must be rewritten as an effective stress to account for porosity in the sample, and Eqns. (5-3) and (5-4) have a component P_{app}/δ, where δ is the density of the compact, added to them to account for the applied pressure dependence in the intermediate sintering stage [38]:

$$D.F. = \frac{\gamma}{\rho} + \frac{P_{app}}{\delta} \tag{5-6}$$

and the final sintering stage [38]:

$$D.F. = \frac{2\gamma}{\rho} + \frac{P_{app}}{\delta} \tag{5-7}$$

In the above equations, γ is the surface energy and ρ is the radius of a pore at a particle-particle neck [38]. In a typical ceramic, the energy associated with γ is ~1 J/m^2 with a range of γ for ceramics reported as 0.7 to 2.5 J/m^2 [39] and 0.9 to 3.0 J/m^2 [40]. With an applied pressure of 70 MPa on a particle with a diameter of 2 μm, Eqn. (5-5) shows that the energy associated with the externally applied stress is ~22 J/m^2. Thus, one increases the initial driving force for densification by ~22 times with such an applied pressure on conventionally sized ceramic particles.

The first set of HIP samples, ramped at 10 °C/min, did not reach full density, even at 1400 °C. While this is not an unreasonable ramp rate for conventional ceramics in HIP processes, as will be detailed below, the applied pressure could not compensate for the reduced time at elevated temperature and the surface-energy driven densification processes taking place there. With a ramp rate of 10 °C/min with a 30 min soak, the total time above 800 °C for the samples sintered at 1400 °C is only 90 minutes. For a ramp rate of 2 °C/min with a 30 min soak, as utilized in the pressureless sintering approach, the total time above 800 °C is 330 minutes.

Therefore, a second set of HIP samples was ramped at 2 °C/min following the hold at 825 °C where the same 200 MPa of Ar gas pressure was applied. Surprisingly, this second set of samples reached full density only at 1400 °C, the same temperature required for pressureless sintering. Shown in Figure 5-18(a) is an SEM micrograph of

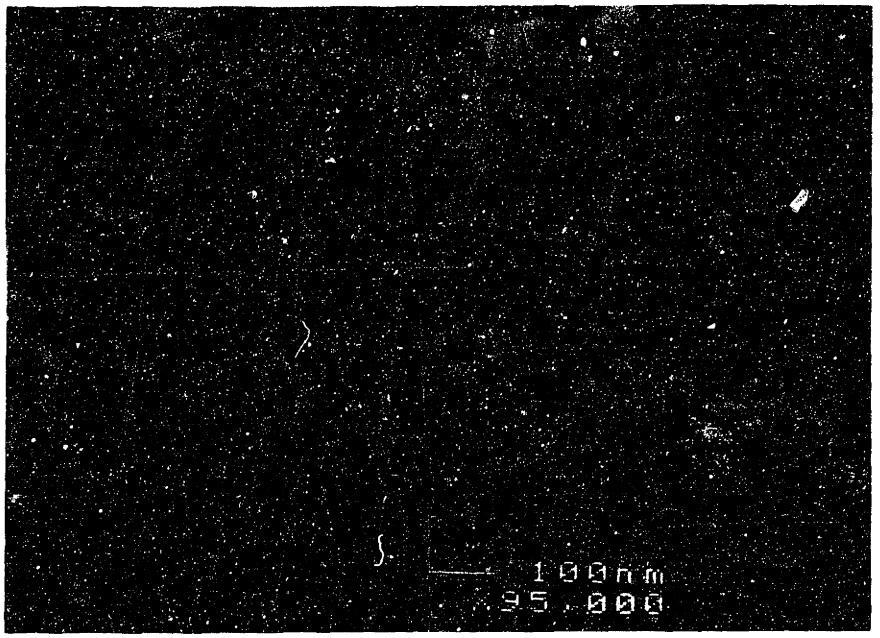

Figure 5-18a: SEM image of fracture surface of HIP at 1350 °C.

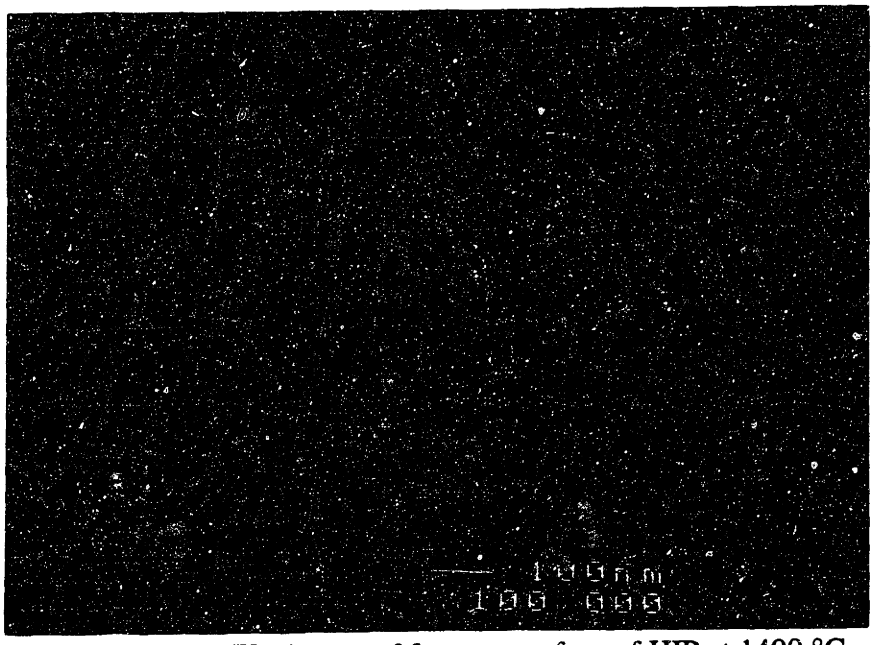

Figure 5-18b: SEM image of fracture surface of HIP at 1400 °C.

the nano-TiN HIPed at 1350 °C. This sample is < 95% dense. Shown in Figure 5-18(b) is a dense (99%) sample of nano-TiN HIPed at 1400 °C. The actual density of the HIP sample at 1400 °C was slightly higher, but within experimental uncertainty, compared to the density of the UN800 sample pressureless sintered at 1400 °C. One can also see in these micrographs evidence of the Arrhenius-like dependence of grain growth on temperature as well as the effects on grain growth of approaching full density as materials are sintered and open porosity disappears. For a temperature difference of only 50 °C, the grain size has nearly doubled from ~80 nm at 1350 °C to 155 ± 20.3 nm at 1400 °C. Because the same sintering times and temperatures were required to achieve full density in both the UN800 and HIP materials, it is not surprising that the final grain size for the two processes is identical within experimental uncertainty. Not only are the grain size values within the error bars of the measurement itself, but with the strong dependence on temperature that grain growth in these materials was shown to be, even a slight difference in 1400 °C set points of the temperature monitoring and control devices used in the pressureless sintering and HIP processes could account for the observed minor differences in grain size.

Eqns. (5-5) through (5-7) show why the applied pressure during densification did not contribute as large a benefit to the sintering of nanocrystalline materials as it does in conventional materials. During the initial stages of densification, assuming a particle radius of 5 nm, the applied pressure contribution to the sintering driving force is only 0.3 J/m^2, a fraction of the surface energy term. At intermediate times, taking an average pore diameter of 4.3 nm as measured and assuming a surface energy value of 1 J/m^2, the pressureless sintering contribution to the driving force is 465 MPa. This value is somewhat larger than the contribution of 333 MPa resulting from the applied pressure of 200 MPa scaled by a relative density of 60%. In the final stages of sintering, as shown in Eqn. (5-7), the disparity in these terms increases even more. As full density is reached, the density (δ) increases causing the P_{app} driving force term to be reduced, while the pore size (ρ) shrinks to zero, causing the surface energy driving force term to go to infinity. Thus, at all stages of sintering the nano materials, the contribution to the driving force for densification from the surface energy term is greater than the contribution of the P_{app} term. It should be noted that the almost two-fold increase in driving force at intermediate stages due to the applied pressure likely had a positive contribution to the densification

behavior at those times. However, as only points closer to full density were examined in the HIP process reported here, this effect was not detected. An additional factor in the above analysis is the non-agglomerated nature of these powders and the very sharp, and very small, pore size distribution in the UN800 compacts. These characteristics, along with the extremely high surface area of the starting powders, allowed the full benefit of pressureless sintering driving forces to be realized in these materials. It should also be noted briefly that the success observed in processing nanocrystalline materials by the pressure-assisted densification procedure of sinter forging [41] is likely due much more to grain boundary sliding and shearing mechanisms which are occurring and aiding densification in those instances than it is to any explicit "pressure" effect. Of course, in an agglomerated material, the applied pressure may also serve to break up agglomerates, thereby aiding the densification process as well.

As was shown in Figure 5-14 above, when sintering both the EXP (a) and the UN800 (b) materials, appreciable amounts of Ti_3O_5 are crystallized upon sintering. However, as shown in Figure 5-14(c), the HIP samples at 1400 °C show no evidence of this Ti_3O_5 phase, or any other Ti-O related phase. Given that these materials were not exposed to the atmosphere until they reached full density, this result is not surprising. However, what was surprising was that the chemical analysis results showed reduced, but still very appreciable, amounts of oxygen present in these HIP materials. The oxygen content was 7.9 wt%, the nitrogen content was 18.4 wt% and the titanium content was 73.7 wt%. This is a significantly lower amount of oxygen than was found in the UN800 (13.7 wt%) or EXP pellets (12.9 wt%) sintered at 1400 °C. Given Eqn. (3-2) which shows the weight one monolayer of oxygen can contribute to a high surface area material, as well as the evidenced cited in Chapter 4 regarding the detection of appreciable Ti-O peaks in ESCA data of nano-TiN powders which had been exposed to only ~ 15 ppm oxygen in a glovebox environment, it would appear that these high surface area nitrides are so prone to oxidation that they will oxidize with exposure to even a very minimal amount of oxygen. While oxygen could be introduced into the HIP or the UN800 samples through leaks in the evacuable pellet dies or CIP bags during transfer to and from the glovebox, further evidence for the assertion that the main source of oxygen is the ppm levels in the glovebox was presented above in the IR results. These results showed that even unexposed powders which were loaded and sealed in the IR cell in the glovebox have

significant Ti-O signals. The fact that Ti-O compounds are not in evidence by XRD in the HIP samples may be due to the potentially reduced amounts of this phase in the HIP samples containing 5 wt% less oxygen. Another source of oxygen in the HIP materials may be the Pyrex glass in which they were encapsulated for HIPing. There is a report of the attempted deposition of TiN films on soda-lime glass producing only a titanium oxide film. The source of the oxygen in these films was attributed to the glass itself [42]. The different method by which this oxygen would be introduced into the material may account for it not forming the Ti_3O_5 phase. As with the UN800 materials, there was no observation of secondary phases by SEM in the HIP materials.

5.3.4 Mechanical Characterization Results

The results of the mechanical characterization of these materials is presented in Table 5-1. Data presented represented averaged values of 10-15 indentations. The fracture toughness was computed using Eqn. (5-1) and a value for E of 470 MPa. As was the case for the theoretical density, there is also a spread in values of E in the literature for TiN. For "fully dense" materials, the range is from 400 MPa [43] to 640 MPa [44], with values of 440 MPa [45], 490 MPa [46] and 590 MPa [13] reported as well. The 490 MPa is a "projected value" determined from plots of E versus density in nano-TiN of various grain sizes [46]. The data was fit to a line of the form:

$$E = E_0 (1 - 3.9\,\Theta) \tag{5-8}$$

where Θ is the porosity and extended to 100% density to determine E_o. Given that the value for E_o of 490 MPa was in reasonable agreement with other values in the literature, and the fact that it was determined very recently for nano-TiN, Eqn. (5-8) with a value of 99% density (Θ = .01) was used to calculate the value used for E of 470 MPa. It should be noted that in addition to Andrievski [46], other researchers have shown that E in fully dense nanocrystalline materials is comparable to that measured in a coarse-grained counterpart [47,48]. Thus, one is justified in using a literature value, especially one determined on materials with a submicron structure, to determine K_c. The fracture toughness of the HCS and EXP samples was not determined because the porous nature of the samples caused very small radial cracks to form such that the required criteria of c

$\geq 2a$, where c is the characteristic dimension of the radial/median crack and a is the characteristic dimension of the hardness impression, was not satisfied [4].

TABLE 5-1: Mechanical Characterization Results

Sample	Hardness H_v (GPa)	Fracture Toughness K_c (MPa $m^{1/2}$)
HCS	1.7 ± 0.2	-
EXP	15.7 ± 0.7	-
UN800	23.2 ± 1.9	4.0 ± 0.2
HIP	22.4 ± 1.5	4.2 ± 0.2

The H_v value for the HCS samples is meaningless due to the high porosity (~35%) of these samples and is included only for completeness. The hardness of the EXP materials also reflects the porosity of these samples. There are reports of badly oxidized TiN powder that does not sinter well with the oxygen impurity causing microporosity, embrittlement and cracking in sintered parts that leads to a reduction in the observed mechanical properties [49]. This appears to be the case with these EXP powders as well.

A full comparison of the processing and properties of the UN800 and HIP samples to other nanocrystalline and conventional TiN materials reported in the literature follows this section. However, the hardness values reported here are among the very highest recorded for TiN and clearly reflect the effects of a nanostructured material with a reduction in the size of the strength-degrading flaws in the sintered material. The fracture toughness values are comparable to those reported in other dense TiN materials. No dependence on, or benefit from, a nanostructure is expected for fracture toughness values.

The experimental equivalence of the properties of the HIP and UN800 materials suggests that these materials which are sintered to equivalent densities with equivalent grain sizes without the presence of a second phase are relatively insensitive to the small difference (~ 5 wt%) in oxygen content. The somewhat smaller spread in the hardness data as well as the slightly higher average value of the fracture toughness in the HIP samples may be due to a greater degree of process uniformity processed in these samples due to the applied pressure during sintering.

5.3.5 Comparison of Sintering and Mechanical Characterization Results to Other TiN

The results presented above are particularly noteworthy due to the processing conditions which have been required by others to produce similarly dense TiN materials with comparable properties. Previous efforts by other researchers with lower quality starting powders either failed to achieve full density or required complicated processing schemes, such as high applied gas pressures (5 MPa N_2) [22] or high applied compaction pressures (4 GPa) [50], to achieve comparable densities. Sintering and properties results reported in the literature for both nanocrystalline and conventional TiN are described in the following sections in detail.

5.3.5.1 Nanocrystalline TiN Sintering Results

Andrievski, working with powder with a surface area of 14 m^2/g and an average particle size of 80 nm, has done much of the previous work on the consolidation of nano-TiN. With a pressureless sintering process at 1500 °C, the endpoint of the study, he produced a material which was 86% dense. It had a H_v of 10 to 18 GPa, a final grain size of 0.5 to 5 μm and a K_c value of 2.4 MPa $m^{1/2}$ [6]. Thus, he decided to pursue a fairly extreme pressure-assisted densification process whereby he applied a pressure of 4 GPa for 5 min at various elevated temperatures. As can be seen in Eqns. (5-5) through (5-7), a load of 4 GPa will help significantly in the pressure-assisted sintering of nanopowders. With the 4 GPa load applied throughout sintering, he was able to use decreased sintering temperatures to achieve 96 – 98% density at 1130 – 1200 °C. The H_v at a load of 0.5 N was 24.0 ± 1.0 GPa for samples pressed at 1130 °C and 23.5 ± 1.1 for those processed at 1200 °C; E was determined to be 412 ± 20 GPa [17] The grain size, as determined by SEM, was 100-200 nm [46]. Andrievski claimed to detect no phases other than TiN via XRD [50]. He very recently obtained and processed some higher quality nano-TiN powder, the source and characteristics of which, other than a particle size of 16-18 nm, has not been published in the literature [46]. To densify these materials he applied loads of 4 – 7.7 GPa at temperatures up to 1300 °C and made 95% dense materials with a H_v of 26.0 ± 1.0 GPa with a grain size of 30-60 nm as measured by SEM [46]. Given that this sample still had 5% porosity, the potential for maintaining this grain size to full density is unknown. He found that the hardness, while higher than that measured in conventional sintered or hot-pressed TiN, did not have the 4-6 times improvement such as that found in

nanocrystalline metals and intermetallics with a dramatically decreased grain size. He attributed the observed improvement in hardness to the nanocrystalline structure of his materials. While this processing approach was highly effective in producing nano-TiN with excellent properties, the practicality of actually forming a part in this type of process with applied pressures of 4 to 7.7 GPa is very low.

Naβ *et al.* very recently made use of still another nano-TiN under development at H.C. Starck. This powder had a specific surface area of 56 m^2/g and a primary particle size between 30 and 40 nm [51,52]. Because these powders were strongly agglomerated, they dispersed them with guanidine propionic acid leading to surface modification of the powders and green compacts of 50% density with an average pore size of 7 nm. This pore size value is slightly higher than that observed in our samples (4.3 nm) due to the packing of larger particles. This colloidal processing approach produced materials with a final grain size of 400 nm and 98% density at 1400 °C. The H_V of these materials was 21.5 GPa. As a side note related to our results, at 1300 °C these materials were 96% dense with 70 nm grains; however, as we also observed, greatly accelerated grain growth was experienced as the materials reached near full density.

Ogino *et al.* have prepared ultrafine grained (5-7 nm) TiN by sintering submicron TiN powders (0.1 to 0.2 μm) synthesized by ball milling of Ti in a nitrogen atmosphere [53]. The main drawback of this synthesis route was the incorporation of 8.8 at% Fe and 3.0 at% Cr into the powders due to contamination from the stainless steel vials and balls. By the time near full density (99%) was achieved at 1300 °C, the grain size had increased to ~ 200 nm. The hardness in these materials (~ 9.9 GPa) was also extremely low, presumably due to the large incorporation of metallic elements. Evidence for this effect comes from the fact that radial cracking was not observed in the indentation microhardness testing with loads up to 9.8 N.

Dransfield and Jones pressureless sintered one of the nano-TiN powders made by Tioxide (T25) to near full density by 1600 °C [54]. The final grain size is not stated in their paper; however, it appears to be at least 2-4 μm, based on the micrographs presented in their paper. The K_c of these materials was 3.6 MPa $m^{1/2}$. A hardness value was not reported.

Cao *et al.* produced nano-TiN by evaporation of Ti in a DC arc-plasma in a nitrogen atmosphere at 150 Torr. The average particle size of the nano-TiN was 15 nm. These

materials were compacted *in-situ* at 2.5 GPa under vacuum and were pressureless sintered. At 1300 °C, the endpoint of this study, the samples were ~ 95% dense and had a grain size of 180 nm. Rapid grain growth between 1100 °C (60 nm) and 1300 °C (180 nm) was observed during sintering. The hardness in these non-dense materials was ~ 12.8 GPa [55].

Rabe and Wäsche report sintering results on a nano-TiN under development at H.C. Starck [22]. This powder, described in Chapter 4 and above in the discussion on the development of oxygen-rich second phases in sintered nano-TiN, is utilized in a gas pressure (5 MPa N_2) sintering apparatus. It may be sintered to >98% density at 1300 °C in 30 min and is "almost pore free" with a mean grain size of 100 nm. After a soak for 30 min at 1400 °C, they achieved 99% density with the 5 MPa N_2 overpressure, but don't report the final grain size. It is worth noting that when they used a pressureless sintering process comparable to ours of 30 min at 1400 °C, they achieved only 95% density. They also observed significant grain growth with elevated temperature. For instance, after sintering at 1600 °C for 30 min in the pressureless process, the final grain size was 800 nm.

Rabe and Wäsche also report on sintering a Tioxide TiN (T36, different from that described in Chapter 4 and used by Dransfield and Jones) in the same gas pressure apparatus (5 MPa N_2) at 1550 °C with a 20 min hold time [23]. This Tioxide TiN was also generated by a plasma synthesis technique and had a surface area of 36 m^2/g with a particle size range of 15-30 nm. Final densities of 95.5% were reached in sintering this material. As detailed above, this material contained a high level of oxygen and a considerable amount of an oxygen-rich second phase. Unfortunately, Rabe and Wäsche don't give any property data for either of their sintered TiN materials. Given the similarities in microstructure and oxygen content between our materials and theirs, it would have been interesting to compare property results.

5.3.5.2 Conventional TiN Sintering Results

No successful pressureless sintering results with conventional TiN powders have been reported in the literature. However, a variety of pressure-assisted processes have been utilized to densify conventional TiN. These processes and the results achieved with them are outlined briefly in the following paragraphs.

One of the first efforts at producing a dense TiN was made by Yamada *et al.* They used a hot press process with 3 or 5 GPa applied for 60 min on 50 nm powders to produce materials which were ≥ 95% of theoretical density at 1500 °C. They found at higher sintering temperatures that this was an end point density. These samples had a 1.45 μm grain size and a H_v of 18 GPa when dense [18, 56]. Yamada also used a HIP process of 200 MPa at 1600 °C to produce a material which was 98.5% dense [57]. No property values for these materials were reported.

Moriyama *et al.* used conventional hot-pressing of micron-sized powders at 2100 °C and an applied load of 140 MPa to produce a 93% dense material. These samples had a grain size of 10 μm or greater and a porosity-reduced H_v of 8.5 GPa [58].

Rapoport *et al.* used powders with particle sizes of 1.5 – 1.8 μms from H.C. Starck. They hot pressed these powders, which were very similar to the HCS powders used as a basis for comparison in our work, at 40 MPa and 1600 °C for 30 min to produce materials which were 97.5% dense. The final grain size in these samples was 5 - 6 μm and the hardness was 18.1 GPa [59].

Torizuka *et al.* very recently described a sinter plus HIP effort that started with 2.0 μm powders and produced 100% dense materials. They used a HIP at 200 MPa and 1600 °C after initial pressureless sintering at 1700 °C. It is noteworthy that after the pressureless sintering at 1700 °C, the materials were only 86% dense. The observed final grain size is in excess of 20 μm [60]. H_v of these materials was 13.7 GPa while the K_c was 4.3 MPa $m^{1/2}$.

Berdikov *et al.* used hot-pressing of ultradispersed TiN to produce a 99% dense TiN. These materials had a final grain size of 100-300 nm, a K_c value of 3.5 MPa $m^{1/2}$ and a H_v value of 15.7 GPa. Additionally, he reported a value for E of 440 MPa [45].

Okuda *et al.* used 1.47 μm powders in a HIP process of 196 MPa at 1500 °C for 2 hours to produce a 98.9% dense TiN material with a final grain size of 3 μm. The K_c of these materials was 3.7 MPa $m^{1/2}$. No hardness data was presented [43].

As a basis for further comparison with our results, a TiN single crystal (111) film deposited by a magnetron sputtering process yielded a H_v of 22.6 ± 1.96 GPa, which is very comparable to the values measured in our nanocrystalline UN800 and HIP samples. It should be noted however, that this test was done with only a 0.05 N load and thus may even be an overestimate of the single crystal hardness value of TiN [61]. More recently,

extremely hard films of TiN have been produced. The hardness of the best films typically ranges from 24.5 – 39.2 GPa [14]. However, other film hardness values of 18.6 – 24.3 GPa [62], more in line with those values produced in the pressureless sintering process outlined here, have also been reported.

In order to facilitate comparison of the processing and property results reported above, Table 5-2 was prepared. Materials in that table are ranked by decreasing hardness. Because of different processing and measurement techniques, it should be noted that for all the hardness and grain size comparisons shown in the table and discussed above, small differences in values are likely not significant. However, at the same time, it should be noted that our H_v data is among the very highest values reported for this parameter in TiN and is certainly higher than that observed in the conventionally sintered or hot-pressed conventional materials. Additionally, these hardness values were achieved in a pressureless sintering process without the use of applied pressure or sintering additives.

The values of H_v in Table 5-2 for TiN materials which are near full density and don't have some other interfering issue such as the 11.8 at% metals in Ogino's materials [53], can be plotted versus the inverse square root of grain size as shown in Figure 5-19. The data point for the UN800 materials is shown as an oval in Figure 5-19. This plot indicates that TiN shows an increasing hardness (H) with decreasing grain size (G) as described by:

$$H = H_o + \mathrm{k}\, G^{-1/2} \tag{5-9}$$

Down to a certain grain size this effect is observed for a majority of nanocrystalline metals and intermetallic compounds [47,48,63], but demonstrated instances of this behavior in nanocrystalline nitride ceramics are rare due to the difficulty in maintaining a fine grain size in a fully dense material. This same behavior has also been noted in nanocrystalline TiO_2 [31]. Additionally, Averback *et al.* found, as we did, that the H_v of their dense nano-TiO_2 was about equal to that in single crystal TiO_2 [31].

The effect of grain size on fracture strength, and thus hardness, in ceramics has generally been interpreted in terms of a dependence

$$\sigma = f(G^{-1/2}) \tag{5-10}$$

TABLE 5-2: Comparison of Processing Routes and Properties of TiN

Researcher(s)	Technique/Conditions	Density	Grain Size (nm)	H_v (GPa)
R.A. Andrievski [46]	Hot Press: 4 – 7.7 GPa, 1300 °C (16 – 18 nm)	95%	30 - 60	26.0 ± 1.0
R.A. Andrievski [46,50]	Hot Press: 4 GPa, 1200 °C (80 nm)	98%	100 - 200	23.5 ± 1.1
Castro and Ying	**Pressureless: 0.1 MPa N_2, 1400 °C**	**99%**	**140**	**23.2 ± 1.9**
B.O. Johansson [61]	Magnetron Sputtering	100%	Single Crystal	22.6 ± 2.0
R. Naβ [51,52]	Pressureless: 1400 °C (colloidal processing)	98%	400	21.5
E. Rapoport [59]	Hot Press: 40 MPa, 1600 °C	97.5%	5,000 – 6,000	18.1
T. Yamada [18,56]	Hot Press: 40 MPa, 1600 °C	95% (of theo.)	1,450	18.0
S. Torizuka [60]	Pressureless (1700 °C) plus HIP (200 MPa, 1600 °C)	100%	20,000+	13.7
R.A. Andrievski [6]	Pressureless: 1500 °C (80 nm)	86%	500 - 5000	10 - 18
L. Cao [55]	Pressureless: 1300 °C (2.5 GPa initial compaction)	95%	180	12.8
M. Moriyama [58]	Hot Press: 140 MPa, 2100 °C	94%	10,000+	10 - 11
Y. Ogino [53]	Pressureless: 1300 °C (ball milled powders, 11.8 at% Fe/Cr)	99%	200	9.9
T. Rabe [22]	Gas Pressure Sintering: 5 MPa N_2, 1300 °C	98%	100	-

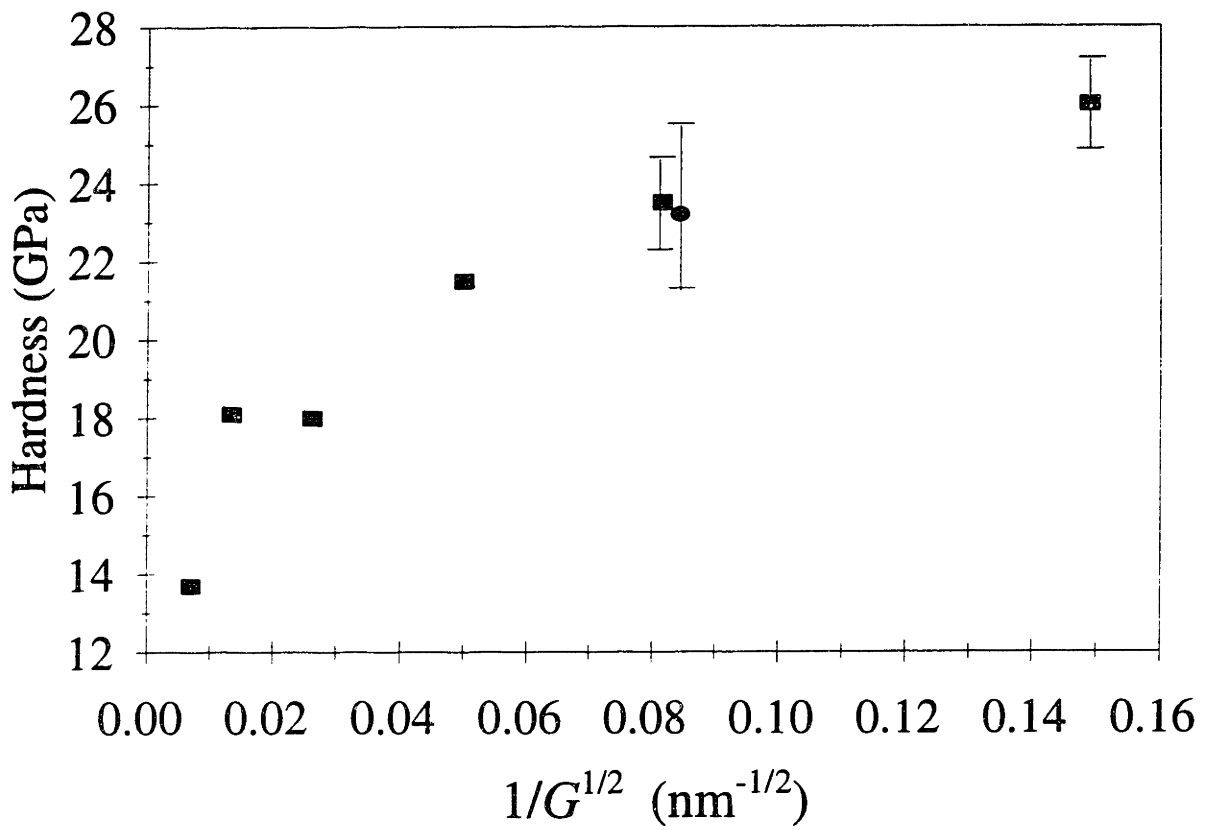

Figure 5-19: Hardness dependence on grain size for TiN.

where σ is the fracture strength and G the grain size [64,65]. Davidge and Evans suggest that the strength of a ceramic may be controlled by either the stress to propagate inherent flaws or the stress to nucleate and/or propagate flaws formed during a plastic deformation process [64]. Thus, there are two regions for the variation of fracture strength with grain size, both of which show a $G^{-1/2}$ dependence. At larger grain sizes, fracture is initiated at inherent flaws with a dependence

$$\sigma \propto \frac{1}{C^{1/2}} \tag{5-11}$$

where C is the inherent flaw or crack length [64]. This flaw size C is related to microstructural features such as the pore or grain size. In fact, it has been shown in fully dense MgO that $C \propto G^{0.8}$ [64]; thus, in this first region (Region I), fracture occurs by the extension of inherent flaws and $\sigma \propto G^{-1/2}$. At finer grain sizes, dislocations may pile up against a stable barrier, such as a grain boundary, and a large stress concentration is generated in the vicinity of these dislocations. If this stress is not relieved by plastic flow, cracks may be initiated at the pile-up. The shear stress τ is given by

$$\tau = \tau_0 + \frac{k_s}{L^{1/2}} \tag{5-12}$$

where τ_0 is the dislocation flow stress, k_s is a term that depends on the effective surface energy for localized crack initiation and L is the length of the pile-up [64]. In this second region (Region II), with the grain boundary acting as a dislocation source, the minimum value for the crack initiation stress is obtained with $L = G$. Thus, in Region II at finer grain sizes, where fracture is initiated by plastic flow, again, $\sigma \propto G^{-1/2}$. Carniglia [65] has shown that strength/grain size data for various ceramics, including Al_2O_3, BeO and MgO, follow this type of two-stage behavior as outlined by Davidge and Evans [64]. The classic model of Hall-Petch fracture is based on the same ideas of plastic deformation of grains and the pile-up of dislocations at grain boundaries outlined for Region II; however, the Petch model does not incorporate the concept of a pre-existing flaw or crack [66].

Given that dislocations are seldom observed in nanostructured ceramics [48] and the fact that dislocations in brittle ceramics are relatively immobile at low temperatures even when present [67], it would appear that the hardness improvement observed in our

nano-TiN is not due to "Region II," or classical Hall-Petch, plastic deformation/dislocation fracture. Additionally, Averback *et al.*, while stating that the reasons for their observed Hall-Petch-like behavior in nano-TiO_2 are "presently unclear," do note that dislocations are unlikely to be involved for grain sizes below 400 nm [31]. Furthermore, diffusional creep processes, with $\dot{\varepsilon} \propto \sigma$, in addition to typically occurring at higher temperatures, do not have a $G^{-1/2}$ dependence. For instance, the steady-state creep rate for Nabarro-Herring creep is proportional to G^{-2} [68,69] and that for Coble creep is proportional to G^{-3} [70]. Thus, it seems most probable that the increased hardness for TiN with decreasing grain size, over the grain size range outlined above, is due to reductions in the inherent flaw sizes (Region I behavior) with reductions in the particle and grain sizes of the materials studied.

As noted above, there is no evidence in the literature for an increase in K_c values in a nanostructured material. For instance, in fully dense TiO_2, when the grain size was less than 500 nm, the fracture toughness was independent of grain size and similar to that found in single crystal TiO_2 [48]. There is even one report of a decrease in K_c in an ultrafine grained SiC [47]. Thus, it is not surprising that the K_c values reported here for the UN800 (4.0 MPa m $^{1/2}$) and the HIP (4.2 MPa m $^{1/2}$) materials fall within the range of other values (3.5 – 4.3 MPa m $^{1/2}$ [45,60]) for TiN described in the literature.

5.4 Summary

This chapter describes greatly enhanced sinterability in the nano-TiN produced in the tubular flow reactor. A dense (99%), extremely hard (23.2 GPa) nanostructured (140 nm) TiN has been produced through a pressureless sintering process emphasizing improved powder handling procedures. The microstructure that develops in the sintered samples is a very strong function of the quality of the starting powders. The enhanced sinterability of the nano-TiN, likely due to its very narrow pore size distribution in the green state, as well as the need to address the oxidation tendencies of nano-nitrides, has been demonstrated.

5.5 References

[1] P. Kubelka and F. Munk, "Ein Beitrag zur Optik der Farbanstriche," *Z. Tech. Phys.*, **12** 593-601 (1931).

[2] P. Kubelka, "New Contributions to the Optics of Intensely Light-Scattering Materials. Part I," *J. Opt. Soc. Am.*, **38** 448-457 (1948).

[3] M.I. Mendelson, "Average Grain Size in Polycrystalline Ceramics," *J. Am. Ceram. Soc.*, **52** [8] 443-446 (1969).

[4] G.R. Anstis, P. Chantikul, B.R. Lawn, and D.B. Marshall, "A Critical Evaluation of Indentation Techniques for Measuring Fracture Toughness: I, Direct Crack Measurements," *J. Am. Ceram. Soc.*, **64** [9] 533-538 (1981).

[5] Y. Sakka, S. Ohno, and M. Uda, "Oxidation and Degradation of Titanium Nitride Ultrafine Powders Exposed to Air," *J. Am. Ceram. Soc.*, **75** [1] 244-248 (1992).

[6] R.A. Andrievski, R.A. Lyutikov, O.D. Torbova, V.I. Torbov, V.G. Vil'chinskii, O.M. Grebtsova, E.P. Domashneva, A.A. Eremenko, and A.Z. Rakhmatullina, "Gas Evolution and Porosity Changes During Sintering of Highly Dispersed Titanium Nitride," *Inorg. Mater.*, **29** [12] 1474-1477 (1993).

[7] M. Primet, P. Pichat and M.V. Mathiu, "Infrared Study of the Surface of Titanium Dioxides," *J. Phys. Chem.*, **75** [9] 1216-1220 (1971).

[8] T. Lopez, E. Sanchez, P. Bosch, Y. Meas, and R. Gomez, "FTIR and UV-Vis (Diffuse Reflectance) Spectroscopic Characterization of TiO_2 Sol-Gel," *Mater. Chem Phys.*, **32** 141-152 (1992).

[9] B.A. Morrow, "Surface Groups on Oxides," pp. A196-A200 in Spectroscopic Characterization of Heterogeneous Catalysts, (Elsevier, New York, 1990).

[10] R.M. Silverstein, G.C. Bassler, and T.C. Morrill, Spectrometric Identification of Organic Compounds, (John Wiley & Sons, New York, 1991).

[11] R.A. Nyquist, C.L. Putzig, and M.A. Leugers, Infrared and Raman Spectral Atlas of Inorganic Compounds and Organic Salts: Infrared Spectra, (Academic Press, Boston, 1997).

[12] F.L. Riley, "Nitrides" pp. 3206-3210 in Encyclopedia of Materials Science and Engineering, Vol. 4, ed. M.B. Bever, (Pergamon Press, 1986).

[13] H. Holleck, "Material Selection for Hard Coatings," *J. Vac. Sci. Technol. A*, **4** [6] 2661-2669 (1986).

[14] J. Patscheider, L. Shizhi, and S. Veprek, "Plasma-Induced Deposition of Titanium Nitride from $TiCl_4$ in a Direct Current Glow Discharge: Control of the Chlorine Content and Gas-Phase Nucleation," *Plasma Chemistry and Plasma Processing*, **16** [3] 341-363 (1996).

[15] H.C. Starck Product Literature for Titanium Nitride.

[16] CRC Handbook of Chemistry and Physics, 72nd ed., ed. D.R. Lide, (CRC Press, Boston, 1991).

[17] R.A. Andrievski, G.V. Kalinnikov, A.F. Potafeev, and V.S. Urbanovich, "Synthesis, Structure and Properties of Nanocrystalline Nitrides and Borides," *Nanostr. Mater.*, **6** 353-356 (1995).

[18] T. Yamada, M. Shimada, and M. Koizumi, "Fabrication and Characterization of Titanium Nitride by High Pressure Hot Pressing," *Am. Ceram. Soc. Bull.*, **59** [6] 611-616 (1981).

[19] R.A. Andrievski, "Compaction and Sintering of Ultrafine Powders," *J. Powd. Metall.*, **30** [1] 59-66 (1994).

[20] T. Vasilos and W. Rhodes, "Fine Particulates to Ultrafine-Grain Ceramics," pp. 137-172 in Ultrafine-Grain Ceramics, ed. J.J. Burke, N.L. Reed, and V. Weiss, (Syracuse University Press, 1970).

[21] R.A. Andrievski, V.I. Torbov, and E.N. Kurkin, "Nanocrystalline Titanium Nitride," pp. 649-655 in Plansee Proceedings: Coating Technology, Volume 3, (Metallwerk Plansee, Reutte, 1993).

[22] T. Rabe and R. Wäsche, "Development of Dense Nanocrystalline Titanium Nitride," *Ceram. Trans.*, **51** 793-798 (1995).

[23] T. Rabe and R. Wäsche, "Sintering Behavior of Titanium Nitride Powders," *Nanostr. Mater.*, **6** 357-360 (1995).

[24] R. Wäsche and G. Steinborn, "Influence of Dispersants in Gelcasting of Nanosized TiN," *J. Europ. Ceram. Soc.*, in press.

[25] H. Iwasaki, N.F.H. Bright, and J.W. Rowland, "The Polymorphism of the Oxide Ti_3O_5," *J. Less-Comm. Metals*, **17** 99-110 (1969).

[26] M.J. Mayo, "Superplasticity of Nanostructured Ceramics," pp. 361-380 in Mechanical Properties and Deformation Behavior of Materials Having Ultra-Fine Microstructures, ed. M. Nastasi, D.M. Parkin, and H. Gleiter, (Kluwer Academic Publishers, Netherlands, 1993).

[27] M.J. Mayo, "Thermomechanical Stability of Nanocrystalline Microstructures and Their Role in Enhancing Superplastic Deformation," pp. 541-550 in Superplasticity in Advanced Materials, ed. S. Hori, M. Tokizane, and N. Furushiro, (The Japan Society for Research on Superplasticity, 1991).

[28] W.D. Kingery and B. Francois, "Grain Growth in Porous Compacts," *J. Am. Ceram. Soc.*, **48** [10] 546-547 (1965).

[29] R.J. Brook, "Pore-Grain Boundary Interactions and Grain Growth," *J. Am. Ceram. Soc.*, **52** [1] 56-57 (1969).

[30] T.K. Gupta, "Possible Correlation Between Density and Grain Size During Sintering," *J. Am. Ceram. Soc.*, **55** [5] 276-277 (1972).

[31] R.S. Averback, H.J. Höfler, H. Hahn, and J.C. Logas, "Sintering and Grain Growth in Nanocrystalline Ceramics," *NanoStr. Mater.*, **1** 173-178 (1992).

[32] C.A. Bruch, "Sintering Kinetics for the High Density Alumina Process," *Ceram. Bull.*, **41** [12] 799-806 (1962).

[33] R.L. Coble, "Development of Microstructure in Ceramic Systems," pp. 658-679 in Ceramic Microstructures: Their Analysis, Significance and Production, ed. R.M. Fulrath and J.A. Pask, (John Wiley & Sons, New York, 1968).

[34] R.L. Coble and J.E. Burke, "Sintering in Ceramics," pp. 197-251 in Progress in Ceramic Science: Volume 3, ed. J. E. Burke, (The MacMillan Company, New York, 1963).

[35] G.R. Chol, "Influence of Milled Powder Particle Size Distribution on the Microstructure and Electrical Properties of Sintered Mn-Zn Ferrites," *J. Am. Ceram. Soc.*, **54** [1] 34-39 (1971).

[36] M.J. Mayo and D.J. Chen, "Densification Versus Grain Growth in Nanocrystalline ZrO_2 - 3 mol% Y_2O_3: How to Win," pp. 227-236 in Synthesis and Processing of Nanocrystalline Powder, ed. D.L. Bourell, (The Minerals, Metals & Materials Society, 1996).

[37] W.D. Kingery, H.K. Bowen, and D.R. Uhlmann, Introduction to Ceramics, 2nd ed., p. 469 (John Wiley & Sons, New York, 1976).

[38] R.L. Coble, "Diffusion Models for Hot Pressing with Surface Energy and Pressure Effects as Driving Forces," *J. Appl. Phys.*, **41** [12] 4798-4807 (1970).

[39] D. Vollath and K.E. Sickafus, "Synthesis of Ceramic Oxide Powders in a Microwave Plasma Device," *J. Mater. Res.*, **8** [11] 2978-2984 (1993).

[40] I.J. McColm and N.J. Clark, Forming, Shaping and Working of High Performance Ceramics, pp. 13-19, (Chapman and Hall, New York, 1988).

[41] H.J. Höfler and R.S. Averback, "Sinter-Forging of Nanocrystalline TiO_2," pp. 9-14 in Nanophase and Nanocomposite Materials, ed. S. Komarneni, J.C. Parker, and G.J. Thomas, (Materials Research Society, Pittsburgh, PA, 1993).

[42] S.R. Kurta and R. G. Gordon, "Chemical Vapor Deposition of Titanium Nitride at Low Temperatures," *Thin Solid Films*, **140** 277-290 (1986).

[43] K. Okuda, K. Shibata, M. Yoshinaka, K. Hirota, and O. Yamaguchi, "Fabrication and Mechanical Properties of TiN/ZrO_2 Composites by Hot Isostatic Pressing," *J. Mater. Sci. Lett.*, **15** 1615-1617 (1996).

[44] E. Török, A.J. Perry, L. Chollet, and W.D. Sproul, "Young's Modulus of TiN, TiC, ZrN and HfN," *Thin Solid Films*, **153** 37-43 (1987).

[45] V.F. Berdikov, Y.N. Vil'k, O.I. Pushkarev, and E.A. Lavrenova, "Micromechanical Characteristics of Hot-Pressed Titanium Nitride from Ultradispersed Powders," *Strength of Mater.*, **25** [3] 228-230 (1993).

[46] R.A. Andrievski, "Physical-Mechanical Properties of Nanostructured Titanium Nitride," *Nanostr. Mater.*, **9** 607-610 (1997).

[47] K. A. Padmanabhan and H. Hahn, "Microstructures, Mechanical Properties and Possible Applications of Nanostructured Materials," pp. 21-32 in Synthesis and Processing of Nanocrystalline Powder, ed. D.L. Bourell, (The Minerals, Metals & Materials Society, 1996).

[48] H. Hahn and K.A. Padmanabhan, "Mechanical Response of Nanostructured Materials," *Nanostr. Mater.*, **6** 191-200 (1995).

[49] Y. Yamamoto and J. Suzuki, "Titanium Nitride Base Cermets with High Toughness," U.S. Patent 4563215, (1986).

[50]. R.A. Andrievski, "Particulate Nanostructured Silicon Nitride and Titanium Nitride," *ACS Symposium Series*, **622** 294-301 (1996).

[51] R. Naβ. S. Albayrak, M. Aslan, and H. Schmidt, "Processing and Sintering of Nanosized TiN," pp. 47-54 in Advanced Materials in Optics, Electro-Optics and Communication Technologies, P. Vincenzini, ed., (Techna Srl, 1995).

[52] R. Naβ, S. Albayrak, M. Aslan, and H. Schmidt, "Colloidal Processing and Sintering of Nano-Scale TiN," *Ceram. Trans.*, **51** 591-596 (1995).

[53] Y. Ogino, M. Miki, T. Yamasaki, and T. Inuma, "Preparation of Ultrafine-Grained TiN and (Ti,Al)N Powders by Mechanical Alloying," *Mater. Sci. Forum*, **88-90** 795-800 (1992).

[54] G.P. Dransfield and A.G. Jones, "The Pressureless Sintering of an Ultrafine, Plasma Synthesized Titanium Nitride Powder," pp. 529-534 in Euro-Ceramics II: Basic Science and Processing of Ceramics, (DKG, Cologne, 1993).

[55] L. Cao, S.O. Yang, and Y. Tang, "Synthesis of Titanium Nitride Nanostructured Materials," *Trans. Mat. Res. Soc. Jpn.*, **16B** 1505-1508 (1994).

[56] T. Yamada, M. Shimada, and M. Koizumi, "Fabrication and Characterization of Titanium Nitride by High Pressure Hot Pressing," *Ceram. Bull.*, **59** [6] 611-616 (1980).

[57] T Yamada, M. Shimada, and M. Koizumi, "Fabrication of TiN by Hot Isostatic Pressing," *Yogyo-Kyokai-Shi*, **89** [11] 621-625 (1981).

[58] M. Moriyama, K. Komata, and Y. Kobayashi, "Mechanical and Electrical Properties of Hot-Pressed TiN Ceramics Without Additives," *J. Ceram. Soc. Jpn.*, **99** 286-291 (1991).

[59] E. Rapoport, C. Brodhag, and F. Thévenot, "Hot Pressing of Titanium Nitride Powders," *Revue de Chimie minérale*, **22** [4] 456-466 (1985).

[60] S. Torizuka and T. Kishi, "Effect of SiC and ZrO_2 on Sinterability and Mechanical Properties of Titanium Nitride, Titanium Carbonitride and Titanium Diboride," *Materials Transactions, JIM*, **37** [4] 782 - 787 (1996).

[61] B.O. Johansson, J.-E. Sundgren, J.E. Greene, A. Rockett, and S.A. Barnett, "Growth and Properties of Single Crystal TiN Films Deposited by Reactive Magnetron Sputtering," *J. Vac. Sci. Technol. A*, **3** [2] 303-307 (1985).

[62] X.Y. Li, F.J. Wang, T.C. Ma, and Y.K. Wang, "Characterization of TiN Coatings Prepared by Ion-Beam-Enhanced Deposition," *Mater. Sci. Eng. A*, **139** 225-229 (1991).

[63] R.A. Andrievskii, "Synthesis and Properties of Nanocrystalline Refractory Compounds," *Russian Chem. Rev.*, **63** [5] 411-427 (1994).

[64] R.W. Davidge and A.G. Evans, "The Strength of Ceramics," *Mater. Sci. Eng.*, **6** 281-298 (1970).

[65] S.C. Carniglia, "Reexamination of Experimental Strength-vs-Grain Size Data for Ceramics," *J. Am. Ceram. Soc.*, **55** [5] 243-249 (1972).

[66] N.J. Petch, "Cleavage Strength of Polycrystals," *J. Iron Steel Inst.*, **174** [1] 25-28 (1953).

[67] M.G.S. Naylor and T.F. Page, "Microstructural Studies of the Temperature-Dependence of Deformation Structures Around Hardness Indentations in Ceramics," *J. Microscopy*, **130** 345-360 (1983).

[68] F.R.N. Nabarro, "Steady-State Diffusional Creep," *Philos. Mag.*, **16** [140] 231-237 (1967).

[69] C. Herring, "Diffusional Viscosity of a Polycrystalline Solid," *J. Appl. Phys.*, **21** 437-445 (1950).

[70] R.L. Coble, "A Model for Boundary Diffusion Controlled Creep in Polycrystalline Materials," *J. Appl. Phys.*, **34** [6] 1679-1682 (1963).

6. Suggestions for Future Work

The time, effort and expense which went into designing and building the reactor should allow it to continue to produce interesting and novel nanocrystalline materials for several years to come. While the only metals evaporated to date are Si, Ti and Al, the flexibility and robustness of the thermal evaporation system should allow the evaporation of almost any metal with a melting point below 1900 °C. While pursuing the synthesis of other pure metals and nitrides would be worthwhile, the production of very high surface area, unagglomerated nanocrystalline oxides in this reactor should also be considered. The main concern to pursuing these oxide syntheses would be the presence of oxygen in the gas stream. The injection and ionization of O_2 in the microwave plasma should cause no significant difficulties. The main problem would be the back-flow of oxygen-containing gas from the injection point over the copper electrodes of the thermal evaporation source. However, by minimizing the total amount of O_2 gas flow, as well as by correctly choosing the proportion between upstream and downstream injection and gas flows, it should be possible to work around this issue. Additionally, the vacuum pump fluids should be changed to be made compatible with oxygen species in the gas stream.

Given the success in the evaporation of both Ti and Al, as well as other on-going research efforts in this laboratory, the synthesis of nanocrystalline TiO_2 and Al_2O_3 in this reactor should be seriously considered. In addition to producing a much less agglomerated powder than is possible by the chemical precipitation route, it may be possible to utilize the microwave plasma component of the reactor for the direct synthesis of nanocrystalline α-Al_2O_3, a desirable high temperature phase of Al_2O_3. As described in Chapter 3, the high temperature of the plasma has allowed the direct synthesis of high temperature phases of various materials such as the β-Si_3N_4 reported in this thesis or the β-Mn and γ-Fe reported by Iwama.

Zr, with a melting point of ~1852 °C, is just at the edge of the thermal evaporation temperature limit, but may be a metal precursor for interesting nitride and oxide materials. ZrN is another extremely hard, refractory nitride with unusual properties, but, as was the case with TiN, it is also relatively unsinterable and of little significant use currently. ZrO_2 is a much more widely used and studied material; synthesis of nano-ZrO_2 in the reactor should yield the same benefits of a relatively unagglomerated, very high

surface area powder with a narrow, monodisperse particle size distribution as were seen with nano-TiN.

As a final synthesis suggestion, it may be possible to produce more fully nitrided Si_3N_4 in the reactor if the collection filter were physically moved forward to the tail end of the plasma plume. In this manner, Si/Si_3N_4 particles deposited on the filter could experience essentially an infinite residence time as they were held in the end of the plasma of activated nitrogen species. Thus, the long times described in section 4.4 required for diffusion of N through the Si_3N_4 product shell may be achieved. Potential drawbacks to this approach may be interparticle sintering of the nanoparticles deposited on the filter leading to hard agglomeration as well as the potential for the metal filter material destructively interfering with the microwave plasma.

From a processing perspective, an interesting sintering study would be to examine the effect of mixing various amounts of a nanocrystalline powder with a commercial powder. By "doping" the commercial powder with some amount of nanocrystalline material, it may be possible to achieve good particle packing as the finer, nanocrystalline powders fill in the interparticle packing voids of the larger conventional powder. Benefits to using such an approach might be the use of smaller quantities of the more expensive nanocrystalline materials while still facilitating densification of the readily available conventional powders.

Further conventional mechanical testing of these materials will be problematic in that producing large enough samples for testing in typical apparatus will be difficult. The exception to this, of course, would be nano-indentation testing, requiring only small volumes of material. While mechanical testing at elevated temperature would be interesting, the equipment issues for performing such testing in a controlled atmosphere will be quite challenging, and will also likely be complicated by sample size issues.

7. Conclusions

The focus of this thesis was in synthesizing and processing nanocrystalline nitride ceramics with low-temperature sinterability by exploiting the high diffusivities, extreme reactivities and ultrafine microstructure characteristic of nanocrystalline materials.

The high-quality, non-agglomerated nanocrystalline powders were synthesized through the novel tubular reactor, designed and built as part of this thesis project. This reactor made use of a forced gas flux and filtration system to increase nanocrystal production rate and collection efficiency, as well as improve the properties (particle size, degree of agglomeration, surface area) of the nanocrystals synthesized beyond those produced by alternate synthesis routes. This reactor represents a 10-fold increase over the production rates achievable in the traditional batch-type reactors for the synthesis of nanocrystalline materials. A key in tailoring the characteristics of the powder produced in the reactor was the use of a microwave-generated plasma. This high temperature N_2-plasma, in addition to facilitating the nitridation of the nanoparticles to produce nanocrystalline nitrides *in-situ*, served to extend the time for particle growth by coalescence, leading to a less agglomerated and more monodisperse-sized product.

The effects of synthesis parameters on the generation of nanoparticles, in terms of the size, morphology, and composition of the particles produced in the Si-N and Ti-N systems have been presented. The nano-Si synthesized (particle size: 6 nm, surface area: 485 m^2/g) undergoes external nitridation and conversion to Si_3N_4 by the relatively low temperature of 1050 °C. The Si_3N_4 (particle size: 11 nm, surface area: 270 m^2/g) and TiN (particle size: 9 nm, surface area: 225 m^2/g) nanoparticles produced in this reactor are among the very highest, if not the highest, quality (smallest size, highest surface area, least agglomeration) powders currently cited in the literature for these nitrides. An analysis of the nitridation kinetics in the Si-N and Ti-N systems differentiated between the formation processes of these materials in this reactor. The covalent nature of the bonding in Si_3N_4 greatly limited the diffusivity of N through the forming Si_3N_4 product shell, and thus limited the degree of nitridation and conversion. However, the mixed bonding of TiN led to higher effective diffusivities for N, and, in the presence of the microwave plasma, full stoichiometry in these materials was achieved.

Examination of the surface properties of these nanocrystalline nitrides, in conjunction with the sintering results utilizing them, highlighted the need for processing

which addresses the proclivity for oxidation of these materials. In particular, it was found that upon exposure to air the surfaces of these powders were greatly enriched in OH, NH_x, C and O-related species. IR and TGA results suggested that these ultrahigh surface area materials pick up at short times almost all the gaseous adsorbents which they are going to scavenge, with further continued oxidation the only significant change with time. The more contaminated surfaces of powders exposed to the atmosphere led to less effective sintering.

The microstructures developed from sintering in the TiN system demonstrate the enhanced sinterability of nano-TiN and the tremendous potential for pressureless sintering of monodisperse, high surface area nanocrystalline nitride powders. The processing scheme outlined generated dense, nano-structured TiN, with final grain sizes of ~140 nm, through a pressureless sintering process emphasizing improved powder handling procedures. These fine-grained materials have values of H_v (23.2 GPa) which are among the highest recorded in the literature for TiN. These sintering and property results are particularly noteworthy in comparison to those noted previously in the literature due to the complicated processing conditions required by other researchers utilizing lower quality starting powders. With the extremely high surface areas of the starting powders and the very small and narrow pore size distribution (average pore diameter of 4.3 nm) in the green compacts of the nano-TiN, pressure-assisted densification had little to no effect on the sintering times and temperatures required to reach full density. Additionally, other than a partial reduction in the amount of the oxygen incorporated, those materials processed by hot isostatic pressing have essentially equivalent properties to those processed via the pressureless sintering route. In addition to the demonstration of a novel synthesis procedure for the production of nanocrystalline nitrides, this thesis has yielded new knowledge on the processing and properties of non-oxide ultrafine ceramic materials.

Biographical Note

The author received his S.B. in Materials Science & Engineering from the Massachusetts Institute of Technology (MIT) in 1992. His undergraduate thesis with Prof. Yet-Ming Chiang on "Stress-Induced Kinetic Demixing in Yttria-Stabilized Zirconia" was recognized as the best senior thesis in MIT's Department of Materials Science & Engineering that year. As an undergraduate, he was awarded membership in the Tau Beta Pi, Phi Beta Kappa and Sigma Xi honor societies and was certified as an Engineer-in-Training in the Commonwealth of Massachusetts. He was also a four year U.S. Army ROTC scholarship recipient and was commissioned as a 2nd Lieutenant in the U.S. Army Chemical Corps upon graduation.

He began working toward a Sc. D. in ceramics at MIT in the Fall of 1992, joining the newly formed research group of Professor Jackie Y. Ying in the Department of Chemical Engineering. He was a National Defense Science & Engineering Graduate Fellow from 1992 to 1995. He won the Outstanding Presentation Award at the Third International Conference on Nanostructured Materials in July, 1996 and a Materials Research Society Graduate Student Award in December, 1996. He is a member of the American Ceramic Society, Materials Research Society, and The Minerals, Metals & Materials Society.

Following completion of the Chemical Officer Basic Course at the U.S. Army Chemical School at Ft. McClellan, AL, he is taking a position as a Senior Research Engineer within 3M's Ceramic Technology Center in St. Paul, MN.

THESIS PROCESSING SLIP

FIXED FIELD: ill. _____ name _____

index _____ biblio _____

▶ COPIES: (Archives) Aero Dewey Eng Hum

Lindgren Music Rotch (Science)

TITLE VARIES: ▶☐ _____

NAME VARIES: ▶☐ _____

IMPRINT: (COPYRIGHT) _____

▶ COLLATION: 199 l

▶ ADD. DEGREE: _____ ▶ DEPT.: _____

SUPERVISORS: _____

NOTES:

cat'r: date:

page: 538

▶ DEPT: MatSci&E

▶ YEAR: 1997 ▶ DEGREE: Sc.D.

▶ NAME: CASTRO, Darren Thomas